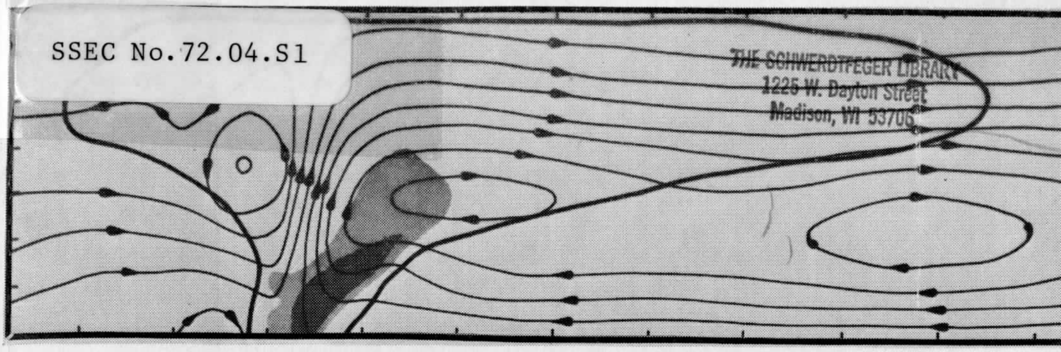

ANNUAL REPORT - 1971:

STUDIES OF THE ATMOSPHERE USING AEROSPACE PROBINGS

Volume I: Theoretical Studies

Principal Investigator: V. E. Suomi
Director: John A. Young
Contributors: Larry J. Mahrt
Robert E. Schlesinger

SPACE SCIENCE AND ENGINEERING CENTER, UNIVERSITY OF WISCONSIN

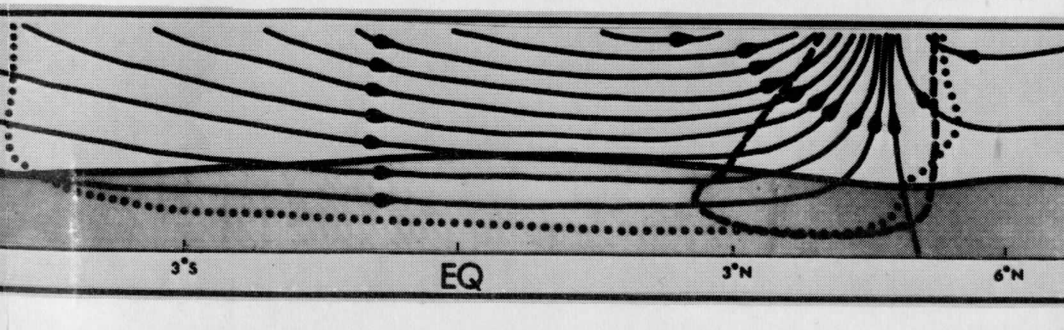

COVER DESCRIPTION

The top drawing denotes airflow streamlines relative to a moving squall line in R. E. Schlesinger's numerical model. The heavy line encloses the main cloud and anvil, and the shaded areas falling rain, which in this case is systematically constrained from exerting a drag on the air.

Below is a representation of cross-equatorial flow streamline in and above the planetary boundary layer (shaded area), taken from L. J. Mahrt's numerical study. In the case shown, a uniform unbalanced northward flow which terminates at a convergence zone at $4\frac{1}{2}$° N. In contrast to middle latitudes, this zone does not coincide with a low pressure center.

Space Science and Engineering Center
The University of Wisconsin
Madison, Wisconsin

STUDIES OF THE ATMOSPHERE USING AEROSPACE PROBINGS

Annual Report on

ESSA Grant E-230-68-(G)

1971

The research reported in this document has been supported by the

National Oceanic and Atmospheric Administration

April, 1972

ERRATA

Annual Report—1971: Studies of the Atmosphere Using Aerospace Probings: Volume I—Theoretical Studies

P. 174 – Equation (19) should read on the left-hand side of the equation:

$$\nabla^2 p' + \frac{\partial}{\partial z}\left(g\bar{p}\frac{p'}{\bar{p}}\right).$$

P. 181 — In the first paragraph, line 5, (x_i, x_j) should read (x_i, z_j).

P. 182 — In the last line (x_i, x_j) should read (x_i, z_j).

P. 184 — After Eq. (53) it should read: The amplitudes $|\hat{Q}_{up}|$ and $|\hat{Q}_c|$ are easily found to be

P. 202 — In Eq. (78), add a + between the two fractions. Eq. (79) should read:

$$T^n_{M,j} = T^{n-1}_{M,j} + \Delta_n t\left[-u^{n-1}_{M,j}\left(\frac{\delta_{up}T}{\delta x}\right)^{n-1}_{M,j} - w^{n-1}_{M,j}\left(\frac{\delta_{up}T}{\delta z}\right)^{n-1}_{M,j} - w^{n-1}_{M,j}\gamma_d\right]$$

P. 205 — The left-hand side of Eq. (92) should read: $\hat{\eta}^n_{i,1}$.

Add a bracket to the end of Eq. (93).

P. 210 — The left-hand side of Eq. (108) should read: $\overline{w'w'}$

P. 227 — The caption for figure 20 should read: Same as figure 17, but for case M_1. (7 grid shifts)

P. 247 — In the paragraph after Eq. (110), the sentence should read: Figures 17 through 21 through . . .

In the paragraph above Eq. (111), the first sentence should read: Figures 42 through 50 show . . .

P. 251 — In figures 48 and 49, the diagrams are upside down, backwards and in reverse order.

P. 259 — In the middle of the first paragraph, figure 39 should read figure 37.

P. 260 — In the first paragraph, figure 4 should read figure 5.

P. 262 — In figure 55, the second diagram labeled (h) should read (b).

P. 271 — (except for figure 31) should read (except for figure 30) in first paragraph.

P. 273 — The third line of the first paragraph should read: whereas if the jet is above F the downdraft should form to its left. *

P. 290 — (figure 29) should read (figure 28) in last paragraph.

P. 305 — The first sentence should read: Comparing figure 76 with figure 11, . . .

P. 330 — Eq. (127) should read $\frac{\partial u^*}{\partial t} + \frac{\partial p^*}{\partial x} = 0$.

P. 331 — The last part of Eq. (133) should read: $\underset{\sim}{0} = \begin{pmatrix} 0 \\ 0 \\ 0 \\ 0 \end{pmatrix}$.

P. 341 — Eq. (173) should read:

$$(R_p)^{n+1}_{i,j} = (\nabla_c^2 \psi_p)^{n+1}_{i,j} - \hat{\eta}^{n+1}_{i,j}$$

P. 342 — The denominator of Eq. (178) should read

$$(\Delta z)^2, \qquad 2 \leq i \leq M-1$$

P. 344 — Eq. (181) should read:

$$T = \bar{T} = R_1^2 T'_{max} \mid G(x-x_c, R_2, R_1)\mid \sin \frac{\pi z}{H}$$

$$\text{for } 0 \leq z \leq H, \quad |x-x_c| \leq R_2$$

P. 346 — Eq. (188) should read:

$$W' = b_1' + b_2'(X'-x_{i'}) + b_3'(Z'-z_{j'}) + b_4'(X'-x_{i'})(Z'-z_{j'}).$$

P. 352 — Fujita, T., 1959: "Precipitation and Cold Air Production in Mesoscale Thunderstorm Systems," J. Met., 16, 454-466.

P. 352 — Hirt, C. W., 1966: "Heuristic Stability Theory for Finite-Difference Equations," J. Comp. Phys., 2, 339-355.

PREFACE

The research reported in this volume concludes two substantial attempts to advance our understanding of cloud-producing circulations which may be usefully applied to geosynchronous satellite data. In particular, both papers contain significant implications for the development and motion of both "tracer" and cumulonimbus tropical cloud systems to be viewed by the ATS and SMS satellites.

The first paper by Larry J. Mahrt demonstrates the important modifications of flow near the equator caused by parcel accelerations and the effects of "friction" in the planetary boundary layer. This should be useful in interpreting and analyzing patterns of tracer cloud displacements. In addition, the paper also brings out a mechanism for the production of rising motion which could account for an active convection zone at a typical ITCZ latitude.

The paper by Robert E. Schlesinger shows how squall lines may be systematically influenced by environmental wind shear and low-level moisture. The results specifically relate quantities such as anvil growth, over-all circulation and liquid water content to environmental jet-stream flow and available moisture, all of which could eventually be estimated from satellite altitudes.

It is a pleasure to acknowledge these contributions by our associates.

Verner E. Suomi
Principal Investigator

John A. Young
Theoretical Studies Director

Scanner's note:

This page is blank.

CONTENTS

A NUMERICAL STUDY OF ADVECTIVE EFFECTS ON BOUNDARY LAYER FLOW AT LOW LATITUDES

Larry Joe Mahrt

Abstract:

Certain simplified steady boundary layer flows are examined at low latitudes where the Coriolis parameter is small and momentum advections may be large. These flows are studied both analytically and with a multi-level two-dimensional numerical model. This model is designed to include a one-layer representation of the free atmosphere where pressure adjustments are allowed. Analyses of several finite difference schemes in terms of numerical stability and truncation errors for the equations of motion are conducted to aid in the construction of the model. Two main flow types are found by specifying the pressure or heating field: drift-"ordinary" boundary layer flow where momentum advections are large, and quasi-geostrophic-Ekman flow where advections are small.

Quasi-Ekman flow directed toward lower latitudes is modified by momentum advections associated with the latitudinal variation of the Coriolis parameter. The rate of modification depends on the orientation and strength of the pressure gradient field. Low level flow crossing or originating from near the equator is quite different from Ekman flow, due to large horizontal momentum advections in the boundary layer and in the overlying frictionless drift flow. The low level wind vector of this ordinary boundary layer flow rotates more slowly with height and often in the opposite sense of Ekman rotation. The boundary layer depth is considerably thinner than that predicted by Ekman theory, especially near the equator. The magnitude of this

---

Presented as a thesis in partial fulfillment of the requirements for the degree of Ph. D. (Meteorology).

rotation and the boundary layer depth are nearly independent of latitude. Also, in contrast to Ekman flow, the cross isobar flow and horizontal divergence increase with height everywhere for slowly varying pressure gradient fields. However, the horizontal divergence may reverse sign with height when the horizontal pressure gradient varies rapidly with latitude. Latitudinal transitions between this flow and quasi-Ekman flow can generate significant vertical motions due to the thicker and stronger cross isobar flow of the ordinary boundary layer. These vertical motions produce significant vertical advections of momentum which can influence the depth of the frictional boundary layer.

When the pressure is not specified independent of the flow, mass redistribution by the flow forces pressure adjustments so that in the unheated region the frictionless flow is quasi-nondivergent and the frictionless zonal flow component (which may approximately obey a "constant angular momentum" latitudinal profile) is quasi-geostrophic. The low pressure system generated by a given specified heating distribution is less intense at lower latitudes where the boundary layer can more easily produce vertical motions. When the flow is forced by latent heat release parameterized in terms of boundary layer vertical motion, the same basic low level flow regimes result that occur with specified pressure or specified heating.

CONTENTS

Contents—continued

LIST OF SYMBOLS

c_d	surface drag coefficient
c_p	specified heat capacity of air at constant pressure
D	Ekman depth
E	Ekman number
f	Coriolis parameter
g	acceleration of gravity
K	eddy viscosity
$\vec{k}$	vertical unit vector
k_0	geophysical boundary coefficient
L	horizontal scale length; latent heat of condensation
P_0	1000 mb
p	pressure
q	specified humidity
R	specific gas constant
R_0	Rossby number
T	Temperature
t	time
U_g	zonal geostrophic wind
u	zonal velocity
$\vec{V}$	horizontal velocity vector
$\vec{V}_g$	total geostrophic wind
$\vec{V}_z$	vertical derivative of V
v	meridional velocity
W_b	vertical velocity at the top of the boundary layer
w	vertical velocity
α	specific volume
α_0	angle between surface wind and surface geostrophic wind
β	Rossby parameter
Γ	vortex strength

γ	long wave absorbivity of the atmosphere
ζ_g	geostrophic vorticity
θ	potential temperature
κ	ratio of the specific gas constant to the specific heat capacity for dry air
ν	kinematic viscosity air
ρ	density
σ	Stefan-Boltzmann constant
τ	stress
τ_0	surface stress
ϕ	latitude; geopotential height
ψ	stream function
Ω	angular velocity of rotation of the earth
ω	vertical velocity in pressure coordinates; oscillation frequency

All other symbols are defined in the text.

1. INTRODUCTION

The flow in the lowest part of the low latitude troposphere near the earth's surface can strongly influence the entire wind and pressure fields of many low latitude tropospheric circulation systems. For example, low level vertical fluxes of moisture are often essential to the development and maintenance of these circulation systems since they may be primarily driven by latent heat release, and moisture at low latitudes is concentrated near the surface. Vertical motions forced by low level flow convergences can also modify the tropospheric pressure field through redistribution of mass. In certain flow situations, strong upward advections of lower momentum air from near the surface can directly modify the wind field at higher levels.

Unfortunately, the dynamics of low level flow at low latitudes is not always well understood because of the simultaneous importance of transports of momentum by both the turbulent and mean scales of motion. While the Ekman (1905) solution and various modifications thereof can approximate many midlatitude low level flow situations, these solutions often fail in low latitude regions where the Coriolis parameter decreases rapidly with decreasing latitude and momentum advections and time accelerations are often important.

While a number of factors not included in the Ekman solution influence equatorial low level flow, the main emphasis of this study is on the influence of momentum advections associated primarily with the large latitudinal variation of the Coriolis parameter. Of special interest will be differences in the basic characteristics of these low level flows compared to those of mid-latitude Ekman-type flows and transitions between different types of low level flows. Also of interest will be pressure adjustments initiated by low level vertical fluxes of mass and latent heat.

"Boundary layer" is defined in the Glossary of Meteorology as "the layer of fluid in the immediate vicinity of a boundary surface." More specifically, the term "boundary layer" for this study refers to the lowest portion of the troposphere where turbulent momentum transports due to the presence of the earth's surface are important. This turbulence may be associated with the roughness of the earth's surface, or it may be convectively driven by heating at the earth's surface. With neutral static stability or stable stratification, the boundary layer is primarily a result of mechanical turbulence in which case a "mechanical boundary layer" might be defined. When surface heating induces dry thermals or convective clouds which dominate momentum transports, a convective boundary layer might be defined. From a synoptic or macroscale viewpoint, where convective cloud elements appear as turbulent scale phenomena, the layer of convection could be considered to be a convective boundary layer.

Transports in the boundary layer occur over a wide spectrum of time and spatial scales. However, the boundary layer flow is generally divided into the mean flow and perturbations from the mean flow. The above two types of boundary layers are based on transports by the perturbation flow. However, the earth's surface may also strongly influence the wind field through transports by the mean flow. For example, it will be seen in this study that upward advection of low momentum fluid near the surface may be quite important in regions of strong rising motion. The region of influence of the lower boundary through vertical advections of momentum will be referred to as a vertical inertial boundary layer.

On the basis that horizontal variations of surface temperature may significantly contribute toward vertical wind shear maintenance, a "baroclinic boundary layer" could also be defined.

For convenience, the term "frictional boundary layer" will refer to the region adjacent the earth's surface where small scale turbulence (i.e., excluding convective clouds) due to the presence of this surface is important.

The "free atmosphere" will then refer to the region above the frictional boundary layer.

1.1 Observational Evidence

The isolation of an individual boundary layer effect in terms of distortion of observed vertical wind profiles is made difficult by the fact that the various effects may occur simultaneously and interact through momentum advections. Nonetheless, there must be some observational evidence of low latitude boundary layers, even if the evidence does not fulfill an Ekman-like concept of a boundary layer.

From observations it appears that major changes in the mean planetary boundary layer flow occur only within 10° of the equator. Using several thousand observations, Gray (1968) concluded that there was little significant difference in veering of the wind (rotation in the Ekman sense) in the lowest kilometer between 20°–30°N and 10°–20°N. He estimated that veering in this layer due to frictional effects averaged about 8–9°.

In contrast, Robitaille and Zipser (1970) observed that winds in the lowest layers over the Line Islands (2° to 6°N, 157° to 162°W) exhibited both systematic veering and backing. They found that veering generally occurs with northerly wind components, while backing generally occurs with significant southerly wind components. The tendency for veering for a given wind direction increased with increasing latitude. In an analysis where advections were ignored, Estoque (1970) concluded that at Christmas Island (2°N, 157°W) March to April 1967, a mean backing of the wind of 14° in the lowest kilometer could be primarily a result of thermal winds.

Figure 1 shows mean wind profiles and hodographs for a number of Pacific stations (0 to 20°N, 155° to 175°E) for April to July 1958. Veering dominates in the lowest layers except at Kapingamarangi (1°N), where both veering and backing are observed. Major changes are seen to occur in the boundary layer around 6°N. At higher latitudes it appears that frictional effects dominate in the lowest 500 m to the extent that $\vec{V}_{zz}$ is relatively large, while westerly thermal winds dominate above 1000 m. South of 6°N the role of the frictional terms above the surface layer are not clear in that $\vec{V}_z$ and $\vec{V}_{zz}$ are quite irregular. Perhaps momentum advections, low level baroclinicity and momentum diffusion are all significant factors. It is of interest to note that the mean position of the spring ITCZ, as indicated by mean satellite cloud pictures (Kornfield and Hasler, 1969), is also in the approximate vicinity of 6°–7°N.

Figure 2, taken from Palmén and Vuorela (1963), shows the mean meridional flow averaged around the globe which is then the mean cross

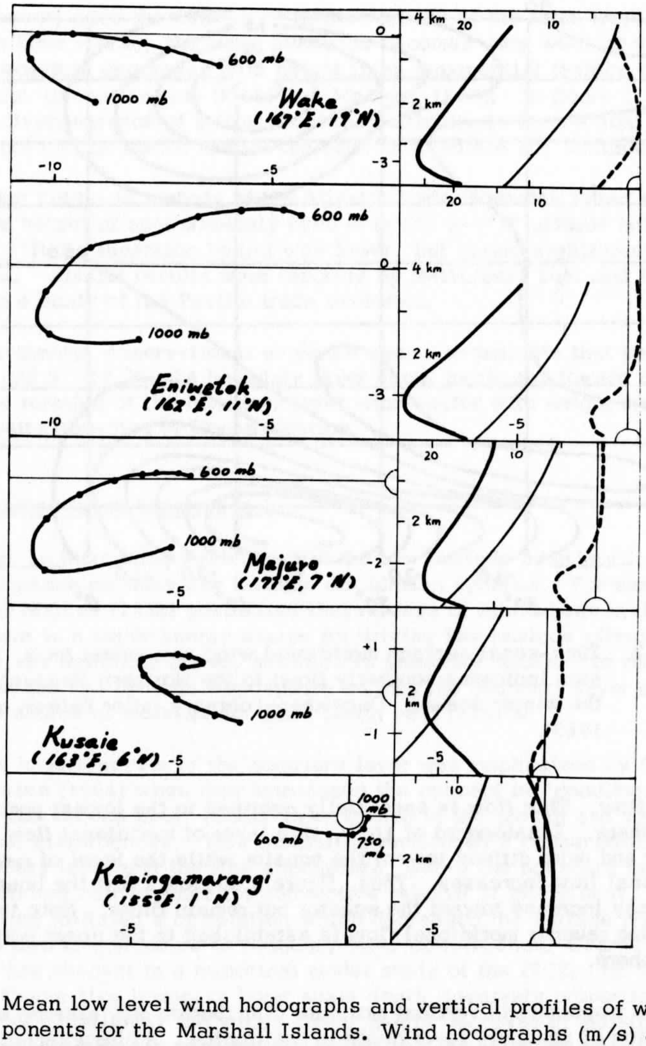

Figure 1. Mean low level wind hodographs and vertical profiles of wind components for the Marshall Islands. Wind hodographs (m/s) are shown in the left half of the figure where dots indicate pressure levels at 500 mb increments. In the right half of the figure, solid thick lines designate vertical profiles of zonal wind (m/s), dashed lines meridional wind profiles (m/s) and solid thin line water vapor mixing ratio profiles (g/kg). The data represents an average of four daily soundings, April–July 1958.

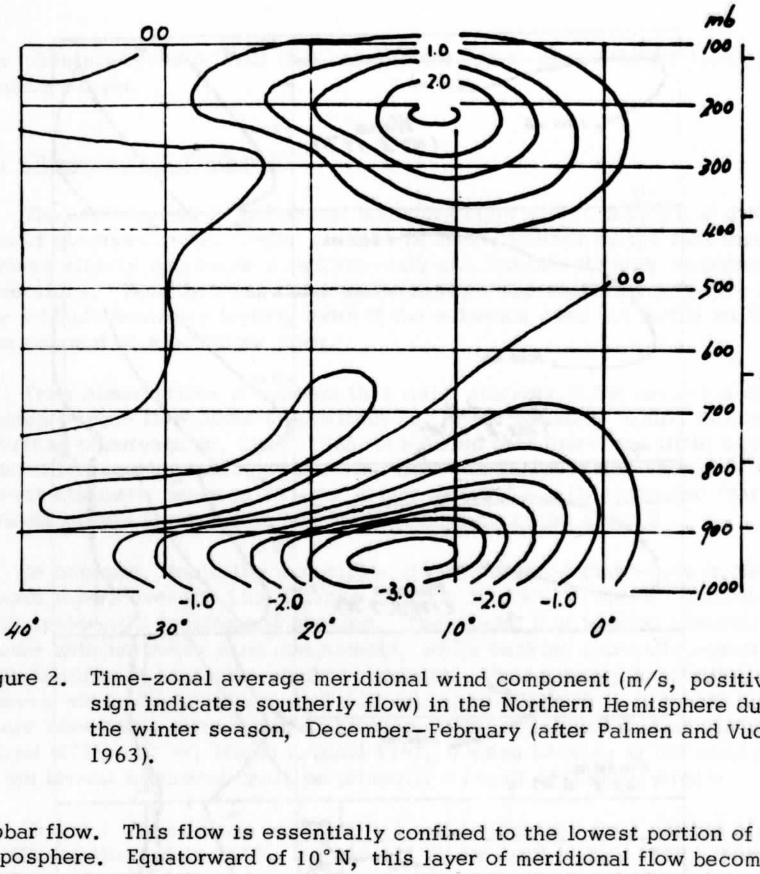

Figure 2. Time-zonal average meridional wind component (m/s, positive sign indicates southerly flow) in the Northern Hemisphere during the winter season, December–February (after Palmen and Vuorela, 1963).

isobar flow. This flow is essentially confined to the lowest portion of the troposphere. Equatorward of 10°N, this layer of meridional flow becomes thicker and more diffuse toward the equator while the level of maximum meridional flow increases. Thus, figure 2 suggests that the boundary layer depth may increase toward the equator but remain finite. Note that a compensating reverse meridional flow is established in the upper portion of the troposphere.

The tropospheric vertical moisture distribution may also be used as an indication of boundary layer depth in the tropics. A characteristic of the tropical atmosphere is that moisture is usually concentrated in the lowest layers. With surface evaporation as the primary source of moisture, one might speculate that the concentration of the moisture in the lowest layers is a reflection of the influence of turbulent transports of moisture in the boundary layer. For example, the trade inversion, where moisture content decreases most rapidly with height, may coincide with the top of the frictional boundary layer since its strong thermal stability inhibits mixing.

However, near the equator or in the vicinity of the Inter Tropical Convergence Zone (ITCZ), the trade inversion becomes very weak or vanishes and the moisture decreases with height in an exponential fashion without significant discontinuities (Riehl and Malkus, 1958). In figure 1, the gradual disappearance of a first order discontinuity in the vertical profile of moisture can be traced toward the equator to within 10° latitude.

Ficker (1936) in a study of the Atlantic trade inversion found a mean inversion height of approximately 2000 m in the 0–5°N latitude belt, while north of 5°N the inversion height was lower, but varied significantly with longitude. Similar results were reported by Neiburger, Beer and Leopold (1945) in a study of the Pacific trade inversion.

In summary, observational evidence seems to indicate that between the equator and 5°–10°N, the boundary layer depth increases toward the equator while the rotation of the boundary layer wind vector with height may be in the opposite direction of Ekman rotation.

1.2 Boundary Layer Importance

There is increasing evidence that the low latitude boundary layer is a major influence on many low latitude circulation systems. For example, Riehl and Malkus (1958) postulated that release of latent heat in the tropical atmosphere is a major energy source for driving low latitude circulations. However, as indicated above, moisture is primarily confined to the lowest portion of the low latitude troposphere so that the boundary layer must be the main source of moisture for such latent heat release.

This important role of the boundary layer was emphasized by Charney and Eliassen (1964) when they introduced the concept of "conditional instability of the second kind" (CISK) in reference to the growth and maintenance of tropical disturbances. This instability envisaged a cooperation between the boundary layer and the free atmosphere, where the boundary layer provided moisture convergence for convective release of latent heat. In turn this heating initiated a circulation which decreased the surface pressure, which in turn is conducive to boundary layer convergence. Charney (1968) applied this concept in a numerical model study of the ITCZ. He found that with an Ekman-like boundary layer scale depth (inversely proportional to the square root of latitude) and with a linear height decrease of moisture, the ITCZ could not form near the equator where the strongest boundary layer convergence occurred above the low level concentrations of moisture. However, Charney also noted that "more observational and theoretical (boundary layer) work is needed before an adequate (CISK) theory can be formulated."

As a direct consequence of confinement of moisture to lower levels, it is expected that boundary layer convergence is often necessary for convective clouds on all scales of organization. For example, Gray (1968) concluded that because most cumulus clouds over the tropical oceans have bases of approximately 600 m above the ocean surface (~ 950 mb), convergence in the lowest 500–600 m is required for cumulus development. He further noted that, based on mean summertime vertical distributions of temperature and moisture in tropical storm development regions, only vertical motion established by convergence below 900 mb can produce net tropospheric warming.

Another consequence of this low latitude vertical distribution of moisture is that the tropical atmosphere is often decidedly convectively unstable from the surface up to about 650 mb (Gray, 1968, and Jorden, 1958). Sufficient synoptic scale rising motion resulting from boundary layer convergence would then tend to decrease the static stability of the lower troposphere. However, this effect might be relatively small in the mature disturbance where the convective redistribution of heat is large, i. e., where release of latent heat aloft and cooling due to mesoscale downdrafts in the lower layers dominate local temperature tendencies.

Boundary layer cross isobar mass transports may also significantly reduce horizontal pressure gradients: a process sometimes referred to as "boundary layer spin down." For example, boundary layer rising motion causes adiabatic expansion which results in net cooling aloft unless it is exceeded by latent heat release.

1.3 Theoretical Low Latitude Boundary Layer Studies

Theoretical studies of low latitude boundary layers in the atmosphere are limited in scope, although fluid dynamic studies of low latitude boundary layers on other rotating spheres are more extensive. A number of such studies are discussed in The Theory of Rotating Fluids by H. P. Greenspan (1968).

A scaling parameter, which can be used to relate boundary layers of various scales, is the nondimensional Ekman number; $E = \frac{\nu}{\Omega L^2}$ where L is a typical scale length. In the case of the atmosphere, the Ekman number might be defined as $\frac{2K}{|f| H^2}$ where H is a typical depth scale such as the depth of the troposphere. The Ekman number can be thought of as measuring the importance of the friction term relative to the Coriolis term.

The classical Ekman (1905) theory yields a boundary layer scale depth of $(\frac{2K}{|f|})^{1/2}$ which is commonly referred to as the "Ekman depth" and symbolized by D. In this case the Ekman number becomes D^2/H^2. As the equator is approached the Ekman depth approaches infinity. However, it is expected that Ekman's solution may be modified by thermal stratification and momentum advections in this region.

Thermal stratification can influence the boundary layer in two ways. Vertical motions induced by the boundary layer will result in pressure adjustments in a stratified atmosphere, and, secondly, turbulence may be inhibited or initiated by the stratification depending on whether the stratification is stable or unstable.

Pedlosky (1969) analyzed a stably stratified fluid rotating between two concentric spheres with constant eddy viscosity where advections were neglected. He found that at low latitudes where rotational effects are small, the static stability became a primary restraining influence on boundary layer depth. At these latitudes the boundary layer depth was proportional to the fourth root of thermal stability instead of the Ekman depth. However, the stratification of the lower part of the earth's atmosphere, which is often concentrated in the trade inversion at lower latitudes, tends to weaken toward the equator so that the above restraints on boundary layer depth may be reduced.

The Ekman spiral may also be modified by momentum advection terms, especially at low latitudes where latitudinal variations of the Ekman depth and wind solution become large. If advection terms are important above the boundary layer, the Ekman solution is modified, since the unmodified Ekman solution asymptotically approaches the geostrophic wind (zero advections) with height. One would expect advections above the boundary layer to be more important at lower latitudes where the Coriolis parameter is small. This tendency is expressed in the nondimensional Rossby number, $R_0 = \frac{V}{fL}$ where V is a horizontal scale velocity and L is a horizontal scale width. The Rossby number, which is an estimate of the importance of horizontal advections relative to the Coriolis forces, becomes large at low latitudes as the Coriolis parameter becomes small.

If the horizontal advection term is one of the more important terms, an entirely different type of flow regime from geostrophic flow may be established. For example, Winn-Nielson (1970) discussed three idealized types of pure inertial flow on an equatorial β-plane corresponding to: a) trajectories entirely in one hemisphere, b) trajectories crossing the equator repeatedly, and c) trajectories which have the equator as an asymptote.

Scale analysis of frictionless low latitude motions suggests that horizontal advections of momentum will become important relative to the Coriolis term when the Rossby number is greater or equal to one. Assuming an equatorial β-plane, a horizontal scale width (of the importance of horizontal advections) equal to the distance from the equator and a scale velocity equal to the geostrophic wind (U_g), the Rossby number is greater than one for $y < \sqrt{U_g/\beta}$. Therefore, $\sqrt{U_g/\beta}$ might be viewed as an estimate of the horizontal influence of the equator through horizontal advections. For example, such a region can be generated by flow across the equator when the pressure gradient does not vanish at the equator (geostrophic wind reverses sign at the equator).

Several special cases of low latitude boundary layer flow where advections are important have been theoretically studied. Charney (1969) and Young (1969) found vertical advections to be quite important in the special case of steady longitudinally symmetric zonal boundary layer flow at the equator. It was concluded that a finite boundary layer depth at the equator was possible only in the westerly geostrophic wind case, where divergence and sinking motion occurred at the equator so that downward advections of higher momentum balanced the diffusion term. It was also concluded that the horizontal scale length of the influence on the equator through horizontal advections was proportional to $\sqrt{U_g/\beta}$.

P. Pushistov (1970) numerically examined steady longitudinally symmetric equatorially symmetric boundary layer flow on an equatorial β-plane. In order that relaxation methods could be used, Pushistov chose a special baroclinic pressure field so that the advecting velocity of the corresponding solution did not change sign with height. Pushistov found that the Ekman type boundary layer flow from higher latitudes was modified considerably near the equator. Strong rising motion was produced near the equator where meridional flow vanished.

It then appears that momentum advections and thermal stratification effects may become important at low latitudes so that the Ekman solution is no longer a good approximation to the low level flow. Additional clues to the character of possible alternative type boundary layer flows may be revealed by briefly reviewing a number of fluid dynamics studies.

Boundary layers on a sphere rotating in an otherwise quiescent fluid (where gravity induced by the sphere is unimportant) have been studied both analytically and experimentally. With a simple transformation of coordinate systems, this problem could be related to that of a fluid rotating about a stationary sphere where the frictionless velocity relative to the sphere away from the sphere's boundary layer is $\Omega r \sin \phi$, where r is the radial distance from the sphere's center. Experimental studies (e. g., Bowden and Lord,

1963) reveal that in the boundary layer adjacent to the surface of the sphere, meridional flow toward the equator is frictionally induced. Since the flow is symmetric with respect to the equator, the boundary layer flows from both hemispheres converge at the equator and produce a narrow and very intense radially outward jet; that is, a vertical inertial boundary layer. This inertial jet has little effect on the incoming boundary layer flow as long as the Ekman number is small (as in the case of the atmosphere away from the equator). Analytical treatments of the above problem appear to apply very well except in the vicinity of the equator (Howarth, 1951, and Banks, 1965).

Studies of nonturbulent rotating fluids over a flat surface have often been used to infer properties of flow on a rotating earth.[1] The centrifugal terms $(\Omega \times \vec{V})$ in vortex flows play a similar role to the Coriolis terms on a rotating sphere; for example, a steady state balance may exist between the centrifugal and horizontal pressure gradient forces above the boundary layer, while in the boundary layer near the solid surface, additional frictional forces induce cross isobar flow toward low pressure.

Bodewadt (1940) solved this problem with similarity methods in the case of solid rotation above the boundary layer. A number of studies, of which many are summarized in Greenspan (1968), have been devoted to the reanalization of this problem. The similarity solutions have been essentially verified by other methods such as the series expansion technique carried out by Rogers and Lance (1964). The above studies indicate that the boundary layer undergoes fairly regular variations from the center of the vortex to large radii. Various degrees of rotation of the boundary layer wind vector with height result, depending on the geometry of the problem. The boundary layer depth is independent of radius and varies according to $E^{\frac{1}{2}}$. In the case of the infinite rotating flat plate, vertical motion is also independent of radius.

The potential vortex boundary layer has been examined by a number of investigators including G. I. Taylor (1950), Schwiderski and Lugt (1964), and R. K. Smith (1968). In general, the boundary layer wind vector rotates with height, boundary layer depth decreases toward the center and rising motion occurs near the center of the vortex while sinking motion is established at large radii.

---

[1] It might be noted that the boundary layer on a rotating sphere in an otherwise quiescent fluid exhibits at high latitudes properties very similar to that of a boundary layer over a rotating disc where the rotation rate is independent of latitude.

Kuo (1971) studied a vortex which appears to be particularly appropriate to possible application to the atmosphere. The inner part of the vortex is in solid rotation (Ω = constant) with a relatively high angular velocity, and is thus analogous to high latitudes on a rotating sphere. In the outer portion of the vortex, the frictionless flow is approximately potential flow ($\Omega \sim \frac{1}{r^2}$) with relatively small angular velocity, and is thus analogous to low latitudes on rotating sphere. The inner region is then of high absolute cyclonic vorticity (2Ω) while the outer region is characterized by weak absolute cyclonic vorticity ($\frac{1}{2} \frac{\Gamma}{r^2}$, where Γ is a constant sometimes referred to as the vortex strength).

In spite of the fact that this type of vortex is more complicated than the solid rotation vortex or the potential vortex in that vertical and radial variations of the flow are not mathematically separable, Kuo was able to find an approximate boundary layer solution using an iterative momentum integral technique. Unlike the above two cases, Kuo's vortex was characterized by two distinct boundary layer flow regimes corresponding to the two regions of large and small absolute vorticity. In the inner region, the flow is of the Ekman-like type, with an oscillatory distribution of the velocities in the vertical. In the outer region, vertical wind profiles were without such oscillations. The inner region boundary layer was thin but intense, while the outer region boundary layer was thick and diffuse. In the inner region, where relative vorticity is equal to twice the angular velocity, vertical velocity at the top of the boundary layer varies according to the square root of relative vorticity. Note that the Ekman solution (Charney and Eliassen, 1949), which predicts a first power vorticity law, also reduces to a square root vorticity relationship when the vorticity is proportional to the local angular rotation ($\Omega \sin \phi$). Chang and collaborators (1969) also observed these two boundary layer regions in a similar type vortex produced in the laboratory.

Noting that boundary layer flow in Kuo's vortex primarily advected momentum from low rotation regions to regions of high rotation, some inferences can be proposed about the analogous atmospheric case, i.e., flow away from the equator. For example, it might then be expected that the low latitude boundary layer (relative to the high latitude boundary layer), will be characterized by weak rotation of the boundary layer wind vector with height and thick, but finite, boundary layer depth.

The application of the results of Kuo's vortex to atmospheric flows hinges upon the fact that the centrifugal and Coriolis forces in a crude sense play similar roles in the boundary layer. This similarity is exhibited in atmospheric vortex solutions in which case both centrifugal and Coriolis forces are simultaneously present. These solutions have included horizontal momentum advections; however, vertical advections were neglected. Unfortunately, scale analysis indicates that vertical advections are typically of the same order of magnitude in the boundary layer where vertical wind shears and horizontal divergence may be large. Neglecting such advections Haurwitz (1935, 1936) and Syono (1949) applied perturbation techniques to vortex flow on a rotating earth and found that the boundary layer depth tends to be inversely proportional to the absolute vorticity of the frictionless flow.

So far the discussion has been limited to steady state boundary layer flows. For completeness and to help put the above flow types in perspective, it will be instructive to briefly examine time-dependent low level flows. Of interest is the fact that the boundary layer flow responds to forcing functions at a different rate than the frictionless flow. Stokes (1851) found that the boundary layer depth of a fluid, responding to a flat plate oscillating in its own plane, is $\sqrt{\nu/\omega}$ where ω is the oscillation frequency of the plate. Lamb (1879) showed that Stokes' problem is equivalent to a fluid over a stationary flat plate driven by an oscillating forcing function.

Holton, Wallace and Young (1971) computed the linear boundary layer response to an oscillating pressure field of frequency ω corresponding to an inviscid free mode derived by Matsuno (1966) for an equatorial β-plane. The boundary layer scaling depth is found to involve $\sqrt{\frac{2K}{(\omega-f)}}$ such that the boundary layer depth is singular at the "critical latitude" $y = \omega/\beta$. The boundary layer wind suffers a dramatic phase shift across this critical latitude. Vertical motion at the top of the boundary layer at higher latitudes is proportional to the square root of relative vorticity (i.e., Ekman). Equatorward from the critical latitude, the Coriolis influence is so small that the flow is essentially described by Stokes' second problem. As a result, the vertical motion phase is nearly independent of latitude in this region (in contrast to the Ekman flow). Thus, this study, as well as Kuo's vortex study, indicates two distinct boundary layer regions corresponding to different rates of local rotation.

1.4 Simplified Boundary Layer Representations

Most investigators of tropical disturbances are more interested in effects of the boundary layer on the free atmosphere rather than the kinematics or dynamics of the boundary layer flow itself. Consequently, when boundary layer effects are included in tropical studies, they are usually parameterized, since explicit inclusion of the boundary layer would cause modeling complications. As a result, an important by-product of boundary layer theory is parameterization of boundary layer effects.

Table 1

Basic Boundary Layer Flow Characteristics for Various Flow Types

Flow type	Boundary Layer Depth	Vertical motion at the boundary layer top	Wind vector rotates with height
Vortex flows			
Solid rotation	$(K\Omega)^{1/2}$	$(K\Omega)^{1/2}$	yes
Kuo's vortex		$(K/\Omega)^{1/2}\zeta$	in high rotation region
Flow on a rotating earth			
Ekman flow	$(K/\Omega \sin \phi)^{1/2}$	$(K/\Omega \sin \phi)^{1/2}\zeta$	yes
Stably stratified flow without advections (Pedlosky, 1969)	$\left(K \frac{\Delta T}{\Delta Z} \Big/ \Omega^2\right)^{1/4}$		yes
Equatorially symmetric flow at the equator (Chapter 4)	K/W		no
Vortex flow on a rotating earth (Haurwitz, 1935, and Syono, 1951)	$[2K/(\zeta + 2\Omega \sin\phi)]^{1/2}$	$[2K/(\zeta+2\Omega\sin\phi)]^{1/2}\zeta$	yes
Time-dependent flows			
Stokes' second problem	$(2K/\omega)^{1/2}$		no
Matsuno wave for $y < \omega/B$ (Holton, Wallace and Young, 1971)	$[2K/(\omega-2\Omega \sin \phi)]^{1/2}$		no

Previous application of such parameterizations is now briefly reviewed. Generally, vertical motion at the top of the boundary layer, W_b, is parameterized in terms of easily calculated frictionless flow variables, while vertical fluxes of latent heat out of the boundary layer are often parameterized in terms of W_b. Derivations of W_b parameterizations are usually based on an assumed boundary layer balance between the horizontal pressure gradient, Coriolis and frictional terms.

For example, Charney and Eliassen (1949) assumed an Ekman spiral with constant Coriolis parameter and zero divergence in the direction of the geostrophic wind and found that

$$W_b = \frac{\sin(2\alpha_0)}{2} \sqrt{2K/|f|}\, \zeta_g \qquad (1)$$

where ζ_g is the relative vorticity of the geostrophic wind and α_0 is the angle between the surface wind and the surface geostrophic wind. A number of theoretical studies of tropical disturbances and CISK (Rodenhuis, 1971) have incorporated this formula. Syono (1951) derived a similar formulation for W_b based on his vortex solution (see table 1).

In another linear treatment, Priestly (1967) integrated the equations of motion to the top of the boundary layer, H, where vanishing stress is assumed. Taking the curl,

$$W_b = \frac{\vec{k} \cdot \alpha \nabla \times \vec{\tau}_0}{f} + \beta \int_0^H \frac{v\,dz}{f} \qquad (2)$$

The second term is due to the horizontal variation of the Coriolis parameter and must be neglected since its evaluation requires the solution of the boundary layer cross isobar component. In fact, at low latitudes where this term is significant, the balance of forces underlying the above derivation becomes questionable. Neglecting the second term,

$$W_b = \frac{\vec{k} \cdot \alpha \nabla \times \vec{\tau}_0}{f} \qquad (3)$$

Young (1970) generalized this formulation to include influences of low level baroclinicity.

To apply the above formulation, both the direction and magnitude of surface stress are required. Priestly (1967) in a study of macroscale momentum fluxes for zonal-mean circulation, assume that, to a first approximation,

$$\vec{\tau}_0 = \rho c_d \vec{V} |\vec{V}| \qquad (4)$$

where $\vec{V}$ is the wind at the top of the boundary layer. Charney (1968), replacing $\vec{V}$ with the geostrophic wind, applied this empirical relationship to compute W_b in a numerical ITCZ study.

As an alternative to parameterizing W_b, a number of tropical disturbance studies contain one-level representations of the boundary layer. Most models represent the friction term by a "mean diffusion," $\frac{\alpha\tau_0}{H}$, where stress is assumed to vanish at H and the surface stress, τ_0, is specified with a drag law involving the wind at the top of the boundary layer.

Such models usually assume a balance between the pressure gradient, Coriolis and diffusion terms and in the case of vortex studies, the centrifugal term. Ooyama (1969) recently concluded that the results of his tropical cyclone numerical model were significantly improved when advection terms were included in the one level representation of the boundary layer. He further argued that in the tropical cyclone, neglect of advection terms at the boundary layer level was a much greater weakness than neglecting advections aloft. One level representations of the boundary layer have also used "Rayleigh" type damping, $-k\vec{V}$ for the friction term where k is a specified constant (Fujita, et al., 1969).

Latent heat release is often parameterized in terms of moisture convergence in the boundary layer which is proportional to the mixing ratio and vertical motion at the top of the boundary layer. Syono (1951) found that the radial distribution of precipitation rate in typhoons correlated well with the product of a surface mixing ratio and his parameterization of W_b for a vortex. Charney and Eliassen (1964) parameterized latent heat release in a two-layer representation of the hurricane-free atmosphere in terms of convergence of moisture in the boundary layer where W_b was computed from their earlier parameterization, and the release of latent heat aloft was determined according to the parcel theory. With the inclusion of surface evaporation and entrainment aloft, Kuo (1965) devised a more general parameterization.

In general, parameterizations of the boundary layer have neglected momentum advections. Since it appears that advections may be especially important at lower latitudes, one might expect the above parameterizations to be less valid there compared to mid-latitudes.

1.5 The Problem to be Examined

From the above literature survey, it is evident that a large number of questions pertaining to low latitude boundary layers remain unanswered. One of the more important unanswered questions appears to be the role of momentum advections, particularly those associated with the large latitudinal variation of the Coriolis parameter. Therefore, this study will focus on the role of momentum advections in the low latitude boundary layer in terms of the basic characteristics of the kinematics and dynamics of the resulting low level flow and in terms of the influence of the low level flow on the overlying frictionless flow through vertical fluxes of mass momentum and latent heat. Of special interest will be basic differences between the low latitude boundary layer and the Ekman-like boundary layer and the transitions between these two flow types.

So that the dynamics of the flow can be more easily understood, this study will be restricted to steady longitudinally symmetric flows generated by a height-independent pressure field. The relationship of such simplified flows to actual low latitude atmospheric flows will now be briefly discussed.

Scale analysis indicates that the ratio of the local time derivative to the advection term is $\frac{\Delta y}{VT}$, where T is a characteristic time scale of the system being considered and Δy is its latitudinal extent. Satellite cloud pictures and empirical case studies (Kornfield, et al., 1967, and Fujita, et al., 1969) indicate that time changes between the equator and 10°N are most pronounced in the ITCZ vicinity where "nephsystems" propagate in an easterly direction along the ITCZ. The above-mentioned studies indicate that in this region T is 0 (1 day) (corresponding to a period of a few days), Δy is 0 (300 km) and V is 0 (10 m/s), so that $\frac{\Delta y}{VT}$ is 0 (1/3). Thus, one could conclude that neglect of local time changes in a study of wave motions would result in significant errors. However, south of the ITCZ, the southeasterly trade flow exhibits remarkable persistence. For example, Wiederanders (1961) found that the southeasterly surface trade winds crossing the Pacific equator were characterized by very high constancies of about .80. Consequently, the assumption of steady state appears to be a good approximation in this region. Of course, on a time scale smaller than is considered in this study, time variations associated with diurnal and semidiurnal oscillations would be important. However, it appears reasonable to delay the study of time variations of the wind field until the relationship between the steady wind field and the pressure field is better known.

Longitudinal variations also appear to be small south of the Northern Hemisphere ITCZ where trades may be established over large longitudinal extents as is evident in streamline analyses prepared by Fujita et al. (1969) from satellite low level cloud velocities. Even the nephsystems in the ITCZ are elongated in the east-west direction so that longitudinal variations are considerably smaller than latitudinal variations. The dominance of latitudinal variations in many low latitude flow situations may be related to the fact that the percentage latitudinal variation of the Coriolis parameter, cot (ϕ), is markedly larger at low latitudes, becoming infinite at the equator. As a result, the dynamics of the flow may be even more longitudinally symmetric than indicated by the kinematics of the flow.

From a time average point of view, the greatest importance of latitudinal variations is even more pronounced. For example, Kornfield and Hasler (1969), using satellite cloud pictures averaged over fifteen-day periods, found preferred regions of clouds on either side of the equator which were essentially oriented along an east-west axis. Palmen (1964) and Bjerknes and Venkateswaren (1957) have reported that meridional transports of heat and angular momentum at low latitudes are dominated by the longitudinally symmetric component of the flow. Similarly, Van de Boogard (1964) concluded that the transport of water vapor by this component dominates the transport due to eddies for 0°–20° latitudes. Mean pressure and streamline fields illustrated in the Marine Climatic Atlas of the World (1955) and the Climatological and Oceanographic Atlas for Mariners (1959) also exhibit a degree of longitudinal symmetry. Of course, one cannot necessarily make complete inferences on the dynamics of the average flow from the above-average wind fields. Latitudinal variations then seem to be in general more important than longitudinal variations for large scale low latitude circulations, in spite of longitudinal asymmetries resulting from traveling disturbances, ocean-land contrasts and longitudinal variations of sea surface temperature.

Variations in sea surface temperatures and land-ocean temperature contrasts may also cause significant low level baroclinicity. However, measurements of equatorial pressure fields of sufficient resolution to describe such baroclinicity are in general not presently available. At any rate, it would seem more logical to study baroclinic effects after a relationship between the pressure and wind fields have been established for a barotropic atmosphere.

In summary, it appears that the dynamics of the wind and pressure fields of much of the immediate equatorial region may be described by quasi-longitudinally symmetric and quasi-steady-state conditions. While it cannot be denied that local time variations and longitudinal variations of the equatorial wind and pressure fields and vertical variations of the equatorial pressure fields are often important, the additional complications associated with their inclusion do not seem justified at this stage of low latitude boundary layer research. Instead, it appears to be more appropriate to first establish basic differences between the low latitude boundary layer and the mid-latitude boundary layer associated with momentum advections at low latitudes. The inclusion of some of the above-mentioned effects would then be a logical expansion of this study. Of course an individual effect, such as the β effect, cannot be isolated from observations since all of the various effects interact through advections. However, it is maintained in this study that certain basic characteristics of the low latitude boundary layer can be more easily understood with the above restrictions.

The organization of the rest of this study is as follows: In chapter 2 the representation of turbulent transports of momentum is handled. Further simplified boundary layer flows are analytically considered in chapter 3 to reveal basic characteristics of different types of boundary layer flows. A boundary layer numerical model is constructed in chapter 4, while in chapter 5 numerical results of the boundary layer wind field corresponding to various specified pressure fields are discussed. There is a discussion in chapter 6 of a one-layer compressible free atmosphere and its response to boundary layer forcing. In chapter 7 a numerical model of this one-layer free atmosphere is added to the boundary layer numerical model, so that pressure adjustments to boundary layer forcing are allowed. Chapter 8 discusses numerical results of the wind and pressure fields corresponding to various specified heating fields.

2. REPRESENTATION OF TURBULENT MOMENTUM TRANSPORTS

In this chapter, a mathematical representation of turbulent transports of momentum in the boundary layer is chosen for the boundary layer study. Upper and lower boundary conditions for the equations of motion will be reviewed first and then representation of the momentum diffusion term is selected.

2.1 Boundary Conditions

Since the equations of motion in the boundary layer are second order in the vertical coordinate, two boundary conditions are required. These conditions can be specified at the lower boundary and at a level sufficiently high so that the momentum diffusion term is no longer important. Various possible boundary conditions can be expressed in the general linear form

$$a\vec{V} + b\vec{V}_z = c \tag{5}$$

Let us briefly review some of the possibilities.

1) The most general case, $a \neq 0$, $b \neq 0$, and $c \neq 0$, is generally not applied to the equations of motion.

2) The case of specifying velocity ($b = 0$) has two commonly-used possibilities. $\vec{V}$ is specified to be geostrophic ($c \neq 0$) at the top of the boundary layer or $\vec{V} = 0$ ($c = 0$) is specified as a "no slip" lower boundary condition.

3) The specified vertical wind shear case $(a = 0)$ also has two often-used possibilities. Shear can be specified at the lower boundary (perhaps indirectly through a stress relationship). Zero vertical wind shear $(c = 0)$, which is generally equivalent to zero stress, is often specified as an upper boundary condition.

4) $c = 0$, $a \neq 0$, and $b \neq 0$ implies that $\vec{V}_z = k_0 \vec{V}$ where k_0 is a specified constant (in reality k_0 is a function of the flow).

Two main combinations of boundary conditions are used in this study. When comparison with the Ekman solution is desired, a no-slip lower boundary condition and a zero wind shear upper boundary condition are specified. When closer physical reality is desired, the no-slip condition is replaced by the relationship $\vec{V}_z = k_0 \vec{V}$ which is intended to parameterize the surface layer. This relationship will be referred to as the "geophysical boundary condition" and k_0 is referred to as the "geophysical boundary coefficient."

2.2 Numerical Assignment of the Geophysical Boundary Coefficient

In this section k_0 is evaluated in several different ways. Taylor (1915) modified the Ekman spiral by applying this type of lower boundary condition where the observed surface wind direction was used to determine k_0.

This coefficient can also be determined by combining the stress relationship $\vec{\tau} = \rho K \vec{V}_z$ and the surface drag relationship $\vec{\tau}_0 = \rho c_d |\vec{V}| \vec{V}$ where c_d is a drag coefficient.[2] Then at the surface

$$\vec{V}_z = c_d |\vec{V}| \vec{V} / K \tag{6}$$

Rosenthal (1962) linearized the above drag law in a hurricane boundary layer study by replacing $\vec{V}$ by the gradient wind. The drag law is linearized in this study by replacing $\vec{V}$ by a constant scale velocity V. Then

$$k_0 = c_d V / K \tag{7}$$

The geophysical boundary coefficient can also be estimated by assuming a log wind profile in the surface layer. The horizontal adjustment scale of this layer as indicated by flow over a surface roughness discontinuity in an

---

[2] The surface drag relationship $\vec{\tau}_0 = \rho c_d |\vec{V}_g| \vec{V}_g$ can also be used where c_d is now the geostrophic drag coefficient. However, such a formulation does not appear to be appropriate at low latitudes where the wind may be highly ageostrophic.

empirical study by Lettau and Zabransky (1968) and in numerical modeling studies of Nickerson (1968) and Wagner (1966), is of the order of a few kilometers. Consequently, on a synoptic macroscale, the neglect of advections in the surface layer and the assumption of instantaneous adjustment of the surface flow with the local pressure field and overlying flow, appears to be reasonable. Then, assuming a log layer for unidirectional flow ($V_z = (|\vec{\tau}_0|/\rho)^{1/2}/k_z$) where k is the Karman constant), and estimating $|\vec{\tau}_0|/\rho$ from the surface drag relationship, we obtain

$$\begin{aligned} \vec{V}_z &= \vec{V} c_d^{1/2}/kz \\ k_0 &= c_d^{1/2}/kz \end{aligned} \tag{8}$$

The geophysical drag coefficient can also be evaluated by noting that the log layer for unidirectional flow implies that $\tau_0/\rho = v^2k^2/[\ln(z/z_0)]^2$. Then, using the stress relationship and replacing V by the scale velocity, we obtain

$$\begin{aligned} \vec{V}_z &= \vec{V}\, Vk^2/K[\ln(z/z_0)]^2 \\ k_0 &= Vk^2/K[\ln(z/z_0)]^2 \end{aligned} \tag{9}$$

Several estimates of k_0 from the above three formulations are listed in table 2. An empirical relationship constructed by Deacon and Webb (1962) for the drag coefficient appropriate to flow over water with neutral thermal stability is

$$c_d = (1 + .07|\vec{V}|\,s/m) \times 10^{-3} \tag{10}$$

This relationship with $|\vec{V}| = 5$ m/s is used in table 2. On the basis of results in table 2, the value $k_0 = 1.5 \times 10^{-3}$ m^{-1} is used in this study.

2.3 Formulation of the Diffusion Term

In this section the representation of the momentum diffusion term is formulated. Since this study views the boundary layer from space and time scales considerably larger than those of boundary layer turbulence, momentum transports due to turbulence must be parameterized. Such parameterizations are usually of the form $\tau = \rho K \vec{V}_z$ where K, the eddy viscosity, is specified a priori or related to the mean vertical wind shear by a mixing length formulation $K = \ell^2|\vec{V}_z|$, where ℓ is the mixing length.

Table 2

Estimates of the Geophysical Boundary Coefficient

Expression for k_0	Parameter values	k_0 value
$k_0 = c_d V/K$	$K = 5 m^2/s$ $V = 5 m/s$ $c_d = 1.35 \times 10^{-3}$	1.35×10^{-3} m^{-1}
$k_0 = \sqrt{c_d}/kz$	$k = .4$ $z = 20$ m $c_d = 1.35 \times 10^{-3}$	4.6×10^{-3} m^{-1}
$k_0 = Vk^2/K[\ln(z/z_0)]^2$	$V = 5 m/s$ $z_0 = .02$ cm $z = 20$ m $K = 5 m^2/s$ $k = .4$	1.21×10^{-3} m^{-1}

For this study neither approach appears to be clearly superior. There are a number of shortcomings in each of these two methods. Considerable evidence exists that stresses due to turbulent transfers of momentum are not simply related to the mean vertical wind shear as suggested by the above relationships. In such cases the stress relationship is not valid and/or eddy viscosity is dependent on other factors in addition to mean wind shear. For example, Starr (1968) discussed atmospheric cases where momentum transfers of smaller scales of motion may even be in the opposite direction of the mean wind gradient. In the case of convection, turbulent transfers of momentum and eddy viscosity may be more strongly related to stability than to mean wind shear. For example, Lettau (1958) demonstrated a strong dependence of eddy viscosity on the diurnal variation of stability. Zipser (through personal communication) has observed that strong vertical wind shears across the trade inversion where eddy viscosity and turbulent transports are expected to be small. Chia and Sage (1970) calculated eddy viscosity for air flow between parallel plates (Reynolds numbers from 40,000 to 100,000), where convective transfers were generated by temperature differences between the plates. Stress profiles were determined from measured horizontal pressure gradients thus enabling them to compute eddy viscosities. Their results indicate that eddy viscosity did not vanish with the mean wind shear at the center of the duct as would be predicted by mixing length theory.

Lettau (1964, 1967) has demonstrated how mixing length theory might be complicated by the fact that parcels continuously entrain momentum over the mixing length. Lettau (1970) showed that the turbulent momentum fluxes can be proportional to the mean wind shear only when certain coherence, similarity and symmetry requirements are satisfied by the turbulence. Lettau (1970) suggested that the failure of the mixing length theory in predicting eddy viscosity behavior in the experiments of Chia and Sage (1970) can be attributed to the fact that the turbulence did not satisfy these conditions.

The application of mixing length theories to low latitude boundary layers incurs a number of difficulties. Mixing length theories require the specification of scaling parameters which are in general based in part on the Coriolis parameter and the geostrophic wind (Blackadar, 1962, and Lettau, 1962). The application of such theories to low latitude regions where the Coriolis parameter is small and ageostrophic components may be large, appears to be questionable.

Errors in the scaling of the mixing length profile may be especially critical in a baroclinic boundary layer. Near the top of the frictional boundary layer where stresses are small, vertical wind shears due to the baroclinicity may still be large. However, a mixing length theory, if not properly scaled, may erroneously interpret these vertical wind shears as an indication of significant stresses. As will be seen in chapter 5, strong vertical motions and resulting strong vertical momentum advections may also contribute to vertical wind shear maintenance in and above the frictional boundary layer.

On the other hand, there is evidence which suggests that the wind field at the top of the boundary layer is not as sensitive to the specification of a height-independent eddy viscosity. This occurrence is related to the fact that $\vec{V}_{zz}$ tends to become small near the top of the boundary layer so that the computed friction force (with constant K) also becomes small. Note that figure 1 indicates that $\vec{V}_{zz}$ is generally large only in the lowest layers, while $\vec{V}_z$ may be large throughout the lower troposphere. In other words, in the upper portion of the boundary layer where eddy viscosity should be decreasing with height, $\vec{V}_{zz}$ and therefore $K\vec{V}_{zz}$ are small, so that errors in eddy viscosity do not appreciably affect the wind field. The success of the linear Ekman solution in approximating the wind field above the surface layer in many mid-latitude boundary layer flow situations (Hess, 1959) can be in part attributed to this flow feature. Similar reasons may be responsible for the success of baroclinic-Ekman solutions (with constant eddy viscosity) in approximating the boundary layer wind field over interior Antarctica (Schwerdtfeger and Spanholz, 1970).

Based on the above arguments, the $K\vec{V}_{zz}$ representation of the diffusion term with a priori specification of height-independent eddy viscosity has been chosen for many of the considerations of this study while the mixing length theory will not be used. However, the $K\vec{V}_{zz}$ approach is not without difficulties. A priori specification of eddy viscosity excludes basic nonlinear interactions between the turbulent and mean flow scales, since in actuality eddy viscosity is a function of the wind field. Although this exclusion has not prevented the $K\vec{V}_{zz}$ approximation from yielding reasonable wind solutions for many mid-latitude boundary layers, such an approximation has not been tested with observations of equatorial low level winds. Furthermore, studies of vertical profiles of eddy viscosity in equatorial regions are virtually nonexistent at present.

Another difficulty with this approximation of the friction term is that in the lowest portion of the boundary layer, eddy viscosity increases with height as is evident in figure 3. The use of the geophysical lower boundary condition can in part compensate for this deficiency since it crudely parameterizes the surface layer.

To approximate the decrease of eddy viscosity with height in the upper portion of the boundary layer, the idealized eddy viscosity profile shown in figure 3 is used in certain numerical model experiments. With this profile, eddy viscosity decreases linearly from 500 m to 10% of its maximum value at 1700 m above which eddy viscosity is again height-independent. Since the literature survey in the introduction suggests that the boundary layer is deeper at lower latitudes where the Coriolis parameter is small, the vertical scaling of the idealized eddy viscosity profile is chosen to be somewhat larger than those of the mid-latitude profiles. 1700 m is also typical of trade inversion heights between the equator and 10° latitude (Ficker, 1936). Note, however, that a height-dependent eddy viscosity implies a $K_z\vec{V}_z$ term which, like the mixing length formulation, could erroneously interpret large vertical wind shears near the top of the frictional boundary layer as an indication of large stresses.

A value of $5m^2/s$ is chosen for the height-independent portion of the eddy viscosity profile. This value is thought to be representative of neutral stability over water with wind speeds 5—10 m/s. This value of eddy viscosity in numerical experiments yields profiles where the frictional boundary layer depth, as estimated by the region of large $\vec{V}_{zz}$, compares favorably with low level wind observations in figure 1 and in Estoque (1970). However, because of the uncertainty of the eddy viscosity magnitude, it is varied in certain experiments to study the effect of changing this magnitude.

The height-dependent eddy viscosity profile and the geophysical lower boundary condition are used in numerical experiments where closer physical reality is desired. In experiments where comparison with the Ekman solution

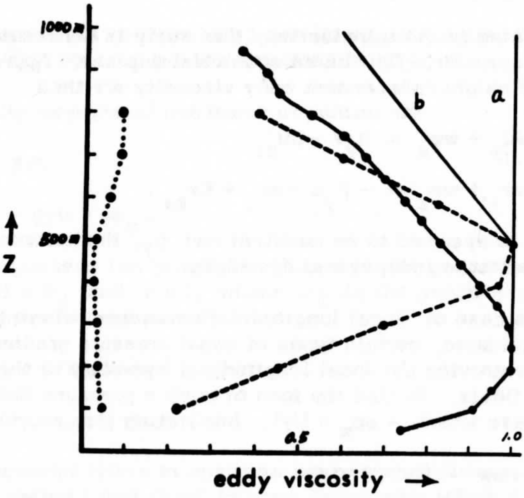

Figure 3. Vertical profiles of eddy viscosity. The plotted values are normalized with respect to the maximum daytime eddy viscosity at each location.

	Source	Location	Stability	Maximum value
Solid line	Lettau (1950)	Leipzig	slightly stable	14.4 m^2/s
Dashed line	Lettau (1958)	Drexel, Neb.	lapse	87.0 m^2/s
Dotted line	Lettau (1958)	Drexel, Neb.	stable	9.2 m^2/s

---

is the primary purpose, a no-slip boundary condition is used with a height-independent eddy viscosity.

3. THEORETICAL ASPECTS OF THE LOW LATITUDE BOUNDARY LAYER

This chapter will analytically examine low latitude boundary flow. Actual flow solutions are difficult because of the nonlinearity of the boundary layer equations of motion. In general, however, qualitative information can be extracted from the equations of motion without actually solving them.

3.1 The Equations of Motion

As stated in the introduction, this study is concerned with steady longitudinally symmetric flow on an equatorial β-plane. Appropriate equations of motion for height independent eddy viscosity are then

$$vu_y + wu_z = \beta_y v + Ku_{zz} \tag{11}$$

and

$$vv_y + wv_z = -\beta_y u - \alpha p_y + Kv_{zz} \, . \tag{12}$$

where α is assumed to be constant and p_y, the horizontal pressure gradient, is assumed to be independent of height.

In the case of "local longitudinal symmetry" where the entire globe is not being considered, certain types of zonal pressure gradients can also be used without destroying the local longitudinal symmetry of the pressure gradient and wind fields. To find the form of such a pressure field, consider the most general case where $-\alpha p_x = f(y)$. Integrating this expression gives

$$-\alpha p = f(y)x + g(y) \, . \tag{13}$$

The meridional pressure gradient force is then

$$-\alpha p_y = f'(y)x + g'(y) \tag{14}$$

and longitudinal symmetry requires that $f'(y) = 0$, so that

$$-\alpha p = \text{constant} \cdot x + g(y) \, . \tag{15}$$

In other words, the zonal pressure gradient must be independent of latitude and longitude. The class of pressure fields where $-\alpha p_x$ = constant is considered numerically in chapter 5.

Note that the Coriolis term, $-2\Omega \omega \cos \phi$, in the zonal equation of motion (11) has been neglected even though it reaches a maximum at the equator. This term is generally considered to be negligible (Haltiner and Martin, 1957). In the case of constant $-\alpha p_y$, the ratio of this Coriolis term to the pressure gradient term $w2\Omega \cos \phi / -\alpha p_y$ can be expressed in the form $w \cos \phi / U_g (5°) \sin (5°)$. Scale analysis in equatorial equations suggests that $\frac{W}{U_g} = 0(10^3)$ for macro-synoptic scale motions so that the above ratio is $0(10^{-2})$. Therefore, this estimation indicates that this Coriolis term can be neglected with approximately one percent accuracy even at the equator.

These equations will be examined first from an analytical viewpoint and then numerically in chapter 5.

3.2 Flow at the Top of the Boundary Layer

Before concentrating on boundary layer flows, solutions at large heights where $\vec{V}_z$ and $\vec{V}_{zz}$ both vanish are examined briefly.

The vertically asymptotic equations of motion are

$$vu_y = \beta y u \tag{16}$$

and

$$vv_y = -\beta y u - \alpha p_y \, . \tag{17}$$

These equations possess two possible solutions: the geostrophic solution in which case $U = U_g$ and $v = 0$, where U_g is the geostrophic wind, and the constant angular momentum solution

$$u = u_0 + \beta/2(y^2 - y_0^2) \tag{18}$$

$$v = v(v_0, u_0, y_0, y) \neq 0 \tag{19}$$

where the 0 subscript refers to upstream boundary conditions. The latter solution will be called "drift flow" in accordance with Mörth (1963).

To find the solution of the meridional drift component, (17) is written in the form $1/2(v^2)y = -\beta y u - \alpha p_y$, v is then obtained by integrating from y_0 to y

$$v^2 = v_0^2 + 2G(y) - 2\alpha(p - p_0) \tag{20}$$

where

$$G(y) \equiv -\beta[-(\frac{u_0 y_0^2}{2} + \frac{\beta}{8} y_0^4) + y^2(\frac{u_0}{2} - \frac{\beta}{4} y_0^2) + y^4 \frac{\beta}{8}] \tag{21}$$

If the Coriolis term (the second term of the right-hand side of (29)) is negligible, then inertial flow results (Winn-Nielsen, 1970). Mörth (1963) solved (17) in the special case where $-\alpha p_y = A =$ constant, in which case

$$v^2 = v_0^2 + 2G(y) + 2A(y - y_0) \, . \tag{22}$$

It is instructive to look at the above equations in terms of geostrophic wind, even though the drift flow may be highly ageostrophic. In the case of a pressure field corresponding to a constant geostrophic wind[3], (20) becomes

---

[3] U_g = constant implies that $P_y \to 0$ as $y \to 0$ and via L'Hopital's rule $-\alpha p_{yy} \to \beta U_g$ as $y \to 0$.

$$v^2 = v_0^2 + 2G(y) + \beta U_g (y^2 - y_0^2). \tag{23}$$

Of interest is the latitude y^* at which the meridional flow vanishes, and which is where the wind first becomes locally geostrophic. The distance between this latitude and the initial latitude will define Y_I, the latitudinal extent of the influence of the initial ageostrophic wind. Y_I can also be thought of as the width of the horizontal inertial boundary layer (i. e., the adjustment zone where horizontal advections are important) resulting from the initial ageostrophic flow.

At y^* where $v(y^*) = 0$, (23) becomes

$$0 = v_0^2 - 2\beta[-(\frac{u_0}{2} y_0^2 + \frac{\beta}{8} y_0^4) + y^{*2}(\frac{u_0}{2} - \frac{\beta y_0^2}{4}) + y^{*4} \frac{\beta}{8}] + \beta U_g (y^{*2} - y_0^2) \tag{24}$$

which is a quadratic equation in y^{*2}. Defining

$$U_{a0} = U - U_g \text{ and } |\vec{V}_{a0}| = |\vec{V}_g - \vec{V}_0|$$

and solving the quadratic equation yields

$$y^{*2} = y_0^2 - 2U_a/\beta + 2|\vec{V}_{a0}|/\beta \tag{25}$$

Since $Y_I = (y^{*2} - y_0^2 - 2y^*y_0)^{1/2}$, (25) suggests that Y_I is largest for large initial ageostrophic wind and low initial latitude. In the case of small ageostrophc wind and high initial latitude, the flow remains quasi-geostrophic. When the initial latitude is the equator,

$$Y_I = [-2U_{a0}/\beta + 2|\vec{V}_{a0}|/\beta]^{1/2} \tag{26}$$

This expression suggests that $\sqrt{\frac{|\vec{V}_{a0}|}{\beta}}$ might be an appropriate horizontal scale width for the influence of the equator through horizontal advections. Similarly, scale analysis in the introduction predicted that this scale width is proportional to $\sqrt{|\vec{V}_g|/\beta}$.

Any mechanism initiating ageostrophic flow will, by definition, generate drift flow. Such a mechanism could be inertial instability. Linear theory for an equatorial β plane predicts that inertial instability results if the absolute geostrophic vorticity, $\zeta_{ag} \equiv \beta_y - (U_g)_y$, is negative (i. e., $(U_g)_y$ must be positive). Since $(U_g)_y = \frac{\alpha p_y}{\beta y^2}$, this condition implies that for a constant horizontal pressure gradient force, inertial instability and possibly drift flow may be initiated between the equator and the latitude y^{**} where $y^{**} = \sqrt[3]{\alpha p_y / \beta^2}$.

3.3 Simplified Boundary Layer Flow Cases

The boundary layer equations of motion (11) and (12) are second order nonlinear partial differential equations, and would be extremely difficult to solve analytically. However, some information can be extracted from qualitative analysis and solutions of simplified cases of these equations.

These equations may be simplified at both latitude extremes. At high latitudes in the case of small $(\alpha p_y)_y$, the equations become linear and the solutions approach the Ekman solution. The equations are also simplified near the equator where Coriolis terms become negligible. However, without further simplification, the equations still remain nonlinear and second order at the equator.

Since the properties of the Ekman solution are well known, our attention will now be focused on the other latitudinal extreme where the Coriolis term vanishes. The boundary layer equations of motion without the Coriolis term can be subdivided into three classes: 1) horizontal advections are important; 2) vertical advections alone are important; and 3) both advection terms are unimportant. The equations in the first class cannot be solved locally since they depend on neighboring flows through horizontal advections.

The latter class of linear equations yields physically unlikely solutions in that the boundary layer depth is infinite for nonzero flow, although this singularity may vanish for height-dependent eddy viscosity or height-dependent horizontal pressure gradient. The equations of the second class, where only horizontal advections are negligible, will result from a pressure field exhibiting "even symmetry" with respect to the equator $(p(y) = p(-y))$ where the meridional flow exhibits "odd symmetry" with respect to the equator $(v(y) = -v(-y))$. In this case, meridional flow (but not meridional flow convergence) vanishes locally at the equator. In the resulting equations, the influence of vertical advections on the boundary layer flow are emphasized, since the Coriolis and horizontal advection terms are neglected. The equations of motion then reduce to

$$\begin{aligned} wu_z &= Ku_{zz} \\ v &= 0 \end{aligned} \tag{27}$$

Since vertical motion is dependent on the horizontal flow convergence, the solution to (27) still depends implicitly on neighboring flows. However, if a vertical motion profile is specified, then (27) can be solved in such a manner that the influence of the specified vertical motions on the boundary layer flow can be studied.

Defining $u' \equiv u_z$ and $w \equiv \overline{W}f(z)$ where $\overline{W} \geq 0$ and $f(z)$ is a normalized vertical motion profile, (27) becomes

$$f(z)u' = \frac{K}{\overline{W}} u'_z . \qquad (28)$$

The equation can be simplified by defining $D \equiv K/\overline{W}$ and $\hat{z} \equiv z/D$ where D is a boundary layer scale depth for u'

$$f^*(\hat{z})u' = u'_{\hat{z}} . \qquad (29)$$

The solution for u' in terms of the normalized vertical motion profile $f^*(\hat{z})$ is then

$$u'(\hat{z}) = u'(0) \exp\left[\int_0^{\hat{z}} f^*(\hat{z})d\hat{z} \right] . \qquad (30)$$

If $f^*(\hat{z}) > 0$ (rising motion occurs at all heights), then either $U(\hat{z}) = 0$ or vertical wind shear does not vanish with height so that the boundary layer depth is infinite. In other words, for a normal boundary layer wind profile ($u_{zz}/u < 0$), the advection of lower momentum from near the surface cannot be balanced by the diffusion term. This dilemma has been discussed by Young (1969) and Charney (1960).

If $f^*(\hat{z}) < 0$ (sinking motion occurs everywhere), then a nontrivial solution with finite boundary layer depth is possible. Let us assume that $f^*(\hat{z})$ can be specified by considering two contributions to horizontal convergence; a term due to the convergence of the frictionless flow aloft which is independent of height, and a boundary layer correction term. Then

$$v_y(\hat{z}) = v_y(\infty) + v_y(\hat{z})_{b.l.} . \qquad (31)$$

The first term vanishes in the case of nondivergent flow above the boundary layer (geostrophic flow) and is nonzero for drift flow above the boundary layer. On the basis of the stress solution (30), it is reasonable to assume that the boundary layer convergence correction term vanishes exponentially with height. With the above divergence formulation (31), and consideration of the mass continuity equation,

$$f^*(\hat{z}) = -(1 - \exp(-\hat{z}/D^*)) - k\hat{z} \qquad (32)$$

where k is zero in the case of geostrophic flow and D^* is the ratio of the scale height of the boundary layer convergence correction term to the boundary layer scale height D. D^* is expected to be $O(1)$.[4]

Integrating $f^*(\hat{z})$, (30) then becomes

$$u'(\hat{z}) \;=\; u_0' \exp[-\hat{z} - D^*(e^{-\hat{z}/D^*} - 1) + k\hat{z}^2/2] \tag{38}$$

If the frictionless flow is nondivergent $(k = 0)$ and the vertical motion and boundary layer scale depths are the same $(D^* = 1)$, then the $1/e$ folding depth for u' occurs at $\hat{z} + e^{-\hat{z}} - 1 = 1$ or $z \simeq 1.84\ K/\overline{W}$. In the other asymptotic case where the boundary layer convergence correction term vanishes $(D^* = \infty)$ so that $f^*(\hat{z}) = -k\hat{z}$, the $1/e$ folding depth for u' is $z = K\sqrt{2/k}/\overline{W}$. It is then apparent from scaling considerations alone that the boundary layer depth in terms of stress is thickest for large eddy viscosity and weak subsidence. Conversely, vertical advection of higher momentum downward is a restraining influence on boundary layer depth, as would be qualitatively expected.

Equation (33) cannot be further integrated explicitly to obtain $u(z)$, since the factor $\exp[-D^* \exp(-\hat{z}/D)]$ would appear in the integrand. The solution of this equation could be approximated by a series expansion; however, for the purpose of this study, we will be content with a numerical evaluation. Vertical wind shear profiles computed from (33) are shown in figure 4.

Note that near the lower boundary where vertical motion is small, vertical wind shear (and stress) vary slowly with height. As a result, the friction term does not reach a maximum until the middle portion of the boundary layer (for constant eddy viscosity). When the scale height of the convergence term is increased to a value greater than $K/\overline{W}$ $(D^* > 1)$, stress is increased, especially in the upper levels, so that an appropriate scale depth for the stress profile is between $K/\overline{W}$ and the convergence scale height. It is also evident in figure 4 that the height-independent divergence term is very efficient in reducing stress in the upper levels. This suggests that the boundary layer depth associated with diverging drift flows may be kept relatively small.

In summary, only the trivial solution $u(\hat{z}) = 0$ is possible with rising motion, if boundary layer depth is required to be finite. In the case of subsidence, the boundary layer depth is proportional to $(K/\overline{W})$.

---

[4] In a baroclinic situation, the term $(1 - \exp(-\hat{z}/D^*))$ could be associated with influences which are not frictionally induced so that D^* is not $O(1)$.

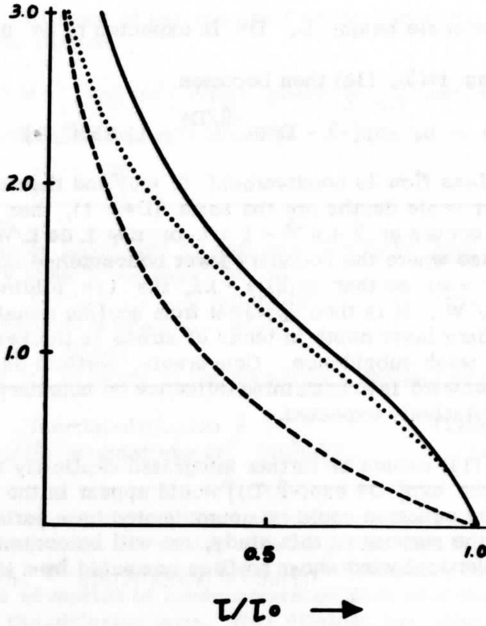

Figure 4. Computed vertical profiles of stress for idealized flow at the equator. τ/τ_0 is plotted for $D^* = 1$, $k = 0$ (solid line), $D^* = 0$, $k = 0$ (dashed line) and $D^* = 1$, $k = .2$ (dotted line).

The above analysis would be valid locally in the case of symmetry of wind and pressure fields about an arbitrary latitude, where the meridional flow and the Coriolis term in the zonal equation of motion would vanish locally. However, Coriolis and horizontal advection terms will in general modify the above analysis. In fact, horizontal advections may often oppose vertical advections in the boundary layer. For example, near the surface where the wind increases with height, horizontal divergence (horizontal advections of lower momentum) implies subsidence and downward advections of higher momentum, and so forth.

a) Dynamical Boundary Layer Regimes in the Vertical

We now turn our attention to the boundary layer equations of motion at an arbitrary latitude in the equatorial region. Since the equations are more complicated, the discussion will be limited to qualitative considerations.

In terms of vertical transports of momentum, one can hypothesize four possible regions in the vertical for barotropic flow. Near the ground the diffusion term is important while vertical advections are small. If vertical motion is sufficiently strong, both vertical advection and diffusion terms may be important above this region. At still higher levels vertical advections may still be important where the diffusion term is no longer important. At high enough levels both of these terms are unimportant.

Of course, the above regions can be further complicated by considering the importance of Coriolis and horizontal advection terms. Scale analysis indicates that horizontal advections are $0(|\vec{V}|^2)$ while the Coriolis term is $0(|\vec{V}|)$. Since velocities increase with height, at least in the lower layers near the ground, the horizontal advection and Coriolis terms, like the vertical advection term, may also increase with height in this region. Above the regions where diffusion terms are important, several dynamical possibilities may occur: both advection terms may be unimportant (quasi-geostrophic flow), horizontal advections may be important (drift flow) or an intermediate layer where vertical advections are important may occur beneath the quasi-geostrophic or drift flows. This latter possibility will be referred to as a vertical inertial boundary layer. Possible dynamical flow classes are listed in table 3, while possible dynamical regions for cross-equatorial flow are schematically illustrated in figure 6.

b) Flow Toward the Equator

Consider the case where flow toward the equator originates from high latitudes where it is initially quasi-Ekman. We will now consider only those advections resulting from horizontal variations of the boundary layer scaling depth due to latitudinal changes in the Coriolis parameter, since this effect is always present at low latitudes (and thus ignore advections resulting from horizontal variations of the geostrophic wind).

The latitude at which the Ekman solution is no longer a valid approximation can be estimated by calculating such advections from the Ekman solution

$$\begin{aligned} v &= U_g e^{-\hat{z}} \sin \hat{z} \\ u &= U_g(1 - e^{-\hat{z}} \cos \hat{z}) \end{aligned} \qquad (34)$$

where $\hat{z} = z/D(y)$ and $D = \sqrt{2K/\beta y}$. Differentiating the Ekman solution

Table 3

Classification of Flow Regimes Based on the Relative Importance of Diffusion and Advections of Momentum

	advections important	advections not important
diffusion not important	drift (horizontal advections only) vertical inertial boundary layer (vertical advections)	geostrophic
diffusion important	inertial-diffusion boundary layer	Ekman boundary layer

$$vv_y = F(y)\,\hat{z}e^{-2\hat{z}}\,\sin(\hat{z})(\sin(\hat{z}) + \cos(\hat{z}))$$

$$vu_y = F(y)\hat{z}e^{-2\hat{z}}\,\sin(\hat{z})(-\sin(\hat{z}) + \cos(\hat{z}))$$

$$wv_z = F(y)e^{-2\hat{z}}(-\sin(\hat{z}) + \cos(\hat{z}))[\hat{z}\,\sin(\hat{z}) + \frac{1}{2}\,(\sin(\hat{z}) + \cos(\hat{z}))]$$

$$wu_z = F(y)e^{-2\hat{z}}(\sin(\hat{z}) + \cos(\hat{z}))[\hat{z}\,\sin(\hat{z}) + \frac{1}{2}\,(\sin(\hat{z}) + \cos(\hat{z}))]$$

$$\text{where} \quad F(y) = U_g^2/2y\,. \tag{35}$$

Noting that the trigonometric terms are $O(1)$, then the magnitudes of the advection terms relative to the Coriolis term magnitude are of the order $U_g/2\beta_y^2$. Then advection terms first become comparable to the Coriolis term (local Rossby number equal to one) at $Y = \sqrt{U_g/2\beta}$. Once again, $\sqrt{U_g/\beta}$ is an appropriate scale factor for the width of a horizontal inertial boundary layer about the equator.

Figure 5 shows various dynamical regions based on the signs of the advection terms for Ekman flow toward the equator ($U_g = -10$ m/s). The role of advections in the upper regions of the boundary layer, as indicated by the Ekman solution, is to rotate the wind vector toward the geostrophic wind direction. The role of advections in the lower layers is to increase both

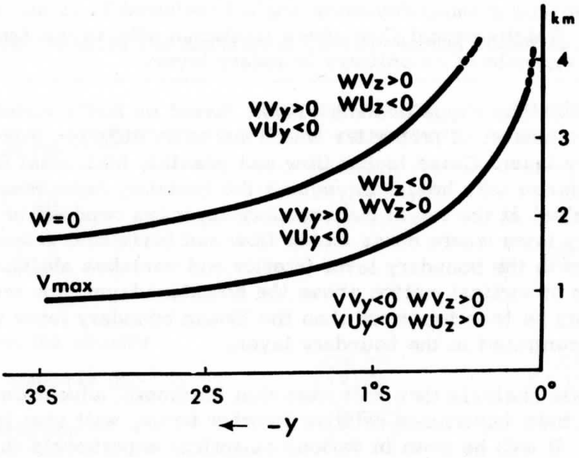

Figure 5. Momentum advection regimes calculated from the Ekman solution for $U_g = -10$ m/s, $K = 5 m^2/s$.

flow components. The effect of these flow changes is to decrease boundary layer depth which suggests that advections may prevent the boundary layer depth from becoming infinite at the equator.

c) Flow Directed Away from the Equator

The frictionless flow crossing the equator or originating at the equator will likely be drift flow downstream from the equator. Of course, in the absence of inertial instability, geostrophic flow aloft is also a theoretical possibility. Assuming drift flow, we will now focus on the underlying boundary layer flow. For convenience, "drift region" will refer to the region which includes both the frictionless drift flow and the underlying boundary layer flow.

There is evidence which suggests that the characteristics of boundary layer flow directed away from the equator may be quite different from the characteristics of boundary layer flow toward the equator. For example, one might expect the boundary layer wind vector to rotate slowly with height (compared to the Ekman spiral) as was discussed in the introduction in reference to a vortex study by Kuo (1971). To describe this boundary layer flow property, the boundary layer wind "deviation angle" is defined as the angle between the boundary layer wind vector and the wind vector at the top of the boundary layer. For reference purposes, the deviation angle associated with the Ekman spiral will be considered to be large. The boundary layer with a small deviation angle is referred to as an "ordinary boundary layer." Unidirectional flow where rotational effects are small would be a classic example of an ordinary boundary layer.

The ordinary type boundary layer, based on Kuo's vortex results, possesses a number of properties which are quite different from the Ekman boundary layer. Cross isobar flow and possibly horizontal flow convergence may increase with height throughout the boundary layer reaching a maximum (drift value) at the top of the boundary layer (as opposed to the Ekman boundary layer where cross isobar flow and horizontal convergence reach a maximum in the boundary layer interior and vanishes aloft). Consequently, in terms of vertical motion above the boundary layer, the ordinary boundary layer may be less important than the Ekman boundary layer where convergences are concentrated in the boundary layer.

Scale analysis then indicates that horizontal advections $0(|\vec{V}|^2)$, as well as their importance relative to other terms, will also increase with height. It will be seen in various numerical experiments that the height-dependence of the importance of horizontal advections plays a major role in the response of the ordinary boundary layer wind field to the pressure field. For example, a height-dependent local Rossby number for flow directed away from the equator might be defined

$$\hat{R}_0(z) = V(z)/\beta y^2 \tag{36}$$

where y is used as an estimation of the horizontal scale length and $V(z)$ is a height-dependent scale velocity. The horizontal adjustment scale of the flow to the pressure field associated with $\hat{R}_0 = 0(1)$ is then $Y = \sqrt{V(z)/\beta}$. This horizontal adjustment scale then increases with height according to the square root of velocity, which suggests that the distance downstream from the equator where advections are no longer important increases with height. Therefore, one might expect the latitude of transition (from drift-ordinary boundary layer flow to quasi-Ekman flow) to increase with height.

In this transition region, the thickness of the layer of cross isobar flow decreases since cross isobar flow in the geostrophic-Ekman regime is limited to the boundary layer. Without considering changes in wind speed, one would then expect horizontal convergence and rising motion in this region. Conversely, subsidence is expected in the transition from Ekman flow to ordinary boundary layer flow.

Various estimates of these transition latitudes discussed thus far are listed in table 4. The horizontal structure of cross-equatorial flow is schematically illustrated in figure 6. The boundary layer characteristics suggested by the above latitudinal asymptotic solutions and qualitative arguments

Table 4

Estimates of the Width of the Horizontal Inertial Region about the Equator

	Free Atmosphere	Boundary Layer
Flow toward the equator		
1. scale analysis (R_0 = 1, Int.)	$\sqrt{U_g/\beta}$	-
2. computed from Ekman solution (R_0 = 1)	-	$\sqrt{U_g/2\beta}$
Flow away from the equator		
1. scale analysis (R_0 = 1)	$\sqrt{\lvert\vec{V}\rvert/\beta}$	$\leq \sqrt{\lvert\vec{V}\rvert/\beta}$
2. drift solution	$\sqrt{\lvert\vec{V}_a\rvert/\beta}$	-

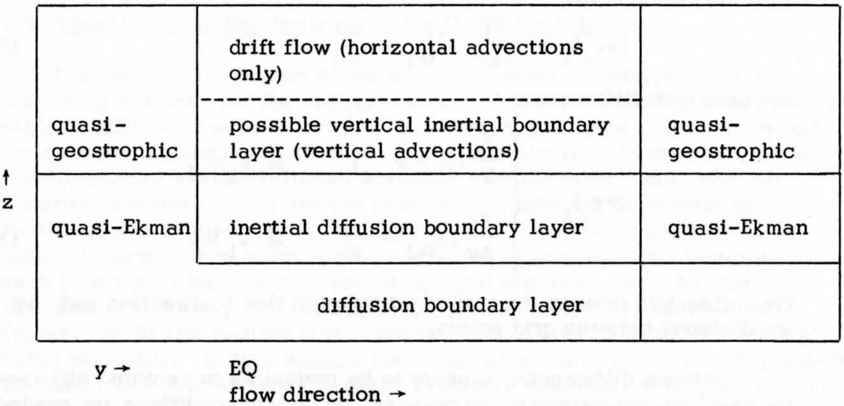

Figure 6. Dynamical Structure of Cross-equatorial Flow

are examined in more detail in chapter 5 where boundary layer flow solutions for certain specified pressure fields are obtained numerically. In the next chapter there is construction of the boundary layer numerical model used to obtain these solutions.

4. THE BOUNDARY LAYER NUMERICAL MODEL

In the first part of the chapter, possible finite difference schemes for a time-dependent boundary layer numerical model are discussed. This discussion emphasizes the finite differencing of the diffusion term, since a diffusion difference scheme not previously tested will be chosen for the model.

4.1 Finite Differencing of the Advection Terms

Two commonly-used advection difference schemes are at our disposal: centered differencing

$$(vv_y)_i = \frac{v_i}{2\Delta y}(v_{i+1} - v_{i-1}) \tag{37}$$

and upstream differencing

$$(vv_y)_i = \begin{cases} \dfrac{v_i}{\Delta y}(v_i - v_{i-1}) & \text{if } v_i > 0 \\[2ex] \dfrac{v_i}{\Delta y}(v_{i+1} - v_i) & \text{if } v_i > 0 \end{cases} \tag{38}$$

The subscripts refer to the grid point index in the y direction and Δy is the distance between grid points.

Upstream differencing appears to be preferable to centered differencing for physical and mathematical reasons. Boundary conditions are needed only at the inflow boundary with upstream differencing, while centered differencing requires boundary conditions at both the inflow and outflow boundaries. Since the equations of motion are first order in the horizontal direction, centered differencing of horizontal derivations would result in a mathematically over-specified problem. Upstream differencing would require two boundary conditions only in the case of inflow at both side boundaries in which case the problem could be viewed (in terms of the equations of motion) as two independent flow problems coupled only indirectly through the mass continuity equation.

To illustrate another undesirable feature of centered differencing, consider a convergence line. Centered differencing would incorporate points on both sides of the convergence line. However, the actual velocity derivative would not directly depend on the velocity on the opposing side of the convergence line. Another physically unappealing characteristic of centered differencing is that a relative maximum may be further increased by the computed advection alone.

From a physical viewpoint, upstream differencing then appears to be preferable and will therefore be used in this study. Unfortunately, it often requires more stringent numerical stability requirements for the advection-diffusion equation as will be seen later in this chapter. Furthermore, the lowest order truncation error associated with upstream differencing involves the second order velocity derivative of the exact solution and is therefore of the same mathematical form as diffusion. Molenkamp (1968) observed that such truncation errors tend to diffuse various properties. Using the boundary layer numerical model developed later in the chapter, various experiments performed for various grid spacings indicated that the total truncation errors were 0(1%) or less.[5]

4.2 Numerical Stability Analysis of the Diffusion Schemes

This section is devoted to the numerical stability analysis of finite difference schemes for the diffusion term. Numerical stability conditions for explicit difference schemes(that do not involve predicted values of the diffusion term) require restrictions on the size of the time increment even for the differenced simple diffusion equation. On the other hand, implicit schemes (schemes which involve predicted values) are in general stable for the simple diffusion equation regardless of the size of the time increment. Unfortunately, most implicit schemes require a matrix inversion at each time step which, for a two-dimensional problem, could be quite laborious. However, two diffusion schemes developed by Du Fort and Frankel (1953) and Saul'ev (1957) are implicit in character but can be evaluated explicitly. In this section two other schemes of this type are presented. Because these four schemes possess favorable numerical stability conditions and can be easily applied, pure explicit schemes and pure implicit schemes are not further considered.

---

[5] A truncation error analysis via Taylor series indicates that the lowest order truncation term is linearly proportional to the grid spacing. Therefore, increasing the grid resolution by a factor of two should decrease the truncation error by approximately a factor of two so that the size of the truncation error can be estimated.

We use the Fourier analysis method to derive the numerical stability conditions of these four schemes for the linearized meridional boundary layer equation of motion

$$v_t + \bar{V} v_y + \overline{W} v_z = K v_{zz} + P$$
$$P = - f\bar{U} - \alpha p_y \tag{39}$$

where P is the sum of the terms not involving v . The following stability analysis is also applicable to the linearized zonal boundary layer equation of motion since it is of the same form as the above equation.

Applying forward differencing for the time derivative and upstream differencing for the advection term, the above equation in the case of $\overline{W} > 0$ and $\bar{V} > 0$ becomes

$$v_{i,j}^{n+1} = v_{i,j}^{n} + \Delta t \left[- \frac{\bar{V}}{\Delta y} (v_{i,j} - v_{i-1,j}) - \frac{\overline{W}}{\Delta z} (v_{i,j} - v_{i,j-1}) + K v_{zz} + P \right] \tag{40}$$

where superscript n is the time level indicator, subscript i refers to the i^{th} horizontal grid point past y = 0, subscript j refers to the j^{th} vertical grid point past z = 0, Δt is the time increment, Δy is the horizontal space increment, and Δz is the vertical space increment. It is easily shown that the stability analysis is not affected by the direction of the flow. The differencing of the diffusion scheme is postponed until after some general comments on numerical stability properties of (40).

Richtmeyer and Morton (1957) noted that when the diffusion equation contains a "source term" (the pressure gradient term in the case of the above boundary layer equations of motion), "legitimate exponential growth" of the numerical solution must be allowed in the stability analysis. If $F^{-1}S$ is the total amplification matrix for the finite difference form of (40), then the appropriate stability condition becomes $|F^{-1}S| \leq 1 + O(\Delta t)$.

In general the lower order terms of the diffusion-advection equation do not affect the stability (with respect to choice of K) of the principal part of the differential equation ($v_t = K v_{zz}$). This has been observed with both the Fourier method of stability analysis (Richtmeyer and Morton, 1957) and with energy methods (Lees, 1960).

However, Williamson (1966) analyzed the numerical stability of several implicit diffusion schemes in the advection-diffusion equation where advection terms employed centered differencing and "legitimate exponential growth" was not permitted. He concluded that there was no simple method to determine the stability condition for the entire advection-diffusion equation from the individual stabilities of the diffusion and advection equations.

The Fourier method of stability analysis is adopted for this study. The Fourier transformed meridional velocity component is

$$v(y, z, t) = v^n \exp\{im[k(i\Delta y) + \ell(j\Delta z)]\} \tag{41}$$

where k and ℓ are the horizontal and vertical wave numbers, respectively, of the Fourier components. The Fourier transformation of (40) is

$$FV^{n+1} = SV^n + P\Delta t \tag{42}$$

where

$$\begin{aligned} S &= 1 - \bar{V}\frac{\Delta t}{\Delta y}[1 - \cos(k\Delta y)] - \overline{W}\frac{\Delta t}{\Delta z}[1 - \cos(\ell\Delta z)] + G \\ &\quad + im\{\bar{V}\frac{\Delta t}{\Delta y}\sin(k\Delta y) + \overline{W}\frac{\Delta t}{\Delta z}\sin(\ell\Delta z)\} \end{aligned} \tag{43}$$

G is a contribution due to the diffusion term which is defined by the Fourier transformation of the finite differenced simple diffusion equation

$$FV^{n+1} = V^n + \Delta t G v^n \tag{44}$$

F and G will always be real as long as the diffusion scheme is symmetric in z. $\hat{K}$ and Δy are chosen as independent constants where $\hat{K} = K\Delta t/\Delta z^2$. The choice of Δy is governed by the numerical stability requirements for the simple advection equation. For the advection equation with upstream differencing, this requirement is $\bar{V}\frac{\Delta t}{\Delta y} < 1$ (Richtmeyer, 1967). For the stability analysis with respect to a given K, both $P\Delta t$ and the horizontal advection terms are $O(\Delta t)$ and all products involving at least one of these terms are at least $O(\Delta t)$. Since $\Delta z = \sqrt{K\Delta t} = O(\Delta t^{1/2})$, $\frac{\Delta t}{\Delta z}$ is then $O(\Delta t^{1/2})$. Grouping terms of $O(\Delta t)$,

$$|S| = \{[(1+G) - \overline{W}\frac{\Delta t}{\Delta z}(1 - \cos(\ell\Delta z))^2 + O(\Delta t)]\}^{1/2} \tag{45}$$

Assuming for a moment that

$$|F^{-1}\{(1+G) - \overline{W}\frac{\Delta t}{\Delta z}[1 - \cos(\ell\Delta z)]\}| \leq 1 \tag{46}$$

then

$$|F^{-1}S| = \{1 + O(\Delta t)\}^{1/2}$$

Or, expanding in terms of $O(\Delta t)$,

$$|F^{-1}S| \leq 1 + \frac{1}{2}O(\Delta t) . \tag{47}$$

Therefore, (46) is a sufficient condition for numerical stability with respect to choice of $\hat{K}$, so that contributions from the horizontal advection term, the imaginary component of the vertical advection term, and terms independent of v, need not be considered in the stability analysis of the finite difference equation of motion (40). Note that if the advection terms had used centered space differencing, their contribution to the amplification matrix, $F^{-1}S$, would be purely imaginary and, therefore, would not affect the stability requirements (with respect to K) of (40) so that (46) would simplify to

$$|F^{-1}(1+G)| \leq 1. \tag{48}$$

Then, to determine the numerical stability requirements of a diffusion scheme with respect to the boundary layer equations of motion with upstream differencing of advection terms, we need only to calculate F and G and apply condition (46). For example, consider the centered explicit diffusion scheme

$$v_{zz} = (v^{n}_{j+1} - 2v^{n}_{j} + v^{n}_{j-1})/(\Delta z)^2 . \tag{49}$$

In this case, $F = 1$ and $G = \hat{K}[2 \cos(\ell\Delta z) - 2]$. The stability condition (46) then becomes

$$|1 + \hat{K}[2\cos(\ell\Delta z) - 2] - \hat{W}[1 - \cos(\ell\Delta z)]| \leq 1 \tag{50}$$

where $W = \overline{W}\Delta t/\Delta z$. Noting that the advection and diffusion term contributions are ≤ 0, the above stability condition reduces to

$$1 - 2\hat{W} - 4\hat{K} \geq 1 \tag{50}$$

or

$$\hat{W} + 2\hat{K} \leq 1 .$$

Two diffusion schemes will now be tested which are similar to the DuFort-Frankel scheme. However, these two schemes involve only two time levels instead of three and possess more lenient stability requirements for the boundary layer equations of motion.

Scheme 1 is of the form

$$v_{zz} = (v^{n}_{j+1} - v^{n+1}_{j} - v^{n}_{j} + v^{n}_{j-1})/(\Delta z)^2 . \tag{52}$$

In this case $F = (1+\hat{K})$ and $G = K[2 \cos(k\Delta z) - 1]$. The stability condition (46) then becomes

$$|(1+\hat{K})^{-1}\{1 - \hat{W}[1 - \cos(\ell\Delta z)] + \hat{K}[2 \cos(k\Delta z) - 1]\}| \leq 1 . \tag{53}$$

Noting that the maximum positive value of the argument of the absolute value signs is 1, this condition reduces to

$$(1 - 2\hat{W} - 3\hat{K})/(1+\hat{K}) \geq -1 \tag{54}$$

which then simplifies to

$$\hat{W} + \hat{K} \leq 1 \,. \tag{55}$$

This condition is an improvement upon the stability condition of the centered explicit diffusion scheme (shown above).

Scheme 2 is of the form

$$v_{zz} = (v^{n}_{j+1} - 2v^{n+1}_{j} + v^{n}_{j-1})/\Delta z^2$$

where $F = (1+2\hat{K})$ and $G = 2\hat{K}\cos(\ell\Delta z)$. Stability condition (46) is then

$$(1+2\hat{K})^{-1} \{1 - \hat{W}[1 - \cos(\ell\Delta z)] + 2\hat{K}\cos(\ell\Delta z)]\}| \leq 1 \,. \tag{56}$$

Again the maximum value of the argument of the absolute value sign is 1, so that this condition reduces to

$$(1 - 2\hat{W} - 2\hat{K})/(1 + 2\hat{K}) \geq -1 \tag{57}$$

which simplifies to

$$\hat{W} \leq 1 \,.$$

Therefore, scheme 2 is unconditionally stable with respect to the choice of K. However, as will be seen in the next section, scheme 1 possesses more favorable truncation error behavior.

It will now be shown that the numerical stability condition of the DuFort-Frankel scheme in the boundary layer equation of motion is stricter than those of the above schemes. The actual stability condition is not derived here since it involves an undue amount of mathematics.

The DuFort-Frankel scheme is of the form

$$v_{zz} = (v^{n}_{j+1} - v^{n+1}_{j} - v^{n-1}_{j} + v^{n}_{j-1})/(\Delta z)^2 . \tag{58}$$

Applying the DuFort-Frankel scheme in (40) and employing centered differencing for the time derivative, the Fourier transformation of the resulting equation can be written in the form

$$\begin{pmatrix} v^{n+1} \\ v^{n} \end{pmatrix} = \begin{bmatrix} A & B \\ 1 & 0 \end{bmatrix} \begin{pmatrix} v^{n} \\ v^{n-1} \end{pmatrix} \tag{59}$$

where $F^{-1} = (1+\hat{K})^{-1}$

$$A = F^{-1}\{2\hat{K}\cos(\ell\Delta z) - 2\overline{W}\,\frac{\Delta t}{\Delta z}\,[1 - \cos(\ell\Delta z) + \mathrm{im}(\sin(\ell\Delta z))]\}$$

$$B = (1-\hat{K})/(1+\hat{K}) .$$

The eigenvalues of this system are

$$\mu = \{A \pm (A^2 + 4B)^{1/2}\}/2 \tag{60}$$

A necessary, but not sufficient condition for numerical stability of the above system, is the VonNeumann condition

$$\mu \leq 1 + O(\Delta t) . \tag{61}$$

This inequality requires that $|A| \leq 1 + O(\Delta t)$, which in turn requires that $|A_r| \leq 1 + O(\Delta t)$ where A_r is the real part of A, substituting for A_r

$$(1-\hat{K})^{-1}\,|2\hat{K}\cos(\ell\Delta z) - 2\hat{W}[1 - \cos(\ell\Delta z)]| \leq 1 . \tag{62}$$

This condition reduces to

$$\hat{K} + 4\hat{W} \leq 1 . \tag{63}$$

This necessary, but not sufficient, condition indicates that for the boundary layer equations of motion, the DuFort-Frankel scheme is inferior to the above schemes because of the more stringent stability requirements. In actual experiments with the boundary layer numerical model, numerical stability for $K = 5\,m^2/s$ required that $\hat{W} \leq O(10^{-3})$. Even though the DuFort-Frankel scheme is unconditionally stable in the case of the pure diffusion equation (DuFort and Frankel, 1953), the addition of an advection term with upstream differencing then results in stringent stability requirements to the extent that this scheme is impractical for use in this study.

Numerical stability conditions for the alternating Saul'ev scheme in the boundary layer equation of motion are quite complicated. It is seen in the next section that for the above boundary layer problem, a certain truncation error term of this scheme becomes excessively large to the extent that numerical stability is not a factor.

4.3 Truncation Error Analysis of the Diffusion Schemes

Assuming that the true solution has enough continuous derivatives, the truncation errors can be estimated from a Taylor series expansion. Truncation errors for various diffusion schemes under consideration are listed in table 5.

Substituting the Taylor expansion into various terms of diffusion scheme 1,

$$\{V(z+\Delta z, t) - V(z, t+\Delta t) - V(z, t) + V(z-\Delta z, t)\}/(\Delta z)^2$$

$$= V_{zz}(z, t) + O(\Delta z^2) + O(\frac{\Delta t}{\Delta t^2}) \tag{64}$$

where $V(z, t)$ is the exact solution and the leading term of $O(\Delta z)^2$ is $\frac{\Delta z^2}{12} V_{zzzz}$ while the leading term of $O(\frac{\Delta t}{\Delta z^2})$ is $\Delta t/(\Delta z)^2 V_t$. The local truncation error for the diffusion term is then

$$\tau = O(\Delta z^2) + O(\Delta t/\Delta z^2) . \tag{65}$$

Similarly, it is easily shown that the truncation errors of scheme 2 are also $O(\Delta z^2) + O(\frac{\Delta t}{\Delta z^2})$ where the coefficient of the latter term is now twice as large.

However, the order of the truncation errors in terms of Δt and Δz is not necessarily an indication of the magnitude of the truncation errors in a modeling situation where the coefficient of these terms are quite variable. Furthermore, it is anticipated that the truncation errors associated with the finite difference diffusion schemes will be small compared to the uncertainty of eddy viscosity. Of particular interest are truncation error terms which do not necessarily vanish as Δt and Δz vanish. In the presence of this type of truncation error, the differenced equation is said to be inconsistent with the exact differential equation being approximated. For example, schemes 1 and 2 contain truncation error terms which are $O(\Delta t/\Delta z^2)$. If Δt does not decrease sufficiently fast as the grid is refined, such truncation terms can actually increase. Such terms will be referred to as inconsistency terms (as opposed to consistent truncation error terms which vanish as Δt and $\Delta z \rightarrow 0$). The inconsistency terms of the diffusion schemes considered in this chapter possess factors of V_t or V_{tt} and, therefore, vanish as steady state is approached. However, these terms may interfere with the achievement of steady state as will be seen below. Since these terms include various derivatives of the exact solution, it is difficult to estimate the size of these terms a priori. A numerical experiment is now constructed to better evaluate the importance of these terms for various values of Δt and Δz.

Table 5

Summary of Properties of Various Diffusion Difference Schemes

Diffusion scheme	Stability		Diffusion equation truncation error	requirement for small inconsistency term
	Diffusion equation	Advection-diffusion eq.		
Centered $U^n_{j+1} - 2U^n_j + U^n_{j-1}$	$\hat{K} \leq 1/2$	$2\hat{K} + \hat{W} \leq 1$	$O(\Delta t) + O(\Delta z^2)$	none
Scheme 1 $U^n_{j+1} - U^{n+1}_j - U^n_j + U^n_{j-1}$	$\hat{K} \leq 1$	$\hat{K} + \hat{W} \leq 1$	$O(\Delta t) + O(\Delta z^2) + O(\frac{\Delta t}{\Delta z^2})$	inconsistency term not a factor
Scheme 2 $U^n_{j+1} - 2U^{n+1}_j + U^n_{j-1}$	unconditionally stable	$\hat{W} \leq 1$	$O(\Delta t) + O(\Delta z^2) + O(\frac{\Delta t}{\Delta z^2})$	$\frac{\Delta t}{\Delta z^2} \lesssim 1$
DuFort-Frankel $U^n_{j+1} - U^{n+1}_j - U^{n-1}_j + U^n_{j-1}$	unconditionally stable	$\hat{K} + 4\hat{W} \leq 1$ (necessary but not sufficient)	$O(\Delta t^2) + O(\Delta z^2) + O(\frac{\Delta t}{\Delta z})$	$\frac{\Delta t}{\Delta z} \lesssim .4$
Alternating Saul'ev $\begin{cases} U^n_{j+1} - U^n_j - U^{n+1}_j + U^{n+1}_{j-1} \\ U^{n+2}_{j+1} - U^{n+2}_j - U^{n+1}_j + U^{n+1}_{j-1} \end{cases}$	unconditionally stable	-	$O(\Delta t^2) + O(\Delta z^2) + O(\frac{\Delta t}{\Delta z})$	$\frac{\Delta t}{\Delta z} \lesssim .9$

In the following hypothetical time-dependent problem, the steady state solution is known exactly so that the total accumulated truncation error can be computed for the steady state numerical solution. It is hoped that the behavior of the truncation errors in this simplified problem will also be appropriate to the full boundary layer equations of motion.

The time-dependent linearized boundary layer equations of motion are

$$\begin{aligned} u_t &= Ku_{zz} + Fv \\ v_t &= Kv_{zz} + f(U_g - u) \; . \end{aligned} \tag{65}$$

The problem is generalized by scaling the variables

$$\begin{aligned} v^* &= v/U_g \\ t^* &= t\,f/2 \\ z^* &= z/\sqrt{2K/f} \\ & f > 0 \; . \end{aligned}$$

Dropping the asterisk notation, the scaled equations become

$$\begin{aligned} u_t &= u_{zz} + 2v \\ v_t &= v_{zz} - 2(u-1) \; . \end{aligned} \tag{66}$$

The above system can be reduced to a simple initial value problem in one variable by hypothetically specifying the u component according to its steady state solution (Ekman)

$$u(z,t) = 1 - e^{-z} \cos z \tag{67}$$

so that

$$v_t = v_{zz} + 2e^{-z} \cos z \; . \tag{68}$$

The initial conditions and boundary conditions consistent with the exact solution are

$$\begin{aligned} v(z,0) &= .1 \\ v(0,t) &= 0 \\ v(H,t) &= e^{-H} \sin H \end{aligned} \tag{69}$$

where H is the nondimensional depth of the model. The exact steady state solution to this simplified problem is then

$$V_s = e^{-z} \sin z \text{ .} \tag{70}$$

In the numerical experiments below, $H = 1.42$ and $T = 2.5$, where T is the nondimensional real time of the experiment. Except in cases where inconsistency terms were important, steady state was achieved at $t = T$ to the extent that $(v - V_s)$ is steady at a one percent level. In the case where v is the steady state numerical solution, $(v - V_s)$ is the total accumulated truncation error.

τ^*, the maximum value of $(v - V_s)$ for all the grid points at $T = 2.5$, is plotted in figure 7. These figures illustrate that the behavior of τ^* in terms of Δt and Δz depends critically on which truncation error terms are most important. For example, figure 7a indicates that τ^* for scheme 2 is proportional to Δz^2 when $\Delta t/\Delta z^2 \lesssim 1$ in which case the inconsistency term must not be a significant factor. However, when $\Delta t/\Delta z^2 \gtrsim 1$, the inconsistency terms dominate so that τ^* increases rapidly with increasing $\Delta t/\Delta z^2$ as can be seen in figure 7b. Similar behavior is observed with the DuFort-Frankel and Saul'ev schemes where $\Delta t/\Delta z$ is the critical parameter instead of $\Delta t/\Delta z^2$, as seen in table 5. As predicted by linear numerical stability analysis, instability dominates the truncation error of scheme 1 when $\Delta t/(\Delta z)^2 > 1$ so that the inconsistency term of scheme 1 never becomes important for the above problem.

The inconsistency term of scheme 2 slowly decreases in time which may be related to the fact that this inconsistency term of the DuFort-Frankel scheme tends to oscillate in time. DuFort and Frankel (1953) noted that when the inconsistency term (which is proportional to V_{tt}) becomes large, the differenced simple diffusion equations become consistent with a hyperbolic equation of the form $v_t = Kv_{zz} - Bv_{tt}$ rather than the original parabolic form. The inconsistency term associated with the alternating Saul'ev scheme also exhibited a tendency to oscillate in time.

However, the above results are valid only for the above particular initial conditions. Since the coefficients of the leading terms of the inconsistency contributions are V_t or V_{tt}, the inconsistency terms will be smaller when the initial conditions are specified closer to the steady state solutions. This is illustrated in figure 7c with an experiment using the alternating Saul'ev scheme where the initial conditions are $v(z, 0) = V - .01$.

The above experiments are prejudiced against the runs with large time steps in that τ^* is evaluated at time T while the number of time steps required to reach time T is not considered. For example, when the number of time steps is always 10^3, then the inconsistency term (at $T = 10^3 \Delta t$) no

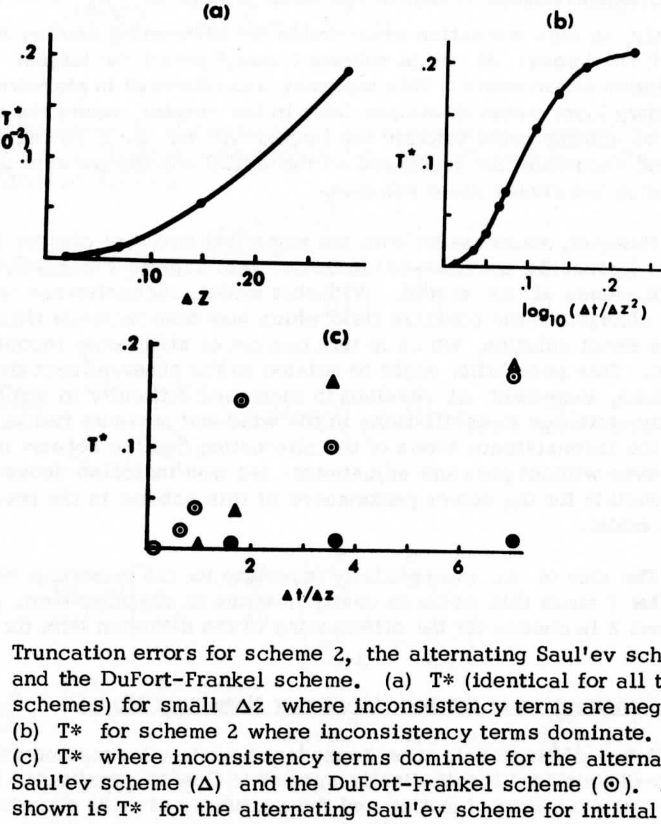

Figure 7. Truncation errors for scheme 2, the alternating Saul'ev scheme and the DuFort-Frankel scheme. (a) T* (identical for all three schemes) for small Δz where inconsistency terms are negligible. (b) T* for scheme 2 where inconsistency terms dominate. (c) T* where inconsistency terms dominate for the alternating Saul'ev scheme (Δ) and the DuFort-Frankel scheme (⊙). Also shown is T* for the alternating Saul'ev scheme for intitial conditions close to the final solution (●).

longer increases rapidly with increasing Δt so that τ^* obeys the curve in figure 7a.

The most preferable scheme of the four tested depends on the particular value of Δz desired. In general, scheme 1 can be ruled out on the basis of its numerical stability restrictions. When the equations include advections, the DuFort-Frankel scheme can also be ruled out on the basis of numerical stability restrictions. The major concern of the alternating Saul'ev scheme and scheme 2 are inconsistency terms. The ratio of the inconsistency term of the former scheme to that of the latter scheme is $\frac{\Delta t/\Delta z}{\Delta t/(\Delta z)^2} \sim \Delta z$. Consequently, in high resolution experiments the alternating Saul'ev scheme would permit the largest Δt while scheme 2 would permit the largest Δt in low resolution experiments. This tendency was observed in experiments with the boundary layer model developed later in the chapter, where the alternating Saul'ev scheme could tolerate the largest Δt for $\Delta z \lesssim 200$ m. Again, the largest allowable Δt increased as the initial conditions were specified closer to the steady state solution.

However, experiments with the numerical model of chapter 7 (where pressure adjustments are allowed) indicated that scheme 2 was slightly preferable for all values of Δz tested. With this model, inconsistency terms can induce changes in the pressure field which may then increase time derivatives of the exact solution, which in turn can cause still larger inconsistency terms. This possibility might be related to the observed fact that, for both schemes, increased Δt resulted in increased difficulty in achieving a steady state due to oscillations in the wind and pressure fields. The fact that the inconsistency terms of the alternating Saul'ev scheme tend to oscillate even without pressure adjustments (as was indicated above) may be responsible for the poorer performance of this scheme in the pressure adjustment model.

The size of Δt is especially important for the numerical model of chapter 7 since this model is costly in terms of computer time. As a result, scheme 2 is chosen for the differencing of the diffusion term for this study.

4.4 Construction of the Boundary Layer Numerical Model

A two-dimensional, time-dependent boundary layer numerical model of three-dimensional longitudinally symmetric flow is constructed in this section. Only two equations of motion and the continuity of mass equation are needed as the pressure field is specified a priori in chapter 5 and is specified by means of a model of the overlying free atmosphere in chapter 8. Although the equations of motion are numerically iterated in time, the primary emphasis of this study is the resulting steady state solutions.

The locally longitudinally symmetric equations of motion on an equatorial β-plane are

$$u_t + vu_y + wu_z = \beta yv - \alpha p_x + Ku_{zz} \tag{80}$$

$$v_t + vv_y + wv_z = -\beta yu - \alpha p_y + Kv_{zz} \tag{81}$$

where α, the specific volume, is a constant, β is a constant =

$2.27 \times 10^{-11}\ S^{-1}\ m^{-1}$ and K, p_y, and p_x are independent of height. The continuity of mass for incompressible flow is

$$v_y \times w_z = 0 . \tag{82}$$

Choosing upstream differencing for advection terms, forward differencing for the time derivative, and scheme 2 for the diffusion term, (80) and (8 1) can be written in the form

$$u^{n+1}_{i,j} = \left(1 + \frac{2\Delta tK}{(\Delta z)^2}\right)^{-1} \left[u^n_{i,j} - \frac{\Delta t v^n_{i,j}}{\Delta y} \left\{ \begin{matrix} u^n_{i,j} - u^n_{i-1,j} \\ u^n_{1+i,j} - u^n_{i,j} \end{matrix} \right\} \right. \tag{83}$$

$$\left. - \frac{\Delta t\, w^n_{i,j}}{\Delta z} \left\{ \begin{matrix} u^n_{i,j} - u^n_{i,j-1} \\ u^n_{i,j+1} - u^n_{i,j} \end{matrix} \right\} + \Delta t\beta y_i v^n_{i,j} + \Delta t(-\alpha p_x)_i + \frac{\Delta tK}{(\Delta z)^2}(u^n_{i,j+1} - u^n_{i,j-1}) \right]$$

$$v^{n+1}_{i,j} = \left(1 + \frac{2\Delta tK}{(\Delta z)^2}\right)^{-1} \left[v^n_{i,j} - \frac{\Delta t v^n_{i,j}}{\Delta y} \left\{ \begin{matrix} v^n_{i,j} - v^n_{i-1,j} \\ v^n_{i+1,j} - v^n_{i,j} \end{matrix} \right\} \right. \tag{84}$$

$$\left. - \frac{\Delta t w^n_{i,j}}{\Delta z} \left\{ \begin{matrix} v^n_{i,j} - v^n_{i,j-1} \\ v^n_{i,j+1} - v^n_{i,j} \end{matrix} \right\} - \Delta t\beta y_i u^n_{i,j} + \Delta t(-\alpha p_y)_i + \frac{\Delta tK}{(\Delta z)^2}(v^n_{i,j+1} + v^n_{i,j-1}) \right]$$

In certain experiments where K is a function of height, an additional $K_z u_z$ friction term results which employs centered differencing

$$(K_z u_z)_{i,j} = (K_z)_{i,j}(u_{i,j+1} - u_{i,j-1})/2\Delta z \tag{85}$$

At the lower boundary (j = 1) two types of boundary conditions are imposed on the wind field:

a) the no-slip condition where $u_{i,1} = v_{i,1} = 0$

b) the geophysical boundary condition where

$$\frac{u_{i,2} - u_{i,1}}{\Delta z} = \frac{k_0}{2}(u_{i,2} + u_{i,1}) \cdot \qquad (86)$$

The latter condition reduces to $u_{i,1} = k_0 u_{i,2}$ where $\hat{k}_0 = [1 - (k_0 \Delta z/2)]/[1 + (k_0 \Delta 2)/2]$. Estimates of k_0 in chapter 2 yielded values $k_0 = 1.5\ 10^{-3}$m which corresponds to $\hat{k}_0 = .74$ for $\Delta z = 200$ m. The resulting relationship between $u_{i,1}$ and $u_{i,2}$ compares reasonably well with observations at the Line Islands (Estoque, 1970), although such comparisons are hampered by possible low level baroclinicity. Similarly, this value of $\hat{k}_0$ yields boundary layer solutions at 10° to 15° latitude which exhibit veering with height comparable to the veering observed by Gray (1968) at these latitudes. In the no-slip case $z = (j-1)\Delta z$, while in the geophysical boundary condition case $z = (j-1)\Delta z + z^*$, where z^* is the height of level 1, equal to 50 m. For convenience in discussions of numerical results, height will always refer to the distance above level 1. At the upper boundary, $j = J$, zero shear (zero stress) is specified

$$u_{i,J} = u_{i,J-1}$$

$$v_{i,J} = v_{i,J-1} \cdot$$

With upstream advection, side boundary conditions are not needed at outflow points. Two types of boundary conditions for u and v are used at inflow points:

a) if the side boundary is at higher latitudes, the Ekman solution is specified;

b) if the equator is a side boundary as in the case of pressure even symmetric with respect to the equator, $v(z) = 0$ is specified while $u(z) = 0$ may be specified or $u(z)$ may be calculated from the appropriate equation of motion.

The differencing of the mass continuity equation employs centered differencing in the horizontal and a vertically staggered grid where vertical motion is defined at intermediate levels.

$$w_{i,j+1/2} = w_{i,j-1/2} + \frac{\Delta y}{2\Delta y}(v_{i+1,j} - v_{i-1,j}) \qquad (87)$$

where $w_{i,1} = 0$. To compute $w_{i,1\frac{1}{2}}$, a linear profile of v_y in the vertical is assumed between $j = 1$ and $j = 2$ so that

$$w_{i,1\frac{1}{2}} = -\frac{\Delta z}{2}\left[\frac{3}{4}(v_y)_{i,1} + \frac{1}{4}(V_y)_{i,2}\right. \cdot \qquad (88)$$

When w is needed at the side boundary, then (87) employs an uncentered estimate of v_y so that

$$\begin{aligned} (v_y)_I &= (v_{I,j} - v_{I-1,j})/\Delta y \\ (v_y)_1 &= (v_{2,j} - v_{1,j})/\Delta y \end{aligned} \tag{89}$$

where $i = I$ is the right side boundary of the model. Vertical motion at the integer levels is computed by averaging

$$w_{i,j} = \frac{1}{2}(w_{i,j+1/2} + w_{i,j-1/2}) \ . \tag{90}$$

To illustrate flow in the $y - z$ plane, a stream function is defined by the relationship $\psi_z = v$. Defining ψ at intermediate levels and using centered differencing,

$$\begin{aligned} \psi_{i,1/2} &= 0 \\ \psi_{i,j+1/2} &= \psi_{i,j-1/2} + \Delta z \, v_{i,j} \ . \end{aligned} \tag{91}$$

The geometric characteristics of the grid system are

$\Delta z = 200$ m

$\Delta y = 50$ km

$\Delta t = 500$ s

$D = 400$ m where D is the depth of the model.

The location of the side boundaries, which vary with each experiment, are placed sufficiently far away from the equator so that regions where advections are not important are established near each side boundary. The Ekman solution is specified everywhere as initial conditions. To achieve steady state, the equations of motion are iterated for a real time of approximately sixteen days.

It might be mentioned that boundary layer numerical models have been constructed where Δz increases with height to give higher resolution in the lower part of the boundary layer (Estoque, 1962). However, advections are most important in the middle and upper part of the boundary layer, so that a constant Δz appears to be more appropriate for this study which focuses on boundary layer modifications due to advections. In certain experiments, the surface layer (where higher resolution is most desirable) is parameterized by the geophysical lower boundary condition.

While the numerical analysis results of the one-dimensional Ekman problem do not apply exactly to this numerical model, the results can be used to indicate approximate truncation error magnitudes. Those results indicate that for quasi-Ekman flow with scheme 2 and $\Delta t = 5 \times 10^2$ s and $\Delta z = 200$ m, the inconsistency truncation term will be negligible compared to the other truncation term. The results further indicate that the maximum truncation errors for quasi-Ekman flow will be $\lesssim O(.1\%)$ for $D = 1400$ m (corresponding to $y = 2°$ latitude for $K = 5\text{m}^2/\text{s}$ and $\lesssim O(1\%)$ for $D = 630$ m (corresponding to $y = 10°$ latitude for $K = 5\text{m}^2/\text{s}$). Various experiments indicated that increasing the resolution by a factor of two or four changes the solution by $O(.1\%)$ at lower latitudes and $O(1\%)$ at latitudes higher than 10°. These results then indicate that truncation errors are $\lesssim O(1\%)$.

5. NUMERICAL BOUNDARY LAYER FLOW SOLUTIONS GENERATED BY SPECIFIED PRESSURE FIELDS

In this chapter, steady state boundary layer flow solutions determined by the boundary layer numerical model are discussed for various specified pressure fields. These solutions are somewhat hypothetical since in reality the flow would modify the pressure field through mass redistribution. However, the main purpose of this chapter is to reveal basic latitudinal changes in boundary layer features associated with latitudinal changes in the Coriolis parameter. It will be seen in this chapter and in chapter 8 (where pressure adjustments are allowed) that many of the basic features of the various boundary layer flow types are not sensitive to the details of the particular pressure fields (Climatological and Oceanographic Atlas for Mariners, Vol. I, 1959, or Marine Climatic Atlas of the World, 1955) indicate that the mean surface horizontal pressure gradients decrease toward the equator. Daily surface pressure charts for equatorial regions (World-Weather Maps, Deutscher Wetterdienst, 1957) exhibit fairly weak horizontal pressure gradients, except in the vicinity of well-developed disturbances. However, in many low latitude situations, weak horizontal pressure gradients can produce moderate wind speeds, since this term is essentially balanced by advective or time accelerations.

Two main types of pressure fields are specified for the numerical experiments in this section. One type consists of pressure fields which are "even symmetric" with respect to the equator and correspond to a constant zonal geostrophic wind of 10 m/s. This type of pressure field appears to simulate some of the features of the above mean pressure fields. To study cross-equatorial flow, a second class of pressure fields corresponding to a constant horizontal pressure gradient are specified.[6] The particular significance of this type of pressure field is that the latitudinal changes of the characteristics of the corresponding steady state flow are solely due to influences of latitudinal variations of the Coriolis parameter. A horizontal pressure gradient magnitude of 4×10^{-5} m/s^2 (which corresponds to a geostrophic wind magnitude of 8 m/s at 2° latitude) appears to be typical of equatorial surface pressure fields and at the same time yields wind speeds in the numerical model typical of observed cross-equatorial flows. This value is used in most constant pressure gradient experiments, although it is varied in special experiments to study the effect of changing the pressure gradient magnitude.

The various specific pressure fields which are used in this chapter are summarized in table 6. As established previously, our principal interest in the steady flow corresponding to these pressure fields is the role of the momentum advection terms and the basic characteristics of the boundary layer where advection terms are important. Therefore, in most of the experiments, a height-independent eddy viscosity and a no-slip lower boundary condition is specified so that modifications of the known Ekman solution by advections are most clear. On the other hand, in experiments where a geophysical lower boundary condition or height-dependent eddy viscosity is used, the isolation of the effects of advection is more difficult. For example, with the application of the geophysical boundary condition, the deviation angle of the boundary layer flow is reduced from that of the known Ekman solution, even where advections are not important. As decided in chapter 2, eddy viscosity will be in general specified to be 5m^2/s, although this value is varied to study the effect of changing the eddy viscosity magnitude. Another experiment is conducted where a height-dependent eddy viscosity is employed.

Experiments with cross-equatorial flow are discussed first. For reference purposes only pressure decreases toward the north so that the flow crosses the equator from south to north. The first experiment (constant meridional pressure gradient) is referred to as the prototype experiment. It is discussed in some detail, as it contains many flow features common to the flows of other experiments. The discussions of the flows of the other experiments are more brief and emphasize differences from the prototype experiment.

Before summarizing results of the maintained boundary layer experiments, a special section is devoted to the discussion of boundary layer vertical motions.

---

[6] Cross-equatorial flow is also generated by a pressure field corresponding to a constant geostrophic wind magnitude where the geostrophic wind reverses sign at the equator. However, this pressure field is irregular in that p_{yy} reverses sign at the equator.

Table 6

Summary of Numerical Experiments of Chapter 5, $A = 4 \times 10^{-5}$ m²/s and $B = 10$ m/s . The complimentary solutions where $\alpha p_y = +A$ can be obtained with a simple 180° rotation of the coordinate system.

Experiment number	Special Remarks	Pressure Field
1.		$\alpha p_y = -A$
2.		$U_g = By/\lvert y \rvert$
3.		$\alpha p_x = \alpha p_y = -A$
4.		$\alpha p_x = -\alpha p_y = +A$
5.		$\alpha p_x = -A$
6.	$u_{eq} \neq 0$	$U_g = +10$ m/s
7.	$u_{eq} = 0$	$U_g = +10$ m/s
8.		$\alpha p_y = -\frac{1}{2}A$
9.	$K = 10$ m²/s	$\alpha p_y = -A$
10.	height-dependent K	$\alpha p_y = -A$
11.	$\hat{k}_0 = .74$	$\alpha p_y = -A$

5.2 Boundary Layer Flow Generated by a Latitudinally Independent Meridional Pressure Gradient

To be discussed in this section is the prototype experiment, where the pressure gradient force is directed toward the north with a constant value of 4×10^{-5} m/s². Most of the basic features of the steady state boundary layer flow corresponding to various other specified pressure fields are essentially contained in the steady state flow of this experiment. This is due to the fact that the basic latitudinal changes of the boundary layer flow character (with the assumptions of this study) are closely related to latitudinal variations of the Coriolis parameter. One exception is the flow generated by an equatorially even symmetric pressure field where meridional flow vanishes at the equator. This case is discussed later in the chapter.

The pressure and steady state wind fields of the prototype experiment are illustrated in figure 8 and the streamlines of the steady state flow in the meridional-vertical plane are shown in figure 9a. Note that even though the horizontal pressure gradient is independent of latitude, the response of the wind field to this pressure field varies considerably with latitude. For example, a general region of subsidence about 400 km wide and approximately symmetric with respect to the equator and a relatively narrow region of rather intense rising motion in the vicinity of 8°N are produced by the latitudinal boundary layer flow transitions. In the vicinity of the equator, the flow changes from quasi-Ekman flow to drift-ordinary boundary layer flow. This transition will be referred to as the "equatorial transition." Downstream from the equator, the flow changes from drift-ordinary boundary layer flow to quasi-Ekman flow. This transition will be referred to as the "downstream transition."

Both vertical and horizontal advections are important in the transition regions while only horizontal advections are important in the drift region between the two transition regions. As would be expected from scale analysis (chapter 3), advection terms are small in the lowest layers and increase with height so that the downstream transition latitude increases with height; that is, the transition zone slopes upward toward higher latitudes.

The boundary layer flow in the drift region is quite different from Ekman flow in that: a) the wind vector backs with height; b) cross-isobar flow reaches a maximum at the top of the boundary layer where it obtains the non-geostrophic drift value; and c) the boundary layer depth increases more slowly toward the equator.

Since the basic flow regimes and flow transitions associated with other pressure fields are similar to those of the flow of this experiment, the various flow regions are now discussed in detail for this experiment and are treated more briefly for subsequent experiments.

a) The Equatorial Transition Region

Around 3°S the Ekman solution is no longer a good approximation due to the importance of horizontal advections. At this latitude, deviations from the Ekman zonal wind solution exceeds twenty-five percent except in the lowest portion of the boundary layer.

Around 2°S, increases in the meridional flow (cross-isobar flow) in the upper portion of the boundary layer become important as the flow aloft becomes drift.[7] Figure 10 shows that the height of the maximum meridional flow increases toward the equator, reaching the top of the boundary layer near the

---

[7] The linear inertial instability theory of chapter 3 predicts that drift flow must occur equatorward from $y = (\alpha p_y/\beta^2)^{1/3} \simeq 4°\text{S}$.

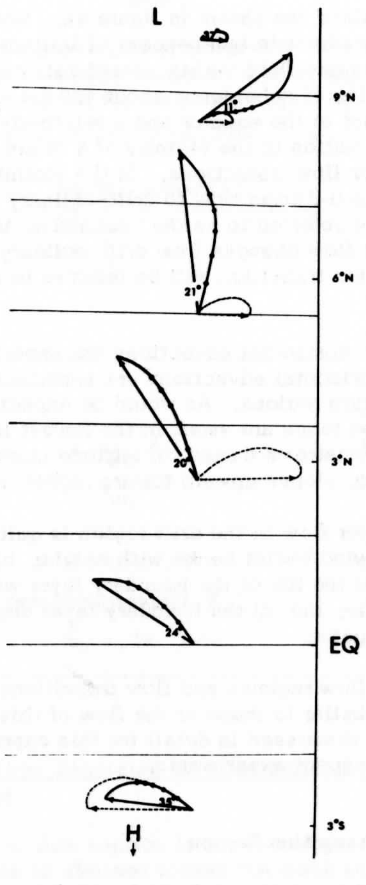

Figure 8. Boundary layer wind hodographs and surface pressure fields for the prototype experiment. Solid thin lines denote surface isobars at increments of . 1 mb. Wind hodographs (solid lines) where dots indicate elevations 200 m, 400 m ... 1000 m are shown for various latitudes. The hypothetical Ekman hodographs as interpreted by the grid system (dashed lines, not defined at the equator) are also shown. The angle between the 200 m wind and the 4000 m wind is also indicated. Actual latitudinal boundaries of the numerical experiment are 8°S and 12°N.

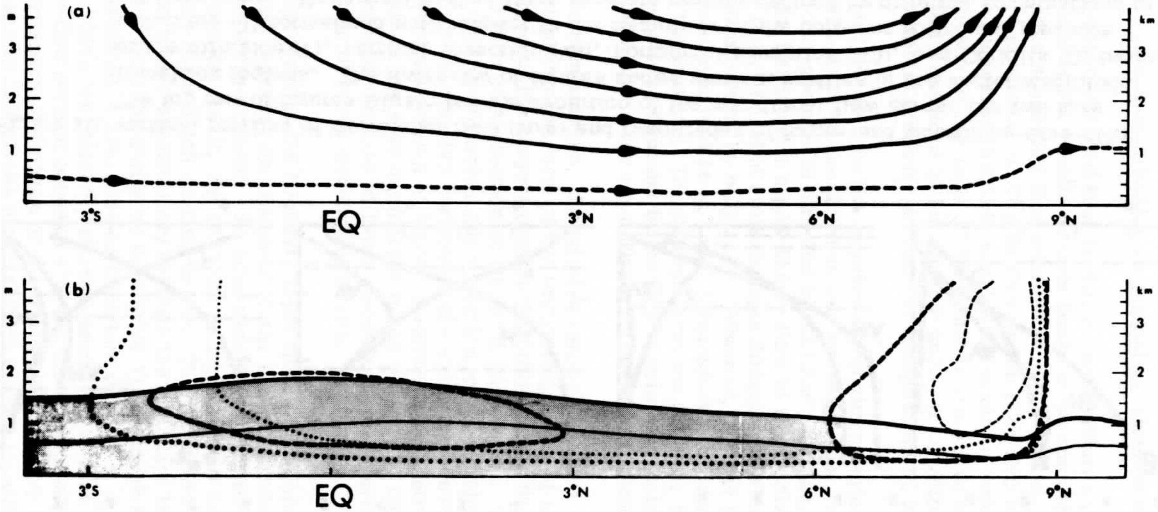

Figure 9. Streamlines and relative forces for the prototype experiment. (a) shows streamlines in the y - z plane for increments of 4×10^3 m^2/s where the dashed line is the 2×10^2 m^2/s streamline. (b) shows relative "force" isolines for values of .20 (thin lines) and .50 (thick lines) for the diffusion term (solid lines), the vertical advection term (dashed lines) and the horizontal advection term (dotted lines). Shading denotes the region where the relative diffusion terms exceeds .20.

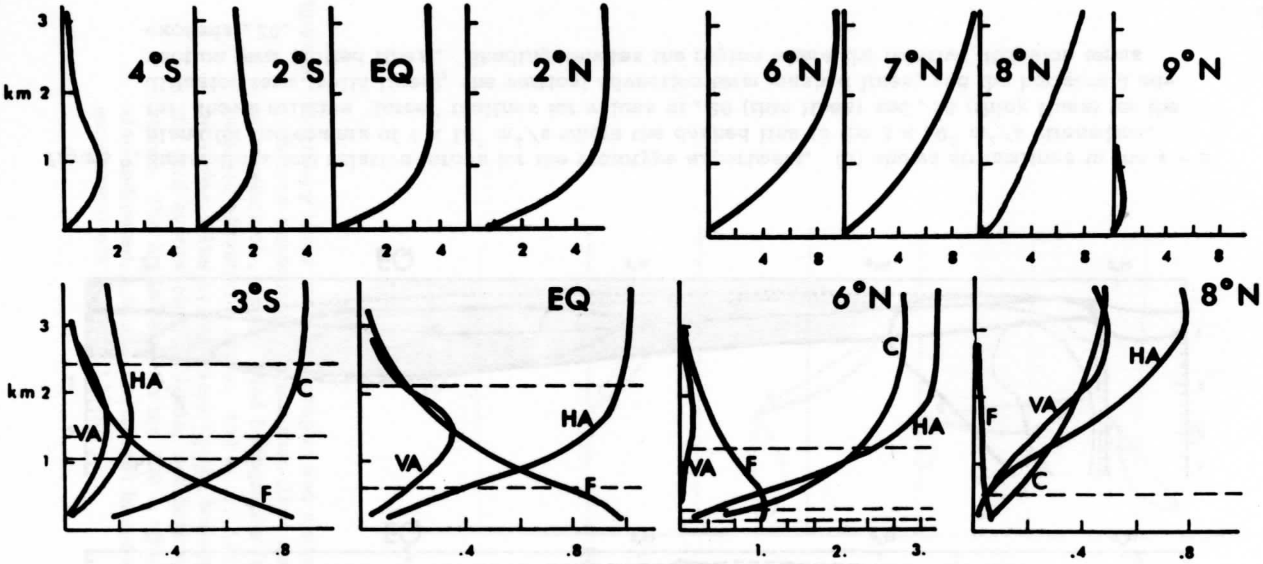

Figure 10. Vertical profiles of meridional flow (m/s) and magnitudes of forces and momentum advections. The top row of figures illustrates the evolution of the meridional flow across the two flow transition regions. The lower row of figures shows vertical profiles of the vector magnitude of the diffusion (F), vertical advection (VA), horizontal advection (HA), and Coriolis (C) terms which are all normalized with respect to the magnitude of the constant horizontal pressure gradient force. Horizontal dashed lines separate regions defined by different combinations of terms whose relative importance exceeds .20.

equator. The thickness and strength of the meridional flow also increase in the flow direction resulting in general subsidence at the equator.

It might be noted that satellite cloud pictures (Kornfield et al., 1967) indicate that the Pacific equator tends to be consistently cloud free. Zipser (1970) has suggested that subsidence and adiabatic warming balance the observed radiational cooling in this region (Cox and Hastenrath, 1970). Zipser further suggested that this subsidence could be linked to the maintenance of the "equatorial dry zone." Note that in the above numerical experiment, subsidence is produced at the equator solely by a latitudinal flow transition, as the horizontal pressure gradient is independent of latitude.

The flow aloft in the equatorial transition region is changing direction with latitude more rapidly than the low level flow, which always contains a significant component directed toward low pressure. In fact, from the Southern Hemisphere quasi-Ekman flow to the Northern Hemisphere quasi-Ekman flow, the wind aloft changes direction 180° while the 200 m wind changes direction by only 110°. Whereas, the net backing (from 200 m to the boundary layer top) is 41° at 5°S (quasi-Ekman flow), the wind backs only 24° at the equator. Downstream from the equator, the wind vector still backs with height (as opposed to the Ekman solution) so that the basic boundary layer characteristics are entirely different from those of the Ekman solution.

For convenience, the relative force or relative advection term at a grid point refers to the ratio of the vector magnitude of the term to the vector magnitude of the largest term at that grid point. Such a measurement of a term is then an indication of its local importance. The .20 and .50 isolines of the relative diffusion and advection terms are shown in figure 9b. It is seen that the relative horizontal advection term first exceeds .20 around 3°S. Downward advections of higher momentum associated with boundary layer subsidence are also significant in the vicinity of the equator. However, horizontal advections of lower momentum are generally larger so that a net advection of lower momentum results.

The depth of the boundary layer flow approaching the equator increases at a much slower rate compared to the Ekman boundary layer depth (which is infinite at the equator). As advection terms become important and the Coriolis terms become small, the Coriolis parameter is no longer an appropriate boundary layer depth scaling factor. The downward advections of higher momentum may significantly restrain the boundary layer depth (as would be expected from the analyses in chapter 3), although the stronger horizontal advections must also play an important role. $\delta_{.20}$ defined as the depth above which the relative diffusion term is less than .20, increases by about twenty-five percent between 4°S and the equator where it achieves a maximum. This dynamical definition of the frictional boundary layer depth is preferable to kinematic definitions for this study, since significant vertical wind shears in a vertical inertial boundary layer may extend well above the region where the diffusion term is important.

Figure 10 shows vertical profiles of forces and advection terms for various latitudes. As predicted by scale analysis (chapter 3), Coriolis and advection terms are relatively small in the lowest layers and increase with height. As a result, the pressure gradient term in the lowest layers is essentially balanced by the diffusion term. Note that in the upstream quasi-Ekman flow, horizontal advections, $O(|\vec{V}|^2)$, like the cross-isobar flow, reach a maximum within the boundary layer and become small at the top of the boundary layer. In contrast, cross-isobar flow and horizontal advections at the equator increase with height throughout the boundary layer, reaching a maximum aloft.

Vertical advections at the equator increase with height in the lower layers due to increasing vertical motion with height and reach a maximum in the interior of the boundary layer. Above this height, decreasing vertical wind shear is the dominant factor so that vertical advections decrease with height. At these upper levels of the boundary layer, the vertical profiles of the diffusion and vertical advection terms are nearly identical so that the top of the friction and vertical inertial boundary layers approximately coincide.

b) The Drift Region Downstream from the Equator

Figure 8 shows that downstream from the equator, the flow is much stronger and from an entirely different direction than would be predicted by the geostrophic-Ekman solution. The flow above the boundary layer is "drift." Horizontal advections are important at all levels, as indicated in figure 9b, except in the lowest portion of the boundary layer. Figure 9a shows that vertical motions are small relative to the transition regions. In fact, relative vertical advections are less than .10 in the entire region between the two transition regions.

As opposed to the Ekman solution, the boundary layer wind vector backs with height where the net backing is about 20° and nearly independent of latitude. It might be mentioned that backing of the boundary layer wind vector with height is observed at Christmas Island (2°N, 157°W) in a substantial majority of the cases when the wind contains a southerly component (Robitaille and Zipser, 1970), while backing is seldom observed with northerly wind components. This suggests that cross-equatorial flow in the atmosphere may result in a rotation of the boundary layer wind vector with height in the opposite direction from Ekman rotation. Of course, low level baroclinicity may also be an important influence on the observed low level wind field.

It is also of interest to note that the deviation angle is quite small in the drift region (relative to quasi-Ekman flow). Recall that Kuo (1970) found in his vortex study that the deviation angle of the wind was quite small in regions of low absolute vorticity. Drift flow corresponds to zero absolute vorticity, while weak cyclonic vorticity is generated in the underlying boundary layer flow. Even though the Coriolis term is one of the larger terms in the steady state balance throughout most of the drift regime, the net backing is nearly independent of latitude. As a result, the change to net veering is concentrated in the downstream transition region. One is reminded of the study of the boundary layer flow response to low latitude wave motions (Holton, Wallace, and Young, 1970) where the boundary layer wind direction was nearly independent of latitude south of a critical latitude and suffered a dramatic shift at the critical latitude.

The boundary layer depth of the drift region is considerably thinner than the hypothetical Ekman boundary layer depth, especially near the equator. Based on absolute friction forces, it increases slowly with latitude, reaching a maximum just prior to the downstream transition region. However, the meridional flow and horizontal advections increase with latitude so that the boundary layer depth based on the relative diffusion term (e.g. $\delta_{.20}$) decreases slowly with latitude. This depth reaches a minimum at the downstream transition where horizontal advections reach a maximum.

It might be mentioned that in terms of the level where the wind asymptotically reaches 99% of its maximum value, the boundary layer depth reaches a maximum at the equator and then decreases downstream where the flow is accelerated. This depth reaches a second maximum in the downstream transition region where the flow is rapidly decelerated. This measure of boundary layer depth (which includes influences of vertical advections even above the frictional boundary layer) is also observed to decrease (increase) in the flow direction in many other accelerated (decelerated) flow situations (Schlichting, 1968).

Figure 10 shows that at 6°N the pressure gradient force is essentially balanced by momentum diffusion in the lowest levels. Above this layer is a diffusion-inertial boundary layer where both momentum diffusion and horizontal advections are important. At higher levels the diffusion term vanishes and the flow becomes drift.

c) The Downstream Transition Region

The meridional drift component reaches a maximum at about 7°N so that horizontal convergence and rising motion occur downstream. Upward vertical advections of lower momentum prevent the flow immediately above the frictional boundary layer from becoming drift as a vertical inertial boundary layer is established. This inertial boundary layer extends above the 4000 m level so that the flow at the top of the model is not yet drift. Drift theory predicts that the meridional flow will vanish at about $10\frac{1}{2}$°N where the frictionless flow becomes geostrophic. As is expected from scale analysis (chapter 3), the transition to quasi-geostrophic-Ekman flow occurs at lower latitudes at lower levels. For example, the transition to quasi-Ekman flow for the upper main portion of the boundary layer is between $8\frac{1}{2}$°N and 9°N.

Since the flow transition slopes upward toward higher latitudes, horizontal convergence is established beneath horizontal divergence (associated with the drift flow) in the low latitude portion of the transition region. The heights of maximum convergence and maximum rising motion also increase with increasing latitude. In contrast, divergence occurs at all levels in the equatorial transition, and achieves a maximum at the top of the boundary layer.

The strongest convergences result near the top and above the frictional boundary layer, since cross-isobar in the drift-ordinary boundary layer regime flow increases with height while in the quasi-Ekman regime it is essentially limited to the boundary layer interior. As a result, very intense rising motion is produced in the vicinity of $8\frac{1}{2}$°N where the flow transition in the upper main portion and above the frictional boundary layer occurs. This convergence is quite intense as the drift cross-isobar flow is larger than the geostrophic wind by a factor of about five.

Since the horizontal pressure gradient is specified to be independent of latitude, this strong rising motion results entirely from a flow transition associated with the latitudinal variation of the Coriolis parameter. In other words, a lower troposphere convergence zone can be generated at low latitudes without a pressure minimum or even a decrease of the horizontal pressure gradient in the flow direction. These results also suggest that such an east-west oriented convergence zone may separate two different flow types where horizontal advections are important equatorward from the convergence zone.

Also, associated with the downstream transition is a shift from backing to veering. Figure 8 indicates that at $8\frac{1}{2}$°N veering is established in the lower layers where the flow is already quasi-Ekman. The wind backs with height at higher levels where the transition is still downstream at higher latitudes.

The strong rising motion of the downstream transition produces large upward vertical advections of lower momentum. Since the rising motion is considerably stronger above the frictional boundary layer where vertical wind shears may still be large, the largest vertical advections occur above the frictional boundary layer. In contrast, the largest vertical advections in the equatorial transition region were established in the interior of the boundary layer and vanished at the top of the frictional boundary layer. In the vertical inertial boundary layer above the frictional boundary layer of the downstream transition, the relative advection term reaches a maximum of .72, approximately twice as large as the maximum value in the equatorial transition. However, the horizontal advections of higher momentum are still generally stronger so that a net advection of higher momentum results. Although horizontal advections were also larger than vertical advections in the equatorial transition, the signs of the two advection terms were reversed.

Figure 10 illustrates several different flow regimes in the vertical at 8°N. Again in the lowest levels, the pressure gradient force is essentially balanced by momentum diffusion. At higher levels Coriolis and advection terms become important. Above one kilometer is a thick layer where $\vec{V}_{zz}$ and the diffusion term are small, but $\vec{V}_z$ and vertical advections (the vertical inertial boundary level) are important. Eventually $\vec{V}_z$ must vanish with height so that the flow becomes drift.

Horizontal advections of higher momentum decrease rapidly across the downstream transition region. The slope of the transition zone is not as evident in terms of the importance of horizontal advections (compared to deviations from the Ekman solution), since in the drift region in the lower levels, horizontal advections are small even though deviations from the Ekman solution are large.

As a result of the rapid decrease of the size of horizontal advections, the boundary layer depth ($\delta_{.20}$) increases across the downstream transition. Thus, the ordinary boundary layer appears to be thinner than the Ekman boundary layer even as far away from the equator as 8° latitude.

In conclusion, the steady flow generated by a latitudinally independent pressure gradient field may vary considerably with latitude. In particular, cross-equatorial flow generates a boundary layer flow downstream from the equator which is quite different from classical Ekman boundary layer flow. Flow transitions between this boundary layer and quasi-Ekman boundary layers produce significant boundary layer vertical motions. In the next three sections the cross-equatorial boundary layer flow problem is examined with various other types of pressure fields.

5.3 Flow Toward the Equator Generated by a Pressure Field Corresponding to Constant Geostrophic Wind

The pressure field of the second experiment corresponds to a constant geostrophic wind magnitude with decreasing pressure toward the north so that southerly cross-equatorial flow is generated. The particular significance of this pressure field is that advections in the quasi-Ekman flow toward the equator arise solely from latitudinal variations of the boundary layer scaling depth (since the geostrophic wind is independent of latitude). The various flow regimes and flow transitions associated with the prototype pressure field also occur with this pressure field. However, in this case, we will confine our attention to the flow approaching the equator. The pressure field and the corresponding steady state wind field are illustrated in figure 11.

The Ekman flow is modified at a more rapid rate as the flow approaches the equator. This is expected from an analysis (chapter 3) where advections computed from the Ekman solution for constant geostrophic wind were found to be $O(y^{-3/2})$. Figures 11 and 12 reveal that meridional flow near the equator is reduced from the Ekman case. In the upper portion of the boundary layer, this is accomplished by horizontal advections of lower meridional momentum associated with the increasing thickness of the meridional flow toward the equator. In the lower part of the boundary layer, meridional flow is reduced in part by upward advections of lower meridional momentum. Horizontal advections of higher zonal momentum resulting from the increasing boundary layer depth toward the equator, increase the zonal flow component. As a result of increased zonal flow and decreased meridional flow, the deviation angle is also reduced near the equator. These advections also occur in the prototype case, but their influence on the wind field is complicated by the simultaneous presence of advections resulting from latitudinal variations of the geostrophic wind.

Due to the decreased meridional flow, the strong divergence and subsidence of the Ekman solution near the equator (associated with the increase of the Ekman depth toward the equator) are reduced considerably in the steady state solution.

Horizontal advections associated with the steady flow, as illustrated in figure 12b, are smaller than those calculated from the Ekman solution, since horizontal advections tend to decrease horizontal flow variations. Although vertical motions are reduced from those associated with the Ekman solution, vertical advections are increased in the lower levels near the equator where vertical zonal wind shears are increased.

5.4 Prototype Pressure Field Rotated Clockwise 45°

As mentioned in the introduction, easterly waves and longitudinal variations of surface temperature may typically generate low level longitudinal pressure gradients at low latitudes. In the third experiment, the prototype pressure field is rotated clockwise 45°. The surface isobars, illustrated in figure 13, are then oriented in a southeast-northwest direction where the

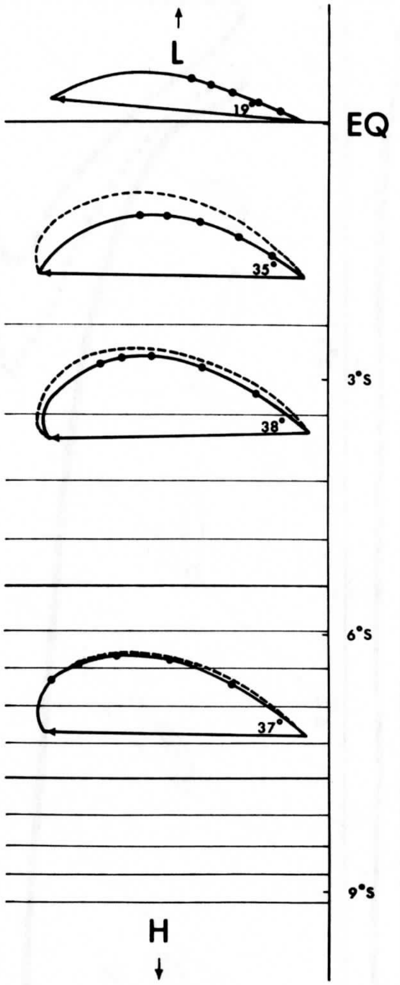

Figure 11. Boundary layer wind and surface pressure fields for experiment 2. Actual boundaries of numerical experiment are at 10°S and 10°N. See figure 8 for further explanation.

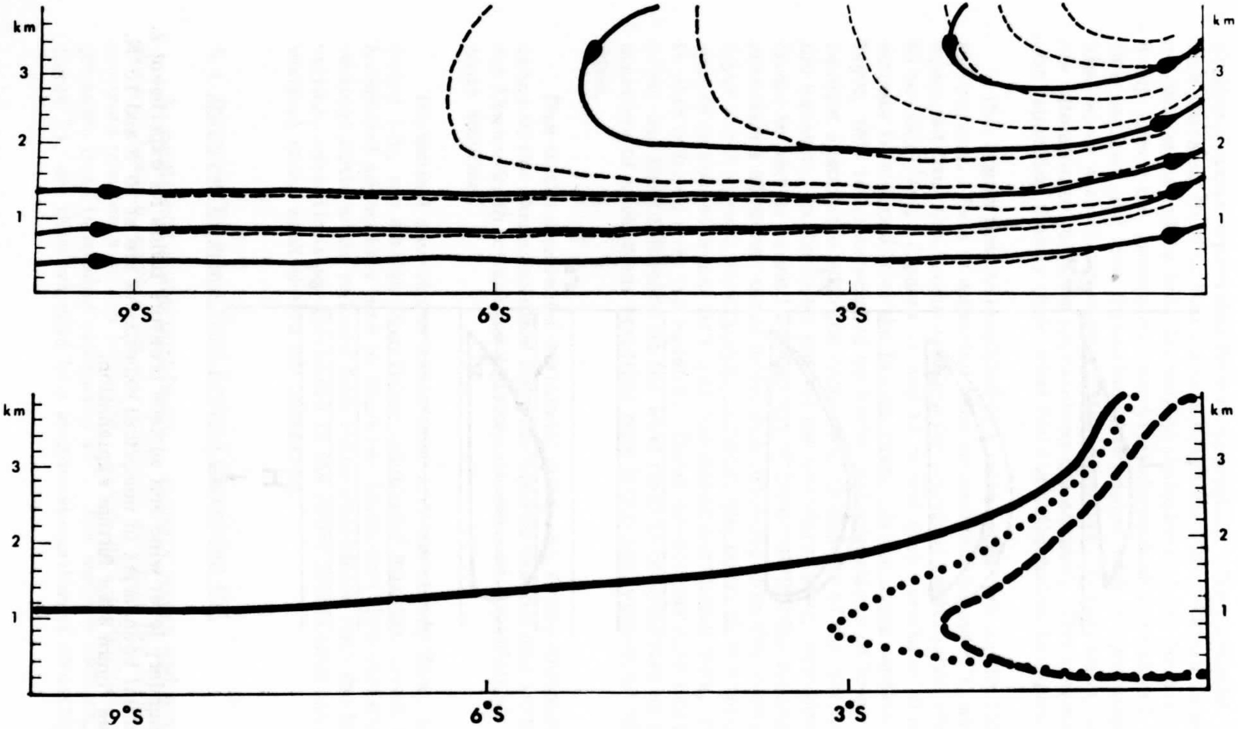

Figure 12. Streamlines (a) and .20 relative "force" isolines (b) for experiment 2. Dashed lines (a) denote Ekman streamlines (all streamlines in increments of 1×10^3 m^2/s). See figure 9 for further explanation.

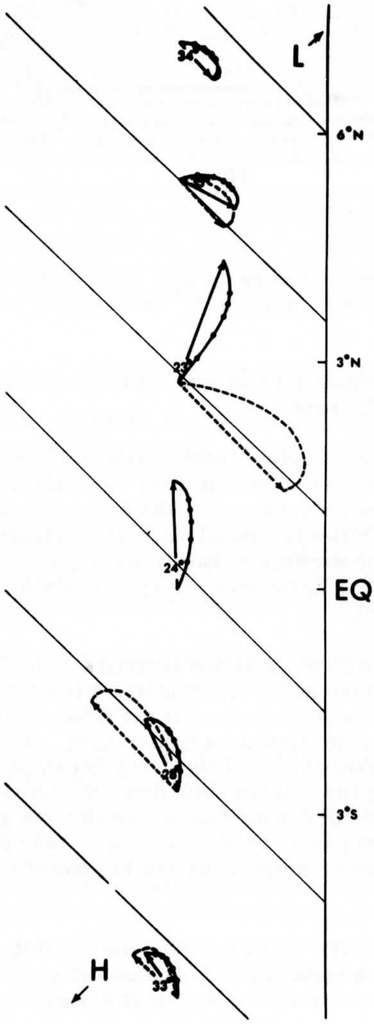

Figure 13. Boundary layer wind and surface pressure fields for experiment 3. Actual boundaries of numerical experiment are at 10°S and 10°N. See figure 8 for further explanation.

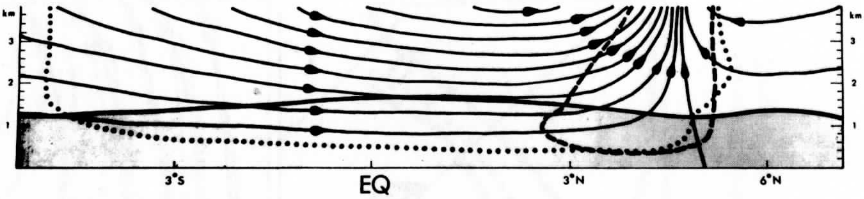

Figure 14. Streamlines (increments of 2 × 10^3 m^2/s) and .20 relative "force" isolines for experiment 3. See figure 9 for further explanation.

magnitudes of the meridional and longitudinal pressure gradients are equal and independent of latitude.[8]

The initial Ekman boundary layer meridional flow corresponding to this pressure field is stronger in the Southern Hemisphere. As a result, the steady southerly flow extends across the equator to about $4\frac{1}{2}$ °N where a convergence of two flows is established, as is shown in figures 13 and 14. In other words, a convergence of two flows occurs without a pressure minimum, due solely to the latitudinal variation of the response of the wind field to this pressure field.

The steady state flow above the boundary layer does not become the particular drift solution presented in chapter 3 since longitudinal pressure gradients modify the angular momentum of the flow. However, we will still refer to this steady state flow as a type of drift, since horizontal advections of momentum are balanced by the horizontal pressure gradient and Coriolis terms. Figure 13 shows that the drift flow downstream from the equator is in the opposite direction of the meridional geostrophic wind. Immediately upstream from the convergence zone, the flow at 4000 m, which is nearly pure cross-isobar flow, is no longer drift due to upward advections of lower momentum.

In the boundary layer upstream from the equator, figure 14 shows that horizontal advections resulting from latitudinal variations of the boundary layer depth and geostrophic wind are large compared to the prototype experi-

---

[8] It was noted in chapter 3 that longitudinal pressure gradients must be independent of latitude in order to preserve "local longitudinal symmetry."

ment. This occurrence is related to the presence of a meridional geostrophic wind component so that the advecting velocity in the upstream quasi-Ekman flow is larger. Consequently, the "equatorial transition" begins farther upstream from the equator. For example, figure 14 indicates that the relative horizontal advections first exceed .20 around 5°S as compared to 3°S in the prototype experiment. Similarly, the 200 m deviation angle at 3°S is reduced to 28°, compared to 35°, in the prototype experiment.

In conclusion, comparisons between this experiment and the prototype experiment indicate that the steady state wind field at low latitudes may be more sensitive to the orientation of the pressure gradient field compared to the mid-latitude flows. This greater sensitivity is related to the rapid latitudinal variation of the Coriolis parameter which reverses sign at the equator.

5.5 The Prototype Pressure Field Rotated Counterclockwise 45°

In the fourth experiment, the prototype pressure field is rotated counterclockwise 45° so that the surface isobars are oriented in a southwest-northeast direction as is schematically indicated in figure 15.

In contrast to the preceding experiments (where zonal pressure gradients were directed in the opposite direction), a divergence zone with vanishing meridional flow is established at about 1°S. As a result, the meridional flow and horizontal momentum advections are weak at the equator.

The resulting steady state zonal equation of motion is then approximately

$$wu_z \simeq Ku_{zz} - \alpha p_x$$

Scale analysis (where $u_z \sim U/D$) indicates that the ratio of the vertical advection term to the diffusion term is WD/K. This ratio in this experiment is $O(1)$ as downward advection of higher momentum is essentially balanced by momentum diffusion. These two terms are then large compared to the pressure gradient term which is balanced by their difference. Since these two terms tend to be proportional to the zonal wind speed (as indicated by scale analysis), unusually high zonal winds in excess of 50 m/s are generated above 2000 m at the equator.[9]

---

[9] Similarly, very large zonal winds are produced in the numerical experiment where the pressure gradient is directed entirely toward the west in which case horizontal advections of zonal momentum vanish at the equator.

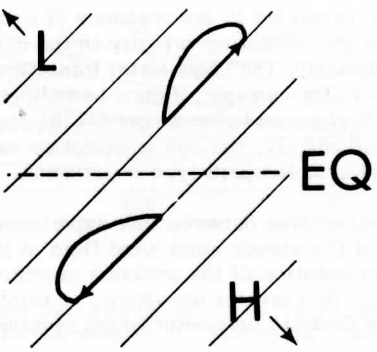

Figure 15. Schematic illustration of the Ekman hodographs and the surface pressure field for experiment 4.

Assuming the above problem is correctly posed (Ku_{zz} being a reasonable approximation to the diffusion term), it might then be concluded that in cases of significant zonal pressure gradients directed toward the west, subsidence, weak meridional flow and very high zonal winds are generated at the equator. However, the maintenance of these zonal pressure gradients in the presence of such large cross-isobar flow seems unlikely since mass redistribution would alter the pressure field before steady state flow is achieved. As a result, the details of the steady state flows corresponding to pressure gradients directed toward the west are somewhat academic and will not be discussed further in this study.

5.6 Boundary Layer Flows Generated by Equatorially Symmetric Pressure Fields

In the following sections boundary layer flows corresponding to pressure fields which are "even symmetric" with respect to the equator $[p(y) = p(-y)]$ are examined. With the same side boundary conditions specified at the same distance from the equator in each hemisphere, the resulting zonal flow is "even symmetric" with respect to the equator while the meridional flow is "odd symmetric" with respect to the equator $[v(y) = -v(-y)]$. Therefore, meridional flow and horizontal advections vanish at the equator. The latitudinal extent of the influence of these special flow properties at the equator depends on whether the flow and flow advections are directed toward or away from the equator. The case of flow toward the equator is considered first.

a) Flow Toward the Equator

Various pressure fields with low pressure at the equator or with the pressure gradient directed toward the east generate flow toward the equator in each hemisphere. The resulting impingement of the two flows at the equator produces very strong rising motion and large upward vertical advections of lower momentum in the immediate vicinity of the equator. One is reminded of the radially outward equatorial jet produced in the equatorially symmetric solid rotating sphere experiments of Bowden and Lord (1963), since the vertical motions in each case are very intense and are confined to a very narrow latitudinal belt about the equator.

However, the study of this equatorial vertical jet with the boundary layer numerical model is not properly posed for several reasons. The horizontal resolution is far too crude to adequately resolve this vertical jet. In reality, horizontal nonhydrostatic pressure gradients opposing the flow would be generated by the impingement of the two flows. Finally, the mass redistribution associated with the strong mass convergence would modify the hydrostatic pressure field. As a result of these effects, numerical solutions in this region may be quite unrealistic.

However, in the case of a constant pressure gradient directed toward the east (experiment 5) a number of interesting features occur outside this immediate equatorial region. This pressure field and the corresponding steady state wind field are illustrated in figure 16. Note that the entire geostrophic wind is directed in the meridional direction. Consequently, horizontal advections in the upstream quasi-Ekman flow (due to latitudinal variations of the boundary layer depth and geostrophic wind) become important at higher latitudes compared to previous cases, as is evident in figure 17.

Associated with the increase of the hypothetical geostrophic-Ekman flow toward the equator, the steady state boundary layer flow also increases toward the equator, although at a slower rate. Horizontal advections of lower momentum cause the boundary layer flow to be significantly weaker than predicted by the Ekman theory, even as far from the equator as 5° latitude.

Equatorward from 5° latitude, the importance of horizontal advections and deviations from the Ekman solution increase rapidly toward the equator. The boundary layer deviation angle decreases toward lower latitudes, vanishing at the equator where the flow is zonal at all levels. The most dramatic changes in boundary layer flow occur in the region of a strong rising motion in the immediate vicinity of the equator.

For completeness, it might be mentioned that equatorially symmetric flow (where meridional flow vanishes at the equator) is also generated by a pressure field corresponding to a constant easterly geostrophic wind with low pressure at the equator. The resulting flow is nearly identical to the flow upstream from the equator in the case of a pressure field corresponding to a constant easterly geostrophic wind magnitude. The primary differences between the two cases (upstream from the equator) occur in the immediate vicinity of the equator where the applicability of the numerical solution is questionable in the case of equatorially symmetric flow as mentioned above.

b) Flow Away from the Equator

When the flow is directed away from the equator, the influence of vanishing meridional flow is no longer limited to the immediate vicinity of the

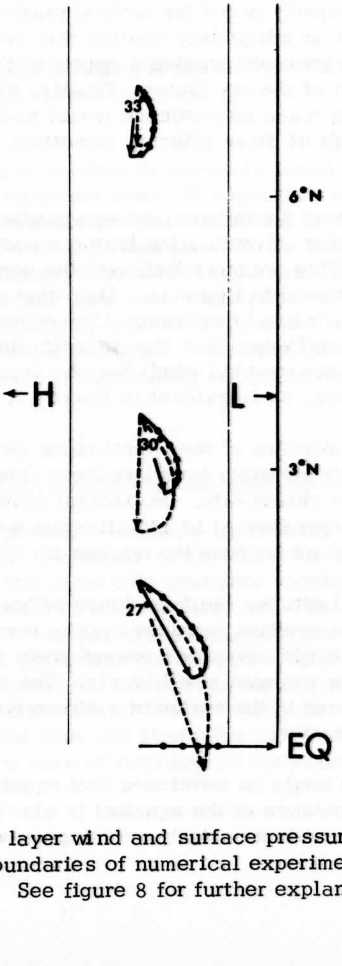

Figure 16. Boundary layer wind and surface pressure fields for experiment 5. Actual boundaries of numerical experiment at 0° latitude and 15° latitude. See figure 8 for further explanation.

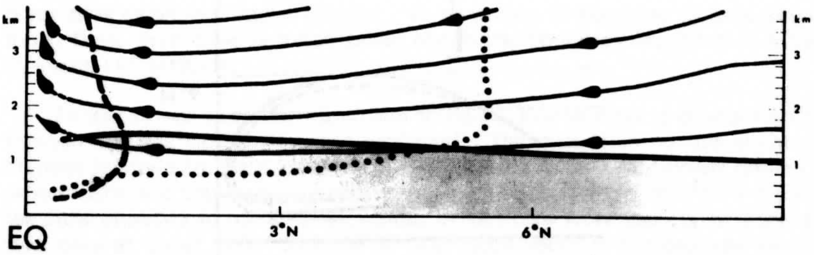

Figure 17. Streamlines (increments of 2×10^3 m^2/s) and .20 relative "force" isolines for experiment 5. See figure 9 for further explanation.

equator since the flow now advects low latitude flow properties away from the equator.

Pressure fields with high pressure at the equator or pressure gradients directed toward the west generate flow away from the equator. In the atmosphere high pressure at the equator may occur between two ITCZ's located on either side of the equator. Consider the case of a pressure field corresponding to constant westerly geostrophic wind (where the horizontal pressure gradient vanishes at a pressure maximum at the equator). The zonal equation of motion at the equator is then

$$wu_z = Ku_{zz} .$$

Since the flow is divergent at the equator, the zonal wind has a nonzero solution in addition to the null solution as was discussed in chapter 3. With this pressure field, zonal flow at the equator and then zero flow at the equator are produced in experiments 6 and 7, respectively.

In experiment 6, nonzero flow at the equator is numerically generated by initially specifying the equatorial zonal flow to be the zonal Ekman solution at $\frac{1}{2}$° latitude. In this case, the equatorial zonal flow changes so slowly with time that a quasi-steady state is achieved where the flow aloft is quasi-geostrophic even near the equator. In experiment 7, a steady state solution with zero flow at the equator is numerically generated by initially specifying zero flow at the equator.

Figures 18–21 show that the dynamics of the flows of these two cases are quite different. For example, in the case of quasi-geostrophic flow near the equator, a latitudinal width of only about 4° is required for the pressure gradient field to generate sufficient meridional flow for the boundary

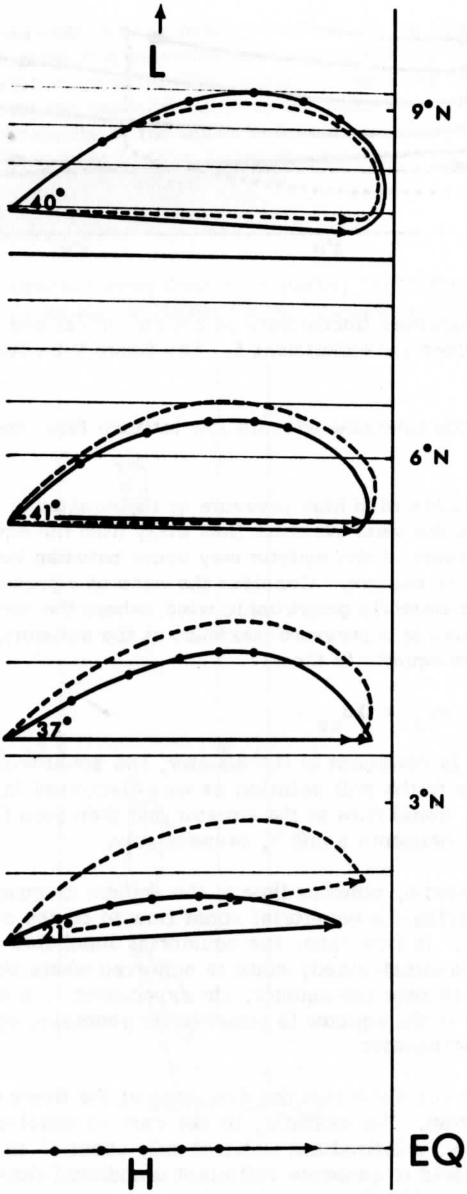

Figure 18. Boundary layer wind and surface pressure fields for experiment 6. Actual boundaries of numerical experiment at 0° latitude and 15° latitude. See figure 8 for further explanation.

layer flow to become quasi-Ekman. In contrast, to the case of zero equatorial flow, drift flow is established above the boundary layer which extends to about 11° latitude.

In the former case the transition to quasi-Ekman flow is gradual so that intense vertical motions are not produced. The transition occurs at the highest latitude in the middle portion of the boundary layer where cross-isobar flow and horizontal advections are largest. In the drift flow case, the flow changes to quasi-geostrophic Ekman flow more rapidly in a transition zone at about $11\frac{1}{2}$° latitude so that large vertical motions and vertical advections are produced. It then appears that drift flow is not only responsible for the dramatic boundary layer flow transitions (which have occurred downstream from the equator in various preceding numerical experiments) but also delays the transition to quasi-Ekman flow in the upper main portion of the boundary layer.

Of particular interest in the drift flow case is the region between about 5° latitude and the downstream flow transition. In this region the influence of the Coriolis parameter becomes significant but the drift flow prevents the boundary layer flow from becoming quasi-Ekman. The Coriolis term gradually replaces the horizontal advection term as a dominant term in the equations of motion. Net boundary layer veering begins to increase significantly with increasing latitude as the layer of quasi-Ekman flow adjacent to the ground slowly thickens. The downstream transition is not as abrupt compared to the prototype case which can be in part attributed to its higher latitude.

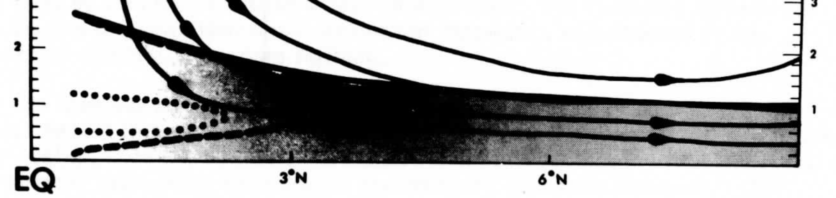

Figure 19. Streamlines (increments of 1×10^3 m^2/s) and .20 relative "force" isolines for experiment 6. See figure 9 for further explanation.

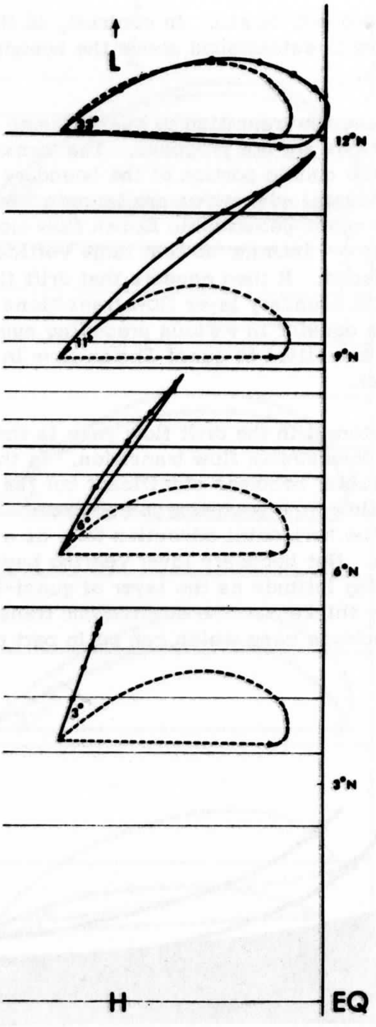

Figure 20. Boundary layer wind and surface pressure fields for experiment 7. Actual boundaries of numerical experiment are 0° latitude and 15° latitude. See figure 8 for further explanation.

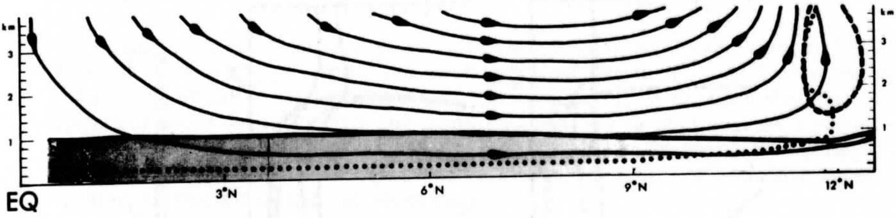

Figure 21. Streamlines (increments of 4×10^3 m^2/s) and .20 relative "force" isolines for experiment 7. See figure 9 for further explanation.

In summary, the latitudinal extent of the influence of the equator is considerably greater when the flow and flow advections are directed away from the equator. This is true whether the flow crosses the equator or whether the meridional flow vanishes at the equator.

In the next four sections (experiments 8–11), a number of variations on the prototype experiment are conducted to study the effect of changing certain specified parameters.

5.7 Variation of Specified Parameters

a) Variation of the Horizontal Pressure Gradient Magnitude

In the eighth experiment, the horizontal pressure gradient magnitude is decreased by a factor of two. The quasi-Ekman flow is approximately decreased by a factor of two as would be expected. The boundary layer depth of the quasi-Ekman flow does not change since it is independent of the pressure gradient at a given latitude.

In contrast the flow in the drift region is decreased by a factor of only 1.6. Recall that the drift speed is $O(|\alpha p_y|^{1/2})$ so that horizontal advections are $O(|\alpha p_y|)$ in the drift region. Figure 22a verifies that the importance of horizontal advections decrease as the pressure gradients decrease. One would expect the relative diffusion term in the drift region to increase as pressure gradients decrease, since the diffusion term is $O(|\vec{V}|)$ and the horizontal advection term (the largest term) is $O(|\vec{V}|^2)$. Figure 22a shows that only slight increases in boundary layer depth $(\delta_{.20})$ occur.

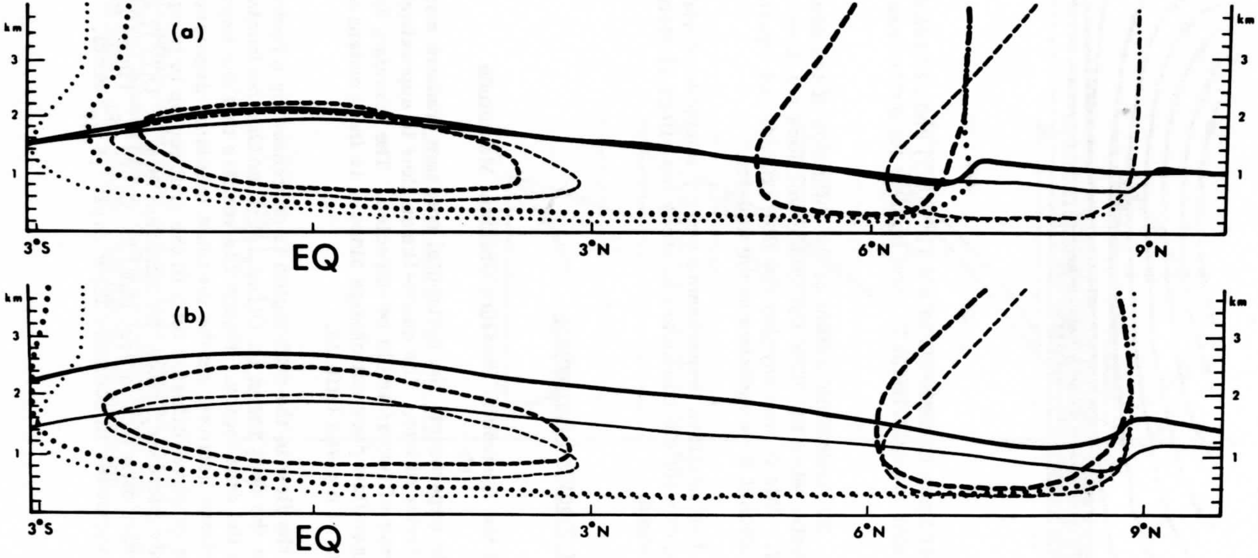

Figure 22. .20 relative "force" isolines for experiment 8 (a) and experiment 9 (b) compared to those of the prototype experiment (thin lines). See figure 8 for further explanation.

b) Increased Eddy Viscosity

Figure 22b illustrates that as eddy viscosity is increased from $5 m^2/s$ to $10 m^2/s$ (experiment nine), the boundary layer depth $(\delta_{.20})$ increases by a factor of about $\sqrt{2}$ at all latitudes. Consequently, it appears that the boundary layer depth in drift and transition regions is approximately proportional to the square root of eddy viscosity (as occurs in quasi-Ekman regions). This dependency is also observed in various other types of boundary layers as was discussed in the Introduction.

Note that the regions where vertical advections are important are located at somewhat higher levels. This can, in part, be attributed to the increased vertical scale height of the wind field associated with the increased eddy viscosity, in which case vertical motions do not become important until higher levels and vertical wind shears are important to higher levels. Conversely, simple analytical considerations (chapter 3) demonstrated that vertical advections of momentum could influence the frictional boundary layer depth. It then appears that the depth of the frictional boundary layer and the height of the layer where vertical advections are important are intimately interrelated at the equator. This interdependence is also evident in the next two sections where eddy viscosity is specified to be height-dependent and the geophysical boundary condition is applied.

c) Height-Dependent Eddy Viscosity

In experiment 10, a height-dependent eddy viscosity is specified (as formulated in chapter 2) where eddy viscosity is constant up to 500 m and then decreases linearly with height to ten percent of this value at 1700 m, above which eddy viscosity is again constant.

The primary effect of specifying this height dependence is to reduce the importance of the diffusion term in the upper portion of the boundary layer. Hence, figure 23a shows that the boundary layer depth is reduced, especially at lower latitudes where the boundary layer depth, in the case of height-independent eddy viscosity, extends well above the 500 m level. Also, as a result of decreased boundary layer depth, wind speeds and the importance of horizontal advections are larger at a given height in the boundary layer. Since the diffusion term contains a contribution dependent on vertical wind shear $(K_z \vec{V}_z)$, the magnitude of this shear above the frictional boundary layer is small compared to the constant eddy viscosity case. In particular the vertical inertial boundary layer above the frictional boundary layer in the downstream transition is considerably thinner.

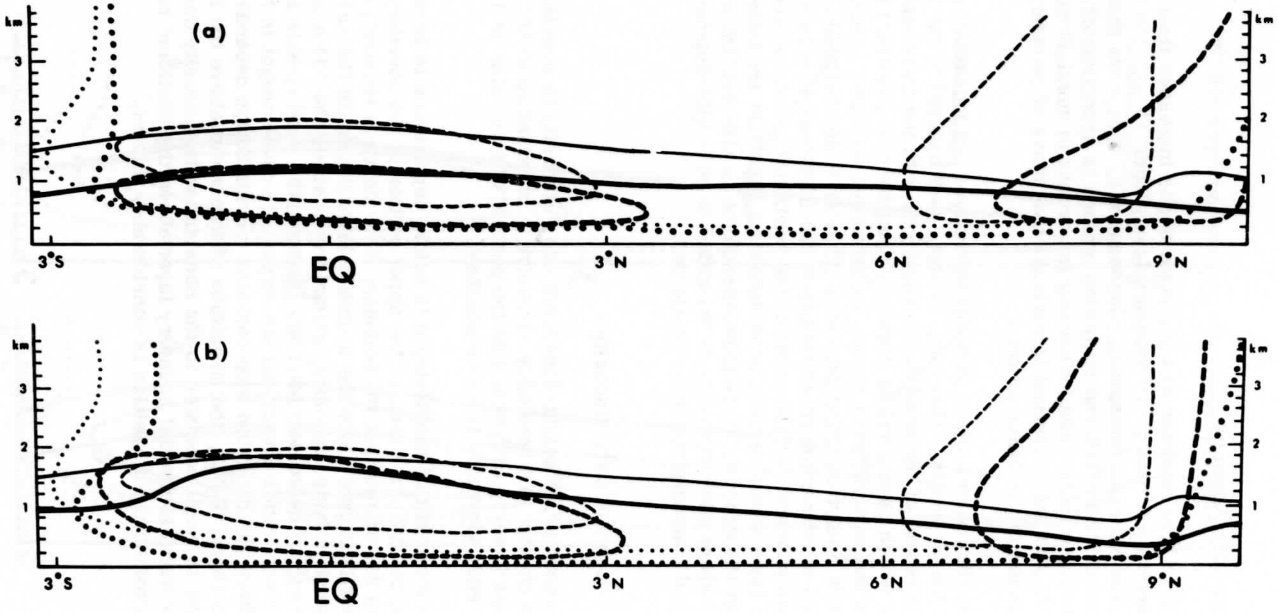

Figure 23. .20 relative "force" isolines for experiment 10(a) and experiment 11(b) compared to those for the prototype experiment (thin lines). See figure 8 for further explanation.

d) Application of the Geophysical Boundary Condition

Figure 23b shows that the application of the geophysical lower boundary condition (experiment 11) results in smaller boundary layer depths $(\delta_{.20})$. Figure 24 shows that wind speeds are stronger in the lower levels. The boundary layer deviation angle is reduced by about forty percent to fifty percent in both the quasi-Ekman flow and the ordinary boundary layer flow. However, the flow upstream from the equator is still Ekman-like in that the cross isobar flow is essentially limited to the interior of the boundary layer.

As a result of the decreased boundary layer depth, significant vertical wind shears are confined to lower levels. Consequently, the height, below which vertical advections at the equator are important, is reduced. Also, due to decreased boundary layer depth, the flow and horizontal advections are stronger in the lower levels. In fact, the wind usually achieves fifty percent of its frictionless value by the 50 m level whereas in the no-slip case, the wind in the drift region often requires 400–500 m to achieve this value.

In summary, varying certain parameters in the above sections did not change the qualitative behavior of the various flow regimes and flow transitions. This suggests that the choice of values of these parameters is not critical to the qualitative discussions of this study.

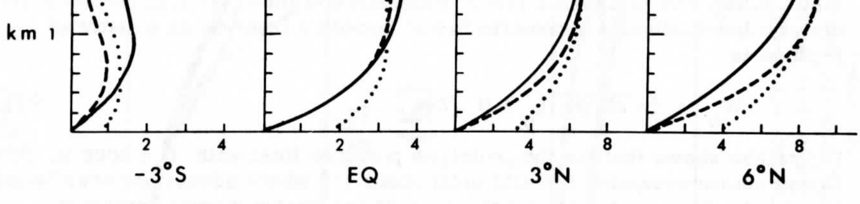

Figure 24. Vertical profiles of meridional velocity (m/s) for the prototype pressure field for height independent K (solid line), height independent K (dashed line) and height independent K with the geophysical boundary condition (dotted line).

5.8 Boundary Layer Vertical Motion

Vertical motion at the top of the boundary layer is one of the most important products of boundary layer theory. By means of this vertical motion, the boundary layer influences the overlying free atmosphere through vertical fluxes of mass and other properties. Attention in this section is devoted to parameterizations of these vertical motions in terms of the wind and pressure fields above the boundary layer.

The vertical motion at H, the top of the boundary layer, can be computed from the integrated mass continuity equation:

$$W_H = -\int_0^H V_y dz \; .$$

The top of the frictional boundary layer may be difficult to establish from the wind field because of the possible simultaneous occurrence of a vertical inertial boundary layer with the frictional boundary layer. As an alternative, $\delta_{.20}$ (the level above which the relative diffusion term is less than .20), could also be used as an indication of boundary layer depth. However, this level may vary considerably with latitude. As a more precise indication of horizontal convergence strength in the boundary layer, a constant height level can be used. The vertical motion at a constant height level appears to be most useful, especially for testing vertical motion parameterizations for use in numerical models.

Vertical motions are considered first for the quasi-Ekman region and then for the drift region. Since the strongest convergence in the quasi-Ekman flow regime is essentially limited to the boundary layer, the exact choice of level H is not critical as long as H is in the vicinity of the boundary layer top. As would be expected, vertical motion parameterizations based on the Ekman solution are good approximations in this region as long as the term due to latitudinal variations of the Ekman depth is included. It is easily shown that Charney and Eliassen's (1949) parameterization of vertical motion at the top of a longitudinally symmetric Ekman boundary layer on an equatorial β-plane is

$$W_b = \frac{1}{2}\sqrt{2K/\beta y}\,(\zeta_g + U_g/2y) \; . \qquad (92)$$

Figure 25a shows that for the prototype pressure field with $H = 2000$ m, this Ekman parameterization is valid until about 4°S where advection terms become important. Note that (92), for the case of constant horizontal pressure gradient, indicates that the β-term $(U_g/2y)$ is equal to the vorticity term; hence, parameterization based on geostrophic vorticity alone would underestimate the true Ekman vertical motion by a factor of two. In fact, with a constant geostrophic wind, vertical motion computed with (92), (see figures 26b and c) is due exclusively to the β-term.

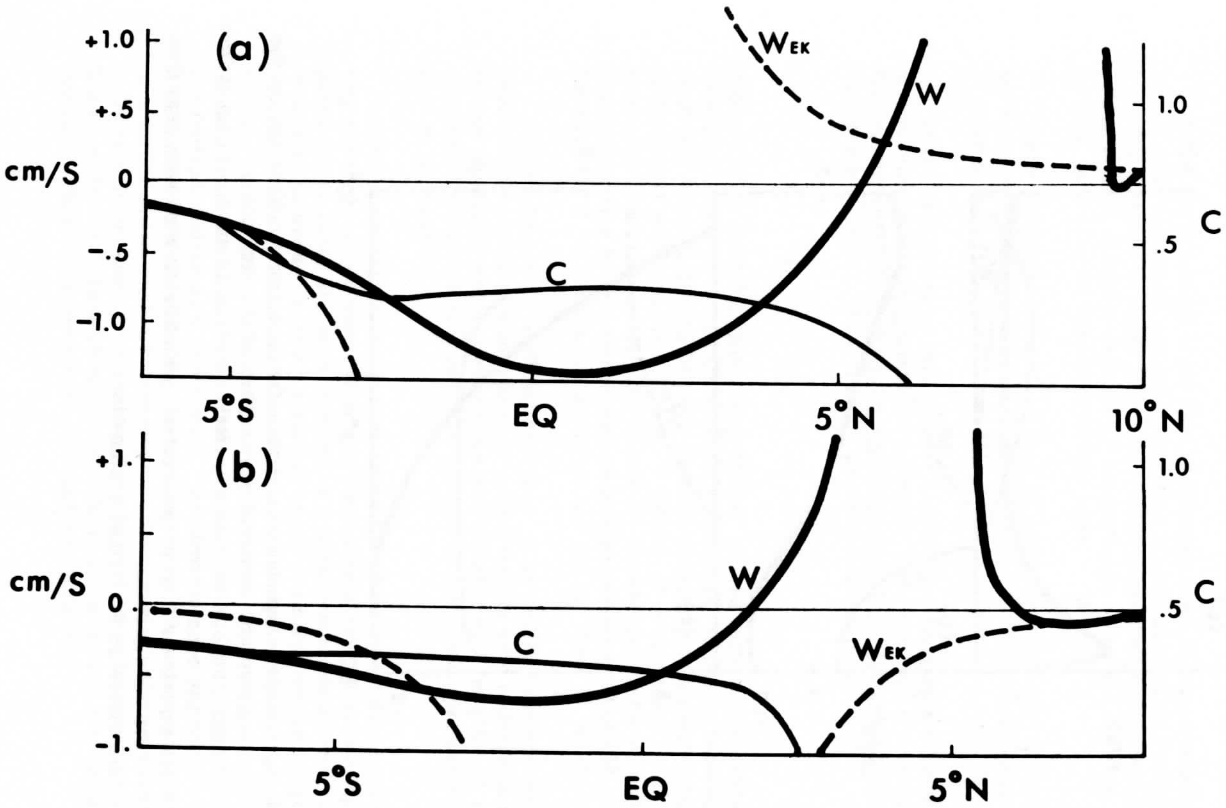

Figure 25. Boundary layer vertical motion for the prototype experiment (a) and experiment 3 (prototype pressure field rotated clockwise 45°). Vertical motion at 2000 m (W), vertical motion computed from the Ekman solution (dashed line labelled W_{EK}) and where appropriate, the parameter C (C) are shown.

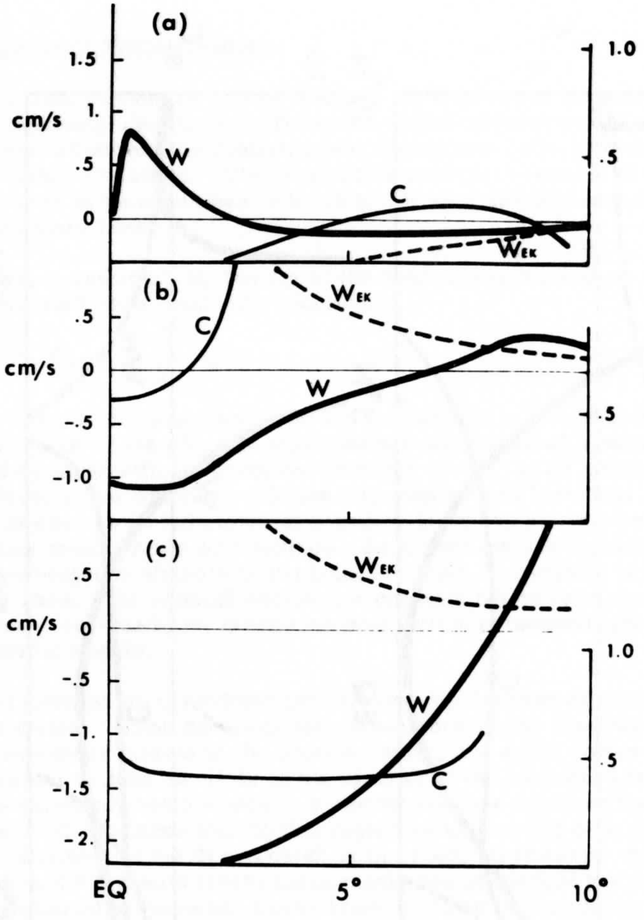

Figure 26. (a) boundary layer vertical motion for experiment 2 (flow toward the equator with constant geostrophic wind magnitude);
(b) experiment 6 (constant easterly geostrophic wind with zonal flow at the equator) and
(c) experiment 7 (constant easterly geostrophic wind with zero flow at the equator).
See figure 25 for further explanation.

When the boundary layer flow is directed more in the meridional direction so that horizontal advections become important at higher latitudes (experiment 3 shown in figure 25b), the Ekman parameterization becomes a poor approximation at higher latitudes. Divergences along the isobars, ignored by (92), may also be important in this case.

Since horizontal advections tend to decrease horizontal variations of the wind field and therefore vertical motions, the Ekman parameterization (92) in general tends to grossly overestimate vertical motions near the equator.

In the drift flows of this chapter, horizontal divergences generally increase with height throughout the boundary layer (as opposed to quasi-Ekman flow where divergence reverses sign with height and becomes small above the boundary layer). As a result, a parameterization of the form

$$W_H = C(v_y)_H H \tag{93}$$

appears to be a useful formulation in that C, the ratio of the average divergence below H to the divergence at level H, is nearly independent of latitude. Figures 25 and 26 show that C is nearly constant in the various drift regions with a value of about .3 (where C would equal .5 if divergence increased linearly with height). Figure 27 shows that in the drift regime, the rate of increase of divergence with height decreases with height. Consequently, if H is chosen to be larger than 200 m, then C would be larger.

Figures 25 and 26 also indicate that C is nearly independent of latitude in the equatorial transition but varies rapidly with latitude in the downstream transition where divergences reverse sign with height. C may also vary rapidly with latitude near the equator in the case of vanishing meridional flow at the equator.

Certain variations in the representation of the momentum diffusion term may affect the above vertical motion parameterizations. For example, in the quasi-Ekman flow, the specification of a height-dependent eddy viscosity results in decreased vertical motion. In the ordinary boundary layer, decreased boundary layer depth (resulting from decreased eddy viscosity, specification of a height-dependent eddy viscosity or application of a geophysical boundary condition) causes increased cross-isobar flow, horizontal divergence and vertical motion at a given level. As a result, C is decreased slightly with increased eddy viscosity (experiment 9) and is increased approximately by a factor of two with a height-dependent eddy viscosity (experiment 10). C is also increased approximately by a factor of two in experiment 11 were low level flow and flow divergences, shown in figure 27, are increased by the application of the geophysical boundary condition.

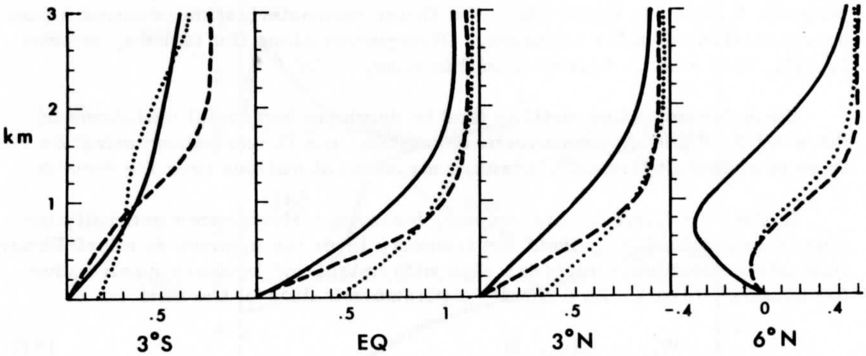

Figure 27. Vertical profiles of horizontal divergence (10^{-5} s^{-1}) for the prototype pressure field for height-independent K (solid line), height-dependent K (dashed line) and height-independent K with the geophysical boundary condition (dotted line). Divergences were computed between columns of grid points.

In conclusion, the drift-ordinary boundary layer vertical motion is approximately proportional to the divergence of the frictionless drift flow for the pressure fields considered in this chapter. It then appears that frictionally induced convergences are not as significant in these drift flows compared to quasi-Ekman flows where low level convergences are primarily due to frictional effects (as the frictionless flow is quasi-nondivergent).

5.9 Summary of the Maintained Numerical Boundary Layer Experiments

In this section, a number of concluding points, based on the preceding numerical experiments, are summarized.

With flow toward the equator, the Ekman solution is a poor approximation due to momentum advections associated with the increasing boundary layer depth toward the equator and latitudinal variations of the geostrophic wind. The latitude where these advections become large varies from a few degrees latitude to five to ten degrees latitude, depending on the strength of the advecting flow which is in turn related to the orientation and strength of the pressure gradient field. Due to momentum advections, the boundary layer depth (based on the relative importance of the diffusion term) increases much more slowly toward the equator than predicted by Ekman theory (in which case the boundary layer depth is infinite at the equator). Rotation of the boundary layer wind vector with height decreases toward the equator.

The meridional flow may vanish at the equator or the flow may cross the equator, depending on the orientation of the pressure field. With a zonal pressure gradient directed toward the west, the divergence of two flows may occur near the equator, in which case extremely large zonal winds are generated. In contrast, a zonal pressure gradient directed toward the east may generate the convergence of two flows near the equator. In the case of small zonal pressure gradients, the flow may be accelerated across and downstream from the equator, excluding cases where the meridional pressure gradient reverses sign near the equator. The sensitivity of the character of the low latitude flow to the orientation of the pressure field is associated with the rapid latitudinal variation of the Coriolis parameter.

When the flow is directed away from the equator, advections are generally more important over a greater latitudinal extent compared to flow toward the equator. In the case of flow crossing the equator, horizontal advections may become important downstream from the equator to the extent that the boundary layer is entirely different from the Ekman boundary layer. The rotation of the wind vector with height in this boundary layer may be weaker and in the opposite direction of Ekman rotation. This occurrence, with the wind directed away from the equator, has been observed by Robitaille and Zipser (1970) at the Line Islands. The magnitude of this rotation in various numerical experiments is nearly independent of latitude. The cross-isobar motion, which increases with height and reaches a maximum at the top of the boundary layer, may be considerably larger compared to that of the Ekman solution. With the pressure fields of this chapter, the horizontal divergence does not change sign with height, but also increases with height throughout the boundary layer. As a result, the boundary layer production of vertical motion may be overshadowed by divergences aloft, in contrast to the quasi-Ekman regime where the boundary layer plays a major role in the free atmosphere vertical field. The boundary layer depth is considerably thinner than the corresponding Ekman boundary layer depth and is nearly independent of latitude.

While the various characteristics of this ordinary type boundary layer are somewhat independent of latitude, transitions between this boundary layer and the quasi-Ekman boundary layer may occur over relatively narrow latitudinal regions. These transitions may produce large boundary layer vertical motions. In the transition from the quasi-Ekman regime to a drift-ordinary boundary layer regime, subsidence results from increasing strength and depth of the cross-isobar flow. This subsidence occurs with a variety of pressure fields and could be in part responsible for the observed cloud-free equatorial dry zone.

On the other hand, in the transition from the drift-ordinary boundary layer regime to the quasi-Ekman regime, strong rising motion is produced by the rapid decrease in strength and depth of the cross-isobar flow or by the convergence of two flows. The particular significance of this convergence zone is that it results solely from a latitudinal transition of regimes where horizontal advections are important equatorward from the convergence zone. As a result, this rising motion does not require a pressure minimum or a latitudinal decrease in the horizontal pressure gradient. This convergence-producing mechanism could be a component in the maintenance of the ITCZ.

The effect of decreasing the eddy viscosity magnitude, specifying height-dependent eddy viscosity or applying the geophysical boundary coefficient is to decrease the boundary layer depth. This may decrease boundary layer vertical motions in the Ekman boundary layer but increases vertical motion at a given level in the ordinary boundary layer.

In the atmosphere, the pressure gradient field may not be maintained in the presence of the large cross-isobar flows in the drift region and large vertical motions at the flow transitions since mass redistribution and vertical transfers of latent heat may be large. In the remaining three chapters of this study, the boundary layer problem is examined where pressure adjustments in response to boundary layer vertical transports of mass, momentum and latent heat are allowed. These pressure field modifications will in turn feed back upon the boundary layer flow.

6. THE FREE ATMOSPHERE AND ITS RESPONSE TO BOUNDARY LAYER FORCING

The main purpose of the remaining portion of this study is to allow the boundary layer to modify the pressure field so that the steady boundary layer flow corresponding to the adjusted pressure field can be examined. The boundary layer will modify the pressure field through redistribution of mass by means of cross-isobar flow. These pressure adjustments are specifically accomplished by adiabatic temperature changes or latent heat release in the free atmosphere induced by boundary layer vertical motions. These modifications in the pressure field will in turn feed back upon the boundary layer flow since the free atmosphere imposes a pressure field on the low level wind field. In cases of strong boundary layer rising motion, vertical advections of lower momentum from near the earth's surface may directly modify the free atmosphere wind field.

These pressure adjustments are allowed in a one layer representation of the free atmosphere. This chapter contains analytical considerations of the response of a one-layer model of the free atmosphere to hypothetical boundary layer forcing. In chapter 8 the role of the boundary layer in determining the pressure field and the steady state boundary layer flow corresponding to the adjusted pressure field are studied with a numerical model. This numerical model is developed in chapter 7 by combining the boundary layer numerical model of chapter 4 with a one-layer model of the lower troposphere free atmosphere which allows for certain simple vertical flow variations. Whereas most previous numerical models have emphasized the free atmosphere and crudely represented or parameterized the boundary layer, this coupled numerical model emphasizes the boundary layer and uses a simple model to allow for pressure adjustments in the free atmosphere.

Although a multilayer representation of the free atmosphere could be of little additional computational difficulty, an internal mode of interaction would be possible, which would prevent easy isolation of boundary layer-free atmosphere interactions. Consequently, we adopt the simplest model of the free atmosphere which is the one-layer representation.

There is considerable evidence that the equatorial free atmosphere is layered and the influence of the boundary layer is essentially limited to the layer or layers in the lower part of the troposphere. Madden and Zipser (1970) found that in the Line Islands region, the troposphere appears to be characterized by a number of definite layers demonstrating both strong time and spatial continuity. Movies of cloud motions constructed from series of satellite cloud pictures indicate that clouds at different levels appear to move in different directions. Chang et al. (1970) noted two types of waves in the equatorial Pacific. Large wave lengths (6, 000 to 10, 000 km) were generally found in the upper troposphere while shorter wave lengths (3, 000 to 5, 000 km) were usually found in the lower troposphere. Simpson et al. (1967), in a case study of a disturbance above 500 mb at about 14°N, found it to be primarily linked to wave motions in the upper part of the troposphere. The disturbance appeared to be uninfluenced by the boundary layer, since wind perturbations below 500 mb did not occur.

Consequently, a one-layer approximation of the lower part of the free troposphere appears to be appropriate for this study. This free atmosphere layer will extend from 800 mb, the assumed top of the boundary layer, to 500 mb where horizontal pressure gradients are required to vanish.

In this chapter, the properties of the wind and pressure fields of the free layer are examined in the presence of cross-isobar flow and horizontal advections of momentum (drift flow). The equations of motion are identical to those of the drift flow discussed in chapter 3 except that the pressure field is now determined by the flow instead of being specified a priori.

Grimes (1937), Crossley (1948), Sellick (1950) and Fujita et al. (1969) and others have studied trajectory solutions for ageostrophic flow at low latitudes where the pressure field was not specified a priori. However, all of these solutions contain restrictions on the horizontal divergence of the wind field. Since our main purpose is to study the response of the free atmosphere to possible boundary layer forcing in terms of mass and latent heat fluxes, restrictions on divergence of the wind field cannot be allowed.

6.1 Basic Equations of Motion

In this section the wind field is expressed in terms of the geopotential field. The equations of motion for frictionless, longitudinally symmetric, steady, height-independent flow on an equatorial β-plane are

$$vu_y - \beta y v = 0 \tag{94}$$

$$vv_y + \beta y u = -\phi_y \tag{95}$$

where ϕ is the geopotential height of a constant pressure surface.

As in chapter 3, (94) indicates that the zonal flow component can be geostrophic $(v = 0)$ or obey a constant angular momentum profile where the zonal flow is independent of the pressure field. Hence

$$u = u_0 + \beta(y^2/2 - y_0^2/2) . \tag{96}$$

For the constant angular momentum solution, (95) can be written in the form

$$(v^2/2 + \phi)y = -\beta y u . \tag{97}$$

Substituting for the constant angular momentum zonal flow solution and integrating from y_0 to y

$$v^2 = v_0^2 - 2(\phi - \phi_0) + 2G(y) \tag{98}$$

where

$$G(y) \equiv -\beta[-(\frac{u_0}{2} y_0^2 + \frac{\beta}{8} y_0^4) + y^2(\frac{u_0}{2} - \frac{\beta}{4} y_0^2) + y^4(\beta/8)] .$$

Equation (98) then expresses the meridional flow in terms of latitude, the initial flow upstream and the geopotential field.

A third equation, which relates the geopotential field to the wind field, will be derived in the following two ways: 1) A mass continuity equation for a one-layer hydrostatic incompressible fluid is used in which case an exact wind and pressure field solution is possible. A classical example of a one-layer incompressible model is Rossby's (1967) study of jet streams. Matsuno

(1966) studied various possible wave modes on an equatorial β-plane with a one-layer incompressible model of the free atmosphere where momentum advections were ignored. He showed that his model was equivalent to a simple two-layer model.

2) A combination of the mass continuity and thermodynamic equations for a one-layer hydrostatic compressible fluid is also used. In this case, an exact solution is not obtained, although essential information is still extracted from the equations. Several sections are then devoted to the effects of boundary layer forcing on the one-layer compressible free atmosphere.

6.2 The Incompressible Case

The incompressible case is treated first. The continuity equation for steady incompressible flow of a one-layer hydrostatic fluid over a flat lower boundary is

$$(v\phi)_y = \tilde{Q} \tag{99}$$

where $\tilde{Q}$ is an externally imposed mass source term which can be thought of as arising from vertical motions out of an underlying boundary layer. ϕ is the geopotential thickness of the fluid. Integrating (99) and solving for ϕ we obtain

$$\phi = [\phi_0 v_0 + \int_{y_0}^{y} \tilde{Q}\, dy]/v \; . \tag{100}$$

A cubic equation in meridional velocity is obtained by substituting for ϕ in (93) and multiplying by $2v$[10]

$$v^3 + p(y)v + q(y) = 0 \tag{101}$$

where

$$p(y) \equiv -2\{(v_0^2/2 + \phi_0) + G(y)\}$$

$$q(y) \equiv 2(v_0\phi_0 + \int_{y_0}^{y} \tilde{Q}\, dy) \; .$$

Note that the mass source terms are contained in $q(y)$ while Coriolis effects

---

[10] Similarly, one could solve for v from the continuity equation and obtain a cubic equation in ϕ.

are contained explicitly in $p(y)$. Also note that if $q(y) = 0$ ($v_0 \neq 0$ or $\int_{y_0}^{y} \tilde{Q}\, dy \not\approx 0$), then the zonal flow cannot in general be geostrophic.

Using Cardan's formulas, the solution to (101) is

$$v = 2\,\mathrm{Re}\,\omega\sqrt[3]{A} \tag{102}$$

where

$$A \equiv -\frac{1}{2}q(y) + \sqrt{R}$$

$$R \equiv (8/27)[p(y)]^3 + \frac{1}{4}q(y)^2$$

$$\omega \equiv -\frac{1}{2} - \frac{1}{2}\sqrt{3}i \;.$$

An evaluation of this solution, shown in figure 28, is discussed in a later section.

6.3 The Compressible Case

In the case of compressible flow, a thermodynamic equation in addition to the mass continuity equation is employed. The thermodynamic equation for a compressible fluid can be written as

$$v\theta_y + \omega\theta_p = Q \tag{103}$$

where θ is the potential temperature, and Q is an externally imposed heating term which may be thought of as resulting in part from latent heat fluxes out of the boundary layer. For a one-layer compressible fluid bounded by two constant pressure surfaces, the horizontal geopotential gradient at the lower pressure surface can be related to the mean potential temperature gradient. To simulate a pressure system confined to the lower troposphere (i.e., a warm core low or a cold core high), the horizontal geopotential gradient is required to vanish at the upper pressure surface. Then at the lower pressure surface where the equations of motion (94) and (95) are applied, the pressure gradient term is $-\hat{\phi}_y$ where $\hat{\phi}$ is the negative of the total geopotential thickness of the layer of pressure thickness Δp. Requiring that the mass average of specific volume in the layer occurs at $\bar{P}$, the arithmetic mean pressure of the layer, the hydrostatic relationship and the equation of state then imply

$$\hat{\phi} = -R\Delta p\bar{T}/\bar{P}$$

where $\Delta p > 0$ and $\bar{T} \equiv T(\bar{P})$. Since on a constant pressure surface

$$
\begin{aligned}
\theta_y &= T_y(P_0/p)^{\kappa} \\
\bar{\theta}_y &= -\bar{P}(P_0/\bar{P})^{\kappa}\,\hat{\phi}_y/R\Delta p
\end{aligned}
\tag{104}
$$

where $P_0 = 1000$ mb and $\kappa = .286$.

The continuity equation for a compressible fluid is written in pressure coordinates as

$$\omega_p + v_y = 0$$

where $\omega = \dfrac{dp}{dt}$.

Assuming linear extrapolation of velocities from the lower pressure surface to the upper pressure surface (where vanishing velocities are specified to correspond to the zero pressure gradient term), the continuity equation at $\bar{P}$ is

$$\omega = \omega_b + \frac{3}{4} v_y \frac{\Delta p}{2} . \tag{105}$$

Here v is the meridional velocity at the lower level and ω_b is vertical motion at the lower pressure surface due to convergence in an underlying boundary layer. Equations (103), (104) and continuity equation (105) imply that at $\bar{P}$

$$
\begin{aligned}
v\hat{\phi}_y + Sv_y &= -\hat{Q} \\
S &\equiv \frac{3}{8} R(\Delta p)^2 \,|\theta_p|/P_0/\bar{P})^{\kappa} \\
\hat{Q} &\equiv R\Delta p(Q - \omega_b\theta_p)/\bar{P}(P_0/\bar{P})^{\kappa}
\end{aligned}
\tag{106}
$$

where $\theta_p < 0$ is assumed, $v\hat{\phi}_y$ is a horizontal temperature advection term, Sv_y is the horizontal divergence contribution to the vertical advection of potential temperature, and $\hat{Q}$ is the total external forcing term which would include both boundary layer induced adiabatic temperature changes and latent heat release.

The solutions of (94), (95), and (106) are determined by S and the side boundary conditions for u, v, and $\hat{\phi}$. S has the same units as geopotential thickness and may be thought of as a "reduced geopotential thickness" based upon a reduced gravity associated with the thermal stratification. In other words, geopotential thickness is the coefficient of the horizontal divergence term in the incompressible mass continuity equation (99), while S is the coefficient of the horizontal divergence term in the compressible thermodynamic-continuity equation (106). With $\Delta p = 300$ mb, $\bar{P} = 650$ mb and θ_p chosen to be 3°K/100 mb (approximately pseudoadiabatic corresponding to a typical tropical lower troposphere), then $S = 1000\ m^2/s^2$. S is thus considerably less than the actual geopotential thickness which is approximately 40,000 m^2/s^2. As a result, stronger divergences are required to balance the horizontal temperature advection term compared to the incompressible case. In terms of fixed Δp and $\bar{P}$, S may also be viewed as a stability parameter.

This compressible case is examined in the remainder of the chapter in terms of qualitative arguments based on the equations of motion and (106), the thermodynamic-continuity equation. The discussion can also be applied to the incompressible case by means of a simple transformation where $\hat{\phi}$ becomes the geopotential thickness of the incompressible fluid, S becomes the mean geopotential thickness and $\hat{Q}$ becomes the mass source term.

6.4 Unforced Flow

In this section, the unforced system $(Q = 0)$ is examined. The effect of the temperature advection and divergence terms on the wind field can be seen by solving for $\hat{\phi}$ from the thermodynamic-continuity equation (106) and substituting into the meridional equation of motion (95). After rearranging terms

$$\beta yu = -\hat{\phi}_y(1 - v^2/S) . \tag{107}$$

In terms of S, the reduced geopotential thickness, we can define the reduced local Froude number, $F = v^2/S$. One can see from the above equation that this number for unforced flow is the ratio of the local advective term to the hydrostatic horizontal pressure gradient term. In terms of u_a, the zonal ageostrophic wind $(u_a \equiv u - U_g)$ and F, (107) reduces to

$$\frac{u_a}{U_g} = F .$$

If the reduced Froude number is nonzero, then the zonal flow component is not geostrophic, although for $F \ll 1$ the zonal flow is quasi-geostrophic. In other words, the zonal flow tends to be most geostrophic for large S (small F), which occurs with thick layers or layers with large static stability. For values of atmospheric parameters listed in the preceding section and for $v \leq 10$ m/s, $F \leq 10^{-1}$ so that the zonal component of the drift flow is quasi-geostrophic where pressure adjustments for unforced flow are allowed.

In marked contrast, recall that when pressure adjustments are not allowed (chapter 5), the zonal drift component above the boundary layer is often highly ageostrophic. In fact, cross-equatorial flow with nonzero meridional pressure gradient at the equator (i.e., geostrophic wind reverses sign at the equator) resulted in the zonal drift component opposing the direction of the zonal geostrophic wind. However, the above adjustment theory for small F indicates that in reality the geostrophic wind does not reverse sign at the equator for cross-equatorial flow if the zonal drift component does not reverse sign at the equator. This requires that the adjusted meridional pressure gradient must vanish and reverse sign at the equator, and so exemplifies the potentially unrealistic nature of the specified pressure fields in chapter 5. The boundary layer corresponding to adjusted pressure fields is studied in chapter 8 with the free atmosphere-boundary layer numerical model.

The behavior of the meridional flow component is easily analyzed with the thermodynamic-continuity equation

$$v_y/v = -\hat{\phi}_y/S \quad . \tag{108}$$

This equation requires that meridional flow toward higher pressure results in horizontal convergence while meridional flow towards low pressure results in divergence. Since decreasing meridional flow also implies decreasing Froude number, flow towards higher pressure becomes less ageostrophic in terms of both flow components. Conversely, both flow components become more ageostrophic with flow towards lower pressure.

Equation (108) also indicates that the percentage change in the meridional velocity must be small since $\hat{\phi}_y/S$ is small. For example, if $|\phi_y| = 10^{-4}$ m/s^2 (which corresponds to a geostrophic wind of 10 m/s at 4° latitude) and other parameter values are chosen as above, only a one percent change in the meridional velocity occurs over a 100 km extent. Small latitudinal changes in meridional velocity occurs over a 100 km extent. Small latitudinal changes in meridional flow and other flow features discussed above are illustrated in figure 28 for the incompressible flow case [(94)–(101)].

The above analysis of the wind and pressure fields is valid only when the heating term is small. In the next section, the influence of heating in the compressible model is qualitatively examined.

6.5 Forced Flow

In this section the flow is forced by an external thermal forcing term, which may be thought of as adiabatic termperature changes resulting from boundary layer induced vertical motions and latent heat release in the free atmosphere associated with latent heat fluxes out of the boundary layer.

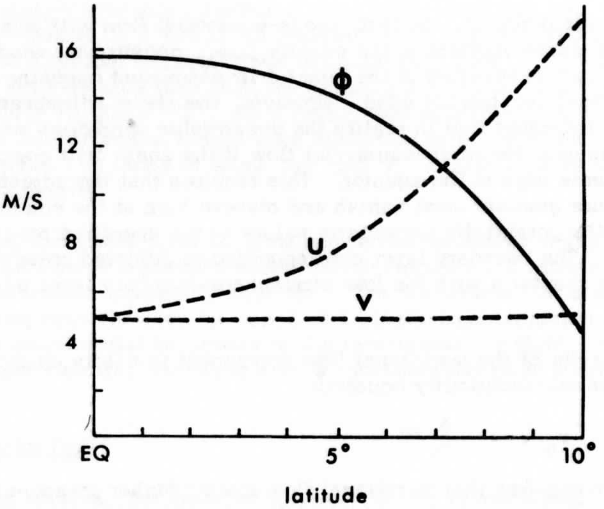

Figure 28. Incompressible flow toward higher latitudes. The geostrophic and actual zonal wind profiles essentially coincide (within the accuracy of the graph).

Recall that the thermodynamic-continuity equation (108) for forced flow is

$$v\hat{\phi}_y + Sv_y = -\hat{Q} .$$

Charney (1963) performed a scale analysis of large scale tropical motions and concluded that horizontal temperature perturbations were small to the extent that temperature advections could be neglected in the thermodynamic equation. Scale analysis in this model for heated regions indicates that the temperature advection term $v\hat{\phi}_y$ is small compared to the divergence term $v\hat{\phi}_y$. For example, estimating derivatives by scale analysis

$$|v_y| \sim |V/L|$$

$$|\hat{\phi}_y| \sim |\Delta\phi/L|$$

it then follows that

$$|v\hat{\phi}_y/Sv_y| \sim |\Delta\hat{\phi}/S| .$$

Choosing L = 300 km to represent a typical ITCZ width and again choosing $|\hat{\phi}_y| = 10^{-4}$ m/s², we obtain $|\Delta\hat{\phi}/S| = .03$. In other words, the external heating is essentially balanced by adiabatic cooling due to convergence of the free atmosphere flow. It might be noted that Charney (1968) also found horizontal temperature advections to be unimportant in the heated region of his ITCZ numerical model. The results of the coupled numerical model discussed in chapter 8 similarly will verify this tendency in heated regions.

The influence of the heating term on the wind field is made clear by combining the thermodynamic-continuity equation (108) and the meridional equation of motion (95) to obtain

$$-\hat{Q}v/S + \beta yu = -\hat{\phi}_y(1 - F) \qquad (109)$$

where $\hat{Q}v/s$ arises from the forcing term and $\hat{\phi}_y F$ is due to horizontal temperature advections. The effect of heating on the wind field then appears to be most important for thin layers and weak thermal stability (i. e., small S). In terms of u_a, the zonal ageostrophic wind,

$$\beta yu_a = F\hat{\phi}_y + \hat{Q}v/S \ .$$

Neglecting the "temperature advection term," on the basis of the scale analysis above, using the definitions of Q and S and rearranging terms, we find that

$$\frac{u_a}{v} = -(Q - \omega_b\theta_p)/\frac{3}{8}\,\theta p\,\Delta p\,\beta y \ .$$

In contrast to the unforced case (where the ageostrophic wind was mainly due to cross-isobar flow), the zonal ageostrophic wind in the forced case may become significant relative to the meridional flow component if the net forcing term (in brackets) is sufficiently large. Note that the influence of the forcing term is inversely proportional to latitude. For example, with the above parameter values, a strong forcing term of 6°C/day would result in $|u_a/v| \geq 1$ only equatorward from 3° latitude. Consequently, one could conclude that the ageostrophic wind is still essentially directed along the pressure gradient except near the equator.

It must be remembered that the zonal wind solution is the constant angular momentum wind profile which is dependent only on the upstream boundary condition and, therefore, mathematically independent of the local pressure field. Thus, the above relationships should be thought of as resulting from adjustments mainly by the pressure (geostrophic wind) field to the wind and heating fields. The relationship between the pressure field and zonal ageostrophic wind is easily obtained by applying the definitions of u_a and U_g

$$|u_a/U_g| \approx |1 - \phi_y^*/\phi_y|$$

where ϕ_y^* is the pressure gradient field corresponding to the coincidence of the geostrophic wind field with the constant angular momentum zonal wind field. The above analysis then indicates that sufficiently large forcing may cause pressure adjustments so that the zonal ageostrophic wind becomes important only at lower latitudes.

6. 6 Boundary Layer Forcing

In this section, the forcing term is related to vertical mass fluxes and latent heat release induced by the ordinary boundary layer. Adopting the philosophy of Charney and Eliassen (1964) and Kuo (1965), it is assumed that the convective release of latent heat in the free atmosphere is proportional to moisture convergence in the boundary layer. Such a relationship appears to be especially appropriate in the tropics where moisture is primarily confined to lower levels (in which case the latent heat supply is closely related to mass flux out of the boundary layer). $\left.\frac{dq}{dt}\right|_C$, the net condensation rate (i.e., the condensation rate less the evaporation rate), can then be related to ω_b by the moisture budget equation

$$\frac{dq}{dt} = - \eta \, \omega_b q_b / \Delta p$$

where horizontal advections and fluxes of moisture out of the top of the free atmosphere layer have been neglected. q_b is the specific humidity at the top of the boundary layer, Δp is the thickness of the layer over which the moisture is uniformly distributed and n is the net fraction of available moisture converted to latent heat release. n is not unity because a certain amount of moisture is used to increase the water vapor content of the atmosphere prior to cloud development and to increase the water vapor content of the environment outside the cloud columns by means of entrainment or diffusion. In addition, a certain amount of condensed water re-evaporates in the downdrafts. n could then be viewed as the efficiency of a synoptic scale disturbance in converting a given boundary layer moisture source into latent heat release. n would then depend on the efficiency of individual convective elements and the percentage of the total area of the disturbance occupied by these convective elements.

From thermodynamic considerations, Kuo (1965) found that for a typical tropical atmosphere convective element, only about twenty-five percent of the initial moisture source would be used in net latent heat release. Braham (1952) found that thundershowers of "nonsevere type" rained out about ten percent of the incoming water vapor, while Newton (1967) found that the severe thunderstorm precipitated out fifty percent of the incoming moisture. In a developing synoptic disturbance, n could be increasing with time since the most severe convections generally occur in the mature stage of the disturbance.

The latent heating rate (°C/S), Q_L, in the case of the above moisture condensation formulation is then

$$Q_L = -k_1\omega_b$$

$$k_1 \equiv \begin{cases} n q_b L(P_0/p)^{R/c_p}/c_p \Delta p & \text{if } \omega_b < 0 \\ 0 & \text{if } \omega_b > 0 \end{cases} \tag{110}$$

To apply this parameterization, a transformation for vertical motion at the top of the boundary layer from xyz to pressure coordinates is needed. The hydrostatic relationship in the xyz coordinate system for steady flow implies that

$$\omega = \frac{dp}{dt} = \vec{V}\cdot \nabla_H p - \rho g_w \quad . \tag{111}$$

Using the geostrophic wind relationship, the ratio of the two terms on the right-hand side is

$$|\vec{V} \cdot \Delta p/-\rho g w| = |v\beta y U_g/g_w| \quad .$$

Various numerical experiments discussed in chapters 5 and 8 indicated that this ratio is $\lesssim 10^{-2}$. Burger showed that this ratio is small when the Froude number is small compared to the Rossby number. For $H = 2$ km, $L = 500$ km, and $f = 10^{-5}\ s^{-1}$, the ratio of the Froude number to the Rossby number is approximately 3.5×10^{-2}. It then appears that the horizontal pressure advection term can be ignored to a first approximation so that

$$\omega = -\rho g w \quad .$$

Numerical experiments in chapter 5 indicated that a reasonable approximation to vertical motion at the top of the ordinary boundary layer is of the form

$$W_b = C v_y H \quad .$$

C is a constant and v_y is the divergence at H, the top of the boundary layer. In pressure coordinates

$$\begin{aligned} \omega_b &= k_2 v_y \\ k_2 &= \rho g CH \end{aligned} \tag{112}$$

where $k_2 > 0$ and ρ is the density at the top of the boundary layer.

The thermodynamic equation (108) can be written in the form

$$v\hat{\phi}_y + Sv_y = -R\Delta p(Q + Q_L - \omega_b \theta_p)/\bar{p}(p_0/\bar{p})^\kappa \tag{113}$$

where Q_L is the convective latent heating term and Q is the sum of the other diabatic heating terms. Using the above formulation for convective latent heat release, (110) and the formulation for W_b (112), and rearranging the terms,

$$\begin{aligned} v\hat{\phi}_y + \hat{S}v_y &= -R\Delta pQ/\bar{P}(P_0/\bar{p})^\kappa \\ \hat{S} &\equiv S[1 + k_2(1 - k_1/|\theta_p|)/\tfrac{3}{8}\Delta p] \quad . \end{aligned} \tag{114}$$

S can be viewed as a reduced geopotential thickness, modified to include the above boundary layer influences. Consequently, the main influence of the ordinary boundary layer can be thought of as merely changing the reduced thickness or the stability parameter of the free atmosphere layer. When convective latent heat release exceeds boundary layer induced adiabatic cooling ($k_1 > |\theta_p|$) so that rising motion out of the boundary layer causes net heating, then $\hat{S} < S$ or the reduced geopotential thickness is decreased.[11] Conversely, this reduced thickness is increased when boundary layer rising motion induces net cooling ($k_1 < |\theta_p|$).

It is then expected that in a drift-ordinary boundary layer regime, the primary role of boundary layer forcing of the free atmosphere (in terms of mass and latent heat fluxes) is essentially limited to modifying the pressure gradient magnitude without changing the basic character of the pressure field. This role appears to be subordinate to the role of the mid-latitude and quasi-Ekman boundary layer. For example, Sutcliffe (1947) demonstrated that low level divergences strongly influence the troposphere wind and pressure fields in the development of mid-latitude synoptic scale disturbances.

6.7 Summary of Free Atmosphere Flow Characteristics

The longitudinally symmetric pressure field of the unforced free atmosphere flow adjusts so that the frictionless flow is quasi-nondivergent and the zonal flow component is quasi-geostrophic even in the presence of cross-equatorial flow. This tendency is strongest for layers with large static stability. Flow towards higher pressure results in decreased ageostrophic

---

[11] Note that sufficiently large boundary layer induced net heating could cause $\hat{S}$ to become negative. Typical values of the appropriate parameters indicate that this can occur only when the thermal stability becomes very small in which case the thermodynamic-continuity equation (108) approaches a singularity. This case will not be considered in this study.

components while flow towards lower pressure becomes more ageostrophic. On the other hand, thermal forcing can produce appreciable horizontal flow convergence, since horizontal temperature advections are small at low latitudes so that diabatic heating must be balanced by adiabatic cooling. Heating near the equator can also produce significant zonal ageostrophic flow.

In contrast to the Ekman boundary layer, the main effect of the ordinary boundary layer may be thought of as merely altering the stability parameter of the free atmosphere layer, and hence may not appreciably affect the basic character of the free atmosphere wind and pressure fields.

7. THE COUPLED NUMERICAL MODEL

In this chapter, a modified one-layer numerical model of the free atmosphere is added to the boundary layer numerical model constructed in chapter 4. In this coupled model, the free atmosphere layer induces a pressure field on the boundary layer flow which can in turn alter the pressure field through vertical fluxes of mass, momentum, and in a special experiment, latent heat.

The one-layer numerical model of the free atmosphere is essentially a finite-difference version of the one-layer model of chapter 6. The primary difference is that the frictionless equations of motion of the coupled model are evaluated at the mean pressure level of the layer while the velocities at the bottom of the layer are given as those at the top of the boundary layer numerical model. The rest of the basic features of the two free atmosphere models are the same. The free atmosphere layer again extends from 800 mb to 500 mb. The horizontal flow components and horizontal pressure gradients are assumed to decrease linearly with height and vanish at the top of the layer so that the geopotential gradient of the 500 mb surface remains zero.

The static stability is again approximately pseudoadiabatic as typically observed in the lower tropical troposphere. Both the pressure increment and static stability are varied in special experiments. The lower pressure surface of the free atmosphere layer is always 800 mb to correspond to the approximate top of the boundary layer numerical model (2000 m).

7.1 Equations of the Free Atmosphere Model

In this section, the basic equations for the free atmosphere portion of the model are presented. The longitudinally symmetric equations of motion on an equatorial β-plane in pressure coordinates are

$$u_t + vu_y + \omega u_p = \beta yv \tag{115}$$

$$v_t + vv_y + \omega v_p = -\beta yu - \phi_y \tag{116}$$

where ϕ is again the geopotential of a constant pressure surface. The thermodynamic equation can be written in the form

$$\theta_t + v\theta_y + \omega\theta_p = Q_L + Q_R + Q \tag{117}$$

where Q_L is the latent heating term, Q_R is the net radiation heating term and Q is now the sum of the other diabatic heating terms. The heating terms are specified in chapter 8. Also needed are the mass continuity equation, the hydrostatic equation and equation of state:

$$v_y + \omega_p = 0 \tag{118}$$

$$\frac{d\phi}{dp} = -\alpha \tag{119}$$

$$p = \rho RT \cdot \tag{120}$$

With (119) and (120), an equation for geopotential thickness is derived

$$\Delta\phi = \int_{P_3}^{P_1} \left(\frac{RT(p)}{p}\right)dp \ . \tag{121}$$

We assume a linear decrease of temperature with pressure

$$T(p) = T_2 + \Delta T(p - P_2)/2\Delta p$$

$$\Delta T = T_1 - T_3, \quad 2\Delta p = P_1 - P_3, \quad P_2 = \frac{1}{2}(P_1 + P_3), \quad \Delta p > 0 \tag{122}$$

where temperatures are calculated using the potential temperature lapse rate and Poisson's relationship. This temperature profile and (121) implies

$$\Delta\phi = RT_2 \ln(P_1/P_3) + R\Delta T(1 - \frac{P_2}{2\Delta p}\ln(P_1/P_3)) \ . \tag{123}$$

For the range of values of the various parameters used in numerical experiments in chapter 8, the terms due to ΔT are $0(1\%)$ or less of the first term. Various numerical experiments verify that the neglect of this term results in very small changes in the pressure and wind fields. Given a reference geopotential height at the top of the layer (P_3), the geopotential at the other levels is calculated from (123).

We then have five unknowns with five equations at our disposal. Horizontal wind components are calculated from (115) and (116) and vertical motions are calculated from (118). Equation (117) and Poisson's equations yield temperatures from which geopotential thickness is determined with

(123). The geometry of this numerical model is illustrated in figure 29.

7.2 Finite Differencing of the Equations

A horizontally staggered grid system is used, where the continuity and thermodynamic equations are evaluated at half integer grid points, while the equation of motion is evaluated at integer grid points. The following relationships are needed:

$$(v_y)_{i+1/2} = (v_{i+1} - v_i)/\Delta y$$

$$(\phi_y)_i = (\phi_{i+1/2} - \phi_{i-1/2})/\Delta y$$

$$\omega_i = 1/2(\omega_{i+1/2} + \omega_{i-1/2})$$

$$v_{i+1/2} = 1/2(v_i + v_{i+1})$$

where Δy is the distance between two integer grid points equal to 50 km.

By evaluating the derivative portion of the advection term implicitly, the norm of the amplification matrix corresponding to the system of Fourier transformed linearized finite difference equations of motion is always less than unity; thus numerical stability is guaranteed and simple wave motions are partially damped (see appendix). The finite differenced equations of motion are then:

$$v_i^{n+1} = v_i^n + \Delta t \left\{ \frac{-v_i^n}{\Delta y} \delta_y v_i^{n+1} - \frac{\omega_i^n}{\Delta p} \delta_p v_i^n - \beta y_i u_i^n - (\phi_y)_i^n \right\} \qquad (124)$$

$$u_i^{n+1} = u_i^n + \Delta t \left\{ \frac{-v_i^n}{\Delta y} \delta_y u_i^{n+1} - \frac{\omega_i^n}{\Delta p} \delta_p u_i^n + \beta y_i v_i^n \right\} \qquad (125)$$

where n designates the time level, δ_y and δ_p designate upstream differencing (see chapter 4) in the y and p directions respectively and Δp is the increment between two pressure surfaces equal to 150 mb.

Although evaluating the Coriolis term implicitly may increase the stability of the system, it would also increase the matrix size by a factor of four, and, therefore, result in undue computational labor. Evaluating the vertical advection term implicitly would result in an additional contribution to the coefficient of v_i^{n+1} and, therefore, jeopardize the diagonal dominance of the system.

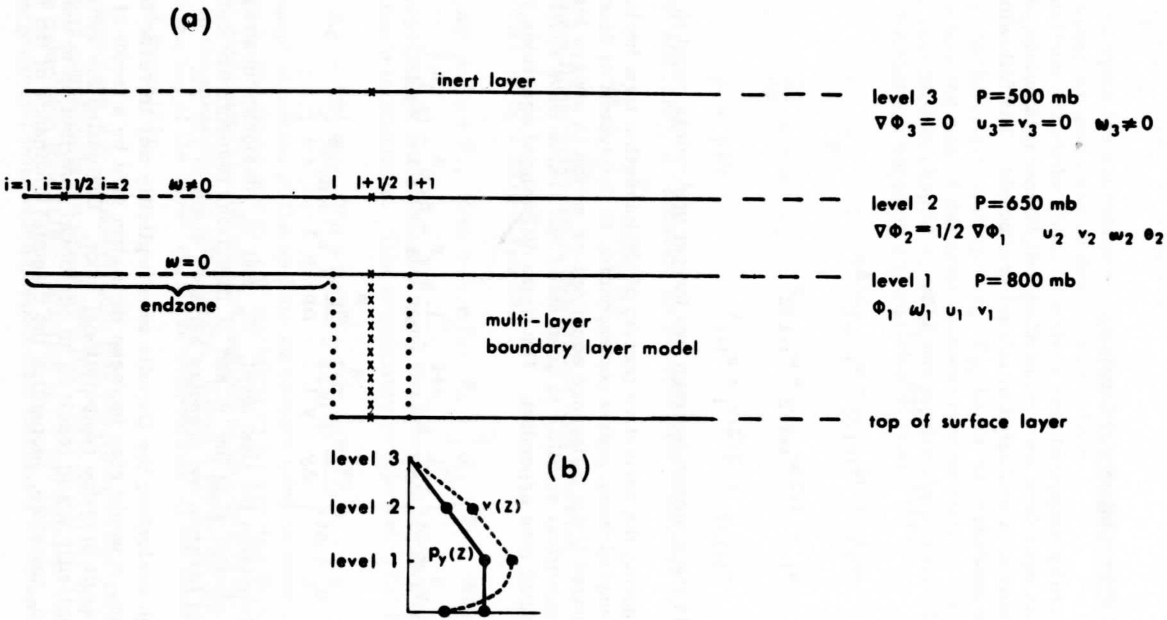

Figure 29. A portion of the coupled numerical model (a) and vertical profiles of typical wind speeds and the horizontal pressure gradient (b).

Equations (124) and (125) applied at the various grid points at level 2 result in the following matrix systems:

$$\begin{aligned} \underset{\sim}{G}\,\underset{\sim}{U}^{n+1} &= \underset{\sim}{H}\,\underset{\sim}{U}^{n} + \underset{\sim}{F} \\ \underset{\sim}{G}\,\underset{\sim}{V}^{n+1} &= \underset{\sim}{H}'\underset{\sim}{V}^{n} + \underset{\sim}{F}' \end{aligned} \quad , \qquad \underset{\sim}{U}^{n} = \begin{bmatrix} u_1^n \\ u_2^n \\ \vdots \\ u_{p-1}^n \end{bmatrix}$$

where P is the number of integer grid points at level 2. $\underset{\sim}{F}$ and $\underset{\sim}{F}'$ are composed of terms which do not involve u and v at interior grid points. Contributions from horizontal advection terms including u_1^{n+1}, u_p^{n+1}, v_2^{n+1} and v_p^{n+1}, which are known boundary velocities, also become part of $\underset{\sim}{F}$ and $\underset{\sim}{F}'$. $\underset{\sim}{G}$ is a tridiagonal matrix of the form

$$\underset{\sim}{G} = \begin{cases} [-V_i^n\Delta t/\Delta y, \quad 1 + V_i^n\Delta t/\Delta y, \quad 0] & \text{for } V_i^n > 0 \\ [0, \quad 1 - V_i^n\Delta t/\Delta y, \quad V_i^n\Delta t/\Delta y] & \text{for } V_i^n < 0 \,. \end{cases}$$

A simplified matrix factorialization version of Gaussian elimination can be used to solve this matrix system so that the number of calculations per time step is approximately the same as would occur with a pure explicit scheme. Diagonal dominance of G (where the absolute value of the diagonal element is greater than the sum of the absolute value of the off-diagonal elements) guarantees that the solutions will remain bounded. This diagonal dominance condition for both sign cases of V is equivalent to

$$(1 + |V|\,\Delta t/\Delta y) > |V|\,\Delta t/\Delta y$$

so that diagonal dominance is absolutely guaranteed irrespective of the size of V, Δt and Δy.

The differenced continuity equation is

$$\omega_{i+1/2,\,2} = \omega_{i+1/2,\,1} - \frac{1}{2}[(v_y)_{i+1/2,\,1} + (v_y)_{i+1/2,\,2}]\Delta p \;.$$

The thermodynamic equation at level 2 uses an explicit scheme with forward differencing in time and upstream differencing for the horizontal advection term. A number of experiments indicate that using such an explicit scheme with the thermodynamic equation is slightly superior to using implicit schemes for both the thermodynamic equation and the equations of motion, at least in terms of suppressing inertia-gravity wave motions. Richtmeyer

(1967) found that $|V\Delta t/\Delta y| \leq 1$ is required for numerical stability for forward differencing in time with upstream differencing of advections.

The differenced thermodynamic equation (117) then becomes

$$\theta^{n+1}_{i+1/2} = \theta^{n}_{i+1/2} + \Delta t \left\{ \frac{-v^{n}_{i+1/2}}{\Delta y} \delta_y \theta^{n}_{i+1/2} - \omega^{n}_{i+1/2} (\theta_p)_{i+1/2} + Q \right\} \quad (126)$$

where δ_y again refers to upstream differencing.

7.3 The Use of Horizontal Diffusion in the Free Atmosphere Model

Horizontal temperature and momentum diffusion of the type $K_V \Delta^2_H \vec{V}$ and $K_\theta \nabla^2_H \theta$, or of a related form, are generally used to suppress wave motions in numerical models where the pressure and wind fields are coupled. While it is certain that smaller scale horizontal transfer processes not resolved by the grid system occur in the free atmosphere (Starr, 1968), it is not clear how well the above parameterizations of horizontal diffusion approximates these processes. As a result, the use of this type of diffusion will be minimized as much as possible in this numerical model.

Of course, some smoothing and damping is already present in the numerical model without explicit horizontal diffusion. A certain amount of smoothing results from the averaging of certain variables associated with the horizontally staggered grid system and truncation errors associated with the above finite difference schemes. Time damping resulting from the implicit character of the difference schemes does not alter the steady state solutions. However, various numerical experiments using conventional boundary conditions (specifying v or v_y and θ or θ_y at the side boundary) indicate that the above smoothing and damping is inadequate for dissipation of transient wave motions. "Averaging out" wave effects by taking mean values over a certain time period is made difficult by the fact that inertia-gravity waves found in the various numerical experiments have a range of periods up to a few days.

As an alternative to adding large horizontal diffusion, an attempt will be made to construct boundary conditions which minimize reflection and generation of wave motions in the free atmosphere model. Outside each of the normal side boundaries, a number of grid points have been added as is indicated in figure 29. These two horizontal zones of grid points are characterized by large coefficients of horizontal diffusion of temperature and momentum so that wave motions which are allowed to propagate freely through the normal side boundaries of the interior of the model (i.e., the model excluding the endzones), are dissipated in the endzones. Houghton and Jones (1969) success-fully used this method to dissipate vertically propagating gravity and accoustic waves. Zero horizontal derivatives of u, v, and θ are then specified only at the far ends of the endzones. It was found that the endzones dissipate wave motions without reflection to the extent that horizontal momentum diffusion can be omitted entirely in the interior of the model.

Recall from adjustment theory (chapter 6) that for unheated flow, the zonal components of the flow remain quasi-geostrophic even though the cross-isobar flow may be significant. As a result, horizontal diffusion is not used for the zonal flow component in the endzone so that it obeys the geostrophic balance of forces as much as possible and inertial-gravity wave generation is minimized. Two types of horizontal damping are used for both v and θ. Horizontal diffusion $K_v v_{yy}$ and $K_\theta \theta_{yy}$, are used to damp waves of small wavelengths while Rayleigh damping, $-K_{Rv} v$ and $K_{R\theta}(\theta-\theta_0)$, is used to damp large wavelength inertia-gravity waves.

In order to prevent wave reflection due to discontinuities in the diffusion terms at the normal boundaries, diffusion coefficients increase exponentially into the endzones (as was done in Houghton and Jones, 1969):

$$K_v = \bar{K}[\exp(-y'/\bar{y}) - 1]$$

where y' is the distance from the normal boundary and $\bar{y}$ is the width of the endzone. In all experiments $K_\theta(y) = \bar{K}_\theta[\exp(-y'/\bar{y}) - 1] + \hat{K}_\theta$ so that $K_\theta(y) = K_\theta$ in the model interior. A number of numerical experiments indicate that the following combination of values appears to be most effective in attenuating wave motions:

$\theta_0 = 280°K$ $\quad\quad$ $\bar{K}_V = 5 \times 10^5\ m^2/s$

$K_\theta = 5 \times 10^5\ m^2/s$ $\quad\quad$ $K_{RV} = 10^7\ s^{-1}$

$K_{R\theta} = 10^7\ s^{-1}$ $\quad\quad$ $\bar{y} = 10^6\ m$

$\hat{K}_\theta = 3.5 \times 10^6\ m^2/s$

Rayleigh damping of momentum and temperature prevents the development of significant pressure gradients and meridional flow in the high latitude portion of the endzones, although pressure gradients may become significant at the low latitude portion of the endzones (near the normal side boundaries of the interior of the model). However, experiments with larger latitudinal extent indicate that these pressure gradients are not a product of the endzone alone. At the normal boundaries, inflow into the interior of the model is generally less than .07 m/s although in certain experiments it is as high as .2 m/s.

7.4 Combining the Boundary Layer Numerical Model with the Free Atmosphere Numerical Model

In this section the boundary layer numerical model constructed in chapter 4 with minor alterations is coupled with the free atmosphere numerical model.

The continuity equation in the boundary layer numerical model and the calculation of stream function, now employ a height-dependent density

$$\rho(z) = \rho(0)e^{-z/H}$$

where $H = R\bar{T}/g$. Using $T = 295°K$ and noting that in the free atmosphere numerical model $\rho(800\text{ mb}) \simeq .965 \times 10^3\ g/m^3$

$$H = 8.45\text{ km}$$

$$\rho(0) = 1.22 \times 10^3\ g/m^3 .$$

Assuming a height-independent density and linear increase or horizontal convergence with height in the surface layer, the vertical motion at the top of the surface layer is

$$w'_{i,1} = \frac{50\text{m}}{4\Delta y}(v'_{i+1,1} - v'_{i-1,1}) \qquad (127)$$

where 50 m (j = 1) is the top of the surface layer and primes are used in this section to indicate variables calculated in the boundary layer numerical model. With the same assumptions we have

$$w'_{i,1\frac{1}{2}} = w'_{i,1} + \frac{\Delta y}{4\Delta y}\{\frac{3}{4}(v'_{i+1,1} - v'_{i-1,1}) + \frac{1}{4}(v'_{i+1,2} - v'_{i-1,2})\} \qquad (128)$$

To calculate vertical motions above $j = 1\frac{1}{2}$, the steady state compressible continuity equation is used

$$\nabla \cdot \rho\vec{V} = 0 .$$

Using centered differencing

$$w'_{i,j+1/2} = \frac{\rho_{j-1/2}}{\rho_{j+1/2}} w'_{i,j-1/2} + \frac{\rho_j}{\rho_{j+1/2}} \frac{\Delta z}{2\Delta y}(v'_{i+1,j} - v'_{i-1,j}) . \qquad (129)$$

At the top of the boundary layer numerical model, vertical motion is needed at half-integer grid points for use in the free atmosphere. To calculate this vertical motion with minimum truncation error, the above continuity equations are also numerically integrated directly between vertical columns of grid points instead of averaging $\omega'_{1,J}$ and $\omega'_{i+1,J}$.

To illustrate the flow in the $y - z$ plane, a mass stream function is defined

$$\psi_z = \rho v \quad .$$

Using centered differencing we have

$$\psi(0) = 0$$

$$\psi_{1\frac{1}{2}} = 150 \text{ m } \rho_{1\frac{1}{2}} v_{i,1}$$

$$\psi_{j+1/2} = \psi_{j-1/2} + \Delta z \, \rho_{1\frac{1}{2}} v_{i,j} \quad \text{for } j > 1 \quad .$$

In the boundary layer numerical model, K is constant from the surface to 500 m and then decreases linearly to ten percent of the maximum value at 1700 m, above which K is again constant. The top of the boundary layer model is at 2000 m which is intended to correspond to a typical height of the trade inversion from 0° to 10° latitude, as was discussed in the introduction. k_0 is equal to .74. Both K and k_0 are varied in special experiments in chapter 8. Zero horizontal wind shear is specified at the side boundaries of the boundary layer model. The vertical grid spacing is 200 m.

The horizontal pressure gradient force in the boundary layer is equal to that at the bottom of the free atmosphere layer so that

$$f(U'_g)_i \equiv (\phi_y)_{i,1} \quad .$$

The wind components at the bottom of the free atmosphere numerical model are given as those at the top level of the boundary layer numerical model (level J) as computed at the last boundary layer interaction

$$u_{i,1} = u'_{i,J}$$

$$v_{i,1} = v'_{i,J}$$

$$\omega_{i+1/2,1} = \omega'_{i+1/2,J}$$

Significant truncation errors result from the calculation of downward advections of momentum from the free atmosphere to the boundary layer since this calculation employs the crude grid increment between levels one and two of the free atmosphere. Furthermore, it is intended that the top of the boundary layer model in regions of subsidence corresponds to the trade inversion where vertical transports are expected to be small. Consequently, vertical advections of momentum downward from the free atmosphere model to the boundary layer model will be neglected. In actual numerical experiments, subsidence and the neglected downward vertical advections are quite small, as would be expected from scale analysis. Upward vertical advections of momentum from the boundary layer model to the free atmosphere model (which may be quite strong in heated areas) are retained. Vertical advections of momentum are not calculated in the endzones.

Referring to figure 29, the following matching conditions between the boundary layer and free atmosphere portions of the numerical model (discussed above) are applied.

$$\beta y_I (U_g)_I = (\phi_y)_{J,1} \qquad \text{for } i = I$$

$$\omega_{i+1.2,1} = \omega'_{i+1/2,J} \qquad \text{for } i \geq I + 1/2$$

$$\left.\begin{aligned} \beta y_i (U_g)_i &= (\phi_y)_i \\ u_{i,1} &= u'_{i,J} \\ v_{i,1} &= v'_{1,J} \end{aligned}\right\} \qquad \text{for } i \geq I + 1 \quad .$$

Initial conditions are in general zero velocities and zero horizontal pressure gradients. The time order of calculation is: 1) evaluation of the continuity equation to obtain vertical motion; 2) evaluation of the thermodynamic equation and calculation of the geopotential fields; 3) evaluation of the equation of motion at level 2; and then 4) in the boundary layer to obtain the wind field there (and hence at level 1).

The latitudinal positions of the side boundaries of the interior of the model vary according to the experiment. They are chosen sufficiently far from the equator so that heating is unimportant in the endzones and a quasi-Ekman region where advections are small is established in the boundary layer near each side boundary. Δy is chosen to be 50 km and Δt is approximately four minutes. Although a quasi-steady state is usually established after a real time of a few days, experiments are run for a real time period of about twenty-three days so that the flow is essentially steady state. After this time period, time accelerations relative to the maximum term are generally $\leq 1\%$. One exception is in regions where the flow and pressure gradient forces nearly vanish, in which case time accelerations may be as large as forty percent of the maximum term.

8. NUMERICAL SOLUTIONS GENERATED IN THE COUPLED MODEL

In this chapter, numerical experiments conducted with the numerical model developed in the preceding chapter are discussed. The flow is forced by specified heating fields in most of the experiments. Of primary interest is the influence of the boundary layer on the pressure field and the characteristics of the boundary layer corresponding to the adjusted steady state pressure field. The specified heating fields do not necessarily accurately describe heating fields associated with the ITCZ. However, it is intended that the problems studied in this chapter relate to the maintenance of a convergence zone in that the response of the pressure field to heating aloft and boundary layer forcing is examined.

The numerical experiments of this chapter can be divided into three basic types. First, heating fields are specified asymmetrically with respect to the equator (single convergence zone) so that cross-equatorial flow is generated. Second, heating fields are specified symmetrically with respect to the equator (convergence zone at the equator or a "double" convergence zone) so that meridional flow vanishes at the equator. Finally, in a special experiment the free atmosphere is heated mainly by latent heat release which is parameterized in terms of vertical motion at the top of the boundary layer numerical model. This experiment is then related to the CISK problem discussed in the introduction.

Heating fields centered about y_0 are specified according to the following general form

$$Q = \bar{Q}\, e^{-(y-y_0)^2/y_p^2}$$

where

$$y_p = 100 \text{ km}$$

$$\bar{Q} = 6\,^\circ\text{C/day} .$$

A heating field of this type was used by Holton (1971) in a study of a forced low latitude disturbance. In the prototype experiment, we chose $y_0 = 7^\circ\text{N}$ (which corresponds approximately to the mean spring ITCZ position in the North Pacific). This experiment is discussed in some detail while the subsequent experiments, listed in table 7, are discussed briefly with emphasis on differences with respect to the prototype experiment. In these subsequent experiments, y_0 will equal 0°, 4°N, and 10°N to study the influence of the convergence zone latitude. An experiment is also conducted where two simultaneous heating sources are centered at $y_0 = 5\frac{1}{2}$°N and $5\frac{1}{2}$°S. To simulate the possible importance of radiative cooling at the equator in a variation of this experiment, weak cooling is added of the form

$$Q = -.2\bar{Q}\, e^{-(y/y_p)^2} \;.$$

8.1 Heating Centered at 7°N

In this experiment, specified heating, centered at 7°N, generates a cross-equatorial flow which terminates at a low pressure convergence zone in the heated region. Consequently, many of the basic flow elements of this experiment were also present in experiments where pressure was specified asymmetrically with respect to the equator (chapter 5). However, in the present experiment, boundary layer vertical motions (such as occurred in boundary layer flow transitions of the experiments in chapter 5) are allowed to modify the pressure field and, hence, the resulting boundary layer flow.

The resulting steady state temperature and geostrophic wind fields are shown in figure 30. It is seen that the lowest pressure (highest temperature) occurs in the heated region, although a relative pressure minimum also occurs at the equator. The roles of the wind field in reference to the thermodynamic processes associated with this steady state temperature field are now discussed. The dynamics of the wind field are studied in subsequent sections.

Table 7

Latitudes of maximum heating and side boundaries of the interior portion of the model for numerical experiments of chapter 8

1. 7° N	7° S - 11° N
2. 10° N	4° S - 14° N
3. 4° N	10° S - 8° N
4. 0°	9° S - 9° N
5. $5\frac{1}{2}$°N, $5\frac{1}{2}$°S	9° S - 9° N
6. $5\frac{1}{2}$° N, $5\frac{1}{2}$°S (cooling at equator)	9° S - 9° N
7. latent heating	7° S - 11° N

a) The Thermodynamic Balance in the Free Atmosphere

Outside the heated area, the steady state thermodynamic balance is essentially between horizontal temperature advections, adiabatic heating, and horizontal temperature diffusion. Scale analysis (chapter 6) indicates that for small F (as in the case in the modeled free atmosphere of the experiments of this chapter), horizontal temperature advections must be small. In this experiment horizontal temperature advections, horizontal temperature diffusion, and adiabatic heating outside the heated region are at least two orders of magnitude smaller than the maximum specified heating. Then for nonzero thermal stability, vertical motions aloft must be small outside the heated area.

Although the net vertical motions at level 2 (650 mb) outside the heated region are indeed small, figure 31 indicates that the horizontal convergences and divergences at a given level are not necessarily small. This is possible because the horizontal divergence changes sign with height so that the net horizontal mass divergence for a column is small. In contrast, recall that in the case of a latitudinally independent pressure gradient field, the horizontal divergence did not change sign with height in the drift-ordinary boundary layer flow, but increased with height throughout the boundary layer. The height dependence of the sign of the horizontal divergence in this experiment is related to the rapid latitudinal variation of the horizontal pressure gradient and the height dependence of the horizontal momentum advection $O(|\vec{V}|^2)$ and Coriolis $O(|\vec{V}|)$ terms. Figure 31 shows that the Coriolis terms and horizontal advections are relatively small in the lowest layers and increase with height. Consequently, in the lower part of the boundary layer, the influence of the pressure gradient term is large so that the horizontal adjustment scale of the flow to a fixed pressure field is small O(100 km). Therefore, weak low level convergence occurs in the vicinity of low pressure at the equator and immediately downstream from the equator where the cross-equatorial flow encounters a weak adverse pressure gradient. This convergence compensates for the divergence of the drift-like flow at higher levels. In contrast, the transition from quasi-Ekman flow to drift-ordinary boundary layer flow generated by a latitudinally independent pressure gradient (chapter 5) produced divergence at all levels at the equator.

In the drift flow above the boundary layer, the Coriolis term and horizontal advections are so large that the horizontal adjustment scale of the flow is large O(1000 km). Therefore, this drift flow is divergent even in the region where the flow encounters an adverse pressure gradient. However, the drift flow is reduced considerably from the case of constant horizontal pressure gradient. In other words, the adjusted pressure gradient reverses sign at the equator to control the cross-isobar mass flux in the drift region and, therefore, control the amount of mass convergence in the convergence zone.

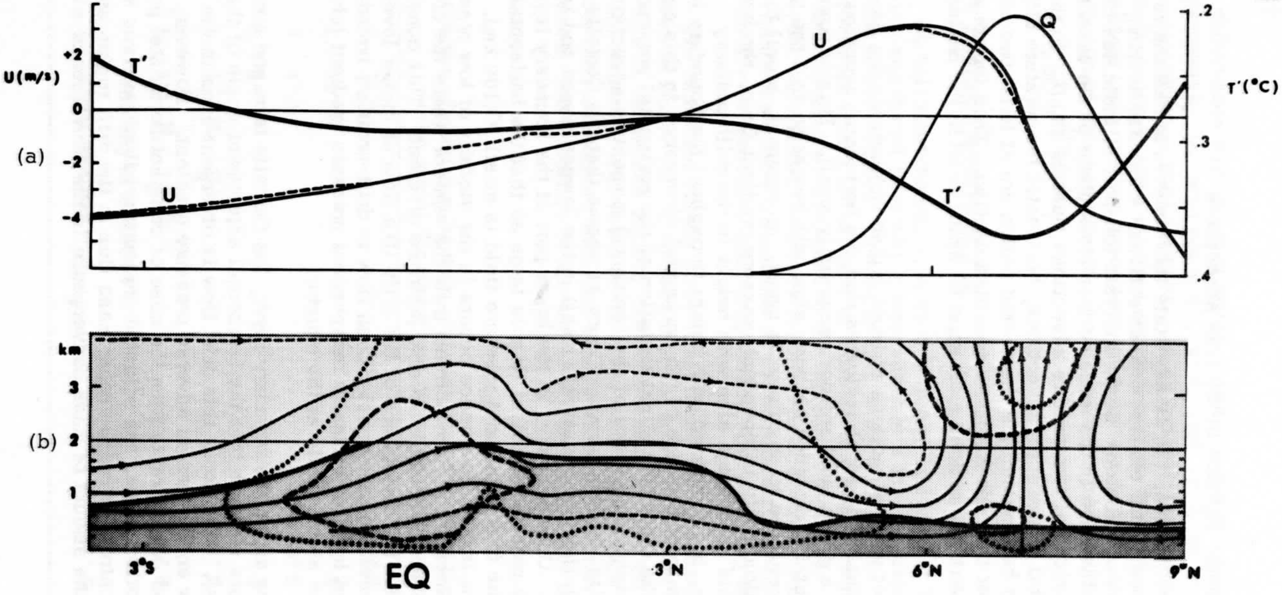

Figure 30. Heating, temperature, wind and relative "force" fields for the prototype experiment. (a) shows the heating field (Q) and temperature perturbation field ($T' = T_{650} - 280°$ K) at level 2 (650 mb) and the geostrophic (dashed line) and actual (U) zonal wind fields at level 1 (800 mb). (b) shows streamlines at increments of 3×10^5 g/ms with special dashed streamlines representing one-half the normal increment and .20 relative "force" isolines for the diffusion (solid line), vertical advection (dashed line) and horizontal advection (dotted line) terms. The top of graph b approximately corresponds to level 2.

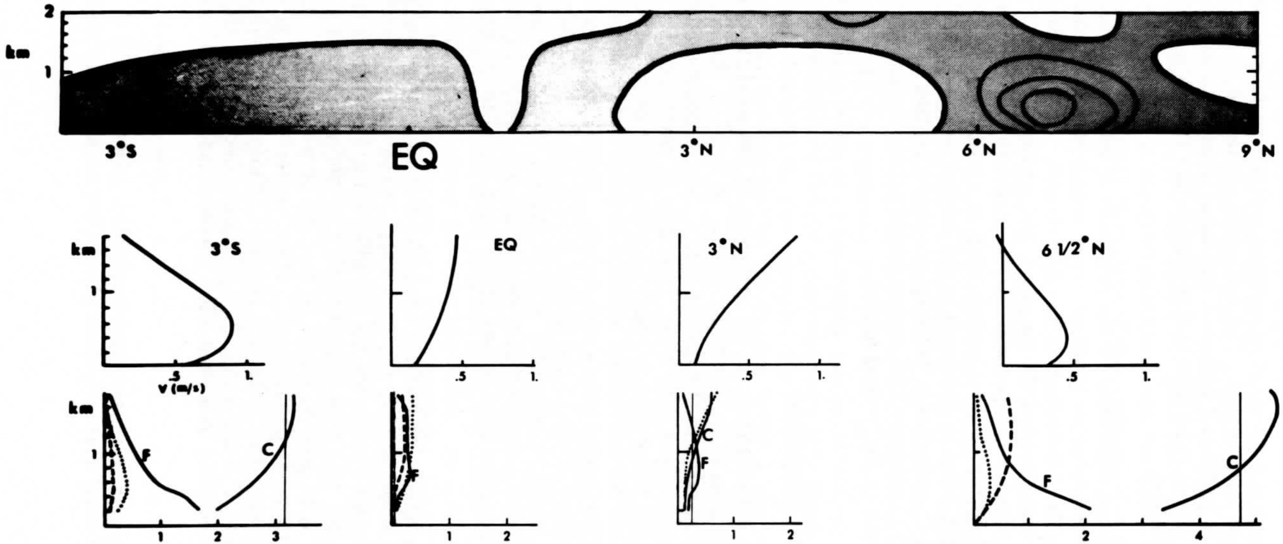

Figure 31. The horizontal divergence field (upper figure, increments of .4 × 10^{-5} s^{-1} where convergence regions are shaded), vertical profiles of meridional flow (m/s, middle row of figures) and vertical profiles of "forces" (10^{-5} m/s^{2}, lower row of figures) for the prototype experiment. The lower row of figures contains the diffusion (F), vertical advection (dashed line), horizontal advection (dotted line), Coriolis (C) and horizontal pressure gradient (thin vertical line) terms.

Above level 1, the horizontal pressure gradient and horizontal velocities decrease with height so that horizontal advections and the horizontal adjustment scale also decrease with height. Consequently, figure 30 shows that the weak meridional flow at level 2 reverses direction (producing weak convergence) immediately downstream from the equator where this flow encounters an adverse pressure gradient.

Therefore, the vertical variations of the response of the flow to horizontal changes in the horizontal pressure gradient cause strong vertical variations of the horizontal divergence in the drift region. In the unheated quasi-Ekman flows (directed toward the equator), the geostrophic wind decreases towards the equator to compensate for the increasing depth of the cross-isobar flow, and so the vertical motion aloft is small. On the other hand, large rising motion must be produced in the heated region, where the thermodynamic balance is essentially between specified heating and adiabatic cooling. Figure 31 indicates that strong convergence occurs in the lower levels in the center of the heated region.

b) The Free Atmosphere Wind Field

We will now focus our attention on the dynamics of the wind field above the boundary layer, and then in the boundary layer. At level 2, the easterly flow is quasi-geostrophic north of the heated region, while south of the heated region the flow resembles drift flow. The flow is never exactly drift or geostrophic due to the importance of vertical advections of momentum. These vertical advections are associated with the decrease of horizontal pressure gradients and horizontal winds with height. Small downward advections of lower momentum south of the heated region cause the flow to be somewhat weaker than would be predicted by drift theory. In the heated region, strong rising motion advects higher momentum from below to the extent that the vertical advection term is one of the main terms in the steady state balance.

In spite of the importance of vertical advections of momentum and the exchange of mass with lower levels, the flow south of the heated region exhibits many of the features predicted by the adjusted unforced drift theory (chapter 6). For example, this flow approximately conserves angular momentum. Furthermore, it is seen in figure 30 that the pressure field adjusts so that the zonal flow is quasi-geostrophic. Since easterly flow is advected on both sides of the equator (the horizontal pressure gradient reverses sign at the equator). North of 3° N the zonal flow and zonal geostrophic flow becomes westerly, corresponding to a weak high pressure ridge in the vicinity of 3° N.

The adjusted pressure field thus has the dual role of: 1) minimizing vertical motions outside the heated region while generating strong rising motion in the heated region, and 2) yielding a pressure field which enables the zonal flow to be quasi-geostrophic. This latter characteristic of the pressure field is particularly restrictive since the zonal flow is nearly independent of the pressure field in regions where vertical advections of momentum are small.[12]

c) The Boundary Layer Wind Field

The boundary layer was discussed above in terms of its divergence field in reference to the thermodynamics of the flow. In this section, other properties of the boundary layer flow are discussed. Since the occurrence of the basic boundary layer flow regimes in the case of cross-equatorial flow is not sensitive to the particular pressure field (as was evident in chapter 5), many of the basic features of the steady low level flow of this experiment are similar to those of the flow corresponding to a constant horizontal pressure gradient (chapter 5). For example, the flow towards the equator is Ekman-like to within a few degrees of the equator while in the vicinity of and downstream from the equator, ordinary-type boundary layer flow is established. Figure 30 shows that again both vertical and horizontal advections are important in the equatorial transition region while in the drift-ordinary regime generally only horizontal advections are important. Again, horizontal advections are generally larger than vertical advections and are of opposite sign.

Differences between the flow of this experiment and the flow of the constant horizontal pressure gradient case are primarily associated with the fact that the pressure gradient in this experiment reverses sign at the equator so that the flow crossing the equator encounters an adverse pressure gradient. For example, the adverse pressure gradient weakens the flow so that horizontal flow advections are less important. As a result, the transition to quasi-Ekman flow occurs at a lower latitude. Since this transition is located upstream from the heated region, it is gradual so that resulting vertical motions and vertical momentum advections are small. In this transition, the vertical distribution of meridional flow and the importance of horizontal advections gradually changes from increasing with height to reaching a maximum in the boundary layer interior and vanishing aloft (quasi-Ekman flow). When stronger heating is specified so that stronger flow is generated, the drift-ordinary boundary layer flow extends to the heated region where a more abrupt transition occurs and the pressure depression is less intense. In the constant

---

[12] Consequently, horizontal temperature diffusion does not appear to have a major influence on the steady state pressure field in this experiment.

pressure gradient case, the flow crossing the equator is characterized by backing until the transition to Ekman-like flow at higher latitudes. However, in this experiment veering occurs in the lower layers downstream from the equator where the flow is weakened by the adverse pressure gradient so that advections are locally quite small. Weak backing still occurs in the upper portions of the boundary layer in this region.

The boundary layer depth in the vicinity and downstream from the equator, as determined by the relative importance of the diffusion term, is large compared to the constant pressure gradient case. This occurrence could be related to the fact that in this experiment, (i) rising motion (and advections of lower momentum) instead of subsidence is established in the boundary layer near the equator, and (ii) flow strength and associated advections are weaker.

The depth of the vertical inertial boundary layer at the equator is somewhat deeper in this experiment compared to the constant horizontal pressure gradient case which may be related to the deeper frictional boundary layer depth at the equator. Recall that results in earlier sections suggested that the depths of the vertical inertial boundary layer and frictional boundary layer were strongly interdependent at the equator.

Figure 31 shows that in the adverse pressure gradient region (beginning at the equator), the diffusion term reaches a maximum in the interior of the boundary layer instead of near the surface. This behavior is related to the unusual vertical distribution of wind speeds associated with the adverse pressure gradient. In fact, figure 31 shows that $v_{zz}/v > 0$ in the lower layers so that the flow is accelerated by the diffusion term. At higher levels, v_{zz}/v vanishes and then becomes negative. Inflection points, where v_{zz} reverses sign, often occur when simple viscous flows are decelerated by adverse pressure gradients (Schlichting, 1968). Sometimes the flow is decelerated to the extent that flow separation (low level back flow) results. However, the adverse pressure gradient does not quite cause flow separation in this experiment since the Coriolis term, not present in the classical flow separation case, enables the low level flow to overcome the adverse pressure gradient. In fact, in the upper portions of the boundary layer the meridional flow is accelerated by the Coriolis term which is larger than the adverse pressure gradient by a factor of about two.

Figure 30 shows that the frictional boundary layer depth decreases rapidly downstream from the adverse pressure gradient region. Here the flow is now accelerated by the pressure field so that horizontal flow advections are large and the relative importance of the diffusion term is small. Figure 31 shows that an inflection point also occurs immediately upstream from the convergence zone in the Ekman-like flow, except now the flow is accelerated by the diffusion term above the inflection point. This occurrence can be attributed to the fact that the meridional low level flow is accelerated by the pressure gradient field while the meridional quasi-drift flow aloft is decelerated by Coriolis forces and upward vertical advections of lower momentum. The boundary layer depth reaches a slight relative maximum in the heated area which may be related to the presence of upward advections of lower momentum.

Finally, it might be mentioned that the height dependence of the low level horizontal flow convergence complicates the relationship of the vertical motion at the top of the boundary layer to the pressure field and the wind field aloft. For example, the parameterizations of this vertical motion in terms of the flow divergence above the boundary layer (chapter 5) is no longer valid in this case where the sign of the horizontal pressure gradient changes with latitude.

In conclusion, the flow of this experiment exhibits a number of significant kinematic and dynamic differences from the flow of the constant pressure gradient case. However, the same basic flow regimes and transitions occur in both cases.

8.2 Heating Centered at Other Latitudes

In the following two experiments, the specified heating fields are centered at a lower latitude (4° N) and at a higher latitude (10° N). Of particular interest are the effects of this latitudinal change on the transition from drift flow to quasi-geostrophic-Ekman flow. It will also be seen that this latitudinal change results in basic changes of the thermodynamic role of the boundary layer.

Figures 32 and 33 illustrate the steady state pressure and wind fields corresponding to heating fields centered at 10° N (experiment 2) and 4° N (experiment 3), respectively. In both cases a very weak relative pressure minimum occurs at the equator. However, in the former case, the specified heating is also associated with a very weak pressure minimum while in the latter case it is associated with a strong pressure minimum which is more intense compared to the case of maximum heating at 7° N.

This behavior of the steady state pressure field is related to the fact that the ability of the boundary layer to produce vertical motion in a convergence zone is inversely proportional to the latitude of the convergence zone. For example, the depth of the cross-isobar flow in the quasi-Ekman regime north of the convergence zone is inversely proportional to the square root of latitude. Furthermore, the frictionless cross-isobar flow directed toward higher latitudes in the drift regime is eventually deflected by the Coriolis influence with increasing latitude. When heating is centered at 7° N and 10° N, convergence is produced by the impingement of two quasi-Ekman

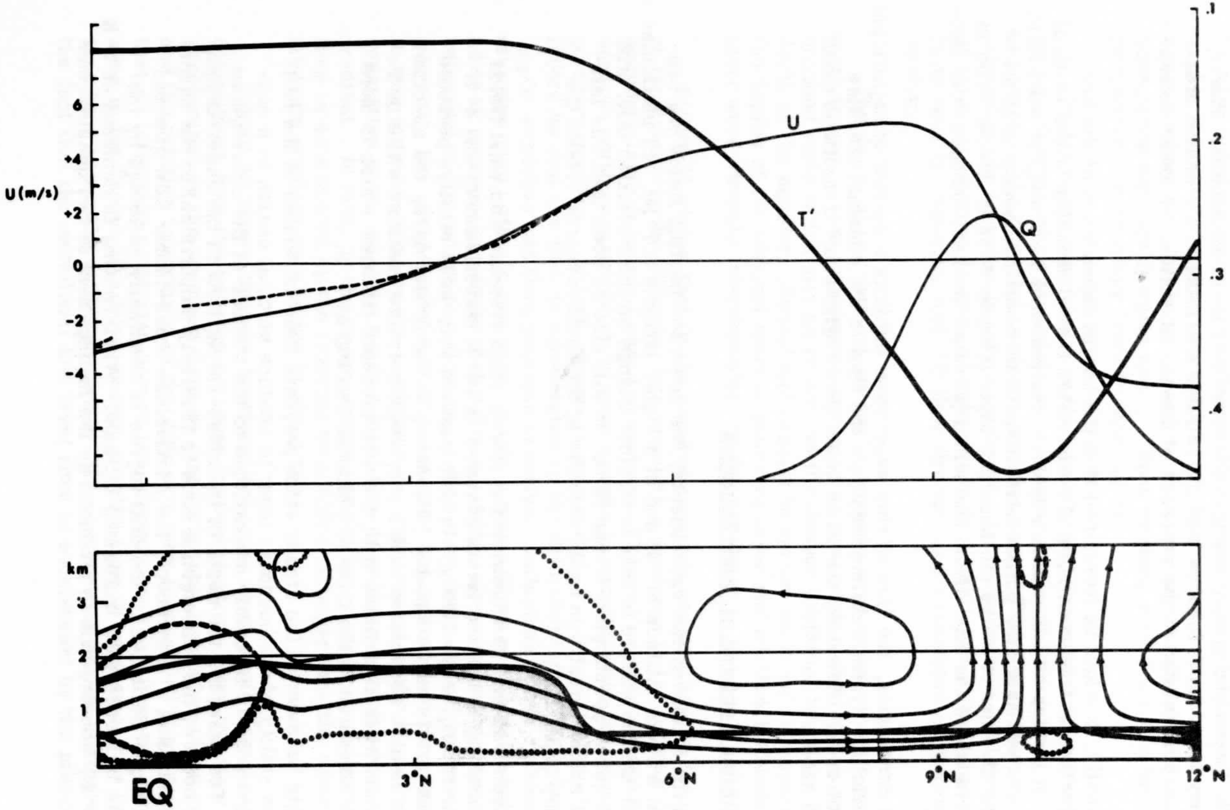

Figure 32. Heating, temperature, wind and relative "force" fields for experiment 2. See figure 30 for further explanation.

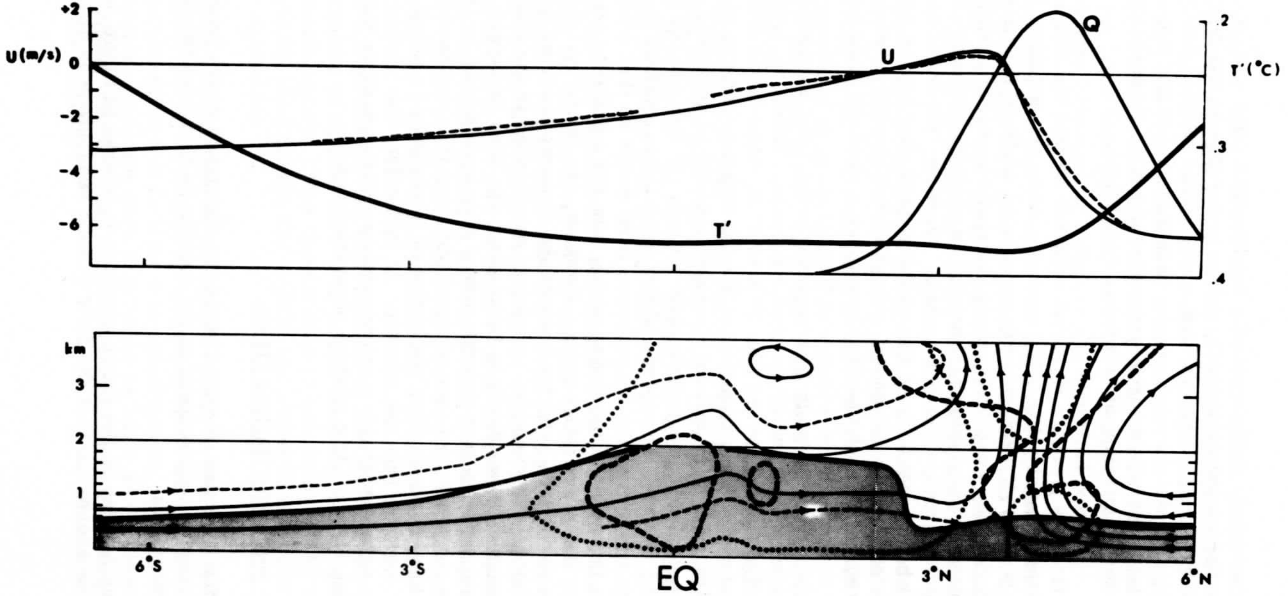

Figure 33. Heating, temperature, wind and relative "force" fields for experiment 3. See figure 30 for further explanation.

flows. On the other hand, in the case of a convergence zone at 4° N, the termination of the deep layer of northerly cross-isobar flow in the drift region produces sufficient vertical motion without a significant relative pressure minimum. In summary, the pressure system near a given heating field is less intense at lower latitudes where the boundary layer can more easily induce vertical motions in the presence of cross-equatorial flow.

At the same time the pressure field has adjusted so that the zonal frictionless flow is quasi-geostrophic. For example, when the specified heating is moved from 7° N to 10° N, the westerly zonal wind south of the convergence zone (which approximately exhibits a constant angular momentum profile) is stronger. The westerly zonal geostrophic wind is similarly stronger corresponding to the more intense pressure system. However, the frictionless zonal flow is just barely westerly as the northerly drift flow approaches the convergence zone at 4° N. Analogously, the geostrophic wind is weak westerly in this region since the heating generates a weak pressure minimum.

Figure 32 shows that the basic flow regimes in the case of maximum heating at 10° N are similar to those of the prototype case. However, when the center of the heating field is moved from 7° N to 4° N, some basic changes in the boundary layer regimes are observed. The convergence zone is now close enough to the equator to prevent the establishment of an extensive drift-ordinary or quasi-Ekman boundary layer regime. In fact, in the presence of stronger heating at 4° N, the regions of low level rising motions in the vicinity of the equator and in the convergence zone merge so that both advection terms are important in the entire region from the equatorial boundary layer transition to the convergence zone. However, the boundary layer downstream from the equator still exhibits many of the features observed in the prototype experiment. For example, veering is established in the lower layers and the boundary layer depth is large where the flow is decelerated by the adverse pressure gradient and thin where it is accelerated by the pressure gradient force. It can then be concluded that the most important boundary layer changes occur when the center of the heating is moved within approximately 5° latitude from the equator. In particular, the heating field may no longer be associated with a strong pressure minimum since the boundary layer can more readily produce mass convergence.

8.3 Equatorially Symmetric Heating Fields

In this section a number of experiments are discussed where heating is specified symmetrically with respect to the equator so that meridional flow vanishes at the equator.

The specified heating of the fourth experiment, shown in figure 34, is centered about the equator so that the flow in each hemisphere is directed toward the equator. Recall that an equatorially even symmetric pressure field corresponding to a constant geostrophic wind with low pressure at the equator (chapter 5) generated intense rising motion at the equator. Figure 34 shows that the pressure field adjusts so that the geostrophic wind magnitude decreases toward lower latitudes and vanishes at the equator. As a result, boundary layer induced rising motions are not as concentrated at the equator so that adiabatic cooling balances the specified heating.

At higher latitudes, where heating is weak, the geostrophic wind magnitude decreases very slowly toward the equator to compensate for the increasing depth of the quasi-Ekman cross-isobar flow toward the equator. Thus, vertical motions and adiabatic heating are small in this region.

Since the geostrophic wind varies slowly with latitude away from the equator, the boundary layer flow is similar to the constant geostrophic wind case (chapter 5). For example, the importance of both advection terms in this experiment is again limited to within a few degrees of the equator so that the boundary layer flow towards the equator is quasi-Ekman except near the equator.

Similarly, the zonal flow aloft is quasi-geostrophic except in the vicinity of strong heating near the equator where it is super-geostrophic due to horizontal advections. At level 2, upward advections of higher zonal momentum are also important near the equator.

In the fifth experiment, the equatorially symmetric heating field, shown in figure 35, is characterized by maxima at $5\frac{1}{2}$ ° latitude on both sides of the equator. Recall that a pressure field corresponding to a constant geostrophic wind with high pressure at the equator (chapter 5) generated significant subsidence at lower latitudes. However, in the adjusted flow, vertical motions (adiabatic heating) and horizontal flow divergences must be small outside the heated area. Since the flow vanishes at the equator, the flow is then very weak between the equator and the heated region.

In the heated region, convergence is then essentially produced by the deceleration of equatorward flow (which is quasi-geostrophic-Ekman approaching the heated region). This deceleration is accomplished by a rapid decrease of geostrophic wind toward the equator and strong upward vertical advections of lower momentum.

Since convergence in the heated region is produced solely by the equatorward flow, large horizontal pressure gradients are required at higher latitudes to generate sufficient flow for this convergence. As a result, the high latitude geostrophic winds are more than twice as large as compared to previous cases where rising motion in the convergence zone was produced by the convergence of two distinct flows.

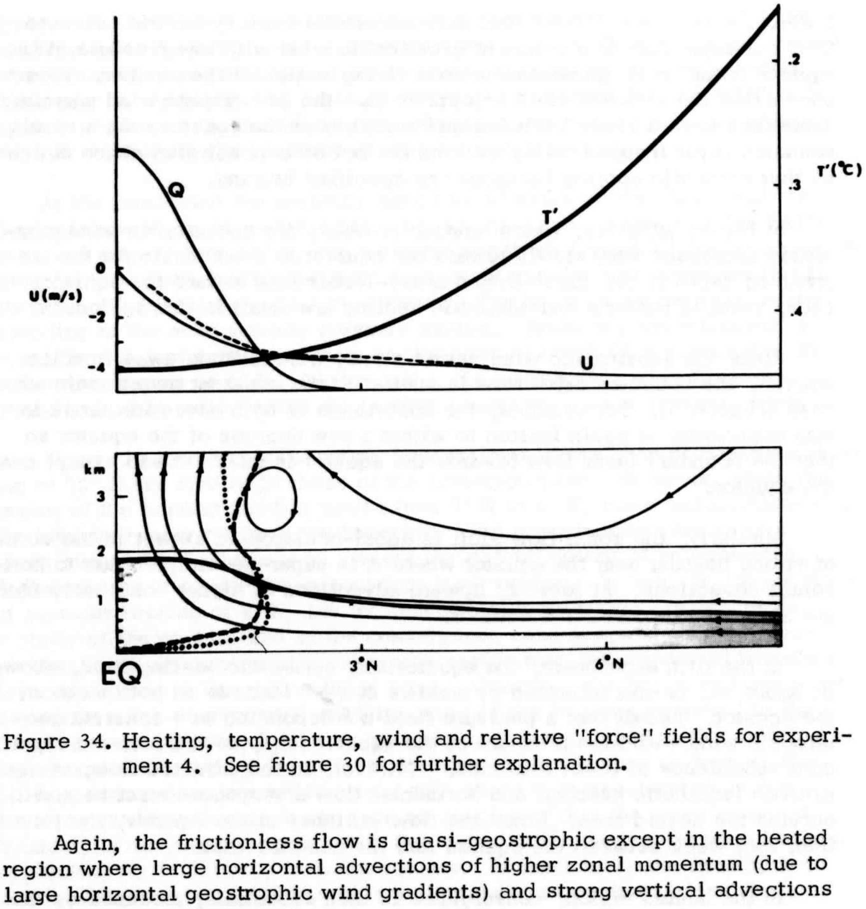

Figure 34. Heating, temperature, wind and relative "force" fields for experiment 4. See figure 30 for further explanation.

Again, the frictionless flow is quasi-geostrophic except in the heated region where large horizontal advections of higher zonal momentum (due to large horizontal geostrophic wind gradients) and strong vertical advections of momentum are important.

In the sixth experiment, cooling, centered about the equator, is added to the above heating field to simulate equatorial radiative cooling (see figure 36). As was mentioned in chapter 5, Zipser (1970) has suggested that tropospheric radiational cooling could be responsible for the observed cloud-free areas in the vicinity of the equator. The adjusted pressure gradients and winds in this experiment still vanish at the equator. However, in contrast to the previous case, a relative pressure maximum now occurs at the equator where divergence (adiabatic warming) is established. A weak pressure minimum now occurs in the heated regions generating a convergence of

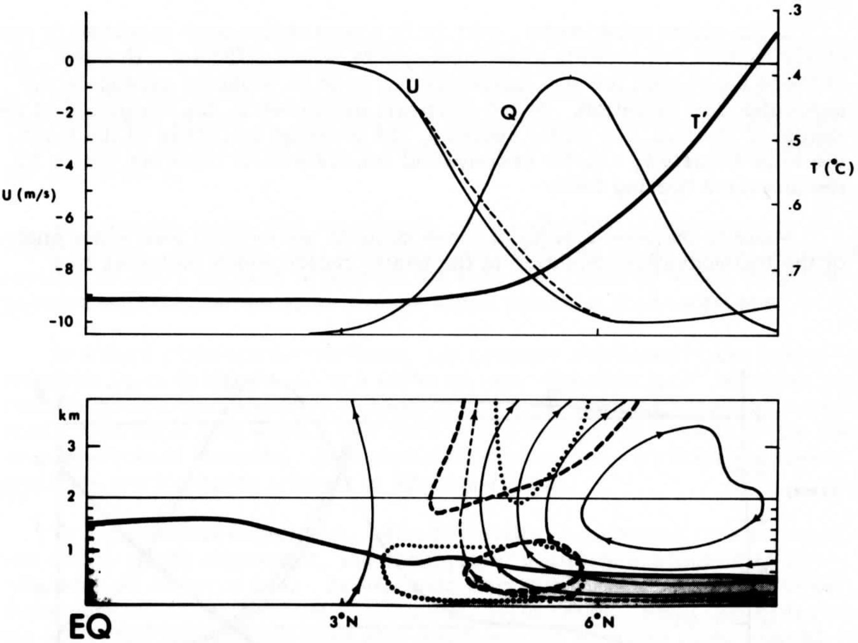

Figure 35. Heating, temperature, wind and relative "force" fields for experiment 5. The temperature perturbation scale is condensed by a factor of two from previous figures and streamlines are in increments of 6×10^5 g/ms (instead of 3×10^5 g/ms). See figure 30 for further explanation.

two flows. Consequently, somewhat weaker flow and pressure gradients are required at higher latitudes compared to the preceding experiment.

In summary, equatorially symmetric heating fields generate quasi-Ekman flows toward the equator which terminate in the heated region. In the case of two heating fields symmetric about the equator, the flow is weak equatorward from the heated area. The convergence in the heated region is then essentially produced by the flow from higher latitudes so that stronger pressure gradients are required at higher latitudes (compared to previous cases).

8.4 Variations on the Prototype Experiment

In the above experiments, certain flow parameters were specified to represent typical low latitude lower troposphere flow conditions. However, many of these parameters are not accurately known or in actuality depend on the particular flow situation. In the following experiments, the magnitude of the specified heating, the static stability, the pressure thickness of the layer, the eddy diffusivity and the geophysical boundary coefficient are varied for the prototype heating field.

Many of the main effects of these changes are evident from scale analysis of the thermodynamic equation in the heated region which indicates that

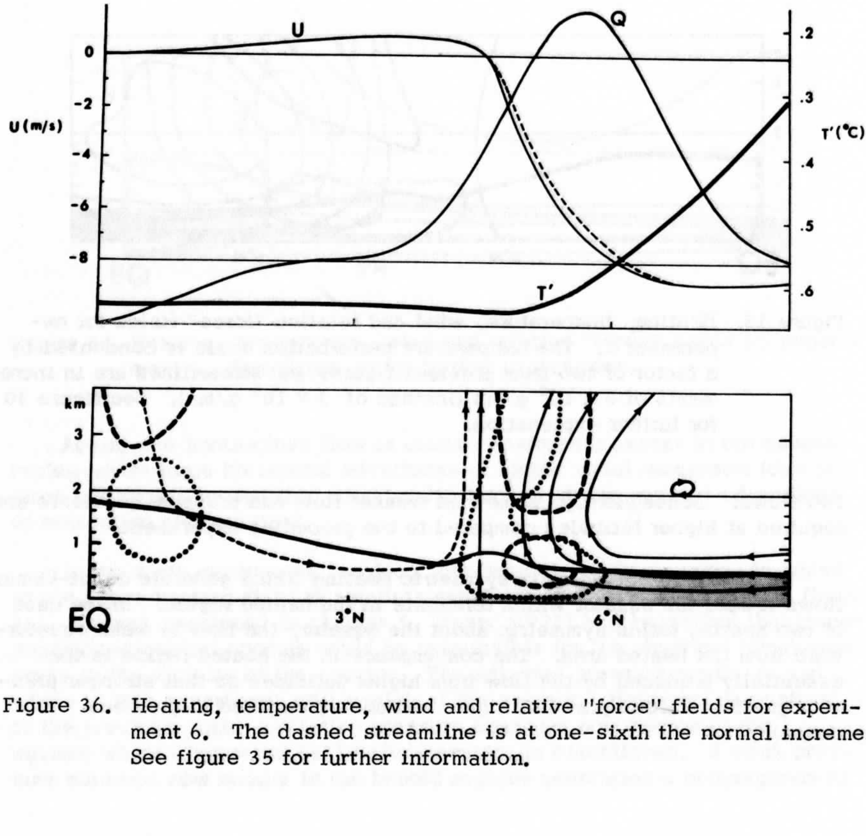

Figure 36. Heating, temperature, wind and relative "force" fields for experiment 6. The dashed streamline is at one-sixth the normal increment. See figure 35 for further information.

$$\omega\theta_p = Q \quad . \qquad (123)$$

Therefore, when heating is increased by a factor of two (variational experiment 1), vertical motions increase by approximately a factor of two which in turn requires increased horizontal pressure gradients. As expected from conclusions in chapter 5, this increase in horizontal pressure gradients and flow strength causes increases in the importance of advections of momentum and temperature.

In a second variational experiment, static stability is decreased by a factor of two. Equation (123) indicates that increased rising motion (adiabatic cooling) is again required to balance the specified heating, which in turn requires a more intense pressure system which occurs in this experiment.

In a third variational experiment, the pressure thickness of the free atmosphere layer is decreased by a factor of two. Equation (123) indicates that vertical motion aloft should not change appreciably from the prototype experiment. One might then expect that horizontal convergence strength in the free atmosphere must increase. As a possible consequence, horizontal pressure gradients are increased slightly in this experiment.

In a variational experiment, eddy diffusivity is increased by a factor of two and in a fifth experiment, the geophysical boundary coefficient is decreased by a factor of two. As expected from results in chapter 5, both of these changes cause increases in boundary layer depth. Small decreases in the horizontal pressure gradient also result so that boundary layer induced rising motion in the heated region is not increased even though the boundary layer depth increases.

All of the above variations of flow parameters resulted in changes in the intensity of the pressure gradient field. However, the same basic flow regions occurred in all of the experiments. Consequently, one can conclude that changes in the magnitude of these various parameters will incur quantitative, but not qualitative, differences in the resulting wind and pressure fields.[13]

8.5 Flow Forced by Parameterized Latent Heat Release

In this experiment, flow is generated by parameterized latent heat release instead of heating specified independent of the flow. Latent heat release (as formulated in chapter 6) is parameterized as the product of vertical motion at

---

[13] For this reason, no figures are shown in this section.

the top of the boundary layer and an efficiency factor k_1 . k_1 is in effect a measure of the efficiency of the system in converting fluxes of moisture from the boundary layer into latent heat release. Estimates of k_1 based on derivations in chapter 6 and various numerical experiments indicate that $k_1 \simeq 10^{-6}\,°\mathrm{K\,ms^2/g}$ appears to be an appropriate value for regions of strong convective activity. Riehl and Malkus (1958) proposed that intense convective elements ("hot towers") in the ITCZ were considerably more efficient in converting available moisture into latent heat release compared to other convective elements. Consequently, we encourage convergence zone development by choosing the following latitudinal dependence of the efficiency factor.

$$k_1 = \begin{cases} \bar{k}_1 + k'_1 \exp[-(y-y_0)^2/y_p^2] & \text{if } \omega_b < 0 \\ 0 \quad \text{if } \omega_b > 0 \end{cases}$$

where:

$$y_0 = 5°\,\mathrm{N}$$

$$y_p = 10^5\,\mathrm{m}$$

$$\bar{k}_1 = 5.5 \times 10^{-7}\ °\mathrm{K\,ms^2/g}$$

$$k_1' = 5.5 \times 10^{-7}\,°\mathrm{K\,ms^2/g}\ .$$

In addition to latent heat release, long-wave radiational cooling may also contribute to the net heating. Charney (1959) derived a linearized form of the radiation budget equation which assumes an isothermal atmosphere transparent to solar radiation and grey to terrestrial radiation, with an earth with zero heat capacity. This results in a Newtonian type cooling where the cooling rate is proportional to a deviation from a radiative equilibrium temperature,

$$Q_R = k_3(T^* - T)$$

$$k_3 \equiv 4g\gamma(2-\gamma)\,\sigma T_m^3/2\bar{P}$$

where γ is the long-wave absorbitivity of the atmosphere and σ is the Boltzmann constant. Employment of the above formula yields $k_3 \simeq 10^{-6}\ \mathrm{s^{-1}}$. This value results in very small cooling effects in various numerical experiments where the initial temperature was assumed to be the radiative equilibrium temperature. Charney (1968) found that the above approximation resulted in very long-wave radiational cooling effects in an ITCZ numerical model.

While the above formulations of heating may be more closely related to the problem of CISK than the a priori specification of a heating distribution, a number of possible elements of CISK are still not considered. For example, Charney (1968) suggested that the height of boundary layer convergence is important since moisture decreases rapidly with height in the lower layers. Longitudinal and temporal variations such as occur with propagation of waves along the ITCZ may be important elements of CISK in this region. Vertical variations of pressure fields and low level static stability may also be important. Rodenhuis (1971) theoretically demonstrated that low level stratification can sharply reduce CISK growth rates. Pike (1970), based on numerical modeling results, suggested that surface sea temperatures and related low level baroclinicity could influence the latitudinal position of the ITCZ.

As CISK develops, convection would become more intense and probably more efficient so that k_1 would increase, enhancing CISK development. On the other hand, Zipser (1969) and Riehl (1968) have illustrated that at low latitudes, latent heat release aloft and cooling at the surface due to downdrafts could significantly increase the static stability which would inhibit CISK growth in the later stages. At any rate, CISK appears to be a complicated instability even with the above incomplete list of influences.

Thus, an experiment with the above numerical model formulation of a CISK-like problem is only a first step toward understanding CISK in the ITCZ region. However, this experiment does reveal some interesting possible interactions between the boundary layer and the free atmosphere not possible in the case of heating specified independent of the flow.

The numerically computed temperature and heating fields after nine days are shown in figure 37. A disturbance, located at the maximum efficiency latitude, reaches maximum intensity at about ten days and vanishes by twenty days. The heating field of this disturbance, compared to the specified heating fields of the preceding experiments, is about thirty percent weaker and is more limited in latitudinal extent. However, due to the different thermodynamic role of vertical motion, the pressure depression is about three times more intense and generates rising motion which is five to ten times stronger.

The unsteady nature of the disturbance can be partially understood by considering the approximate thermodynamic equation in the heated region

$$\theta_t + \omega\theta_p = -k_1\omega_b .$$

Rearranging terms,

$$\theta_t = \omega(|\theta_p| - k_1\,\omega_b/\omega).$$

Net heating results from rising motion of $|\theta_p| - k_1 \frac{\omega_b}{\omega} < 0$. As the central pressure of the heated region decreases and rising motions become more

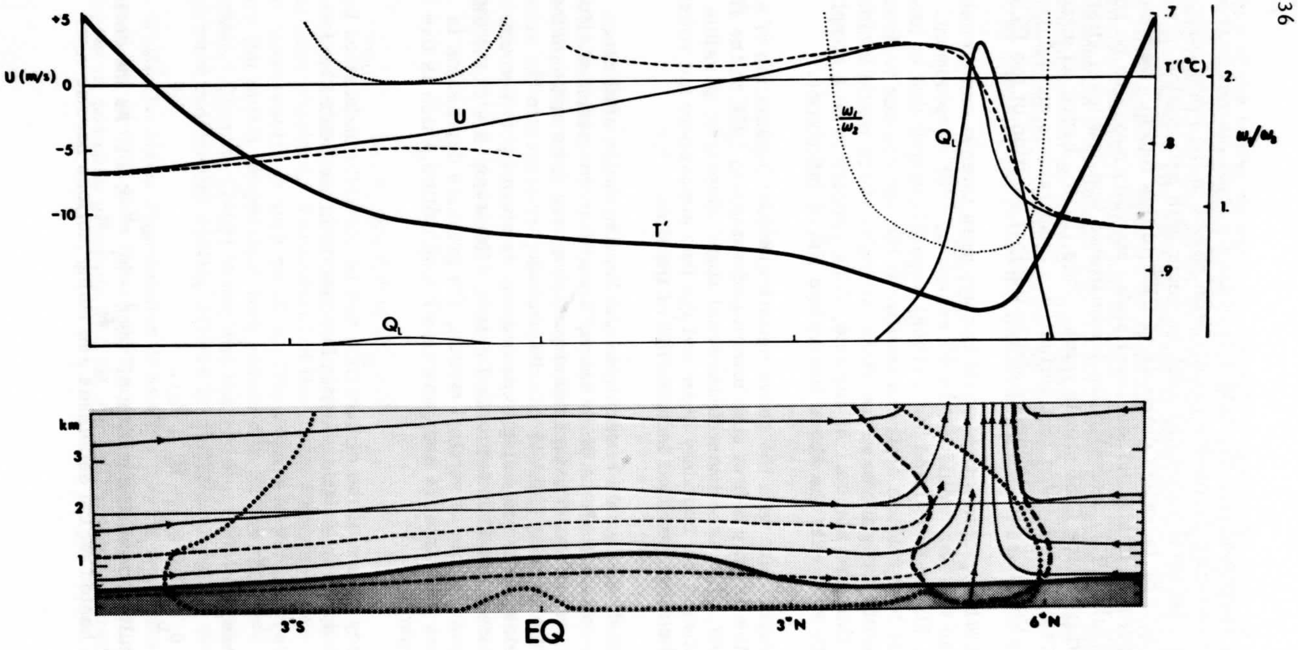

Figure 37. Latent heating (Q_L), temperature, wind and relative "force" fields for experiment 7. The dotted line indicates the ratio of vertical motion at level 1 to that of level 2. See figure 30 for further explanation.

intense, strong upward advections of lower momentum decrease the low level meridional flow and horizontal flow convergences in the heated region. However, in the upper portion of the disturbance, where velocities and pressure gradients decrease with height, upward vertical advections of higher momentum increase the horizontal flow and flow convergences. As a result, $|\omega_b/\omega|$ decreases and eventually net cooling results from the rising motion so that the disturbance decays. In fact, in experiments where the efficiency factor is less dependent on latitude, this mechanism dominates to the extent that the disturbance oscillates both temporally and spatially with a period of one to two days. Figure 37 shows that for the above experiment after nine days, $|\omega_b/\omega|$ reaches a minimum of about .67 in the center of the heated region where rising motion is strongest. Outside the heated region, the divergence reverses sign with height so that $|\omega_b/\omega|$ is larger than one. Weak subsidence occurs outside the heated region so that the thermodynamics of the flow is similar to the unheated regions of the specified heating experiments. With the exception of significant vertical advections at the equator, the basic characteristics of the various flow regimes of previous experiments are also evident in figure 37 for this experiment. This suggests that certain features of the flow in the equatorial lower troposphere (associated with momentum advections resulting from the latitudinal variations of the Coriolis parameter), may be understood by specifying heating or pressure independent of the flow.

9. CONCLUSIONS

While a number of influences on low latitude boundary layer flow have been neglected in this study, many features have been examined which are likely important elements of actual atmospheric low level flows near the equator. In particular, momentum advections associated with latitudinal variations of the Coriolis parameter may become important in various low latitude boundary layer situations. As a result, the influence of low level flow on low latitude free tropospheric circulations may be quite different than expected from Ekman theory. In fact, results in this study suggest that certain observed characteristics of these circulation systems may be related to vertical motion out of a boundary layer where momentum advections are important.

In certain simplified quasi-Ekman flows directed toward the equator, advection terms become important at a distance from the equator which is proportional to $(U_g/\beta)^{1/2}$. This distance for more generalized flows is usually less than 5° latitude for geostrophic winds parallel to the equator and of the order of 5° - 10° latitude when the geostrophic wind is directed toward the equator (in which case the advecting wind is stronger).

When flow crosses the equator or originates near the equator, an entirely different type of low level flow may be established downstream from the equator where horizontal momentum advections are large. In this flow, the rotation of the wind vector with height is relatively small and may even be in the opposite direction of Ekman rotation. The boundary layer depth is considerably smaller than predicted by Ekman theory, especially near the equator. This rotation and the boundary layer depth are both nearly independent of latitude. Cross-isobar flow usually increases with height, reaching a maximum in the drift flow at the top of the boundary layer where the pressure gradient force is balanced by Coriolis and horizontal advection terms. If the horizontal pressure gradient does not vary rapidly with latitude and is independent of height, the horizontal divergence similarly increases with height everywhere (as opposed to Ekman flow).

Where the flow is not thermally forced so that steady state vertical motions aloft must be small, the horizontal pressure gradient adjusts so that the horizontal divergence reverses sign with height. This is possible because the horizontal scale for the adjustment of the flow to a fixed pressure field, like the cross-isobar flow, increases with height. In fact, when the low level flow encounters adverse pressure gradients or is accelerated rapidly by the pressure field, an inflection point in the vertical profile of meridional flow may occur, giving rise to flow acceleration by the diffusion term below and above the inflection point, respectively. Flow separation does not occur since the Coriolis term, not present in the classical flow separation case, enables the meridional flow to overcome the adverse pressure gradient.

Since cross-isobar flow increases with height throughout this type of boundary layer and may be considerably stronger than the geostrophic wind, the transition from quasi-Ekman flow to this flow type in the vicinity of the equator produces significant subsidence for slowly varying horizontal pressure gradients. This generation of subsidence could be partially responsible for the cloud-free equatorial dry zone where it has been suggested that observed radiational cooling is balanced by adiabatic warming. If the flow is not thermally forced in this transition region, the adjusted horizontal pressure gradient may reverse sign with latitude in such a manner that the net divergence (adiabatic warming) is reduced. As a result, a relative pressure minimum may occur at the equator.

In the transition from the above flow to quasi-Ekman flow, strong rising motions may be produced by the decrease of strength and depth of the cross-isobar flow. Since these flow transitions are associated with the latitudinal variation of the Coriolis parameter, this rising motion can occur without a pressure minimum or even a decrease of the horizontal pressure gradient in the flow direction. Such a vertical motion-producing mechanism could be a component of the maintenance of the ITCZ. In this case, the ITCZ would then separate two entirely different kinds of low level flow regimes where horizontal momentum advections are important equatorward from the ITCZ and the flow is quasi-geostrophic-Ekman at higher latitudes.

When the flow is thermally forced, this transition may coincide with the heated region where the convergence of two flows are produced. At lower latitudes, where net cross-isobar flows are usually larger, a less intense pressure system is required to produce sufficient rising motion (adiabatic cooling) to balance a given heating distribution.

In the boundary layer transition regions, upward advections of lower momentum may increase the frictional boundary layer depth while downward advections of higher momentum may decrease this depth. However, other influences such as horizontal advections may also strongly influence the boundary layer depth. For example, in the transition to quasi-Ekman flow, the flow is decelerated and the importance of the diffusion term and the boundary layer depth increases.

The frictionless flow above the boundary layer can also be classified into two types: drift flow, where horizontal advections are important, and geostrophic flow. In the absence of strong heating, the pressure field adjusts so that the flow is quasi-nondivergent and the zonal flow component (which may approximately obey a constant angular momentum profile when vertical advections are small) is quasi-geostrophic.

The above tendencies are based on the study of longitudinally symmetric steady state flows on an equatorial β-plane. The inclusion of longitudinal and time variations would be obvious possible expansions of the above study. However, from a boundary layer point of view a number of other directions of concentration also appear to be of high priority. For example, there is considerable uncertainty about the vertical profile of eddy diffusivity and the validity of such a parameterization in situations of vanishing Coriolis parameter. The validity of expressing stress in terms of vertical mean wind shear in the presence of low level convective activity is similarly uncertain. Low level baroclinicity also likely modifies the dynamics and kinematics of both the mean and turbulent scales of low level flow. Observational evidence indicates that low level baroclinicity at low latitudes may also significantly influence both meso- and macro-synoptic scales of motion. Furthermore, boundary layer vertical motions may cause pressure adjustments in a stratified boundary layer. Finally, there is increasing evidence that interactions between low level flow and the underlying sea may be of major importance in understanding many circulation systems in the tropics.

APPENDIX

Stability Analysis of the Equations of Motion for the Free Atmosphere

The following stability analysis is for the finite differenced equations of motion of the free atmosphere layer (chapter 7, p. 108). These equations in the case $v_i^n > 0$, can be written in the form

$$(v_i^{n+1} - v_i^n)/\Delta t = -\frac{v_i^n}{\Delta y}(v_i^{n+1} - v_{i-1}^{n+1}) + F,$$

where F includes the Coriolis, pressure gradient, vertical advection, and horizontal diffusion terms. It can be easily shown that the numerical stability is independent of the sign of v_i^n. Linearizing the horizontal advection term, multiplying by Δt, defining $\hat{V} = V\Delta t/\Delta y$ and rearranging terms

$$(1 + \hat{V})\, v_i^{n+1} - \hat{V} v_{i-1}^{n+1} = v_i^n + F\Delta t \; .$$

Applying a Fourier transform in the y direction,

$$v_i^{n+1}[1 + \hat{V}(1 - \cos(k\Delta y) + i \sin(k\Delta y))] = v^n + F\Delta t \; .$$

The amplification matrix G (where $v^{n+1} - Gv^n + GF\Delta t$) is then

$$G = [1 + \hat{V}(1 - \cos(k\Delta y)) + i \sin(k\Delta y)]^{-1} \le 1 \; .$$

Therefore, this analysis indicates that numerical stability is guaranteed independent of $V\Delta t/\Delta y$.

ACKNOWLEDGMENTS

I wish to express appreciation to my professor, John Young, who offered many helpful ideas at various stages of this research. Special thanks are also due to Professors David Houghton, Heinz Lettau and Lyle Horn who contributed advice for the research and writing of the thesis. This research was supported by NOAA grant E-230-68-G and NSF grant GA 30676.

REFERENCES

Banks, W. H., 1965. The boundary layer on a rotating sphere, Quart. J. Mech. Appl. Math., 18, 443-54.

Bjerknes, J., and S. V. Venkateswaren, 1957. A model of the general circulation of the tropics in winter, Final Report, Large-Scale Synoptic Processes, Article III. Dept. of Meteor., U. of California, Los Angeles.

Blackadar, A. K., 1962. The vertical distribution of wind and turbulence exchange in a neutral atmosphere, J. Geophys. Res., 67, 3095-3102.

Bodewadt, U. T., 1940. Die Drehstrommung uber festem Grunde, Z. Angew. Math. Mech., 20, 241-53.

Boogaard, H. M. van de, 1964. A preliminary investigation of the daily meridional transfer of atmospheric water vapour between the equator and 40°N, Tellus, 16, 43-54.

Bowden, F. P. and R. G. Lord, 1963. Aerodynamic resistance to a sphere rotating at high speed, Proc. Roy. Soc., A 271, 143-53.

Braham, R. R., 1952. The water and energy budgets of the thunderstorm and their relation to thunderstorm development, J. Meteor., 9, 227-242.

Burger, A., 1958. Scale considerations of planetary motions of the atmosphere, Tellus, 10, 195-205.

Chang, C. C. and collaborators, 1969. Model study of tornado-like vortex, Technical Report, Dept. of Space Science and Applied Physics, The Catholic University, Washington, D. C.

Chang, Chih-pei, V. P. Morris and J. M. Wallace, 1970. A statistical study of easterly waves in the western Pacific, July-December, 1964. J. Atmos. Sci., 27, 195-201.

Charney, Jule G., 1959. On the theory of the general circulation of the atmosphere, The Rossby Memorial Volume, New York.

Charney, Jule G., 1963. Note on large-scale motions in the tropics, J. Atmos. Sci., 20, 607-609.

Charney, Jule G., 1968. The intertropical convergence zone and the Hadley circulation of the atmosphere, unpublished manuscript.

Charney, Jule G., 1969. Private correspondence with Prof. J. A. Young.

Charney, Jule G., and A. Eliassen, 1949. A numerical method for predicting the perturbations of the middle-latitude westerlies, *Tellus,* 1, 38-54.

Charney, Jule G., and A. Eliassen, 1964. On the growth of the hurricane depression, *J. Atmos. Sci.,* 21, 68-75.

Chia, Wu-sun, and B. H. Sage, 1970. Temperature gradients in turbulent gas streams: Investigation of the limiting value of total Prandtl number, *AI Ch. E. J.*, 16, 37-43.

Cox, S. K. and S. Hastenrath, 1970. Radiation measurements over the equatorial central Pacific, *Mon. Wea. Rev.*, 98, 823-832.

Crossley, A. F., 1948. On the relation between wind and pressure, *Quart. J. Roy. Meteor. Soc.,* 74, 379-382.

Deacon, E. L. and E. K. Webb, 1962. Small-scale interactions, *The Sea,* Interscience, New York, 1(3), 48-87.

DuFort, E. C., and S. P. Frankel, 1953. Stability conditions in the numerical treatment of parabolic differential equations, *Math. Tables and other Aides to Computation,* 7, 135-149.

Ekman, V. W., 1905. On the influence of the earth's rotation on ocean currents, *Arkiv. Matem. Astr. Fysik Stockholm,* 2.

Estoque, M. A., 1962. The sea breeze as a function of the prevailing synoptic situation, *J. Atmos. Sci.*, 19, 244-250.

Estoque, M. A., 1968. Vertical mixing due to penetrative convection, *J. Atmos. Sci.*, 25, 1046-1051.

Estoque, M. A., 1970. The planetary boundary layer wind over Christmas Island, U. of Miami final report.

Flicker, H., 1936. Die Passatenversion, *Veroeffentl. Meteorol. Inst., U. Berlin,* 1.

Fujita, T., K. Watanabe and T. Izawa, 1969. Formation and structure of equatorial anticyclones caused by large-scale cross-equatorial flows determined by ATS-I photographs, *J. Appl. Meteor.*, 8, 649-667.

Gray, William, 1968. Global view of the origin of tropical disturbances and storms, *Mon. Wea. Rev.*, 96, 669-693.

Greenspan, H. P., 1968. The Theory of Rotating Fluids, Cambridge Univ. Press, Cambridge, England, p. 328.

Grimes, A., 1937. The movement of air across the equator, Mem. Malayan Meteor. Service, Singapore, 2, p. 14.

Haltiner, G. J. and F. L. Martin, 1957. Dynamical and Physical Meteorology, McGraw-Hill, New York, p. 470.

Haurwitz, B., 1935. The change of wind with elevation under the influence of viscosity in curved air currents, Bei. zur Geophysik, 45, 243-267.

Haurwitz, B., 1936. On the vertical wind distribution in anticyclones, extra-tropical and tropical cyclones under the influence of eddy viscosity, Bei. zur Geophysik, 47, 206-214.

Hess, Seymour, 1959. Introduction to Theoretical Meteorology, Holt, Rinehart and Winston, New York, p. 362.

Holton, J., 1971. A diagnostic model for equatorial wave disturbances: The role of vertical shear of the mean zonal wind, J. Atmos. Sci., 28, 55-64.

Holton, J., J. M. Wallace and J. A. Young, 1971. On boundary layer dynamics and the ITCZ, J. Atmos. Sci., 28,275-280.

Houghton, David D., and W. L. Jones, 1969. A numerical model for linearized gravity and acoustic waves, J. Comp. Phys., 3, 339-357.

Howarth, L., 1951. Notes on the boundary layer on a rotating sphere, Phil. Mag., 42, 1308-15.

Huschke, R. E., 1959. Glossary of Meteorology. American Meteorological Society, Boston, Mass., 638.

Jorden, C. L., 1958. Mean soundings for the West Indies area, J. Meteor., 15, 91-97.

Kornfield, J. and A. F. Hasler, 1969. A photographic summary of the earth's cloud cover for the year 1967, J. Appl. Meteor., 8, 687-700.

Kornfield, J., A. F. Hasler, K. J. Hanson and V. E. Suomi, 1967. Photographic cloud climatology from ESSA III and V computer-produced mosaics, B. of the Amer. Met. Soc., 48, 878-883.

Kuo, H. L., 1965. On the formation and intensification of tropical cyclones through latent heat release by cumulus convection, J. Atmos. Sci., 22, 40-63.

Kuo, H. L., 1971. Axisymmetric flows in the boundary layer of a maintained vortex, J. Atmos. Sci., 28, 20-41.

Lamb, Horace, 1879. Hydrodynamics, Dover Publications, New York, 738 pp.

Lees, M., 1960. Energy inequalities for the solution of differential equations, Trans. Amer. Math. Soc., 94, 58-74.

Lettau, H. H., 1950. A re-examination of the Leipzig wind profile, Tellus, 2, 125-129.

Lettau, H. H., 1957. Exploring the Atmosphere's First Mile, Vol. II, (H. H. Lettau and B. Davidson, editors), New York and London.

Lettau, H. H., 1962. Theoretical wind spirals in the boundary layer of a barotropic atmosphere, Bei. zur Phy. der Atm., 35, 195-212.

Lettau, H. H., 1964. A new vorticity-transfer hypothesis of turbulence, J. Appl. Meteor., 21, 453-456.

Lettau, H. H., 1967. New hypothesis for the relationship between eddy and mean states, The Physics of Fluids, Supplement, 79-83.

Lettau, H. H., 1970. Note on eddy diffusivities, Final Report, U. of Wisconsin, 1-11.

Lettau, H. H., and J. Zabransky, 1968. Interrelated changes of wind profile structure and Richardson number on air flow from land to inland lakes, Annual Report, U. of Wisconsin, 57-80.

Madden, R. A. and E. J. Zipser, 1970. Multi-layered structure of the wind over the equatorial Pacific during the Line Islands Experiment, J. Atmos. Sci., 27, 336-342.

Matsuno, Tarah, 1966. Quasi-geostrophic motions in the equatorial area, J. of the Met. Soc. of Japan, 44, 25-43.

Molenkamp, C. R., 1968. Accuracy of finite-difference methods applied to the advection equation, J. Appl. Meteor., 7, 160-167.

Mörth, H. T., 1962. Fourth Seminar on Tropical Meteorology in Africa, East African Meteorology Dept., Nairobi.

Neiburger, M., C. Beer and L. Leopold, 1945. The California stratus investigation of 1944. U. S. Weather Bureau, Washington, D. C.

Newton, C., 1967. Cumulus convection in the natural atmosphere, Part II, Thermal Convection: A Colloquium, NCAR, Boulder, Colorado.

Nickerson, E. C., 1968. Boundary layer adjustment as an initial value problem, J. Atmos. Sci., 25, 207-213.

Ogura, Y., 1964. Frictionally controlled, thermally driven circulation in a circular vortex with application to tropical cyclones, J. Atmos. Sci., 21, 610-621.

Ooyama, K., 1969. Numerical simulation of the life cycle of tropical cyclones, J. Atmos. Sci., 26, 3-40.

Palmén, E., 1964. General circulation of the tropics, Proceedings of the Symposium on Tropical Meteorology, New Zealand Meteor. Service, Wellington, New Zealand.

Palmén, E., and L. Vuorela, 1963. On the mean meridional circulations in the Northern Hemisphere during the winter season, Quart. J. Roy. Meteor. Soc.,

Pedlosky, J., 1969. Axially symmetric motion of a stratified, rotating fluid in a spherical annulus of narrow gap, J. Fluid Mech., 36, Part 2, 401-415.

Pike, A. C., 1970. The intertropical convergence zone studied with an interacting atmosphere and ocean model, Scientific Report No. 2, U. of Miami.

Priestley, C., 1967. Handover in scale fluxes of momentum, heat, etc., in the atmosphere's boundary layer, Physics of Fluids Supplement, 38-46.

Pushistov, P., 1970. The planetary atmospheric boundary layer in the equatorial region, Izv., Atmospheric and Oceanic Physics, 6, 556-564, translated by D. G. Fry.

Richtmeyer, R. D., 1967. A survey of difference methods for nonsteady fluid dynamics, NCAR Technical Notes 63-2, NCAR, Boulder, Colorado.

Richtmeyer, R. D., and K. W. Morton, 1967. Difference Methods for Initial Value Problems, Interscience, New York, 405 pp.

Riehl, H., 1968. Some aspects of cumulus-scale downdrafts. Atm. Sci. Paper No. 126, Part 1, Colorado State U., Ft. Collins, Colorado, 32 pp.

Riehl, H. and J. S. Malkus, 1958. On the heat balance of the equatorial trough zone. Geophysica, 6, 503-537.

Robitaille, F. E. and E. J. Zipser, 1970. Atmospheric boundary layer circulations equatorward of the intertropical convergence zone, Symposium on Tropical Met., U. of Hawaii, Honolulu, Hawaii.

Rodenhuis, David, 1971. A note concerning the effect of gravitational stability upon the CISK model of tropical disturbances, J. Atmos. Sci., 126-129.

Rogers, M. H. and G. N. Lance, 1964. The boundary layer on a disc of finite radius in a rotating fluid, Q. J. Mech. Appl. Math., 17, 319-30.

Rossby, C. G., 1937. On the mutual adjustment of pressure and velocity distribution in certain simple current systems, J. of Marine Research, I, 1.

Saul'ev, V. K., 1957. On a method of numerical integration of the equation of diffusion, Doklady Akad., Nauk USSR, 115, 1077.

Schlichting, H., 1968. Boundary Layer Theory, McGraw-Hill, New York, 747 pp.

Schwerdtfeger, W. and M. Sponholz, 1970. Theory and observations of the wind in the friction layer over the Antarctic Plateau, Antarctic J. of the U. S., 5, 175-6.

Schwiderski, E. W. and Hans Lugt, 1964. Rotating flows of von Kármán and Bodewadt, The Physics of Fluids, 7, 867-875.

Sellick, N. P., 1950. Equatorial circulations, Quart. J. Roy. Meteor. Soc., 76, 89-94.

Simpson, J., M. Garstang, E. Zipser and J. Dean, 1967. A study of a non-deepening tropical disturbance, J. Appl. Meteor., 6, 237-254.

Smith, R. K., 1968. The surface boundary layer of a hurricane, Tellus, 20, 473-484.

Starr, V. P., 1968. Physics of Negative Viscosity, New York.

Stokes, G. G., 1851. On the effects of the internal friction of fluids on the motion of pendulums, Cambridge Phil. Trans., IX, 9.

Sutcliffe, R. C., 1947. A contribution to the problem of development, Quart. J. Roy. Meteor. Soc., 73, 370-383.

Syono, S., 1949. Approximate solution of nonlinear differential equations of stationary wind of an axially symmetric cyclone and anticyclone and its application, Geophys. Mag. of Tokyo, 20.

Syono, S., 1951. On the structure of atmospheric vortices, J. Meteor., 8, 103-110.

Taylor, G. I., 1915. Eddy motion in the atmosphere, Phil. Trans. Roy. Soc. London, A, 215, 1-26.

Taylor, G. I., 1950. The boundary layer in the converging nozzle of a swirl atomizer, Q. J. of Mech. Appl. Math., 3, 129-139.

U. S. Dept. of Commerce, Office of Climatology, 1959. Climatological and Oceanographic Atlas for Mariners, Vol. I.

U. S. Navy, The Office of the Chief of Naval Operations, 1955. Marine Climatic Atlas of the World, vol. I-IV.

Wagner, N. K., 1966. A two-dimensional time dependent numerical model of atmospheric boundary layer flow over inhomogeneous terrain, Final Report, U. of Hawaii, 1-76.

Wiederanders, C. J., 1961. Analysis of monthly mean resultant winds for standard pressure levels over the Pacific, Hawaii Institute of Geophysics Report No. 13, 83.

Wiin-Nielsen, A. C., 1970. On inertial flow, Report No. 1, Institute for Teoretisk Meteorologi, Copenhagen.

Williamson, David, 1966. Stability of difference approximations to certain partial differential equations of fluid dynamics, J. of Comp. Physics, 1, 51-67.

Young, J. A., 1969. Private correspondence with Jule G. Charney.

Young, J. A., 1970. Mass convergence in a baroclinic Ekman layer, Annual Report, 1969, U. of Wisc., 211-224.

Zipser, E. J., 1969. The role of organized unsaturated convective downdrafts in the structure and rapid decay of an equatorial disturbance, J. Appl. Met., 8, 799-814.

Zipser, E. J., 1970. The Line Island Experiment; Its place in tropical meteorology, and the rise of the fourth school of thought, B. of the Amer. Met. Soc., 51, 1136-1146.

Scanner's note:

This page is blank.

A NUMERICAL MODEL OF DEEP MOIST CONVECTION: THE INFLUENCE OF AMBIENT CONDITIONS AND INTERNAL PHYSICAL MECHANISMS

Robert Edward Schlesinger

Abstract:

The subject of this study is the influence of both ambient conditions and certain internal physical processes upon the behavior of deep moist convection in the atmosphere. By means of a two-dimensional numerical model, an anelastic system of hydrodynamic and thermodynamic equations is integrated in order to simulate convection of the squall-line type. Liquid precipitation and the effect of pressure perturbations upon the buoyancy are included.

The research involves three main phases:

1. The joint influence of the low-level relative humidity and midtropospheric wind shear upon the intensity and persistence of the convection at maturity is investigated. Nine comparative experiments are performed using three values of each parameter, including cases without shear. The various cases are compared in detail with regard to airflow, rainfall rate, temperature and pressure.

2. The dynamics and kinematics are further analyzed for a "prototype" storm (intermediate values of both moisture and shear) which during maturity exhibits a quasi-steady configuration resembling some observed severe thunderstorms.

3. The effects of individual physical mechanisms and alterations in the initial conditions are isolated by performing several variations upon the prototype experiment.

Presented as a thesis in partial fulfillment of the requirements for the degree of Doctor of Philosophy (Meteorology).

It is found that the greater the moisture supply and the weaker the wind shear, the greater the maximum intensity of the convection in terms of both updraft velocity and rainfall rate. Strong shear shortens the life of the updraft if the moisture supply is sufficiently limited but prolongs its life if the moisture supply is sufficiently great. An initial upper-level jet does not favor a more severe storm than a broad upper-level wind maximum, but may help to prolong the mature stage. Drag due to water drops limits the maximum updraft intensity but is not important to downdraft formation, which occurs mainly at cloud edges where evaporation induces negative buoyancy. Net upward accelerations in the updraft are much smaller than the parcel theory would predict; the thermal buoyancy in the accelerating part of the updraft is reinforced by relatively low pressure but much more strongly counteracted by the vertical perturbed pressure gradient force, liquid water drag and the warming of the surroundings due to subsidence. The fall of water drops relative to the air concentrates most of the liquid water in the lower parts of the cloud, enhancing evaporative cooling and downdraft development. Low-level cooling eventually weakens the updraft by isolating it from the supply of potentially warmer air, and contributes to formation of a shallow dome of relatively high pressure.

Contents

INTRODUCTION

1.1 General Remarks on Severe Thunderstorms and Squall Lines

There are few meteorological phenomena more fascinating or awesome than the squall line, defined in the Glossary of Meteorology (1959) as "any non-frontal line or narrow band of active thunderstorms." Squall lines can inflict human, economic and agricultural damage as disastrous as that produced by hurricanes, although over considerably smaller areas and shorter time intervals. With little doubt, untold devastation would be averted if the severity attained by such storms could be lessened. An obvious prerequisite for success in attempting to modify potentially destructive storms is an understanding of the physical processes governing the storms, including their interactions with meteorological phenomena having space and time scales far different from those of the storms. Closer consideration of the key terms in the above definition, i.e., "thunderstorms," "narrow band" and "nonfrontal," will also help to clarify the nature of squall lines as meteorological entities.

Whether isolated or part of a squall line, the thunderstorm is perhaps the most dramatic form of atmospheric convection, a process characterized by its ability to transport and redistribute heat, water vapor and horizontal momentum through active vertical air motions. Atmospheric convection has been classified as "shallow" or "deep" by Ogura and Phillips (1962) according to if its vertical extent is, or is not, much less than that of a dry-adiabatic reference atmosphere, or roughly 30 km. It has been customary to further classify atmospheric convection as "dry" if no condensation of water vapor occurs and as "moist" otherwise. By these criteria, the thunderstorm heads the hierarchy from shallow dry convection (such as cloudless "thermals" or in some cases the sea breeze) through shallow moist convection (such as trade wind cumulus) to deep moist convection.

An individual cumulonimbus cloud exhibits spatial dimensions and time scales radically different from those typical of synoptic-scale features. Its vertical extent can be similar to that of a well-developed cyclone or anticyclone, but its horizontal and vertical dimensions are usually similar. Synoptic-scale features, in contrast, have horizontal dimensions of 1 to 3×10^3 km. A deep convective cloud departs drastically from both hydrostatic and geostrophic equilibrium, unlike the general circulation. Horizontal and vertical velocity perturbations are both of the order of 10 m sec^{-1}. The time scale of a thunderstorm is typically one hour, whereas the main features in the general circulation are identifiable for 100 hours; accordingly, the Coriolis force which is crucially important to the general circulation is of little importance to thunderstorms. Cumulonimbus clouds and their attendant surface pressure disturbances comprise what are referred to as "mesoscale" circulations since these features have horizontal dimensions intermediate between those of synoptic-scale entities and those of much more localized meteorological phenomena such as "dust devils." Yet cumulonimbus clouds are highly significant to the global circulation despite these differences in scale. Riehl and Malkus (1958) concluded that the heat energy exported poleward from the equatorial trough zone at upper levels is supplied largely through the upward heat transport effected by the cumulonimbus towers or "chimneys" within this zone.

A number of one-dimensional theories have been proposed in attempting to describe and account for the behavior of convective clouds. Each has neglected horizontal pressure differences between the convective element and its environment, which is assumed hydrostatic, and none has incorporated precipitation. The theories have provided some valuable guidelines for the behavior of deep moist convection, but are more applicable to shallow non-precipitating clouds than to thunderstorms with their heavy precipitation and large horizontal gradients.

The parcel theory is the simplest and best known model of atmospheric convection and is in particular the basis for such fundamental concepts as potential and equivalent potential temperature along with three forms of instability: static, conditional and convective. However, this theory regards a convective element as moving vertically through a resting environment without disturbing or interacting with it. In the "slice method" of Bjerknes (1938), the parcel theory is modified to take into account the compensatory motions of the surroundings due to mass continuity. The thermal buoyancy of a saturated rising parcel is slightly reduced due to dry-adiabatic warming of its sinking environment. However, both the slice theory and the parcel theory ignore any dilution of a convective element by air from its surroundings. As Stommel (1947) emphasized, an ascending buoyant parcel which entrains unsaturated environmental air but remains saturated is less buoyant than a parcel undergoing no mixing. Whatever the nature of the mixing, the evaporation required to keep the parcel saturated reduces its thermal buoyancy.

The mixing of unsaturated outside air into a cloud has been postulated to occur in two principal modes: macroscale or "dynamic" entrainment, involving an ordered cloud-scale mass inflow, and microscale or turbulent entrainment, accomplished by eddies much smaller than the cloud. The first mode has been described by Houghton and Cramer (1951) and Riehl (1954), and the second by Scorer and Ludlam (1953). Treating a cloud as a steady-state circular cylinder, Houghton and Cramer noted that mass continuity requires ordered inflow into an updraft that accelerates with increasing height. As Riehl emphasized, this type of inflow is due to horizontal pressure forces directed toward the cloud core if friction is not important. In contrast, Scorer and Ludlam suggested that the sporadic protrusion and decay of individual cumulus turrets reflects an intermittent behavior of the updraft as a series of thermals or "bubbles" with approximately hemispherical tops above wakes of air chilled and moistened by yet smaller scale mixing with outside air.

In actual convective clouds, entrainment probably occurs in a combination of the two modes described above. A hybrid theory of Squires and Turner (1962), suggesting entrainment as an ordered inflow independent of horizontal pressure gradient forces, represented a cloudy updraft as a turbulent plume having a steady-state mean flow. As suggested by laboratory experiments, outside air was assumed to be drawn into the updraft with a velocity proportional to that of the updraft. Squires and Turner stressed that both inflow and outflow of mass should occur only if the turbulence of the environment is similar in degree to that of the updraft. Since the environment was assumed to be nonturbulent, and pressure perturbations were neglected in the plume theory, the ordered inflow is apparently due to friction associated with eddies at the periphery of the updraft.

While these one-dimensional theories (except for the slice method) treat the cloud's surroundings as motionless and time-independent, mass continuity and horizontal pressure differences require both an actual cloud and its surroundings to share an overall circulation whether or not the undisturbed state is one of rest. Moreover, convective storms are commonly observed in environments with appreciable vertical wind shear, a factor whose possible importance in determining the structure of a fully developed storm will be a major concern in this paper.

The squall line is a narrow band of thunderstorms in the sense that it is much longer than it is wide. At any one time, its associated radar echo is typically 10 to 30 km wide but up to several hundred kilometers long. Squall lines are often observed to form in the warm sectors of cyclones and nearly parallel to surface cold fronts. The lines are themselves nonfrontal in that they are independent of and generally propagate differently from the fronts. Also, squall lines may occur in the tropics, completely removed from any significant baroclinic zones, as exemplified by the well-known spiral bands in hurricanes.

Synoptic-scale processes associated with frontal zones have long been considered important to the creation of an environment favoring extratropical squall line formation. Ludlam (1963) noted that the geographical regions most subject to severe thunderstorms are underneath 500 mb mean jet streams during the preferred seasons of occurrence. The atmospheric stratification a few hours prior to a severe thunderstorm or squall line often exhibits extreme convective instability in which a tongue of very moist air in the lowest 100 to 200 mb is surmounted by a deep layer having much lower relative humidity and rather weak static stability; the transition layer in between is only a few tens of millibars deep. In describing five characteristic synoptic patterns associated with tornado-producing storms in the central United States, Miller (1959) emphasized the statically and convectively destabilizing effect of differential advection upon the environment of the storms prior to their formation. In particular, each pattern included a dry intrusion at 700 mb on the windward side of an 850 mb moist tongue.

Newton (1967) stressed the apparent role of the inversion which may be present in the transition layer. With its strong static stability, the inversion confines convection beneath it until sufficient lifting occurs to eliminate the inversion, yet allows sufficient heat and moisture advection for the air underneath to acquire extreme convective instability. Fawbush and Miller (1953) noted from a study of numerous severe storm situations in the southern Great Plains that any one particular measure of storm severity, surface hailstone size, was positively correlated with the inversion strength three to six hours prior to storm occurrence.

For the case of an outbreak of severe thunderstorms and tornadoes in Ohio during April 1968, Johnson and Sechrist (1970) concluded from isentropic analyses that a dry tongue similar to Miller's "dry air intrusion" just behind the main convective band resulted from descent of the polar jet from near the tropopause. The dry air into which the convection penetrated was destabilized through isentropic mass convergence brought about by the translation of the subsiding jet into a region of weaker winds. Gravity waves occurring on a subsynoptic scale may also contribute to the destabilization. Air parcels entering or leaving a jet stream are subjected to significant horizontal accelerations, implying a departure from geostrophic balance. Ogura and Charney (1962) showed by linear analysis that this imbalance generates gravity waves with amplitudes proportional to the degree of imbalance.

1.2 The Importance of Vertical Wind Shear to Severe Convective Storms

It has long been observed that shallow cumulus convection is suppressed by vertical wind shear. Also, some results from the well-known Thunderstorm Project described by Byers and Braham (1949) suggest that vertical wind shear may limit the development of isolated thunderstorms having relatively small horizontal dimensions. As part of the project, thunderstorms over Ohio were extensively observed during the summer of 1947; it was found that cloud top heights showed a slight tendency to decrease as the wind shear between about 850 and 300 mb increased from approximately 10 to 25 knots. These results should be interpreted cautiously, since many of the thunderstorm tops extended beyond the vertical range of the radar scope used in the observations, and an arbitrary constant correction height was added to the radar height estimate in such cases. Nevertheless, these findings suggest that vertical wind shear did not aid the development of isolated moderate thunderstorms. Yet we have noted earlier that large severe thunderstorms, sometimes in squall lines, are often observed to occur near middle- or upper-level jet streams.

By a mainly two-dimensional argument, Newton (1950) suggested that the redistribution of horizontal momentum in squall line convection should reduce the vertical wind shear within the storms below that of the ambient wind, leading to horizontal divergence patterns that would imply upward motion and further release of convective instability at the downshear edge, with downward motion and evaporation at the upshear edge. The squall line should thereby propagate downshear until the ambient vertical shear weakens or changes sign. Newton noted that observations of an actual squall line appeared to corroborate this two-dimensional hypothesis.

Newton and Newton (1959) presented a three-dimensional hypothesis on the maintenance of thunderstorms in surroundings showing a veering of wind with increasing height. A cumulonimbus cloud was likened to a circular cylindrical obstacle in a translatory flow. Due to the turning of the wind with height, the ambient flow relative to the cloud should produce low-level inflow into the right front quadrant of the cloud (traveling with the cloud and looking in the direction of its motion) and upper-level inflow into its left rear quadrant. By analogy to hydrodynamic theory in wind-tunnel flow, Newton and Newton surmised that the distribution of dynamic pressure should induce an upward force along the right front edge of the cloud and a downward force along the left rear edge, favoring new growth along its right front edge. It was suggested that this mechanism might be effective even in the absence of positive thermal buoyancy.

One would not expect the above hypotheses to be valid since there are in reality no rigid walls separating a storm cloud from its surroundings. However, Hitschfeld (1960) noted an example of a well-developed thunderstorm whose radar echo remained upright for over an hour despite very strong upper-level wind shear. By treating the storm core as a cylindrical obstacle, and considering the effective broadside force of the relative wind on a thin layer of the obstacle, Hitschfeld concluded that the response time required for the relative wind speed to decrease by half would be directly proportional to its cross-sectional width and inversely proportional to the relative wind speed itself. This would mean that a large storm in a strongly sheared environment might resist the environmental shear much longer than a smaller storm or especially a small cumulus cloud; Byers and Battan (1949) noted that velocities of thunderstorm echoes only a few kilometers across showed shears about two-thirds the corresponding environmental shears.

Some schematic models of severe thunderstorms have stressed the interaction between the thermodynamics of the storms and the relative flow patterns induced by environmental wind shear. These schematic models have been directed largely toward explaining why some large severe thunderstorms in strongly sheared environments retain their configuration for much longer times than less intense thunderstorm cells of the type observed in the Thunderstorm Project. According to Byers and Braham (1949), the mature stage of a typical thunderstorm cell, characterized by both updrafts and downdrafts as well as surface precipitation, lasted only fifteen to thirty minutes. In contrast, radar echoes of some thunderstorms producing significant hailfall or tornadoes have revealed their echoes to persist almost unchanged in size or configuration for thirty minutes or considerably longer. With Ludlam (1962) and Donaldson (1963), Browning stressed the persistence of an echo-free notch at the juncture between the anvil base and the main column of precipitation at the front of a hailstorm echo near Wokingham, England. The notch, termed the "vault," was considered to mark the entry point into the storm core for an updraft sufficiently strong and persistent to suspend precipitation at higher altitudes for thirty minutes or longer. Browning and Donaldson also noted that for a similar thunderstorm near Geary, Oklahoma, the vault persisted almost unchanged for an hour. Fankhauser (1971) noted a large Great Plains thunderstorm which retained its shape and size for well over two hours. Such observations as these suggest that some severe thunderstorms are in an approximately steady state during maturity, provided that the frame of reference moves with the storm core.

The schematic storm models of Newton (1967), Browning (1964) and Fankhauser (1971) all suggest airflow configurations which should tend to prolong a storm in a sheared environment further characterized by very moist (and potentially warm) low-level air surmounted by much drier (and potentially cool) air. Using a two-dimensional argument, and suggesting that air parcels entering the storm should partially conserve the momentum characteristic of their level of entry, Newton indicated that the trajectories of the potentially warm air parcels should create an updraft tilting upshear with height. Most of the falling precipitation should then land in the rear of the storm where it could be readily evaporated into the incoming dry middle-level air. Since evaporation should impart negative buoyancy to this air, a downdraft having horizontal velocities greater than that of the storm core should develop at the rear of the storm. Surface convergence between the resulting forward surge of chilled air and the much-slower-moving warm air in front of it should help to perpetuate the updraft without significant interference from precipitation, while the dry flow into the back of the storm should maintain the downdraft through continued evaporative cooling. Unlike Newton's, the schematic models of Browning and Fankhauser take into account veering of the ambient wind with height as well as increasing speed. The inflow configuration has much the same thermodynamic significance as in Newton's model, but due to the three-dimensionality, the inflows occur on the right flank of the storm (looking in its direction of travel). Browning's model, in particular, is meant to represent what he calls "right-moving" storms, i. e., those which travel to the right of the ambient wind at all levels over their depth. Browning noted that this property would be expected to contribute to a storm's persistence by making possible a stronger relative inflow of dry middle-level air for downdraft maintenance than would be possible were the storm's motion parallel to the wind at middle levels.

1. 3 Basic Considerations in Numerical Modeling of Moist Convection

A full understanding of the highly complicated interactions involved in deep moist convection would require the complete solution of the governing equations. Mainly due to their nonlinearity, there are no known solutions having any mathematically convenient form. With the availability of increasingly large and fast electronic computers during recent years, however, the once forbidding difficulties involved in attempting to solve these equations have been lessened to a considerable extent. Numerical modeling, or obtaining approximate finite-difference solutions over a grid or lattice of points, has furnished a degree of insight not otherwise possible into the physical processes involved in meteorological phenomena from thermals or small cumulus clouds to the global circulation.

Although actual convection is three-dimensional, the time and storage required for a three-dimensional model are formidable even with today's computers. It is not surprising, then, that nearly all numberical convection models described in the literature to date have been one- or two-dimensional. One-dimensional models of precipitating cumulus include those of Das (1964), Takeda (1966a), Srivastava (1967) and Weinstein (1970). The remaining models to be noted in this paragraph have been two-dimensional. The simplest form of atmospheric convection, a buoyant thermal in a shallow dry layer, has been simulated by Malkus and Witt (1959), Lilly (1962) and Ogura (1962). Nonprecipitating cumulus clouds have been modeled by Ogura (1963), Asai (1964), Murray and Anderson (1965) and Orville (1968). Also, Arnason et al. (1968) and Orville (1970) have simulated cumulus clouds including the rain stage. Early squall line models were constructed by Sasaki (1959) and Ogura and Charney (1962). More recently, cumulonimbus clouds in sheared surrounds have been modeled by Takeda (1965, 1966b, 1971).

In view of obvious hazards to aircraft (especially turbulence, lightning and sometimes hail), detailed direct observations of the interiors of cumulonimbus clouds have not been made very extensively. Some of the most comprehensive aircraft observations to date within mature thunderstorms, made during the Thunderstorm Project as described by Byers and Braham (1949), did not sample the uppermost parts of the clouds since the highest altitude flown was only about 8 km. In contrast, in a numerical model the overall structure of a cumulonimbus cloud and its surroundings as well as some of the physical processes involved can be studied in detail without the hazards faced by aircraft. More importantly, a numerical model can enable one to isolate by repeated experiments specific factors in a way not possible with the real atmosphere, which cannot repeat patterns closely enough to satisfactorily approximate a controlled laboratory. Given a number of parameters, one can run a series of numerical experiments in which a particular parameter is varied from one experiment to another while all other parameters are left unchanged, thereby helping to isolate the specific role of the factor or process represented by that parameter. In the governing equations, an individual process can be completely suppressed by simply omitting the corresponding term or terms. The physical significance of that process can be indirectly deduced by comparing the results with those of an otherwise identical experiment in which the process is retained in these equations.

Along with these definite advantages, numerical modeling has fundamental difficulties and limitations. In the model, as in the mathematical problem whose solution it attempts to approximate, initial and boundary conditions must be imposed. Other difficulties include the opposing requirements of accuracy and data storage, truncation error and computational instability, and the problem of modeling physical processes which may be poorly understood or which may occur on spatial scales too small for the computational grid to resolve. These various pitfalls will be explained in the next several paragraphs.

In each direction, the distance between grid points should be twenty to fifty times smaller than the total extent of the grid domain in that direction in order to resolve the basic details of the convective circulation. A disturbance having a wavelength of less than two grid intervals in a particular direction is erroneously represented as a much longer wave. One-dimensional models are obviously most convenient in terms of computing time and program size, but suffer from the fundamental limitation of being unable to incorporate horizontal gradients or pressure perturbations. The bulk of the numerical convection modeling described in the literature has been two-dimensional.

In numerical models, the scheme used for approximating advective derivatives must be free of the undesirable phenomenon known as computational instability, in which components of the numerical solution in one or more wavelengths amplify with time until all other components are masked and the solution becomes physically meaningless. Most widely used differencing schemes are stable if the time step is sufficiently small so that no information can propagate over a distance exceeding the separation between neighboring grid points during the time step. As is well known, acoustic waves are present in the full solutions to the governing equations; since acoustic waves are of little or no significance to convective dynamics but propagate with speeds an order of magnitude faster than does a typical convective disturbance or the air within the disturbance, it is of utmost importance to suppress acoustic waves so that the physically significant parts of the solution are not overshadowed and large amounts of unnecessary computing time may be avoided. As demonstrated by Ogura with Charney (1962) and Phillips (1962), these waves can be filtered out by the so-called anelastic approximation, in which the local time variations of density are ignored in the continuity equation. This approximation still admits gravity waves, whose frequencies are usually much lower than those of acoustic waves but which may at least sometimes be associated with mesoscale convection as suggested by Tepper (1950) and Ogura and Charney (1962). Unfortunately, even a stable numerical solution may still exhibit oscillations which are due entirely to peculiarities of the advective differencing scheme. As noted by Molenkamp (1968), such peculiarities can produce spurious negative values for quantities which in the physical world can never be negative.

Some numerical advective schemes have a peculiarity perhaps less serious than those just mentioned, but which causes any advected property to also be numerically diffused. This pseudo-diffusion, whose strength depends on the grid resolution and the local fluid velocity, can effectively mask any real diffusion resulting from the turbulence one might attempt to model explicitly. Essentially the opposite of computational instability, this difficulty is due to damping of all components of the numerical solution, mainly for the shortest wavelengths, and is really a systematic truncation error. Hirt (1966), Crowley (1968), Molenkamp (1968), and Orville and Sloan (1970) have noted the pseudodiffusive nature of this effect, which will be considered later in more detail.

In trying to devise a realistic model of deep moist convection, one is faced with incorporating precipitation and turbulence, two important physical phenomena which are far from adequately understood. Much of the difficulty stems from the fact that these phenomena take place on spatial scales too small to resolve on the computational grid. Although precipitation may be forming or falling in a region 1 to 10 km or more in width, the individual water drops are only 300 to 1000 microns in diameter. Moreover, many individual processes are operating in connection with precipitation: phase changes of water substance, production and growth of raindrops and often hailstones, and breakup of the largest raindrops into smaller drops. One can obtain general mathematical expressions for turbulent flux divergences by subjecting the governing equations to the well-known Reynolds averaging process described in meteorology textbooks, e.g. by Hess (1959). In numerical modeling, the usually smooth spatial variations resolvable by the grid correspond to the mean fields while the turbulent fluctuations superimposed on the mean fields occur on subgrid scales. The general mathematical expressions are of little help in practice. To compute the turbulent horizontal or vertical flux of a property, one must know the root-mean-square fluctuations of the horizontal or vertical wind and of the property, together with the correlation between the fluctuations. Particularly for heat and moisture in deep convection, not enough is known to make possible thus far any one fully convincing mathematical-physical theory on how these required quantities might be computed. Power spectral analysis of aircraft observations such as those described by Ackerman (1967) or Rhyne and Steiner (1964) have revealed dominant horizontal length scales for turbulent fluctuations and have provided estimates of root-mean-square wind fluctuations, but suggest no particular spatial patterns for correlations.

In view of the difficulties involved in describing mathematically the processes governing precipitation and turbulence, it is necessary to parametrize these processes in terms of their effects on bulk properties resolvable by the grid rather than model them directly. In almost all two-dimensional convection models to date, the subgrid-scale mixing presumably effected through turbulent fluxes has been simulated crudely by linear diffusion terms analogous to molecular viscosity terms, using much larger and usually constant viscosity coefficients to parametrize mixing by subgrid eddies which are still several orders of magnitude larger than molecular mean free paths. Since the turbulent processes being parametrized are highly nonlinear, this frequently used parametrization is mathematically incorrect.

The fact that two-dimensional numerical convection models have yet to explicitly incorporate the ice phase is testimony to the complications involved in handling precipitation. Kessler (1969) has parametrized the conversion of cloud droplets to raindrops, the growth of raindrops by accretion and the evaporation of raindrops falling through unsaturated air, and his approach or ones similar to it have been used in some precipitating cloud models such as those of Arnason et al. (1968) or Liu and Orville (1968). While not suffering from mathematical inconsistencies as obvious as those of the eddy-viscosity approach to turbulence modeling, this approach inevitably involves parameters which are highly empirical, e.g., a representative collection efficiency (for coalescing water drops) or an upper limit to cloud droplet content.

We now turn to the internal physical mechanisms (as they appear in models) which influence the behavior of a storm once it has developed. The effects of pressure perturbations, liquid water drag and fallout of precipitation upon storm dynamics will be of major concern in this paper. In particular, pressure perturbations have been ignored in almost all two-dimensional models except for a very few such as the precipitating cumulus model of Arnason et al. (1968).

Although observations aloft within severe convective storms have not provided comprehensive data on pressure disturbances, Barnes (1970) has described a balloon ascent through part of an updraft in a severe Oklahoma thunderstorm indicating pressure differences of 3 mb or more between the updraft and the environment near 500 mb. Citing such evidence, List and Lozowski (1970) have suggested that the pressure contribution to the buoyancy may be a significant fraction of the thermal contribution in deep convective clouds. Although the model of Arnason et al. (1968) showed pressure deviations of the order of only 0. 1 mb, the vertical gradient force due to the deviations was about 40 percent as large as the thermal buoyancy. This makes it especially important to compute pressure deviations in a two-dimensional thunderstorm model.

One unsettled question is whether downdraft formation in severe convective storms is due mainly to evaporative cooling or to the downward drag of the liquid water itself. The schematic severe storm models considered earlier have emphasized the apparent importance of evaporating precipitation as a cooling agent for dry middle-level air. However, Byers and Braham (1949) indicated that liquid water drag should initiate the downdraft, which should subsequently take on increasingly negative thermal buoyancy with decreasing height if the environment is conditionally unstable. The one-dimensional numerical models of Das (1964) and Srivastava (1967) have also indicated that a downdraft is initiated at levels where the liquid water concentration, and hence its drag, is large. In this context, the results of two nonprecipitating two-dimensional cumulus models should be noted. Ogura (1963) incorporated liquid water drag but his results did not show significant downdraft development; Murray and Anderson (1965) ignored liquid water drag but obtained maximum downdraft velocities about one-third the maximum updraft velocities. In both models, liquid water drag was therefore not necessary for downdraft formation. It is important to run a two-dimensional precipitating cumulonimbus model which includes two otherwise identical experiments, one with drag and the other without.

The effects of liquid water drag and of liquid water fallout might differ substantially, since liquid water exerts a drag whether or not it falls relative to the air. However, while precipitation is not essential to drag, the relative fall of water drops affects the spatial distribution of drag by changing the liquid water distribution. Since this in turn alters the distribution of evaporative cooling, fallout should affect the location and strength of the downdraft whether or not liquid water drag is itself important to its formation. Thus far, numerical cloud models have not made clear the effect of precipitation since they have not included a pair of otherwise identical runs with fallout allowed in one run and not in the other.

The initial conditions for numerical models have commonly consisted of a basic state which depends upon height alone, with some localized thermally buoyant perturbation in the lower atmosphere to generate a convective circulation. Initial conditions of this sort have been used in the early dry convection models of Malkus and Witt (1959), Ogura (1962) and Lilly (1962) as well as in the shallow cumulus models of Ogura (1963), Murray and Anderson (1965) and Arnason et al. (1968). In other convection models, initial conditions have been used not involving localized impulses in the free atmosphere. Orville (1964, 1968) has modeled dry and moist convection over a mountain ridge which is simulated by a triangular obstacle on an otherwise flat lower boundary, with convection initiated as an upslope wind by prescribed heating and (in the moist model) evaporation at the boundary. In the early squall-line models of Sasaki (1959) and Ogura and Charney (1962), a strong cold front was initially assumed. It is not known precisely what mechanism provides the release of convective instability needed for squall line formation, but Tepper (1950) suggested that the pressure jump often observed during squall line passage might be due to a gravity wave generated by an accelerating cold front. It was hypothesized that the gravity wave initiated the squall line through forced lifting of air.

In numerical modeling, the lower boundary of the grid domain is the only mathematical boundary which also corresponds to a true physical boundary, namely the earth's surface. In this case, the need to take viscosity into account has usually dictated no-slip or free-slip conditions on the tangential velocity, with no vertical motion if the boundary is flat. The upper boundary in nearly all convection models has been identified with the depth of the atmospheric layer affected by the convection, and has customarily been treated as a rigid boundary with no motion through it. In deep atmospheric convection, the strong stability above the tropopause affects clouds much the same way a rigid lid would.

The main difficulty involves lateral boundary conditions, particularly if the basic flow includes an ambient wind as have the cloud models of Asai (1964), Takeda (1965, 1966b, 1971) or Orville and Sloan (1970). The other two-dimensional convection models thus far mentioned have simulated isolated buoyant fluid elements in an environment with a base state of rest; in these cases, one lateral boundary has been defined as an axis of symmetry and the other has been treated as a rigid wall. On the other hand, the lateral boundaries in a model that includes am ambient wind with shear correspond to neither axes of symmetry nor walls.

Periodic boundaries, such as were used by Takeda (1965, 1966b) and Asai (1964), are mathematically the most convenient open lateral boundaries. Unfortunately, in one of Takeda's experiments (1966b), the cloud anvil reached one of the lateral boundaries after fifteen minutes of simulated time, thereby re-entering at the other lateral boundary and making further computations of dubious value. Periodic lateral boundaries are not appropriate for modeling squall lines, which tend to occur singly rather than in trains.

At outflow points, physical properties are being advected from within the domain so that it is natural to formulate outflow conditions in terms of interior values. At inflow points, however, properties are being advected from where no numerical information is present, so that inflow conditions should not be formulated in terms of interior information. Without using periodic boundary conditions, the only way to completely avoid this logical difficulty is to specify properties as unchanged while inflow is present at a boundary point. The specification problem will be considered in more detail later.

Even the simplest outflow formulations may generate spurious phenomena. This has been graphically demonstrated by Nitta (1962), who applied a variety of outflow boundary conditions in numerical integrations of the one-dimensional advection equation, considering specific wave-type exact solutions to which the numerical solutions could be directly compared. Nitta found that the schemes generated error waves two grid intervals long which propagated upstream from the outflow point, resulting in phase errors or even computational instability. In two-dimensional convection modeling, which involves a number of important nonadvective processes, there is no reliable way of evaluating lateral boundary errors since the exact solution of the governing equations is not expressible in closed mathematical form.

1.4 Scope of the Research

The research to be described concerns an anelastic two-dimensional numerical model of cumulonimbus convection in an environment initially characterized by a shallow layer of air with high relative humidity surmounted by a deep layer of much drier air with wind shear throughout the middle troposphere. This model simulates a representative cross-section of midlatitude squall line convection in a plane normal to the line. Numerical experiments to be described involve three main objectives to be indicated below.

One main aim is to investigate the joint effects of low-level convective instability, i.e., decrease of initial equivalent potential temperature with height, and of middle-level wind shear upon both the intensity and the persistence of cumulonimbus convection. It was noted that Thunderstorm Project observations did not suggest that vertical wind shear contributes to the development of air mass thunderstorms of relatively small horizontal dimensions, but that strong vertical wind shear may encourage the perpetuation, if not the enhanced development, of larger and usually more severe thunderstorms. Also, it was pointed out that some observed severe thunderstorm echoes have shown a quasi-steady state lasting anywhere from half an hour to over two hours. With this in mind, the following questions arise:

1) What are the basic patterns and interactions involving the fields of airflow, temperature, pressure and rainfall intensity, including relationships between the degree of wind shear and asymmetries in the basic patterns?

2) For a given vertical profile of equivalent potential temperature, does midtropospheric wind shear enhance the peak intensity of a convective storm, prolong its mature stage, or both?

3) Under what combinations of low-level convective instability and middle-level wind shear, if any, can the convective circulation persist in a quasi-steady state?

To investigate the above questions, comparative experiments are run using the relative humidity in the moist lower layer and the intensity of wind shear through the middle troposphere as independent parameters, both referring to the initial base state. Identical base states are assumed for the vertical temperature profiles in all cases in order to vary the degree of low-level convective instability without varying the profile of conditional instability (which depends on the temperature profile but not on the humidity profile). The comparative experiments range over the nine possible combinations for three degrees of midtropospheric wind shear, including for completeness a case without shear, and three values of relative humidity, so that each experiment can be identified with a point in a 3-by-3 rectangular lattice in a moisture-shear plane. This point of view will be particularly helpful in appreciating the joint influences of low-level convective instability and midlevel shear on physical variables.

Since the focus is upon the mature stages of convection rather than the earlier stages or the possible mechanisms for initiation, synoptic-scale effects such as horizontal convergence are not included in the initial base state, which is assumed to depend on height alone. The initial perturbation, assumed the same in all nine cases, is a shallow cloud with a weak convective circulation already present. The convective dynamics, on length scales resolvable by the numerical model, are considered more important in this work than a detailed study of microphysics for cloud droplets and precipitation. Liquid precipitation is included in the model but without direct inclusion of the ice phase, despite the presence of ice in all real cumulonimbus clouds. A highly simplified parametrization due to Takeda (1965, 1966a, 1966b) is used.

A second purpose of the research is to further investigate the dynamics and kinematics of one particular model storm involving moderate or strong shear. This particular storm, designated as the "prototype," exhibits during maturity a quasi-steady flow pattern partially resembling that inferred from the previously cited radar observations of the Geary and Wokingham storms. Several aspects of the prototype not studied in depth for the other comparative cases are analyzed in order to investigate the following questions:

1) How important are the vertical forces which one-dimensional convection models are incapable of including, i.e., the portions of the vertical pressure gradient forces and of the gravitational buoyancy contributed by pressure deviations?

2) What is the pattern of dynamic entrainment, i.e., systematic horizontal acceleration of air into the cloud from its surroundings due to the horizontal component of the pressure gradient force?

3) What are the main differences between the configurations of airflow streamlines and precipitation streamlines resulting from the relative fall of precipitation?

4) During the mature stage of the convection, what are the locations of individual air parcels whose initial positions inside or outside the cloud are specified? To this purpose, analyses of air parcel trajectories precipitation streamlines and the horizontal and vertical components of individual forces are presented for the prototype case.

In the third main thrust of the research, seven variations are performed upon the prototype experiment, the first three of them involving the basic dynamics and the remaining four involving the initial conditions, in an attempt to answer the following questions:

1) Is the liquid water drag essential to the initiation of the downdraft, or does it only restrict the updraft intensity?

2) Is precipitation, i.e., the fall of liquid water droplets relative to the air, essential to either the downdraft or the dissipation of the storm?

3) Does the contribution to the gravitational buoyancy by pressure perturbations (in addition to the thermal contribution) significantly affect either the severity or persistence of the storm?

4) Does a definite upper-level jet help to either intensify or perpetuate the convection?

5) If the transition layer between the moist low-level air and the overlying dry air is deepened, which of the following two opposing effects is more important in determining the intensity of the convection: the decreased instability near the cloud top due to reduced evaporation (during the growth stage), or the increased latent heat energy provided by the greater total supply of water vapor?

6) If the initial moist layer is shallower but sufficiently more unstable thermally so that the maximum intensity of the convection is not significantly changed, is the storm shorter-lived (because of the smaller total supply of water vapor) or longer-lived (because of the greater low-level instability)?

7) Is either the evolution of the convection, or its configuration at maturity, strongly dependent upon the choice of initial perturbation?

To investigate questions 1), 2), and 3), respectively, the vertical equation of motion is altered by omitting the liquid water drag, assuming zero relative fall velocity for all water drops and omitting the pressure term in the gravitational buoyancy. The remaining questions are investigated directly by altering the initial base state in connection with questions 4) through 6) and the initial perturbation in connection with question 7).

The body of this paper consists of seven sections on the following plan. Section 2 deals with the governing equations and the assumptions involved in adapting them to the model. The finite-difference scheme is covered in section 3. Initial and boundary conditions are described in sections 4 and 5, and the parametrization of turbulence in section 6. Detailed presentations of the results for the nine comparative numerical experiments are given in section 7. Finally, in section 8, the results of the further study of the prototype case and of the seven variations upon it are presented.

2. THE GOVERNING EQUATIONS

Following is a list of the main variables and constants which will be used in this paper. Unless otherwise indicated in the text, overbars above variables will denote their horizontal averages and primes will denote departures from these averages.

B	a factor in the source function for the saturation mixing ratio in moist-adiabatic motions, defined in equation (27)
c_p	specific heat of dry air at constant pressure (1.004×10^3 m^2 sec^{-2} deg^{-1})
c_v	specific heat of dry air at constant volume
e_0	saturation vapor pressure over water at 0°C (6.1078 mb)
e_s	saturation vapor pressure over liquid water
F_x	horizontal component of the friction force per unit mass
g	acceleration of gravity (9.80 m sec^{-2})
i	horizontal index for computational grid points
j	vertical index for computational grid points
k	horizontal wave number
L	liquid water content; longitudinal length scale for turbulence
L_c	cloud droplet content
L_p	precipitation content
L_{vw}	latent heat of vaporization (2.500×10^6 m^2 sec^{-2})
m	vertical wave number
n	time level for finite differencing
p	pressure
q_v	mixing ratio for water vapor
q_{vs}	saturation mixing ratio for water vapor
R_d	gas constant for dry air (2.87×10^2 m^2 sec^{-2} deg^{-1})
R_v	gas constant for water vapor (4.61×10^2 m^2 sec^{-2} deg^{-1})
t	time
T	temperature
T_0	273°K
T_v	virtual temperature
u	horizontal velocity of air
V	relative fall velocity of water drops
w	vertical velocity of air
x	horizontal coordinate

z	vertical coordinate
γ_d	dry-adiabatic lapse rate, equal to g/c_p (9.77×10^{-3} deg m^{-1})
δ	a tagging parameter set equal to 1 in saturated air and 0 in unsaturated air
Δx	horizontal grid separation
Δz	vertical grid separation
$\hat{\eta}$	mass-weighted horizontal velocity
θ	potential temperature
θ_e	equivalent potential temperature
ρ	air density
ψ	two-dimensional stream function

Under a number of simplifying assumptions to be covered in detail in this section, the governing equations in this model are the following:

$$\frac{\partial u}{\partial t} = -u\frac{\partial u}{\partial x} - w\frac{\partial u}{\partial z} - \frac{1}{\bar{\rho}}\frac{\partial p'}{\partial x} + F_x \tag{1}$$

$$\frac{\partial w}{\partial t} = -u\frac{\partial w}{\partial x} - w\frac{\partial w}{\partial z} - \frac{1}{\rho}\frac{\partial p'}{\partial z} + g\left(\frac{T_v'}{\bar{T}_v} - \frac{p'}{\bar{p}} - \frac{L}{\bar{\rho}}\right) + F_z \tag{2}$$

$$\frac{\partial(\bar{\rho}u)}{\partial x} + \frac{\partial(\bar{\rho}w)}{\partial z} = 0 \tag{3}$$

$$\frac{\partial T}{\partial t} = -u\frac{\partial T}{\partial x} - w\frac{\partial T}{\partial z} - w\gamma_d + \frac{L_{vw}}{c_p}\delta Bw \tag{4}$$

$$\frac{\partial q_v}{\partial t} = -u\frac{\partial q_v}{\partial x} - w\frac{\partial q_v}{\partial z} - \delta Bw \tag{5}$$

$$\frac{\partial L}{\partial t} = -u\frac{\partial L}{\partial x} - w\frac{\partial L}{\partial z} + \delta\frac{-}{\rho}Bw + \frac{\partial}{\partial z}(VL_p) + \frac{Lw}{\bar{\rho}}\frac{\partial\bar{\rho}}{\partial z} \tag{6}$$

Equations (1)–(6) assume that the flow is two-dimensional in the sense that v and all variations in the y-direction are zero. The model is best thought of as simulating a representative plane cross-section of a squall line along its direction of movement, roughly normal to its orientation. Note that the two-dimensional assumption in itself eliminates the Coriolis force from equation (1). Neglect of the Coriolis force is in fact justifiable since the significant accelerations in squall-line convection take place on time scales two orders of magnitude shorter than a pendulum-day.

2.1 Equations of Motion and Continuity

Under the fundamental assumption of two-dimensionality, the equations of motion and continuity in otherwise general form are as follows:

$$\frac{\partial u}{\partial t} = -u\frac{\partial u}{\partial x} - w\frac{\partial u}{\partial z} - \frac{1}{\rho}\frac{\partial p}{\partial x} + F_x \tag{7}$$

$$\frac{\partial w}{\partial t} = -u\frac{\partial w}{\partial x} - w\frac{\partial w}{\partial z} - \frac{1}{\rho}\frac{\partial p}{\partial z} - g + D + F_z \tag{8}$$

$$\frac{\partial \rho}{\partial t} + \frac{\partial}{\partial x}(\rho u) + \frac{\partial}{\partial z}(\rho w) = 0 \tag{9}$$

where D represents the drag force due to water in liquid or solid form. In this model, freezing is neglected and the drag force is assumed equal to the weight of liquid water, i.e.,

$$D = -g\frac{L}{\rho} \tag{10}$$

as has been done in earlier moist convection models such as those of Ogura (1963), Takeda (1965, 1966) and Arnason et al. (1968). Equation (10) is essentially a result of the assumption that water drops reach their terminal velocity relative to air in a very short time. The form of the friction terms F_x and F_z will be discussed in connection with turbulence.

We now split the pressure p, the density ρ and the virtual temperature T_v into mean and perturbed components

$$\begin{aligned} p &= \bar{p} + p' \\ \rho &= \bar{\rho} + \rho' \\ T_v &= \bar{T}_v + T'_v \end{aligned} \tag{11}$$

where overbars denote horizontal averages across the domain and primes denote departures therefrom. In earlier models, the mean state has invariably been identified with the undisturbed part of the initial state, and has therefore been assumed time-independent as well as in hydrostatic balance. This is reasonable if the integration time is short enough so that the surroundings of the main convective element remain nearly undisturbed.

However, this will be seen not to be the case in this model, since considerable subsidence outside of the cloud leads to sufficient warming to raise the horizontally averaged temperature at some levels by as much as 3°C within the eighty-minute time interval being simulated. This is partly due to the rectangular geometry of the model. By running two numerical models of tropical cumulus convection, one rectangular and the other cylindrical, Murray (1970) demonstrated the exaggerating effect of a rectangular geometry upon the intensity of compensatory sinking relative to that of the updraft. The maximum downward velocity outside the cloud was about forty percent of the maximum in-cloud upward velocity in the rectangular model but only about fifteen percent in the cylindrical model. Such a difference would be expected on physical grounds since mass continuity implies a decreasing ratio of downward to upward motion as the relative area of subsidence is increased.

We assume that $\rho \approx \bar{\rho}$ in equation (10) and in the pressure gradient terms of (1) and (2), which is reasonable since the total variation of ρ at a point is two orders of magnitude smaller than ρ itself. We also assume that $\bar{p}$ and $\bar{\rho}$ are related by the hydrostatic equation

$$\frac{\partial \bar{p}}{\partial z} = - g \bar{\rho} \tag{12}$$

Since we are considering convection in which vertical velocities of 10 m $\sec^{-1}$ or more are expected, and in which the horizontal length scale is not much greater than the vertical length scale, the hydrostatic relation would not be expected to be valid at particular points in space. However, even though the aperiodic lateral boundaries in the model do not guarantee complete compensation of vertical motions, and therefore of net vertical accelerations, the compensation should still cancel out nonhydrostatic effects enough for the horizontally averaged pressure and density to satisfy equation (12) reasonably well. Substitution from equations (11) and (12) into equation (7) yields equation (1) while the vertical equation of motion becomes

$$\frac{\partial w}{\partial t} = - u \frac{\partial w}{\partial x} - w \frac{\partial w}{\partial z} - \frac{1}{\bar{\rho}} \frac{\partial p'}{\partial z} - g \frac{\rho'}{\bar{\rho}} - g \frac{L}{\bar{\rho}} + F_z \tag{13}$$

We next make the basic assumption that the local time derivative of density in the continuity equation can be ignored, so that the general continuity equation (9) simplifies to equation (3). As has been shown by Ogura together with Charney (1962) and Phillips (1962), this approximation filters out acoustic waves while admitting gravity waves. For this reason, a system of equations using (3) to approximate the continuity requirement is often referred to as "anelastic."

Assuming then that $\partial\rho/\partial t = 0$, we identify $\bar{\rho}$ with the initial undisturbed density which depends on height alone. If the vertical variation of ρ is also neglected, (3) simplifies to the continuity equation for incompressible flow. For shallow convection, Ogura and Charney showed by scale analysis and power series expansions that this further simplification is tolerable, and that in fact all density variations can be ignored except in the gravitational buoyancy term $-g\frac{\rho'}{\bar{\rho}}$ which in turn may be replaced by $g\frac{T'_v}{\bar{T}_v}$. This is the well-known Boussinesq approximation, which has commonly been incorporated into shallow convection models such as those of Ogura (1963), Asai (1964) and Arnason et al. (1968). In severe thunderstorms a parcel rising through an updraft may undergo a three-fold or four-fold density decrease, so that the fluid motions plainly cannot be considered even approximately incompressible, making the Boussinesq approximation invalid. But ρ' does not appear in the continuity equation under either the Boussinesq or anelastic approximation, and must then be eliminated in the gravitational buoyancy term of equation (13) by substituting from the linearized equation of state

$$\frac{\rho'}{\bar{\rho}} = \frac{p'}{\bar{p}} - \frac{T'_v}{\bar{T}_v} \tag{14}$$

This step is justifiable since $|p'/\bar{p}| << 1$, $|\rho'/\bar{\rho}| << 1$ and $|T'_v/\bar{T}_v| << 1$ even in deep moist convection. Then (13) reduces to (2).

The anelastic continuity equation implies the existence of a stream function ψ such that

$$\frac{\partial\psi}{\partial z} = \bar{\rho}u, \quad \frac{\partial\psi}{\partial x} = -\bar{\rho}w \tag{15}$$

Defining a mass-weighted meridional vorticity $\hat{\eta}$ by

$$\hat{\eta} = \frac{\partial(\bar{\rho}\,u)}{\partial z} - \frac{\partial(\bar{\rho}\,w)}{\partial x} \tag{16}$$

so that ψ is related to $\hat{\eta}$ by

$$\nabla^2\psi = \hat{\eta} \tag{17}$$

a vorticity equation may be obtained by multiplying both sides of the equations of motion (1) and (2) by $\bar{\rho}$, then cross-differentiating the resulting equations.

The resulting vorticity equation is

$$\frac{\partial \hat{\eta}}{\partial t} = -u\frac{\partial \hat{\eta}}{\partial x} - w\frac{\partial \hat{\eta}}{\partial z} + g\bar{\rho}\left(\frac{1}{\bar{p}}\frac{\partial p'}{\partial x} - \frac{1}{\bar{T}_v}\frac{\partial T'_v}{\partial x}\right) + g\frac{\partial L}{\partial x}$$

$$+ \frac{2w}{\bar{\rho}}\frac{\partial \bar{\rho}}{\partial z}\left(\hat{\eta} - u\frac{\partial \bar{\rho}}{\partial z}\right) + uw\frac{\partial^2 \bar{\rho}}{\partial z^2} + \frac{\partial(\bar{\rho}F_x)}{\partial z} - \frac{\partial(\bar{\rho}F_z)}{\partial x} \tag{18}$$

Note that if the Boussinesq approximation were valid, the terms involving $\partial p'/\partial x$ and the vertical derivatives of $\bar{\rho}$ would not be present. In view of the earlier mentioned evidence that pressure perturbations significantly affect the buoyancy in deep clouds, it was considered essential to somehow incorporate perturbation pressures into the buoyancy in the model.

In order to compute p' itself, one must solve an elliptic partial differential equation obtained by multiplying the equations of motion by $\bar{\rho}$ and then taking the divergence of the two resulting equations, eliminating time derivatives with the help of the anelastic continuity equation. The following diagnostic equation for p' results:

$$\nabla^2 p' + \frac{\partial}{\partial z}\left(g\bar{\rho}\frac{p'}{\bar{p}}\right) = -\frac{\partial}{\partial x}\left(\bar{\rho}u\frac{\partial u}{\partial x} + \bar{\rho}\,w\frac{\partial u}{\partial z}\right) - \frac{\partial}{\partial z}\left(\bar{\rho}\,u\frac{\partial w}{\partial x} + \bar{\rho}w\frac{\partial w}{\partial z}\right)$$

$$+ \frac{\partial}{\partial z}\left(g\bar{\rho}\frac{T'_v}{\bar{T}_v} - gL\right) + \frac{\partial}{\partial x}(\bar{\rho}F_x) + \frac{\partial}{\partial z}(\bar{\rho}F_z) \tag{19}$$

The inversion of the other elliptic equation (17) at each time step already required a significant fraction of the computing time. Furthermore, as has been stressed by Ogura and Charney (1962) and Arnason et al. (1968), p' can be determined only up to an arbitrary constant, and a physically well-motivated choice of the constant is not obvious. Boundary conditions must be made on the normal derivatives of p' rather than on p' itself, a problem closely related to this nonuniqueness. However, one need not solve the divergence equation in order to include the effect of pressure perturbations upon the vorticity. Since p' appears differentiated with respect to x, one can substitute for $\partial p'/\partial x$ from the horizontal equation of motion,

$$\frac{\partial p'}{\partial x} = \bar{\rho}\left(F_x - \frac{\partial u}{\partial t} - u\frac{\partial u}{\partial x} - w\frac{\partial u}{\partial z}\right) \tag{20}$$

This step is explicit, rather than iterative, enabling one to incorporate effects of p' upon the vorticity without adding significantly to the computing time. The finite difference scheme for handling equation (20) will be explained briefly in section 3.

2.2 The Thermodynamic Equation

In general, the First Law of Thermodynamics for an ideal gas may be stated as

$$Q = c_p \frac{dT}{dt} - \frac{1}{\rho}\frac{dp}{dt} \tag{21}$$

where Q is the heating rate per unit mass. For moist air, even in extreme cases, c_p is unlikely to differ by more than two percent from the value for dry air, and ρ usually varies by two percent or less in the horizontal. Therefore, to a close approximation,

$$\frac{dT}{dt} = \frac{1}{c_p\bar{\rho}}\frac{dp}{dt} + \frac{Q}{c_p} \tag{22}$$

with c_p approximated by its value for dry air and $\bar{\rho}$ corresponding to the initial base values of ρ in accordance with the anelastic approximation.

If the total derivatives dT/dt and dp/dt are expanded into local and advective terms, then the following equation results:

$$\frac{\partial T}{\partial t} = -u\frac{\partial T}{\partial x} - w\left(\frac{\partial T}{\partial z} + \gamma_d\right) + \frac{1}{c_p\bar{\rho}}\left(\frac{\partial p'}{\partial t} + u\frac{\partial p'}{\partial x} + w\frac{\partial p'}{\partial z}\right) + \frac{Q}{c_p} \tag{23}$$

using the earlier stated assumption that $\bar{p}$ and $\bar{\rho}$ satisfy the hydrostatic equation and a further assumption that $\partial\bar{p}/\partial t$ is small compared to $\partial p'/\partial t$. To handle correctly the terms involving p', one must solve equation (19) since $\partial p'/\partial t$ and $\partial p'/\partial z$ are present as well as $\partial p'/\partial x$. These pressure terms might be expected to be fairly important for temperature changes, since scale analysis indicates for instance that

$$\frac{1}{c_p\bar{\rho}}\, u\frac{\partial p'}{\partial x} : u\frac{\partial T}{\partial x} \sim \frac{\hat{P}}{c_p\,\bar{\rho}\,\hat{T}} \tag{24}$$

where $\hat{P}$ and $\hat{T}$ are typical magnitudes of perturbations for pressure and temperature, respectively. In the severe thunderstorm described by Barnes (1970), temperature deviations up to 10°C (relative to the distant surroundings of the storm) were observed in the updraft. This would suggest that the ratio $\hat{P}/c_p\,\bar{\rho}\,\hat{T}$ in that case was perhaps 5×10^{-2}, small yet not clearly negligible. In view of the considerable added computing time which the inversion of the elliptic equation (19) at every time step would entail, it was hoped that the pressure terms in (23) would not be crucial to the thermodynamics. Omission of these pressure terms was indeed justified by the results of two preliminary experiments, identical except that these terms were included in one and excluded in the other. Even after seventy-five minutes of simulated time, updraft velocities in the two runs were within about four percent of each other, with no significant differences in the configurations of the two-dimensional fields from one run to the other. Therefore, p' has been neglected in the thermodynamic equation.

Interestingly, additional justification for neglecting perturbation pressure terms in the thermodynamics (but not in the buoyancy) is provided by linearized analysis of stable gravity waves in a deep dry atmosphere, even though the lowest few kilometers in the moist model are unstable for saturated parcel motions (as in the cloud core). Both types of motion are admitted by the anelastic approximation. In appendix A, it is shown by such analysis that neglect of pressure terms in the thermodynamics has very little effect on the frequencies of gravity waves having vertical wavelengths like those occurring in the moist model. Also, in regard to vertical variation of wave amplitude, much less error results if pressure perturbations are neglected in the thermodynamics than in the buoyancy.

Ogura and Phillips (1962) pointed out a different problem connected with the role of perturbation pressure in deep convection. This is the chief reason why the temperature T has been used instead of the potential temperature θ in this model. The analysis of Ogura and Phillips was done in terms of θ rather than T, so that effects of pressure perturbations upon dry adiabatic temperature changes were automatically taken into account. However, as these authors emphasized, the addition of moisture greatly complicates the relationship between the thermodynamic variables when θ is used as a basic dependent variable. In particular, to compute the saturation vapor pressure e_s, which is a function of T alone, one must know p' since

$$\frac{T'}{\bar{T}} = \frac{\theta'}{\bar{\theta}} + \frac{R}{c_p}\frac{p'}{\bar{p}} \qquad (25)$$

This necessitates the inversion of an equation similar to (19), except that θ' instead of T' appears on the right-hand side. But in order to compute θ' where condensation is occurring, the latent heat release must be known. In turn, e_s must be known in order to calculate the rate of latent heat release. Since e_s is the very quantity whose value is desired, the relationship between the thermodynamic variables is seen to be highly implicit.

In actual convection, the diabatic processes contributing to the heating rate Q include condensation, evaporation, sublimation and freezing of water substance. Radiation is presumably of minor significance in view of the relatively short time scale of cumulonimbus convection. However, the ice phase has not been explicitly included, and only pseudo-adiabatic condensation or evaporation has been directly included in the heating term.

Cloud-edge evaporation has been separately incorporated into the model through a static phase adjustment which regards the presence of liquid water in unsaturated air as an unstable state; more will be said concerning this phase adjustment shortly. Following Murray and Anderson (1965),

$$Q = -\delta L_{vw} \frac{dq_{vs}}{dt} = L_{vw} \delta Bw \qquad (26)$$

where q_{vs} is the saturation mixing ratio, δ is zero in unsaturated air and unity in saturated air, and

$$B = g \frac{1 - (R_v/R_d)(c_p T - L_{vw} q_{vs})/L_{vw}}{L_{vw} + (c_p R_d T^2)/[L_{vw} q_{vs} (q_{vs} + R_d/R_v)]} \qquad (27)$$

Omitting the terms involving p' from (23) and using (26), we obtain equation (4).

The expression for B is very nearly the same as that derived by Hess (1959) to account for the difference between the dry-adiabatic and saturated-adiabatic lapse rates of temperature. On the one hand, Hess's expression was derived under the usual assumptions of pesudo-adiabatic parcel ascent, neglecting pressure differences between the parcel and its surroundings. In the observations of Barnes (1970) cited earlier, however, the observed lapse rate was practically saturation-adiabatic from the clouse base up to 490 mb. This suggests that at least up to the maximum updraft level, the parcel theory is satisfactory for calculating temperature changes due to saturated motions. Therefore, equation (26) was used.

2. 3 Moisture Equations

In general form, apart from the omission of diffusion as not being essential to these next few paragraphs, the equations for the time changes of water substance along parcel trajectories are the following:

$$\frac{dq_p}{dt} = \frac{1}{\bar{\rho}} \frac{\partial}{\partial z} (\bar{\rho}\, q_p V) + P - E_p \qquad (28)$$

$$\frac{dq_v}{dt} = -C + E_p + E_c \qquad (29)$$

$$\frac{d(q_v + q_c)}{dt} = -P + E_p \qquad (30)$$

These equations are based on forms used by Arnason et al. (1968). The symbols q_v, q_c and q_p denote the mixing ratios for water vapor, cloud droplets and precipitation, respectively; P represents production of precipitation (by the coalescence of cloud droplets with other cloud droplets or with existing precipitation particles), C the production of cloud droplets by condensation, E_c the evaporation of cloud droplets and E_p the evaporation of precipitation, while V is the terminal fall velocity of liquid water drops relative to the air. The term C is equal to $-\delta dq_{vs}/dt$, where δ and dq_{vs}/dt are as in (26).

Latent heat of fusion has not been explicitly included in the model, but the role of ice crystals in triggering precipitation has been parametrized by a method by Takeda (1965, 1966b). Precipitation is withheld until the model cloud top first reaches the -20°C level, after which any liquid water in excess of 1 gm m^{-3} is assumed to be precipitation and all other liquid water is assumed to be cloud droplets with negligible fall velocity. If L_p and L_c denote the contents (gm m^{-3}) of precipitation and cloud droplets, respectively,

$$L_p = \begin{cases} L - 1.0, & L > 1.0 \ (\text{gm m}^{-3}) \\ 0, & L \leq 1.0 \ (\text{gm m}^{-3}) \end{cases} \tag{31}$$

$$L_c = \begin{cases} 1.0, & L \geq 1.0 \ (\text{gm m}^{-3}) \\ L, & L \leq 1.0 \ (\text{gm m}^{-3}) \end{cases} \tag{32}$$

Since the freezing temperature of water drops in actual clouds varies between 0°C and about -40°C, the -20°C figure may be regarded as a crude average value.

All water drops, whether cloud droplets or precipitation, are assumed to have the same horizontal velocity components as the air. The formulation for V, taken after Takeda (1966a), gives

$$V = \begin{cases} 4.5\, L_p^{1/2} \ (\text{m sec}^{-1}), & L_p \leq 4.0 \ (\text{gm m}^{-3}) \\ 9.0 \ (\text{m sec}^{-1}), & L_p > 4.0 \ (\text{gm m}^{-3}) \end{cases} \tag{33}$$

Note that V = 0 for cloud droplets. This approximation is reasonable since cloud droplets are very small. An upper limit of 9 m $\sec^{-1}$ is taken for V since fall speeds in excess of that value are very rarely observed. The proportionality to $L_p^{1/2}$ at lower values of V follows from Takeda's assumptions that the fall speed is proportional to the radius of the drop and that the radii of individual drops increase exponentially in time due to capture of cloud droplets. In the reference being cited, L_p is first defined as an integral

$$L_p = \int nm \, dR \qquad (34)$$

taken over the spectrum of drop radii R, where n is the number density per unit radius and m represents raindrop mass; Takeda assumed that the radius which maximizes nm is proportional to that maximum, and that no new drops are added to the spectrum.

A weakness of this formulation is the absence of a mechanism for curbing the exponential growth of raindrops, since actual drops break up into smaller ones when sufficiently large. Also, the formulation precludes the modeling of precipitation falling through unsaturated air under a cloud base since the parametrization implies the existence of 1 gm m^{-3} of cloud droplets wherever precipitation is occurring. Nevertheless, as Takeda pointed out in this reference, the relationship between rainfall rate and precipitation content obtained from (33) provides reasonable agreement with observations, especially for values of L_p between about 2 and 5 gm m^{-3} .

In the moisture equations (28)—(30), the first term on the right-hand side of (28) results from the fall of precipitation relative to the air. Another term, $-\frac{q_p}{\bar{\rho}} [\frac{\partial}{\partial x}(\bar{\rho} u) + \frac{\partial}{\partial z}(\bar{\rho} w)]$, drops out because of the anelastic continuity equation. Empirical formulas for P and E_p have been derived by a number of authors including Arnason et al. (1968), Liu and Orville (1968) and Kessler (1969), assuming a drop size spectrum of the form proposed by Marshall and Palmer (1948). However, the detailed modeling of microphysical processes has not been a main objective of the numerical experiments in this thesis. Adding (30) to (28), subtracting (29), and using (26) and (27), we obtain an equation for the liquid water mixing ratio q_ℓ:

$$\frac{dq_\ell}{dt} = \frac{1}{\bar{\rho}} \frac{\partial}{\partial z}(\bar{\rho} q_p V) + \delta B w - (E_p + E_c) \qquad (35)$$

Since $L \approx \bar{\rho} q_\ell$, (35) may be written as follows to a good approximation after expansion of dq_ℓ/dt into local and advective terms:

$$\frac{\partial L}{\partial t} = -u \frac{\partial L}{\partial x} - w \frac{\partial L}{\partial z} + \frac{wL}{\bar{\rho}} \frac{\partial \bar{\rho}}{\partial z} + \frac{\partial}{\partial z}(VL_p) + \delta \bar{\rho} B w - \bar{\rho}(E_p + E_c) \qquad (36)$$

Apart from the evaporation term $-\bar{\rho}(E_p + E_c)$, equation (36) reduces to

(6). Rather than being explicitly represented in (6), the evaporation of liquid water into unsaturated air has been handled by a static phase adjustment similar to that used by Anderson and Murray (1965). The mathematical details of the adjustment are presented in appendix B. If the finite-difference analogues of the temperature and moisture equations yield supersaturation $(q_v > q_{vs})$ or liquid water in the presence of undersaturation $(L > 0$ and $q_v < q_{vs})$ at a grid point during a time step, either state is regarded as thermodynamically unstable and is assumed to adjust instantaneously and isobarically at that location. In the supersaturation case, condensation is assumed to occur until $q_v = q_{vs}$ exactly. Liquid water in unsaturated air is assumed to evaporate until either the wet-bulb temperature is reached or all the liquid water is consumed. After the static phase adjustment, all grid points with any liquid water are exactly saturated. No distinction is made between the evaporation of cloud droplets and the evaporation of precipitation; if the wet-bulb temperature is reached with some liquid water remaining, L_c and L_p are calculated from the final value of L by applying Takeda's formulation described earlier.

The static phase adjustment at unsaturated grid points with liquid water is similar to the final step of the three-stage "entraining parcel" method presented by Stommel (1947). However, in contrast to Stommel's one-dimensional approach, no attempt has been made in this two-dimensional model to specify the rate of dilution of cloudy air by unsaturated outside air. Stommel treated the environment of a cloud as totally passive, not changing with time and not participating in the convective circulation. In a two-dimensional model, as in three-dimensional reality, the convective circulation is shared by the cloud and its surroundings, resulting in horizontal gradients of physical variables both within the cloud and in its environment. In particular, the effects of mixing between cloudy air and its environment can no longer be parametrized by a fixed mass entrainment rate.

3. THE FINITE-DIFFERENCE SCHEME

3.1 Limitations on Accuracy and Storage

The final numerical experiments were performed with a 55-by-21 grid with $\Delta x = 3.2$ km (total length 172.8 km) and $\Delta z = 700$ m (total depth 14 km). Although the horizontal resolution in particular is comparable to the widths of the full domains used in shallow cumulus models, the rather crude mesh was necessitated by central core storage limitations and a need for a relatively long domain. Some thirty doubly-dimensioned variables were involved in the final FORTRAN source program, greatly limiting the permissible number of grid points; the faster moving parts of actual squall lines, mainly in the upper troposphere, may travel well over 100 km per hour.

The limitations on central core storage also limited the accuracy of the time differencing scheme. Consider an M-by-N grid with horizontal index i $(1 \leq i \leq M)$, vertical index j $(1 \leq j \leq N)$, horizontal grid separation Δx and vertical grid separation Δz. Let $Q^m_{k,j}$ denote the value of any variable Q after m time steps at the point (x_i, x_j). For reasons to be explained later in this section, the increment $\Delta_m t$ from the (m−1)st to the mth time level was allowed to vary from step to step so as to preserve computational stability while avoiding unnecessary time steps and hence extra computing time. The forward two-level time difference $\left(\frac{\delta_F Q}{\delta t}\right)^n_{i,j}$ defined by

$$\left(\frac{\delta_F Q}{\delta t}\right)^n_{i,j} \equiv \frac{Q^{n+1}_{i,j} - Q^n_{i,j}}{\Delta_{n+1} t} \tag{37}$$

has first-order accuracy. One may obtain second-order accuracy by using instead the three times levels from $n - 1$ through $n + 1$. In this model, however, storing the doubly-dimensioned variables under three rather than two addresses would have exceeded the central core storage available. Furthermore, second-order differencing for approximating a first-order derivative produces a general solution containing a purely computational mode as well as the desired physical mode. Since forward time differencing does not have this pitfall, it was used despite its lower accuracy.

The advective terms in the equations for vorticity, heat and moisture were handled by the upstream differencing method which has been used with forward time differencing by Ogura (1963), Orville (1964, 1968) and Takeda (1965, 1966b, 1971). Under this scheme, the analogue of the exact two-dimensional advection equation

$$\frac{\partial Q}{\partial t} = -u\frac{\partial Q}{\partial x} - w\frac{\partial Q}{\partial z} \tag{38}$$

is the following:

$$\left(\frac{\delta_F Q}{\delta t}\right)^n_{i,j} = -u^n_{i,j}\left(\frac{\delta_{UP} Q}{\delta x}\right)^n_{i,j} - w^n_{i,j}\left(\frac{\delta_{UP} Q}{\delta z}\right)^n_{i,j} \tag{39}$$

where

$$\left(\frac{\delta_{UP}Q}{\delta x}\right)^n_{i,j} = \begin{cases} (Q^n_{i,j} - Q^n_{i-1,j})/\Delta x & \text{if } u^n_{i,j} \geq 0 \\ (Q^n_{i+1,j} - Q^n_{i,j})/\Delta x & \text{if } u^n_{i,j} < 0 \end{cases} \tag{40}$$

$$\left(\frac{\delta_{UP}Q}{\delta z}\right)^n_{i,j} = \begin{cases} (Q^n_{i,j} - Q^n_{i,j-1})/\Delta z & \text{if } w^n_{i,j} \geq 0 \\ (Q^n_{i,j+1} - Q^n_{i,j})/\Delta z & \text{if } w^n_{i,j} < 0 \end{cases} \tag{41}$$

The popularity of the upstream differencing scheme among modelers has been largely due to its simplicity and its great stability, although it is only of first-order accuracy both in time and in space. Furthermore, the upstream method advects to each grid point only information which is upwind of the point, thereby preserving a physical realism less inherent in centered differencing despite the smaller truncation error.

A recent scheme, forward in time but second-order in space, was derived in detail by Crowley (1968) for the one-dimensional advective equation. If an analogous derivation is performed in two dimensions, the approximation to equation (38) is

$$\left(\frac{\delta_F Q}{\delta t}\right)^n_{i,j} = -u^n_{i,j}\left(\frac{\delta_C Q}{\delta x}\right)^n_{i,j} - w^n_{i,j}\left(\frac{\delta_C Q}{\delta z}\right)^n_{i,j} + \tag{42}$$

$$(u^n_{i,j})^2\left(\frac{\delta^2_C Q}{\delta x^2}\right)^n_{i,j} + 2u^n_{i,j}w^n_{i,j}\left(\frac{\delta^2_C Q}{\delta x \delta z}\right)^n_{i,j} + (w^n_{i,j})^2\left(\frac{\delta^2_C Q}{\delta z^2}\right)^n_{i,j}\Bigg]\frac{\Delta t}{2}$$

where

$$\left(\frac{\delta_C Q}{\delta x}\right)^n_{i,j},\quad \left(\frac{\delta_C Q}{\delta z}\right)^n_{i,j},\quad \left(\frac{\delta^2_C Q}{\delta x^2}\right)^n_{i,j},\quad \left(\frac{\delta^2_C Q}{\delta x \delta z}\right)^n_{i,j} \text{ and } \left(\frac{\delta^2_C Q}{\delta z^2}\right)^n_{i,j}$$

represent the usual centered-difference approximations to $\partial Q/\partial x$, $\partial Q/\partial z$, $\partial^2 Q/\partial x^2$, $\partial^2 Q/\partial x \partial z$ and $\partial^2 Q/\partial z^2$, respectively, at (x_i, x_j) after n time steps.

Standard one-dimensional linear stability analysis reveals that both the upstream and second-order Crowley schemes are neutrally stable or damping for all wavelengths if time steps are sufficiently small, with better preservation of wave amplitudes by the Crowley method. More precisely, consider solutions of the form $Q(x,t) = \tilde{Q}(t)e^{ikx}$ to the one-dimensional linear advection equation

$$\frac{\partial Q}{\partial t} = -U\frac{\partial Q}{\partial x} \tag{43}$$

where U is constant. It is readily verified that

$$\tilde{Q}(t) = \tilde{Q}(0)e^{-ikUt} \tag{44}$$

Note in particular that the amplitude $|Q(t)|$ is constant. Consider the following finite-difference analogues of (43):

$$\left(\frac{\delta_F Q}{\delta t}\right)_j^n = -U\left(\frac{\delta_{UP} Q}{\delta x}\right)_j^n \tag{45}$$

$$\left(\frac{\delta_F Q}{\delta t}\right)_j^n = -U\left(\frac{\delta_C Q}{\delta x}\right)_j^n + \frac{U^2}{2}\left(\frac{\delta_C^2 Q}{\delta x^2}\right)_j^n \Delta t \tag{46}$$

where, in this one-dimensional case, the finite differences $\left(\frac{\delta_F Q}{\delta t}\right)_j^n$, $\left(\frac{\delta_{UP} Q}{\delta x}\right)_j^n$, $\left(\frac{\delta_C Q}{\delta x}\right)_j^n$, and $\left(\frac{\delta_C^2 Q}{\delta x^2}\right)_j^n$ are defined by

$$\left(\frac{\delta_F Q}{\delta t}\right)_j^n = \frac{Q_j^{n+1} - Q_j^n}{\Delta t} \tag{47}$$

$$\left(\frac{\delta_{UP} Q}{\delta x}\right)_j^n = \begin{cases} (Q_j^n - Q_{j-1}^n)/\Delta x & \text{if } U \geq 0 \\ (Q_{j+1}^n - Q_j^n)/\Delta x & \text{if } U < 0 \end{cases} \tag{48}$$

$$\left(\frac{\delta_C Q}{\delta x}\right)_j^n = \frac{Q_{j+1}^n - Q_{j-1}^n}{2\Delta x} \tag{49}$$

$$\left(\frac{\delta_C^2 Q}{\delta x^2}\right)_j^n = \frac{Q_{j+1}^n + Q_{j-1}^n - 2Q_j^n}{(\Delta x)^2} \qquad (50)$$

Equations (45) and (46) are the analogues of (43) that result from use of the upstream scheme and the second-order Crowley scheme, respectively. They possess solutions of the form

$$Q_j^m = \hat{Q}^m e^{ik(j\Delta x)} \qquad (51)$$

where Q_j^m is evaluated at $x = j\Delta x$ and $t = m\Delta t$ for a constant time increment Δt. (Note that m is an exponent on the right-hand side of the last equation, but denotes the time level on the left-hand side.) For the upstream scheme,

$$\hat{Q} = \hat{Q}_{UP} = 1 + \frac{|U|\Delta t}{\Delta x}(\cos k\Delta x - 1) - i\,\frac{U\Delta t}{\Delta x}\sin k\Delta x \qquad (52)$$

while in the case of the Crowley scheme,

$$\hat{Q} = \hat{Q}_C = 1 + \left(\frac{U\Delta t}{\Delta x}\right)^2(\cos k\Delta x - 1) - i\,\frac{U\Delta t}{\Delta x}\sin k\Delta x \qquad (53)$$

The amplitudes $|Q_{up}|$ and $|Q_C|$ are easily found to be

$$|\hat{Q}_{up}| = [1 - 4\theta(1-\theta)\sin^2(k\Delta x/2)]^{1/2} \qquad (54)$$

$$|\hat{Q}_c| = [1 - 4\theta^2(1-\theta^2)\sin^4(k\Delta x/2)]^{1/2} \qquad (55)$$

where $\theta = |U|\Delta t/\Delta x$. Provided $\theta \leq 1$, both schemes are computationally stable for all wave numbers k by the usual definition, namely $|\hat{Q}| \leq 1$. For wavelengths of at least $2\Delta x$, the minimum wavelength resolvable by the grid, both schemes damp the shortest waves most strongly while much longer waves are only slightly damped.

3. 2 Computational Diffusion

We have just seen that although the solutions to the exact one-dimensional linear advection equation neither damp nor amplify with time, all wave solutions of either (45) or (46) decay exponentially in time if the computational stability criterion is met. This is also true of the exact solutions of form $\tilde{Q}(t)e^{ikx}$ to the equation

$$\frac{\partial Q}{\partial t} = -U\frac{\partial Q}{\partial x} + \nu\frac{\partial^2 Q}{\partial x^2} \tag{56}$$

which describes advection and Fickian diffusion of the property Q; ν, a positive constant, is the kinematic viscosity coefficient. In this case,

$$\tilde{Q}(t) = \tilde{Q}(0)e^{-\nu k^2}e^{-ikUt} \tag{57}$$

The degree of damping increases with the wave number, as is also true for waves resolvable by the advective finite-difference schemes being discussed. In fact, a numerical viscosity coefficient ν_N can be found in the following straightforward manner for the upstream method.

Up to second-order accuracy,

$$Q_j^{n+1} = Q_j^n + \left(\frac{\partial Q}{\partial t}\right)_j^n \Delta t + \frac{1}{2}\left(\frac{\partial^2 Q}{\partial t^2}\right)_j^n (\Delta t)^2 \tag{58}$$

If the linear advection equation (43) is differentiated once with respect to t, and the original equation substituted into the resulting mixed second derivative, one obtains

$$\frac{\partial^2 Q}{\partial t^2} = U^2\frac{\partial^2 Q}{\partial x^2} \tag{59}$$

Therefore,

$$Q_j^{n+1} = Q_j^n + \left(\frac{\partial Q}{\partial t}\right)_j^n \Delta t + \frac{U^2}{2}\left(\frac{\partial^2 Q}{\partial x^2}\right)_j^n (\Delta t)^2 \tag{60}$$

To second-order accuracy in space,

$$Q_{j+1}^n = Q_j^n + \left(\frac{\partial Q}{\partial x}\right)_j^n \Delta x + \frac{1}{2}\left(\frac{\partial^2 Q}{\partial x^2}\right)_j^n (\Delta x)^2 \tag{61}$$

$$Q_{j-1}^n = Q_j^n - \left(\frac{\partial Q}{\partial x}\right)_j^n \Delta x + \frac{1}{2}\left(\frac{\partial^2 Q}{\partial x^2}\right)_j^n (\Delta x)^2 \tag{62}$$

Substitution of one of the last two equations (the first if $U < 0$, the second if $U \geq 0$) into the right-hand side of (45), and making use of (47)—(48), one finds that the upstream scheme is equivalent to

$$\left(\frac{\partial Q}{\partial t}\right)_j^n = -U\left(\frac{\partial Q}{\partial x}\right)_j^n + \frac{|U|\Delta x}{2}\left(1 - \frac{|U|\Delta t}{\Delta x}\right)\left(\frac{\partial^2 Q}{\partial x^2}\right)_j^n \tag{63}$$

up to second-order accuracy both in time and space. Now the right-most term of equation (63) has the same mathematical form as Fickian diffusion with an eddy coefficient equal to $|U|\Delta x(1 - U\Delta t/\Delta x)/2$. This motivates a definition of "computational" diffusion: a numerical advection scheme has computational diffusion with a numerical eddy coefficient ν_N if the scheme can be written in the form

$$\left(\frac{\partial Q}{\partial t}\right)_j^n = -U\left(\frac{\partial Q}{\partial x}\right)_j^n + \nu_N\left(\frac{\partial^2 Q}{\partial x^2}\right)_j^n \qquad (64)$$

to second-order accuracy in time and space, with $\nu_N > 0$. This definition is motivated by earlier discussions of Hirt (1966) and Molenkamp (1968) concerning the diffusive effects of advective finite-difference schemes.

The computational diffusion implicit in the upstream differencing scheme differs in a fundamental way from Fickian eddy diffusion, in which the horizontal and vertical friction forces F_x and F_z are given by

$$F_x = \nu_e \nabla^2 u \qquad (65)$$

$$F_z = \nu_e \nabla^2 w \qquad (66)$$

where ν_e is an eddy diffusion coefficient. Unlike ν_e, the computational eddy coefficient for the upstream differencing scheme is proportional to the ambient fluid velocity U and to the grid separation, and of magnitude up to $U\Delta x/2$. Adding a constant wind without changing the gradients of the wind components has the unphysical effect of changing the computational coefficient of diffusion.

Mixing-length arguments suggest that

$$\nu_e \sim L'V' \qquad (67)$$

where L' is the eddy length scale and V' the magnitude of wind gusts due to the eddies. An estimate of ν_e in deep moist convection may be made on the basis of aircraft observations described by Rhyne and Steiner (1964) and Ackerman (1967). For each of eleven traversals through three severe thunderstorms in Oklahoma, Rhyne and Steiner found by power spectrum analysis that the root-mean-square horizontal and vertical gusts were of comparable magnitude and mostly between 3 and 5 m $\sec^{-1}$. Ackerman's spectral analysis suggested that horizontal length scales around 300 m and 700 m predominated for in-cloud fluctuations in wind. These observations then indicate a value for ν_e between about 900 and 3500 $m^2 \sec^{-1}$.

Typical values of U for deep sheared convection are 10 to 30 m $\sec^{-1}$; if Δx is about 3 km, as in this model, then ν_N is 1.5 to 4.5×10^4 $m^2 \sec^{-1}$, i.e., an order of magnitude larger than the real eddy diffusion. The strong diffusion in the upstream scheme did not turn out to be a severe enough handicap to prevent some of the basic features of thunderstorm evolution from being reproduced in the model, but the above analysis does point out some of the drawbacks of this computational effect. It is interesting to note that $\nu_N = 0$ for the Crowley scheme, in spite of its numerical damping which is therefore due to higher-order errors which cannot be detected by the truncated equations (60)–(62).

3.3 Molenkamp's Test

The final choice to retain the upstream scheme for all advective terms despite its rather low accuracy and strong computational diffusion was based largely on the results of a straightforward two-dimensional test devised by Molenkamp (1968) for advective finite-difference schemes. In this test, the scheme to be evaluated is applied to the two-dimensional advective equation (38) in a field of steady rotation about the central point of a square grid. Initially, the variable Q to be advected is positive in a circular region well removed from the center and boundaries, and zero elsewhere. Boundary values of Q are zero at all subsequent times for obvious reasons; Q initially increases linearly along all radii of the circular region to a central maximum. Ideally, this circular region should simply rotate about the grid center without change of size, shape or the configuration of Q since pure advection is the only physical process being modeled in the test. In particular, no spurious oscillations of Q about zero should develop.

Molenkamp's test was applied to the upstream and Crowley schemes under otherwise identical conditions. The parameters involved (grid resolution, number of grid points, initial Q-field, angular velocity and time increment Δt) were the same as in Molenkamp's article except that Δt was taken to be fifty seconds instead of thirty seconds. The configuration of Q after forty time steps is shown for the upstream scheme in figure 1 and for the Crowley scheme in figure 2, with the proper configuration also shown in dashed contours for comparison. The pseudo-diffusion of the upstream scheme is dramatically evident in the reduction of the maximum Q and the pronounced spreading of the region where $Q \geq .03$; also, the positive region has been advected slightly too slowly and the location of the maximum has propagated radially inward. The Crowley method preserves the values in the positive region considerably better than the upstream method. However, the advection speed is more in error than for the upstream scheme, since the apparent center of the positive region is nearly twice as far from the proper location. More seriously, the Crowley scheme produces spurious oscillations about zero, most noticeable upstream of the main positive region in figure 2. On the other hand, the upstream method never leads to negative values of Q in spite of its lower accuracy.

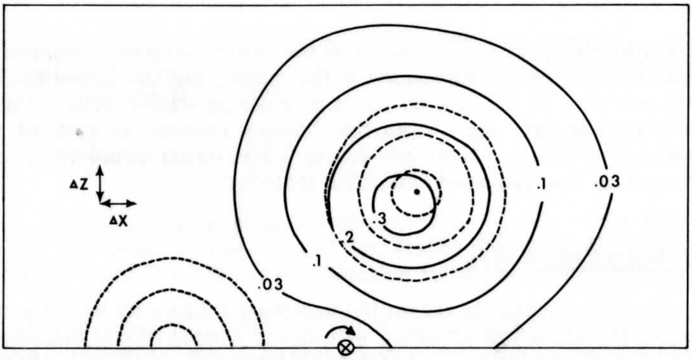

Figure 1. Results of Molenkamp's test (see text) applied to the upstream advective differencing scheme. Only the upper half of the square computational domain is shown. The pivot point is indicated by the circled "X" and the sense of rotation by the curved arrow. The numerically advected Q-field is indicated by solid contours. In order of increasing size, the dashed curves at the lower left represent the initial contours for Q = 0.8, 0.5 and 0.2, while the dashed curves further to the right represent the same respective values for the properly advected Q-field. The dot denotes the center of the properly advected region of positive Q.

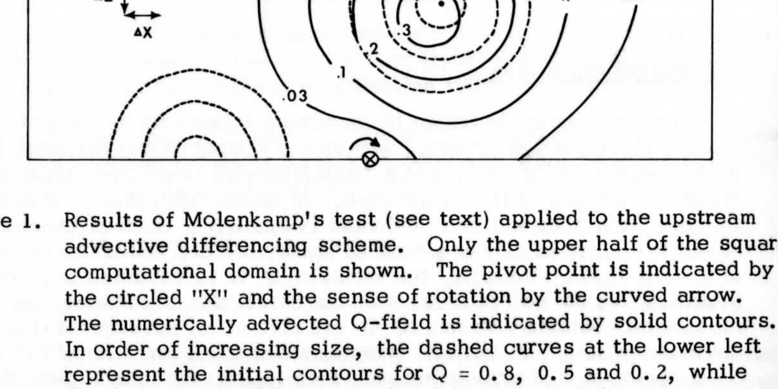

Figure 2. Same as figure 1, but applied to the second-order Crowley advective differencing scheme. Shaded areas correspond to negative values of Q generated by the scheme. Numbers to three decimal places indicate local extremes of the numerically advected Q-field.

An attempt was made to combine the two advective schemes by retaining the upstream method for the moisture variables while applying the Crowley method to advection of vorticity and temperature. However, when this hybrid approach was tried, conspicuous wavy perturbations developed on the streamlines and isotherms upstream of the traveling model cloud, and were quite noticeable even after a small number of time steps. Vertical velocities associated with these perturbations were about a third as large as in the cloudy updraft although no artificial clouds resulted. These waves did not materialize in runs which applied the upstream method to all advective terms, and were evidently the analogue of the nonphysical oscillations revealed by Molenkamp's test.

Orville and Sloan (1970), in their two-dimensional model of a large precipitating cumulus cloud over a mountain ridge, used the Crowley scheme for all advective terms. Any negative rainwater contents were redefined. Within a few minutes after cloud formation downwind of the mountain, wavy perturbations with vertical velocities of several meters per second were noted upstream of the mountain. These disturbances strongly resembled the oscillations which developed in the hybrid run just described. Orville and Sloan referred to them as "hydrothermals," but it appears that they may have been generated numerically at least in part, rather than purely physically.

In the reference cited, Molenkamp also tabulated the main results of his test applied to three other advection schemes which are forward in time but centered in space: Arakawa-Euler, Arakawa-Adams-Bashforth and Lax-Wendroff. The results showed that all these methods produce spurious numerical oscillations much like those produced by Crowley's scheme. In view of the disappointing results of the hybrid run, and Molenkamp's unfavorable findings regarding the other advective schemes, it was finally decided to retain upstream differencing for all advective terms in this model.

3.4 The Variable Time Increment

A complete stability analysis of any differencing scheme for the basic equations is highly cumbersome, even with all moisture excluded. This is especially true for the upstream scheme, which is asymmetric in space. However, no obvious numerical instabilities have arisen in practice by applying in slightly modified form the stability criterion appropriate to the linear two-dimensional advection equation

$$\frac{\partial Q}{\partial t} = -U\frac{\partial Q}{\partial x} - W\frac{\partial Q}{\partial z} \qquad (68)$$

where U and W are constant. This stability criterion may be shown to be

$$\Delta t \le \left(\frac{|U|}{\Delta x} + \frac{|W|}{\Delta z}\right)^{-1} \tag{69}$$

by a method analogous to the one-dimensional stability analysis described earlier. This simple analysis is not completely applicable to the complicated model equations, since they are highly nonlinear and other processes such as gravity waves are changing the wind and temperature, to say nothing of the moisture. In the model, at the beginning of the (n+1)st time step, the increment $\Delta_{n+1}t$ is taken to be the smaller of one minute and $K(\Delta_{n+1}t)_{max}$, where $(\Delta_{n+1}t)_{max}$ is the smallest value of $\left(\frac{|u^n_{i,j}|}{\Delta x} + \frac{|w^n_{i,j}|}{\Delta z}\right)^{-1}$ on the grid and K is taken somewhat smaller than unity based on the argument that decreasing the time step tends to preserve the stability even for nonadvective terms. The upper limit of one minute is chosen in order to avoid possible computational instability due to propagation of gravity waves independent of the wind itself. The variable time increment has been preferred over a constant increment, which would have to be based on the largest velocities to be expected throughout an entire run; in view of the complexity of the governing equations, these maximum velocities are difficult to estimate a priori. The method adopted reduces the number of time steps needed for simulating a given amount of elapsed time, since it allows the time increment to lengthen when convection weakens. In trial experiments, taking K = 0.6 did not result in any obvious instabilities. Therefore K was equal to 0.6 in the final experiments.

3.5 Other Finite-Difference Considerations

In the prognostic equations—the vorticity equation (18), the thermodynamic equation (4) and the moisture equations (5)—(6)—centered differencing is used for computing spatial derivatives in all nonadvective terms except for $\partial p'/\partial x$ appearing in the differentiated buoyancy term of (18). The term $\partial(VL_p)/\partial z$ in (6) arising from the dependence of precipitation fall velocity upon the precipitation content is regarded as a nonadvective term. In obtaining $\hat{\eta}$ during the (n+1)st time step from the finite-difference analogue of the vorticity equation, all quantities on the right-hand side of the equation are evaluated at the nth time step because of the forward time differencing. For use in evaluating $\partial p'/\partial x$, equation (20) is approximated by

$$\left(\frac{\delta p'}{\delta x}\right)^{n}_{i,j} = \bar{\rho}_j \left[(F_x)^{n}_{i,j} - \left(\frac{\delta_F u}{\delta t}\right)^{n-1}_{i,j} - u^{n}_{i,j}\left(\frac{\delta_{up} u}{\delta x}\right)^{n}_{i,j} - w^{n}_{i,j}\left(\frac{\delta_{up} u}{\delta z}\right)^{n}_{i,j} \right] \qquad (70)$$

Note that (70) cannot be applied until the second time step since the local acceleration is lagged to the interval between the (n-1)st and nth time steps. The time lag in $\partial u/\partial t$ is necessary since $u^{n+1}_{i,j}$ cannot be computed until ψ is determined from $\hat{\eta}$. In practice, this difficulty produced no obvious ill effects worth noting, in particular no sign of computational instability.

The elliptic equation (17) relating ψ and $\hat{\eta}$ has been inverted by a slightly generalized version of the Liebmann relaxation procedure described by Thompson (1961) for equal grid intervals. The mathematical details of the method, adapted to the unequal grid intervals Δx and Δz in this model, are deferred to appendix D. After ψ has been determined by this process, u and w are computed at all interior points by approximating equations (15) with centered differences:

$$u^{n}_{i,j} = (\psi^{n}_{i,j+1} - \psi^{n}_{i,j-1})/(2\bar{\rho}_j \Delta z) \qquad (71a)$$

$$w^{n}_{i,j} = -(\psi^{n}_{i+1,j} - \psi^{n}_{i-1,j})/(2\bar{\rho}_j \Delta x) \qquad (71b)$$

Taking advantage of the rectangular shape of the domain, u at the lateral boundaries and w at the top and bottom were obtained from the boundary values of ψ by using (71a) (with i = 1 and M) and (71b) (with j = 1 and N). The various boundary conditions for the model will be presented in detail in section 5.

During the (n+1)st time step, after the static phase adjustment for the nth time step has been made wherever needed, the tagging parameter δ appearing in the thermodynamic equation and in the moisture equations is set to 1 at each saturated grid point and is set to 0 at all other grid points. Since the phase adjustment results in the presence of liquid water at a grid point if and only if the air is saturated at that point, the following criterion has been used: $\delta = 1$ if $L^{n}_{i,j} > 0$, and $\delta = 0$ if $L^{h}_{i,j} = 0$. If a grid point was saturated at the end of the nth time step, δ at the (n+1)st time step is set equal to 1 regardless of the sign of $w^{h}_{i,j}$. Therefore, at a point where the air was saturated and rising (sinking) at the preceding time level, latent heat is assumed to be released (absorbed) during the following time step. This criterion differs from that used by Arnason et al. (1968), who did not allow for absorption of latent heat at saturated grid points with downward motion but assumed the descent to become dry-adiabatic immediately. It was felt that this more restrictive condition would not be appropriate for modeling severe thunderstorms since strong downdrafts are observed within cumulonimbus clouds, not only at cloud boundaries.

4. INITIAL CONDITIONS

4.1 The Base State

The choice of initial base state for temperature and humidity in this model was partly motivated by a composite sounding compiled by Fawbush and Miller (1953) from several dozen occasions three to six hours prior to severe thunderstorms with large hail in the southern plains. The main features of the sounding, taken up to about 400 mb, include a shallow layer of very moist air up to roughly 800 mb with much drier air of rather weak static stability (a lapse rate of 7.5° to 8° km^{-1}) extending from near 750 mb to at least the top of the sounding. The moist layer has slightly greater static stability than the dry layer, but has strong convective instability, while an inversion of about 3° marks the transition layer.

As pointed out in the Introduction, the inversion should be important to the potential severity of convection by enabling air of extremely high θ_e to accumulate underneath it for six to twelve hours without release of latent heat above it. However, the convection itself usually occurs during a considerably shorter time interval, i.e., one to two hours. Moreover, this research has focused upon the mode and intensity of severe convection in its mature stage rather than upon its triggering mechanism or early development. The inversion would be expected to have been weakened or eliminated, and the moist layer deepened by up to 1 km, at the onset of convection after several hours of rising motion on the order of 5 cm sec^{-1}. Figure 3 shows the initial base stratifications of temperature and relative humidity assumed in the comparative experiments. To study the consequences of varying the convective instability, three different constant values of relative humidity (seventy percent, eighty percent and ninety percent) were used from the surface to 2.8 km. The moderately stable layer between 9.1 and 10.5 km allowed the anvils to assume a realistic lenticular shape even though the vertical extents of the more vigorous clouds were limited only by the upper boundary (assumed unsaturated at all times).

The initial undisturbed wind is assumed horizontal ($w = 0$) and therefore nondivergent. Since the synoptic-scale divergence observed prior to severe storms is 1 to 2×10^{-5} sec^{-1}, two orders of magnitude smaller than the

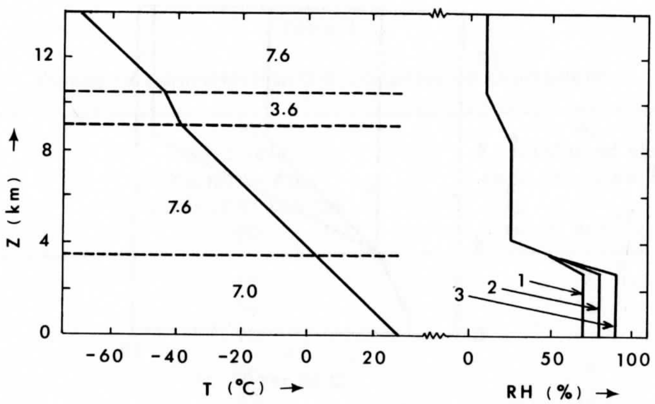

Figure 3. Initial base states for air temperature T and relative humidity RH in the comparative experiments. Left: Numbers in the layers separated by dashed lines indicate the lapse rate $-\partial T/\partial z$ (°C km^{-1}) in each layer. Right: Cases are numbered 1, 2, or 3 according to the assumed constant value H of the relative humidity from the lower boundary to 2.8 km, as shown in table 1.

divergence produced by the convection itself, any large-scale divergence should be quickly overwhelmed by the convection. Furthermore, some effects of the lifting process induced by the synoptic divergence patterns—the deepening of the moist layer and the elimination of its capping inversion—have already been taken into account in the initial sounding. In figure 4, the chief parameter of interest is the intensity of wind shear between 3.5 and 8.4 km. Three constant shear values—0, 2 and 4 m sec^{-1} $(700\ m)^{-1}$—were used in order to compare the modes and intensities of convection under conditions of no shear, moderate positive shear and strong positive shear in the middle troposphere, where much of the shear in severe storm situations often occurs. Positive values of u were assumed at all levels in order to avoid having both inflow and outflow at the same lateral boundary for reasons to be discussed in section 5. Although the wind speed may increase up to the tropopause in some actual situations, the shear in this model was terminated well below the tropopause in order to save computing time. Greater fluid velocities would have required smaller time steps in order to assure computational stability. The shear zone in the moist layer, with $\partial u/\partial z = 1$ m sec^{-1} $(700\ m)^{-1}$ in all cases, was included in order to model the commonly observed increase with height of the wind component along the direction of movement of squall lines, and was not varied from

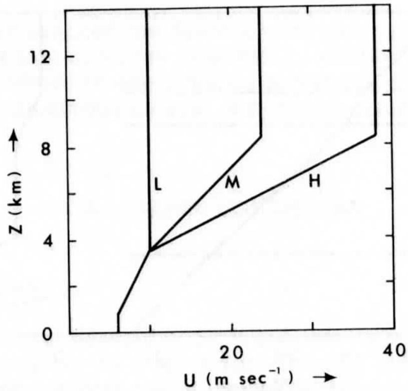

Figure 4. Initial base states for the wind velocity u in the comparative experiments. Cases are identified by the letter L, M or H according to the value of the total wind shear between 3.5 to 8.4 km as shown in table 1.

one run to another since it was desired to isolate the effects of midtropospheric shear. The wind profile with no shear above the moist layer is admittedly unrealistic for storms in the Great Plains, but it was considered important to include this profile in order to have systematic numerical comparisons.

The nine comparative experiments are classified according to the initial low-level relative humidity H and total middle-level wind shear S as listed in table 1. The experiments can be conveniently represented as a lattice of points in a moisture-shear plane, as shown in figure 5. When the comparative experiments are discussed in section 7, similar diagrams will be highly useful for summarizing the joint effects of these two parameters upon maximum updraft intensity, precipitation rate and several other properties of the convection.

The surface pressure in all cases is assumed to be 1000 mb, while the base pressure $\bar{p}$ and density $\bar{\rho}$ at higher levels are assumed to satisfy the hydrostatic equation (12). The numerical method used for computing $\bar{p}$ and $\bar{\rho}$ from the temperature and moisture profiles is presented in appendix C.

Table 1

Values of Parameters in the Comparative Experiments

Case	H, initial relative humidity from surface to 2.8 km (%)	S, total wind shear in 3.5-8.4 km layer ($m\ sec^{-1}$)
L1	70	0
M1	70	14
H1	70	28
L2	80	0
M2	80	14
H2	80	28
L3	90	0
M3	90	14
H3	90	28

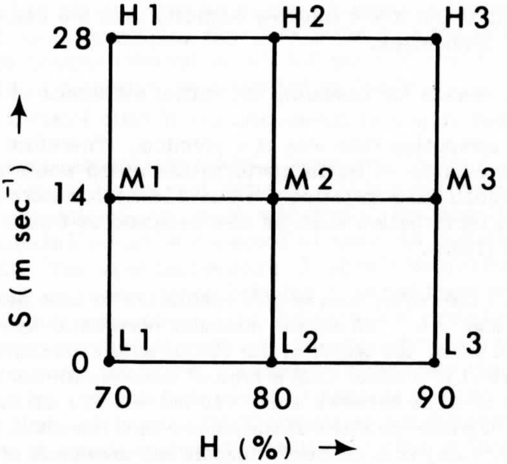

Figure 5. Representation of the initial parameters H and S (defined in table 1) for the comparative numerical experiments as points in moisture-shear space.

4.2 The Initial Perturbation

In addition to a convectively unstable base stratification, the initial conditions must include some sort of localized perturbation in order to generate meridional vorticity and thereby trigger the convection. In past cloud models, various initial perturbations have included: (a) a warm bubble in the lower levels, with or without a higher mixing ratio than the surrounding undisturbed air, (b) a cold front, (c) surface heating and evaporation, and (d) an initial cloud without any momentum perturbation. Deferring the mathematical details to appendix E, we will next describe the initial perturbation chosen for this model and indicate why the alternative formulations listed above were rejected.

Although each of the comparative runs assumes a different initial base state, the perturbation is the same in all cases. It includes a symmetric stream function perturbation between the surface and 4.2 km with a horizontal extent of 16Δx (51.2 km) and centered in the middle part of the grid as shown in figure 6. The maximum updraft is about 1.5 m sec^{-1}, while the maximum compensating downdraft is about 38 cm sec^{-1}. The region of upward motion of width 4Δx (12.8 km) includes a saturated region of width 2Δx (6.4 km) with base at 700 m and top at 3.5 km, having a maximum liquid water content of 1 gm m^{-3} and a maximum temperature perturbation of 1°C at the center. The dry sinking air on either side is up to about .2°C warmer with up to 3% lower relative humidity than the undisturbed air nearer to the lateral boundaries.

The main reason for assuming the initial existence of a cloudy region is that the earliest stages of convection are of little interest in this model. Furthermore, computing time was at a premium. Therefore, it was considered important to prescribe an initial perturbation which would avoid the extra time steps needed for generating a cloud a few kilometers high from a warm and cloudless perturbation such as was assumed by Ogura (1963) or Murray and Anderson (1965).

In view of the rather coarse grid resolution in both directions, with $\Delta x = 3.2$ km and $\Delta z = 700$ m, the minimum horizontal wavelength resolvable is 2Δx or 6.4 km, the width of the initial saturated region. The saturated region is somewhat broader than a typical cumulus element. The lifting condensation level is between about 980 mb and 925 mb for the initial temperature and humidity profiles assumed, so that the cloud base height of 700 m (near 925 mb) is reasonable despite the drawback of not being able to represent in significant detail the fluxes of physical properties into the cloudy region from beneath the base.

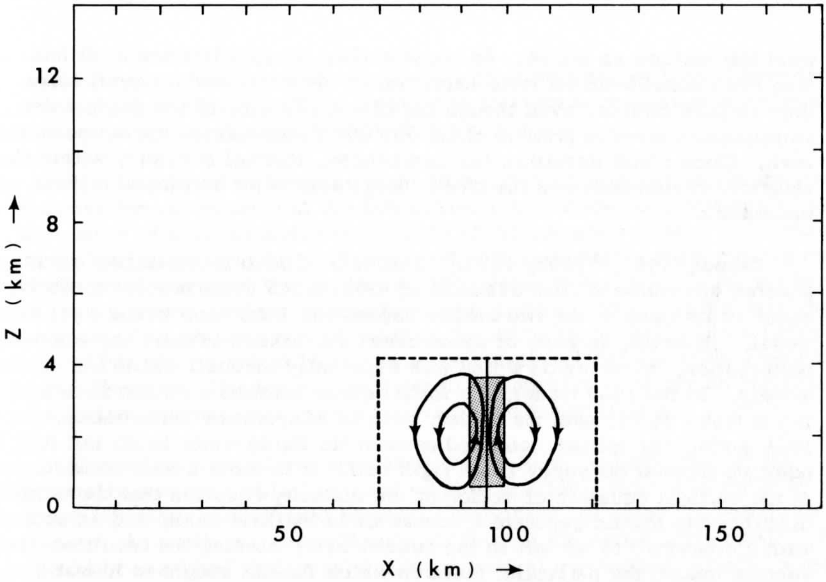

Figure 6. Initial grid domain, showing the initial disturbance described in the text. The dashed lines represent boundaries of the perturbed region. The solid closed contours represent streamlines of pure disturbance flow (deviation from the initial base state); the contour interval is 2×10^6 gm m^{-1} sec^{-1}. The region of initial saturation is indicated by shading.

In their early squall line model, Ogura and Charney (1962) assumed a marked cold front to be present initially. Although squall lines are often observed to form slightly ahead of cold fronts, the modeling of two contrasting air masses would be expected to make the definition of a base state quite difficult. The base temperature $\bar{T}$ should be assigned separate values for each air mass, since defining it as the horizontal average across the grid would imply the physically unreasonable situation of only positive thermal buoyancy in the warm air and only negative buoyancy in the cold air. Even if a sharp boundary is assumed to separate the warm and cold air masses initially, the interface would be expected to become less well-defined with time due to explicit or computational diffusion, making later identification of the air masses impossible at some points.

Orville (1968), in his experiments on mountain convection, considered the convection to be initiated by upslope winds which were induced by surface heating and evaporation prescribed as a function of time. In the present model, by contrast, there appeared to be no compelling reason to treat the surface as active. As noted earlier, destabilization aloft has long been considered far more important to the initiation of squall lines than surface effects, even though the direct modeling of the gradual destabilization process prior to cloud formation was outside the scope of this work. Once cloud formation has commenced, thermal buoyancy within the saturated region becomes the chief energy source for continued release of instability.

Takeda (1965, 1966b, 1971), in models of deep precipitating clouds in sheared environment, has assumed an erect cloud to be present initially, about 10 km deep in the two earlier papers and 2 km deep in the most recent model. However, in none of these cases did Takeda assume any momentum perturbation, an omission which was especially inconsistent in the earlier models. In the 1965 model, the initial cloud featured a concentration of liquid water at and near its center, with no temperature perturbation. In the 1966 model, the initial cloud had most of its liquid water in its left half and positive thermal buoyancy in its right half. It is clear from a consideration of the vertical equation of motion or the vorticity equation that these initial distributions should generate a downdraft in the first case, and an updraft with a downdraft to its left in the second case, biasing the resulting convection toward the particular features which Takeda sought to investigate. However, considerable vertical motion would be necessary in order to form a large cloud. Severe thunderstorms in sheared surroundings often resemble erect columns in the lower and middle troposphere, suggesting that the wind shear within the cloud column is substantially less than that of the nearly horizontal ambient wind. This in turn would imply strong divergence and therefore large vertical motions.. In the most recent model, Takeda's initial cloud is erect with no vertical motion, but only 2 km deep with a top at 3 km, making the assumption of no vertical motion less severely inconsistent than in his earlier models. However, measurements described by Warner (1970) indicate that velocities of 2 to 3 m $\sec^{-1}$ are representative of updrafts in real cumulus clouds of similar depths. It was therefore felt that the initial cloud in the present model should include an updraft at least on the order of 1 m $\sec^{-1}$ for physical consistency.

5. BOUNDARY CONDITIONS

5.1 General Considerations

One concern in the development of the model was the formulation of computationally stable and physically reasonable boundary conditions, especially for the lateral boundaries. The inclusion of a vertically-sheared ambient wind made it necessary to allow flow through the lateral boundaries; some of the basic difficulties entailed in treating lateral boundaries in such a case have already been described in the Introduction.

It was desired to keep the main convective circulation within the computational domain throughout the integration time, since computations might lose some of their significance if much of the circulation were to be "lost" through a lateral boundary. The risk of such information loss appears especially great in squall line modeling since very strong upper-level winds can cause the upper portions of thunderstorms to move 100 km within less than an hour. One obvious way of keeping the disturbance well removed from lateral boundaries would be to use a computational domain much longer than this. However, one would then have to compromise severely on horizontal resolution to avoid inordinate amounts of computing time and storage.

Two other alternatives presented themselves: subtracting out the vertically averaged initial ambient wind to provide a reference frame in which the storm core should be nearly stationary, or using the reference frame of the earth but intermittently displacing the entire grid domain. It should be remarked that in all earlier numerical convection models, a stationary grid has been used, so that this last alternative has not been previously explored.

Removal of the vertically averaged ambient wind was rejected because it was hoped to specify undisturbed inflow throughout the integration time along an entire lateral boundary. With the vertically averaged wind removed from a sheared profile, each lateral boundary would of course be mixed, i. e., with both inflow and outflow. Time-independent specification is probably the simplest physically reasonable inflow condition, since one might expect the flow far upwind of a convective disturbance to remain almost undisturbed. Roache and Mueller (1968) succeeded in specifying the horizontal inflow velocity for all time in their model of incompressible laminar flow with separation downwind of a step. While the scope of Roache and Mueller's experiments differed substantially from that of moist convection, their model was nevertheless similar to the present one in that it featured time integration of a vorticity equation, the use of a stream function and open aperiodic lateral boundaries. In view of these similarities, it appeared worthwhile to specify the horizontal inflow velocity as undisturbed.

A scheme to be explained shortly was devised for bodily shifting the grid so as to keep the leading cloud edge at least a prescribed minimum distance from the outflow boundary. It will be seen that attempts at complete specification of inflow as undisturbed were unsatisfactory, but that an acceptable compromise was achieved by allowing inflow properties to change during each shift and temporarily specifying them in between shifts.

The chief reason for keeping the cloud well removed from the outflow boundary was to help prevent the flow there from becoming sufficiently perturbed to cause inflow at any level. Since each shift entailed the special problem of defining variables at points devoid of previous information, it was desired to avoid any extra complications that might develop if the outflow boundary were to become mixed.

Since both the upper and lower boundaries were assumed flat and rigid, treatment of these boundaries was simpler than that of inflow or outflow. For lack of observational motivation for any more complex treatment, all upper boundary variables except horizontal momentum were kept undisturbed. The main concern in connection with the lower boundary was to simulate, with reasonable realism, the rainfall and horizontal spreading of evaporatively chilled air commonly observed at the surface during thunderstorms.

5.2 The Movable Grid

We now describe the procedure which was used for systematically shifting the grid downwind, directing our attention mainly to inflow during the next few paragraphs.

At the end of a time step, say the <u>nth</u>, after all computations including static phase adjustments have been performed, the grid is translated instantaneously downwind by the amount Δx if liquid water is present at any grid point within a fixed number of grid points, K, of the outflow boundary. Let the superscripts B and A refer to variables before and after the grid shift, respectively. Mathematically, if $L^n_{M-K,\,j} > 0$ for one or more values of j, then $Q^A_{i,\,j} = Q^B_{i+1,\,j}$ for all variables Q, if $2 \le i \le M-1$. The value of K was 12 in the final runs, in order to reduce possible effects due to outflow boundary conditions. The definition of $Q^A_{M,\,j}$ presents a special difficulty since a new outflow boundary is annexed where no previous calculations have been performed, necessitating some form of extrapolation. It appears most natural to define $Q^A_{1,\,j} = Q^B_{2,\,j}$ since the new inflow boundary clearly consists of points which were interior points prior to the translation, which has been assumed instantaneous. This was in fact the final decision regarding $Q^A_{1,\,j}$. It had been hoped to specify inflow as undisturbed at all times, however, even after grid shifts.

In two trial runs, the stream function (and therefore the horizontal velocity and the part of the vorticity contributed by $\partial^2\psi/\partial z^2$) was maintained undisturbed at inflow, even after each grid shift. In one of these runs, all other physical variables at inflow were also specified as undisturbed; in the other, w and the vorticity $\hat{\eta}$ were computed using interior values of ψ by the method of Roache and Mueller (1968), while horizontal gradients were set to zero for T, q_v and L. Unfortunately, in neither case did ψ or the variables derived from it adapt satisfactorily to the inflow conditions. Because the region of significant vertical motion expanded greatly in the horizontal as the convection matured, implausibly large horizontal gradients developed near inflow for these variables. Since this was one of the very difficulties to be avoided in formulating lateral boundary conditions, both attempts at inflow specification were dismissed as unsatisfactory.

5.3 Lateral Boundary Conditions

We now present the final formulation of the lateral boundary conditions for the movable grid, including a fairly detailed explanation of the outflow conditions, which have not been emphasized thus far. Note that in the remainder of this section, the symbol $\overline{Q}_j$ denotes the undisturbed value of a variable Q at the jth level.

Inflow Boundary

Prior to first grid shift: $Q^n_{1,j} = \overline{Q}_j$ for each variable Q (72)

During a grid shift: $Q^A_{1,j} = Q^B_{2,j}$ (73)

Between grid shifts: $Q^n_{1,j} = Q^N_{1,j}$ where N is the time level of the most recent grid shift. (74)

Outflow Boundary

Between grid shifts and prior to the first shift:

$$\psi^n_{M,j} = \psi^n_{M-1,j} + a(\psi^n_{M-1,j} - \psi^n_{M-2,j}), \qquad 0 < a < 1 \tag{75}$$

$$u^n_{M,j} = (\psi^n_{M,j+1} - \psi^n_{M,j-1})/(2\bar{\rho}_j \Delta z) \tag{76}$$

$$w^n_{M,j} = aw^n_{M-1,j} \tag{77}$$

$$\hat{\eta}^n_{M,j} = \frac{\psi^n_{M,j} + \psi^n_{M-2,j} - 2\psi^n_{M-1,j}}{(\Delta x)^2} \quad \frac{\psi^n_{M,j+1} + \psi^n_{M,j-1} - 2\psi^n_{M,j}}{(\Delta z)^2} \tag{78}$$

$$T^n_{M,j} = T^{n-1}_{M,j} + \Delta_n t\left[- u^{n-1}_{M,j}\left(\frac{\delta_{up} q_v}{\delta x}\right)^{n-1}_{M,j} - w^{n-1}_{M,j}\left(\frac{\delta_{up} T}{\delta z}\right)^{n-1}_{M,j} - w^{n-1}_{M,j}\gamma_d\right] \tag{79}$$

$$(q_v)^n_{M,j} = (q_v)^{n-1}_{M,j} + \Delta_n t\left[- u^{n-1}_{M,j}\left(\frac{\delta_{up} q_v}{\delta x}\right)^{n-1}_{M,j} - w^{n-1}_{M,j}\left(\frac{\delta_{up} q_v}{\delta z}\right)^{n-1}_{M,j}\right] \tag{80}$$

$$L^n_{M,j} = 0 \tag{81}$$

During a grid shift:

$$\psi^A_{M,j} = \psi^B_{M,j} + a(\psi^B_{M,j} - \psi^B_{M-1,j}) \tag{82}$$

$$u^A_{M,j} = (\psi^A_{M,j+1} - \psi^A_{M,j-1}(/(2\bar{\rho}_j \Delta z) \tag{83}$$

$$w^A_{M,j} = aw^B_{M,j} \tag{84}$$

$$\hat{\eta}^A_{M,j} = \frac{\psi^A_{M,j} + \psi^A_{M-2,j} - 2\psi^A_{M-1,j}}{(\Delta x)^2} + \frac{\psi^A_{M,j+1} + \psi^A_{M,j-1} - 2\psi^A_{M,j}}{(\Delta z)^2} \tag{85}$$

$$T^A_{M,j} = T^B_{M,j} \tag{86}$$

$$(q_v)^A_{M,j} = (q_v)^B_{M,j} \tag{87}$$

$$L^A_{M,j} = 0 \tag{88}$$

The following points should be stressed regarding both inflow and outflow:

1) Inflow variables are maintained undisturbed only until the first grid translation, and temporarily specified in between successive shifts. During

a shift, the variables which were one grid point downwind of the former inflow boundary become the new inflow variables. The positioning of the initial disturbance somewhat to the right of the grid center makes the first shift necessary before the horizontal gradients near the original inflow boundary exceed about one percent of those typical of the main convection. In practice, the grid has had to be shifted every two to five time steps (one to three minutes) depending upon the speed of the leading cloud edge. Not enough time elapses between consecutive grid translations for unreasonable gradients to develop near inflow, since the temporary specification scheme has resulted in smooth fields near inflow throughout the integration period in the final runs.

2) Although each new inflow boundary just after a shift consists of former downwind points, no use is made of information downwind of the temporary inflow boundary between shifts. This was felt to be more logical than the approach used by Orville and Sloan (1970) in their simulation of a mountain rainstorm. Though initial flow was from left to right at all levels, they allowed their lateral boundaries to become mixed at later times. At all lateral boundary points, regardless of the direction of the horizontal wind component, zero horizontal gradients were assumed for each variable. While that treatment obviously precludes the type of difficulty which spoiled the attempts at complete inflow specification in the present model, it ignores the logical distinction between inflow and outflow points.

3) All of the outflow boundary conditions do make use of information one to two grid points upwind of the boundary, since in this case such a procedure is physically logical. Both during and between shifts, w at outflow is assumed proportional to and smaller than the value one grid point upwind. Trial experiments indicated that setting $a = 0.5$ resulted in more satisfactory flow fields than setting a to either 1 (the limiting case with flat horizontal gradients) or 0.25, so that the intermediate value was used in all final runs. With $a = 1$, the circulation downwind of the main updraft was horizontally compressed in scale, with over-recovery from the increased positive shear below the cloud anvil. That is, rather than simply approaching zero downwind of the leading cloud edge while remaining positive, the wind shear due to the convective circulation (not including the undisturbed ambient wind shear) actually became slightly negative at and immediately upwind of the outflow boundary.

With $a = 0.25$, this circulation was elongated, including the region of negative u where low-level inflow ahead of the storm was greatest, so that the lowest few outflow points even acquired slight inflow. However, with $a = 0.5$, no inflow reached the outflow boundary in any run, and any over-recovery from large u aloft and small u at low levels was quite minor.

4) In anticipation that no cloud will develop downwind of the anvil, the liquid water content at outflow is maintained at zero. In all final runs, saturation was never closely approached downwind of the leading cloud edge, so that this outflow boundary condition on L produced no difficulties.

5) Between grid shifts, T and q_V are computed from the governing equations just as at unsaturated interior points, using upstream differencing for both the vertical and horizontal advection terms under the assumption that no inflow develops at the boundary. The method remained valid in all final runs since $u^n_{M,j}$ remained positive throughout the integration period for all values of j.

During each grid shift, T and q_V are extrapolated by assuming the finite-difference analogues to $\partial T/\partial x = 0$ and $\partial q_V/\partial x = 0$. This is perhaps the simplest form of extrapolation applicable to the new outflow boundary which results every time the grid is translated. One might argue that assuming $Q^A_{M,j} = \overline{Q}_j + a(Q^B_{M,j} - \overline{Q}_j)$ for $Q = T$ and q_v (as has been done for $Q = w$) would be most nearly consistent with the outflow condition on w during a shift. That is, if one physical variable (w in this case) is less disturbed at the outflow boundary than one grid point upwind of it, then the other variables should behave likewise. However, when this was attempted in a trial run with $a = 0.5$, the circulation between the cloud and the outflow boundary was more elongated horizontally than when the flat gradients were postulated, increasing the risk of inflow reaching the boundary.

6) Both during and between shifts, outflow values of u and $\hat{\eta}$ are computed directly from ψ to second-order accuracy, with u simply being computed just as at interior points since the boundary is vertical. Since $\hat{\eta} = \nabla^2\psi$, any formulation of $\hat{\eta}$ independent of that for ψ at outflow was felt to be mathematically less consistent than the formulation chosen. One might thus question the consistency of the lateral boundary conditions posed by Orville and Sloan (1970) and by Takeda (1971) in their convection models. Orville and Sloan postulated $\partial Q/\partial x = 0$ for each variable Q; if $\partial\psi/\partial x = 0$, it is consistent to postulate that $\partial u/\partial x = 0$ but not that $\partial w/\partial x = 0$. In view of the relation between w and ψ, the most appropriate condition on w should be $w = 0$. In Takeda's case, ψ was specified for all time while $\partial w/\partial x$ was assumed to be zero. However, the second assumption implies in finite difference form that $\partial^2\psi/\partial x^2 = 0$, so that ψ at a lateral boundary should be estimated by linear extrapolation and therefore should develop from the time-dependent interior values rather than be specified. Moreover, Takeda's lateral boundaries were mixed, so that his ψ was specified at outflow points in particular, contrary to physical consistency.

5.4 Upper and Lower Boundary Conditions

We now present the formulation of the upper and lower boundary conditions for the model, again indicating why some alternative approaches were rejected.

Lower Boundary

$$\psi^n_{i,1} = 0 \tag{89}$$

$$u^n_{i,1} = u^n_{i,2} \tag{90}$$

$$w^n_{i,1} = 0 \tag{91}$$

$$\eta^n_{i,1} = u^n_{i,1}\,\frac{\bar{\rho}_2 - \bar{\rho}_1}{\Delta z} \tag{92}$$

$$(L_{PV})^n_{i,1} = L^{n-1}_{i,1} + \Delta_n t \left[-u^{n-1}_{i,1} \left(\frac{\delta_{up} L}{\delta x}\right)^{n-1}_{i,1} + \frac{V^{n-1}_{i,2}(L_p)^{n-1}_{i,2} - V^{n-1}_{i,1}(L_p)^{n-1}_{i,1}}{\Delta z} \right. \tag{93}$$

$$(T_{PV})^n_{i,1} = \begin{bmatrix} 2(T_{PV})^n_{i,2} - (T_{PV})^n_{i,3} \ \text{ if } L^{n-1}_{i,2} > 0 \text{ and } w^{n-1}_{i,2} < V^{n-1}_{i,2} \\ T^{n-1}_{i,1} + \Delta_n t \left[-u^{n-1}_{i,1} \left(\frac{\delta_{up} T}{\delta x}\right)^{n-1}_{i,1} \right] \ \text{ otherwise} \end{bmatrix} \tag{94}$$

$$(q_{v_{PV}})^n_{i,1} = \begin{bmatrix} .95 q_{vs}((T_{PV})^n_{i,1}, \bar{p}_1) \ \text{ if } L^{n-1}_{i,2} > 0 \text{ and } w^{n-1}_{i,2} < V^{n-1}_{i,2} \\ (q_v)^{n-1}_{i,1} + \Delta_n t \left[-u^{n-1}_{i,1} \left(\frac{\delta_{up} q_v}{\delta x}\right)^{n-1}_{i,1} \right] \ \text{ otherwise} \end{bmatrix} \tag{95}$$

Upper Boundary

$$\psi^n_{i,N} = \text{constant} = \sum_{j=2}^{N} (\bar{\rho}_{j-1}\bar{u}_{j-1} + \bar{\rho}_j\bar{u}_j)/2 \tag{96}$$

$$u^n_{i,N} = u^n_{i,N-1} \tag{97}$$

$$w^n_{i,N} = 0 \tag{98}$$

$$\hat{\eta}^n_{i,N} = u^n_{i,N}\,\frac{\bar{\rho}_N - \bar{\rho}_{N-1}}{\Delta z} \tag{99}$$

$$L^n_{i,N} = 0 \tag{100}$$

$$T^n_{i,N} = \bar{T}_N \tag{101}$$

$$(q_v)^n_{i,N} = (\bar{q}_v)_N \tag{102}$$

where the subscript PV refers to provisional values of T, q_V and L computed prior to the static phase adjustment. If the adjustment is unnecessary, these values are of course retained in preparation for the next time step.

The following points should be emphasized:

1) The horizontal boundaries are assumed to be free-slip $(\partial u/\partial z = 0)$ with no vertical motion, so that they are streamlines. This is the simplest formulation apart from the no-slip condition $(u = 0)$, which is clearly inappropriate for the upper boundary, since the tropopause often corresponds to an upper-level jet. The earth's surface might be considered a no-slip boundary in the context of boundary-layer flow; in this model, however, the vertical grid resolution of 700 m is comparable to or greater than the thickness of the boundary layer, and the so-called surface wind observations are made commonly a few meters above the ground, much below one vertical grid interval in elevation yet sufficiently removed from the ground to make the no-slip condition inappropriate. Furthermore, abnormally strong surface winds are a key feature of squall lines, and a no-slip lower boundary condition would have precluded the modeling of this phenomenon.

2) The mass-weighted vorticity $\hat{\eta}$ appropriate to this model is related to the ordinary vorticity $\eta = \partial u/\partial z - \partial w/\partial x$ by the equation

$$\hat{\eta} = \bar{\rho}\eta + u\frac{\partial\bar{\rho}}{\partial z} \tag{103}$$

Since $\eta = 0$ because of the boundary conditions on u and w, the rather peculiar condition on $\hat{\eta}$ is chosen in order to be mathematically consistent.

3) If liquid water was present one grid interval above the lower boundary with falling precipitation and/or downward air motion at the preceding time step, the conditions on temperature and moisture simulated the arrival or advection of cold air and precipitation at the ground. Preliminary runs gave nearly linear temperature profiles in the cloud up to the updraft maximum, so that the indicated linear extrapolation of temperature to the surface was considered reasonable. A provisional liquid water content at the lower boundary is computed by applying the governing equation for L (with $w = 0$). This generally results in liquid water where the surface air is not yet saturated. The subsequent static phase adjustment then simulates evaporative surface cooling by falling precipitation. The provisional mixing ratio is taken slightly below the saturation value so that some evaporation is required to keep the lower boundary saturated.

It should be pointed out that the temperature and moisture at the lower boundary could have been treated in other ways which would have been simpler but which were considered less appropriate. The simplest approach would have been to maintain T and q_v at their initial undisturbed values and exclude liquid water, but this would be realistic only for a nonprecipitating cloud. Asai (1964) and Takeda (1965, 1966b, 1971) assumed that temperature and moisture variables showed the same variation with time at a lower boundary point as at the grid point immediately above. However, this would imply that the lapse rate near the surface does not change with time, and that rain reaches the surface as soon as it reaches the first grid level above the surface; such a situation is not realistic for simulating conditions during the passage of a thunderstorm. Except for the horizontal wind component, surface variables remain undisturbed until precipitation first reaches the ground.

4) The upper boundary has been assumed free-slip with no vertical motion, like the lower boundary. There was, however, no particular motivation for modeling a specific type of temperature or moisture perturbation, largely due to the lack of extensive measurements at tops of thunderstorms. The convection was not significantly different in two trial runs, one of which kept T, q_v and L undisturbed at the upper boundary, as in the final formulation. In the other trial run, some cooling and moistening of the upper boundary was allowed even though the cloud top was not

permitted to reach the upper boundary itself. If cloud droplets or precipitation were approaching an upper boundary point from one row beneath, the temperature perturbation at such a point was assumed equal to that immediately below, and the mixing ratio was perturbed by an amount proportional to the perturbation immediately underneath and small enough to prevent saturation. Since this formulation was rather contrived, and the convection was not significantly affected by replacing one upper boundary formulation by the other, the simpler approach was used.

6. TURBULENCE CONSIDERATIONS

The presence of considerable turbulence within deep convective clouds has long been apparent from the sudden altitude changes reported in such clouds by innumerable airplane pilots. Also, time-lapse photographs of cumulonimbus clouds reveal dramatically the familiar boiling appearance of their tops and sides as protuberances having length scales much smaller than those of the clouds continually rise and subside. As noted in section 3, spectral analyses of data from aircraft penetrations of cumulonimbus clouds have indicated that subcloud fluctuations in momentum and temperature have dominant horizontal wavelengths of only a few hundred meters; both horizontal and vertical wind gusts may have root-mean-square values of 3 to 5 m $\sec^{-1}$ with much higher extreme values.

In this model the horizontal and vertical friction forces per unit mass, written symbolically as F_x and F_z in the equations of motion (see section 2) have been identified with the familiar Reynolds stress divergences:

$$F_x = \frac{1}{\rho}\left[\frac{\partial}{\partial x}\,\overline{(-\rho u'u')} + \frac{\partial}{\partial z}\,\overline{(-\rho u'w')}\right] \tag{104}$$

$$F_z = \frac{1}{\rho}\left[\frac{\partial}{\partial x}\,\overline{(-\rho u'w')} + \frac{\partial}{\partial z}\,\overline{(-\rho w'w')}\right] \tag{105}$$

In equations (104) and (105), primes denote instantaneous local departures of a quantity from its mean value obtained by averaging the quantity over a time interval much longer than the time required for an eddy to pass through. Overbars denote local averages taken over such a time interval. *

---

* Or, the average may be taken at a given instant over a region surrounding the point and having dimensions much larger than those of the eddies.

The most common approach in convection modeling has been to assume pure Fickian diffusion, regarding the small-scale eddies as exchanging momentum like molecules. Models adopting this parametrization have included those of Ogura (1963), Asai (1964), Murray and Anderson (1965), Takeda (1965, 1966b, 1971) and Orville and Sloan (1970). This representation was given in equations (65) and (66); the values of the eddy viscosity coefficient ν_e have ranged up to 500 m^2 sec^{-1}. It was mentioned in section 3 that if the Fickian representation is valid, one might expect values of 1 to 3×10^3 m^2 sec^{-1} to be reasonable for cumulonimbus convection on the basis of aircraft observations. Turbulent diffusion might be expected to have the same qualitative effect as Fickian diffusion, i.e., reduction of gradients through mixing. The two processes themselves are, however, quite different in nature, one being linear and the other highly nonlinear, and eddies are not infinitesimally small colliding particles separated by empty space.

Lilly (1962) used a more general "eddy viscosity" approach in a model of dry buoyant convection initiated by an instantaneous thermal line source. In this case, the eddy viscosity coefficient was nonlinear, being proportional to the square of the grid resolution and to the magnitude of the deformation for the grid-scale flow. Lilly noted that if the scale of the eddies is assumed to be limited by the grid separation, such a form for the coefficient is reasonable according to dimensional analysis. However, while the convective element in Lilly's model showed qualitatively reasonable behavior, it did not exhibit the shape preserving stage which one would expect from laboratory experiments. Neglect of eddy fluctuations in the third dimension was considered the main reason for the dissimilarity.

Lilly's approach resembled the mixing-length theory of Prandtl (1925). This theory treats turbulent mixing as a discontinuous process in which an eddy moves along a path while conserving its momentum; the turbulent velocity fluctuation is identified with the difference between the mean velocities of the surroundings at the ends of the eddy path, and is assumed to be instantaneously absorbed by the surroundings. The root-mean-square path length, referred to as the "mixing length," is likened to the mean free path for molecular motions. This analogy is not valid since actual eddies are not separated. Also, due to forces induced partly by pressure perturbations, momentum is not strictly conserved along eddy trajectories but adapts partially to that of the surroundings.

A rather recent hypothesis of Lettau (1967) for relationships between the macroscale and eddy states includes explicit representations for the turbulent fluctuations, and was adopted to the formulation of the friction terms in the model. The vector velocity fluctuation is defined in terms of the mean velocity vector and the eddy displacement vector in a way which recognizes the three-dimensionality of actual turbulence as well as the opposing tendencies of momentum toward conservation and adaptation to the surroundings along eddy trajectories. Two main isotropy assumptions are incorporated: equal root-mean-square values are postulated for all three components of the eddy displacement and for all nine possible space derivatives of these components. All covariances between any two of these twelve quantities are assumed to vanish. For two-dimensional mean flow with $\bar{v} = 0$, the root-mean-square eddy displacement L assumed constant and the effects of fluid compressibility ignored, one obtains the following expressions for $\overline{u'u'}$, $\overline{u'w'}$, and $\overline{w'w'}$:

$$\overline{u'u'} = (\partial\bar{u}/\partial z - \partial\bar{w}/\partial x)^2 \frac{L^2}{3} + 2(\alpha\bar{w})^2 + 3(\alpha\bar{u})^2 \qquad (106)$$

$$\overline{u'w'} = \alpha^2\bar{u}\,\bar{w} \qquad (107)$$

$$w'w' = (\partial\bar{u}/\partial z - \partial\bar{w}/\partial x)^2 \frac{L^2}{3} + 3(\alpha\bar{w})^2 + 2(\alpha\bar{u})^2 \qquad (108)$$

where α is the common value assumed for the nine root-mean-square eddy displacement derivatives in the second isotropy postulate. The terms $\overline{u'v'}$, $\overline{v'v'}$ and $\overline{v'w'}$ are of no importance to the numerical model since they either involve y-derivatives (assumed to vanish in the model) or the missing second equation of motion. We next describe briefly the adoption of equations (106)–(108) to the model.*

The power spectral analyses described by Rhyne and Steiner (1964) suggest that the Reynolds stresses in clear air are an order of magnitude smaller than inside severe storms. Accordingly, equations (106)–(108) are applied only at saturated grid points, and the stresses are neglected at all other points. The mean flow is identified with the total grid-scale minus the initial basic flow in order to assure that the spatial pattern of turbulence obtained from equations (106)–(108) is independent of the reference frame;

---

*In the reference cited, the term corresponding to $\alpha^2\bar{u}\,\bar{w}$ in (107) is erroneously given as $3\alpha^2\bar{u}\,\bar{w}$. Although this error was unintentionally present in the numerical experiments, making the calculated point-by-point friction incorrect, it did not significantly alter the magnitude of the friction terms, which were in either case much smaller than any of the other individual forces. When two-dimensional force fields in the model are discussed in section 8, only the magnitude of the friction will be considered.

in the free atmosphere, the vertical wind shear is presumably much more important in determining convective structure (including turbulence) than is the wind velocity relative to the earth. In the model, L is assumed constant and equal to 500 m, comparable to the dominant wavelengths of wind fluctuations as revealed by the spectral analysis of Ackerman (1967). The assumption of constant L, while probably a considerable oversimplification, is made for lack of observational motivation for any more complex specific formulation. The parameter α is taken equal to 0.1, a value similar to that found for steady two-dimensional jets as noted by Lettau (1967).

Finally, it should be noted that no explicit terms for diffusion of heat or moisture were included in the model. Recall that the upstream differencing scheme contains a purely computational diffusive effect with an eddy coefficient proportional to the fluid speed and to the grid resolution, and that for the rather crude horizontal resolution in this model the horizontal pseudo-diffusion is an order of magnitude greater than what might appear reasonable from observations. In view of this dominant pseudo-diffusion and the elusiveness of any physically convincing non-Fickian representation of heat or moisture diffusion, explicit terms for these processes were omitted.

7. RESULTS OF THE COMPARATIVE EXPERIMENTS

The features of main interest in the comparative experiments will be analyzed largely through three types of diagrams:

1) Height-time or "z-t" diagrams showing the temporal development of the vertical profiles for vertical velocity, liquid water content and equivalent potential temperature in the storm core. The core is taken to be that column of grid points containing the maximum in-cloud upward air velocity, with a few exceptions which will be explained.

2) Fields of the deviations of ψ and T from their undisturbed initial patterns over the entire computational domain at fifty minutes and seventy minutes*; similar diagrams showing the deviation of p at fifty minutes

---

*Each experiment simulated approximately eighty minutes of real time. Results will often be referred to as valid at multiples of ten minutes. Because of the variable time increment, no two model storms could be compared at exactly equal elapsed times. However, the greatest error committed from its initial field.

3) Two-dimensional fields of rainfall rate and the airflow relative to the traveling storm core at fifty minutes for all cases and at seventy minutes for three cases exhibiting especially marked changes between fifty and seventy minutes.

The diagrams of flow relative to the storm will prove most helpful for comparing the numerically generated airflow patterns with those proposed in several two- and three-dimensional schematic models based on observations as well as on theory. The schematic models of Newton (1950), Newton and Newton (1959), Browning and Ludlam (1962), Browning (1964), Goldman (1968) and Fankhauser (1971) have each focused on the airflow relative to the moving cloud core. Furthermore, as will become evident, much of the dynamics of the model storms is more clearly explained relative to the moving cloud than relative to the earth.

In view of the large number of illustrations and the complexity of the results, comparisons between numerical results and observations (or other models, numerical and schematic) will be deferred until after the figures have been presented and analyzed. Immediately preceding the discussion, the combined influence of moisture and shear upon a number of parameters derived from the results will be summarized by plotting each parameter in the "moisture-shear" space introduced at the end of section 4.

7.1 Height-Time Diagrams

The z-t diagrams for the comparative runs are shown in figures 7 throug 15. Parts (a), (b) and (c) of each figure refer to w, L and θ_e respectively. The moisture-shear space shown in figure 5 is swept through in successive columns from left to right: Figures 7 through 9, 10 through 12 and 13 through 15 cover the cases of least, intermediate and greatest moisture, respectively, while each group of three figures sweeps through a column from least to greatest shear.

In this model, the equivalent potential temperature θ_e is not carried along with the main calculations but is computed for diagnostic purposes

---

by using the earliest time level equaling or exceeding a multiple of ten minutes was less than one minute, much less than the time required for significant changes in the convection.

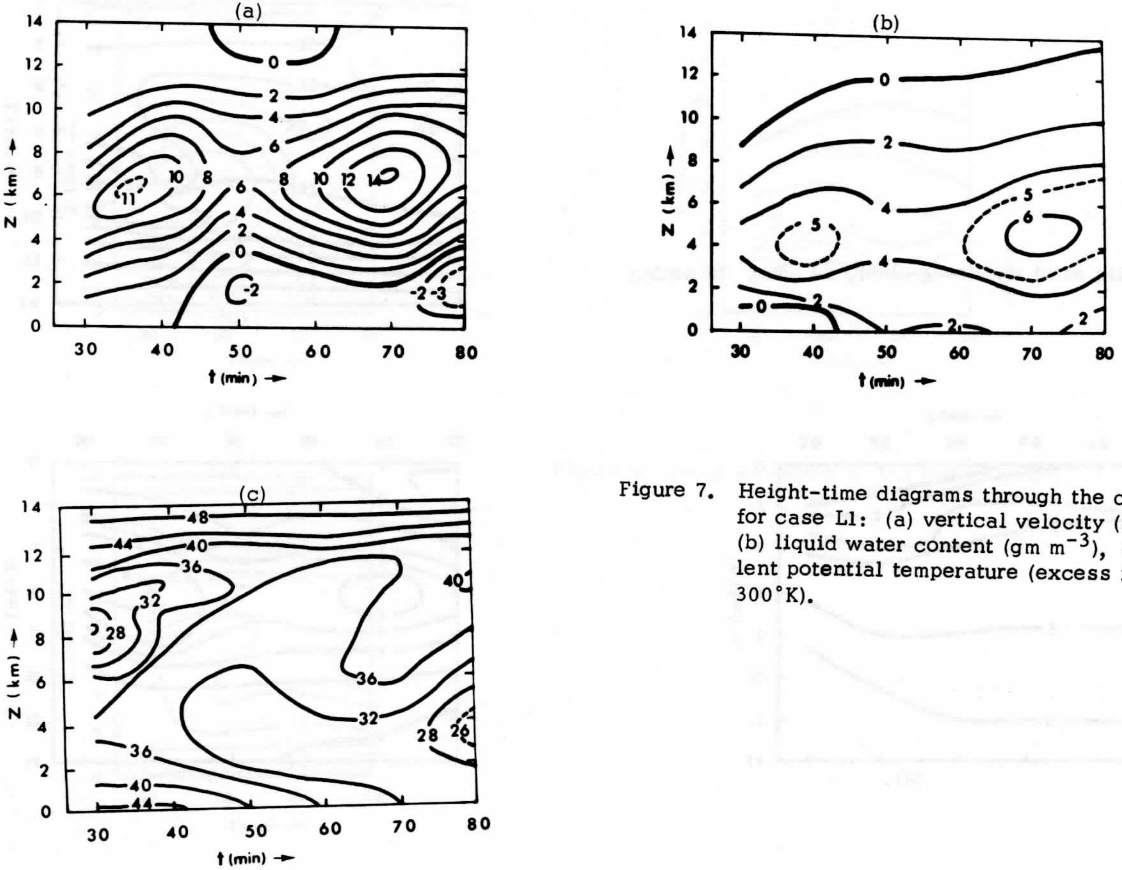

Figure 7. Height-time diagrams through the cloud core for case L1: (a) vertical velocity (m sec^{-1}), (b) liquid water content (gm m^{-3}), (c) equivalent potential temperature (excess in °K above 300°K).

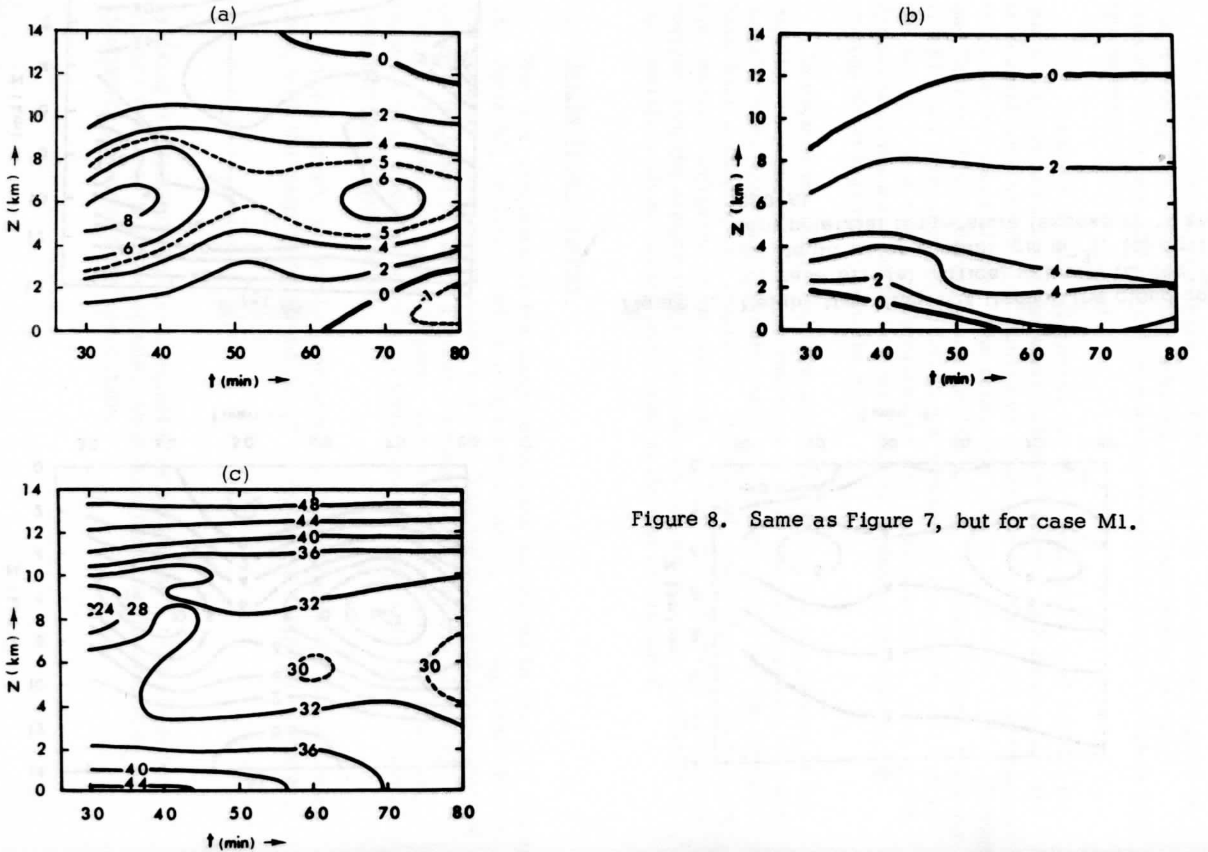

Figure 8. Same as Figure 7, but for case M1.

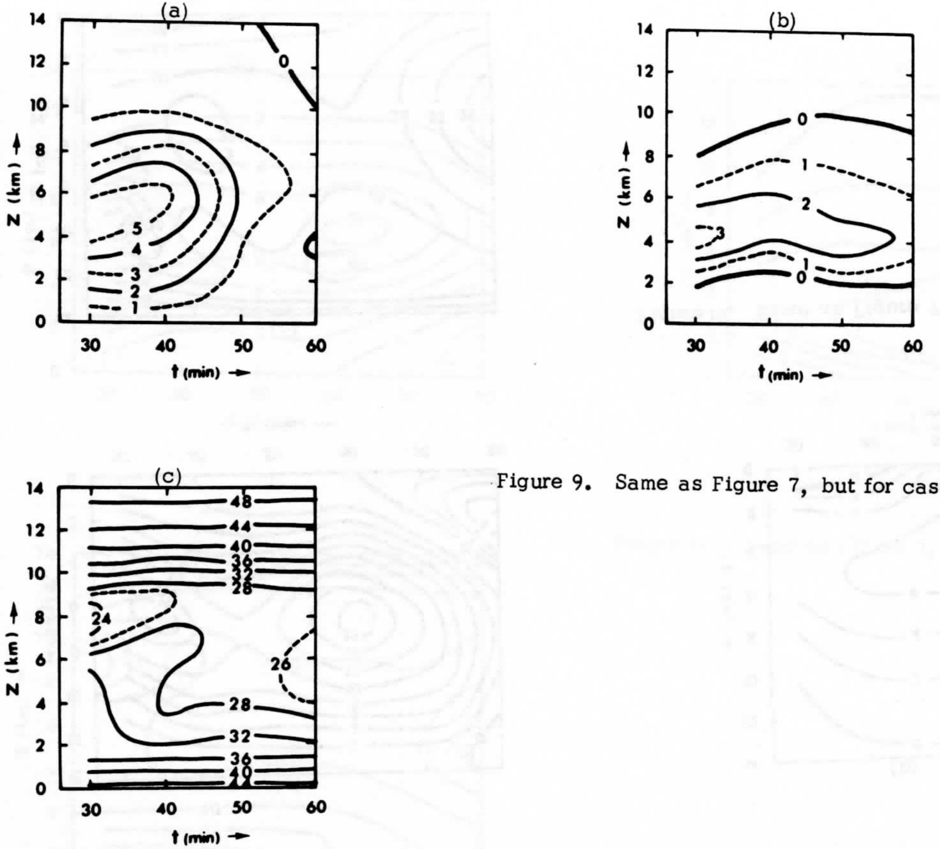

Figure 9. Same as Figure 7, but for case H1.

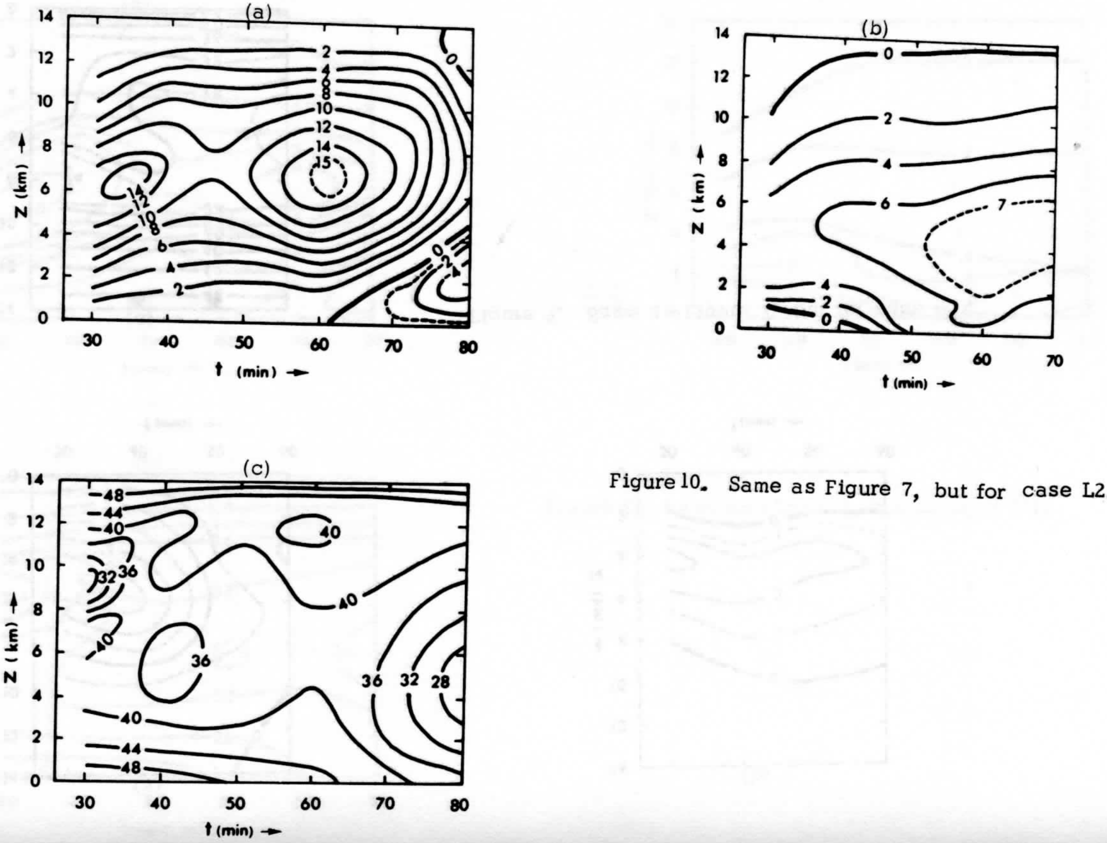

Figure 10. Same as Figure 7, but for case L2.

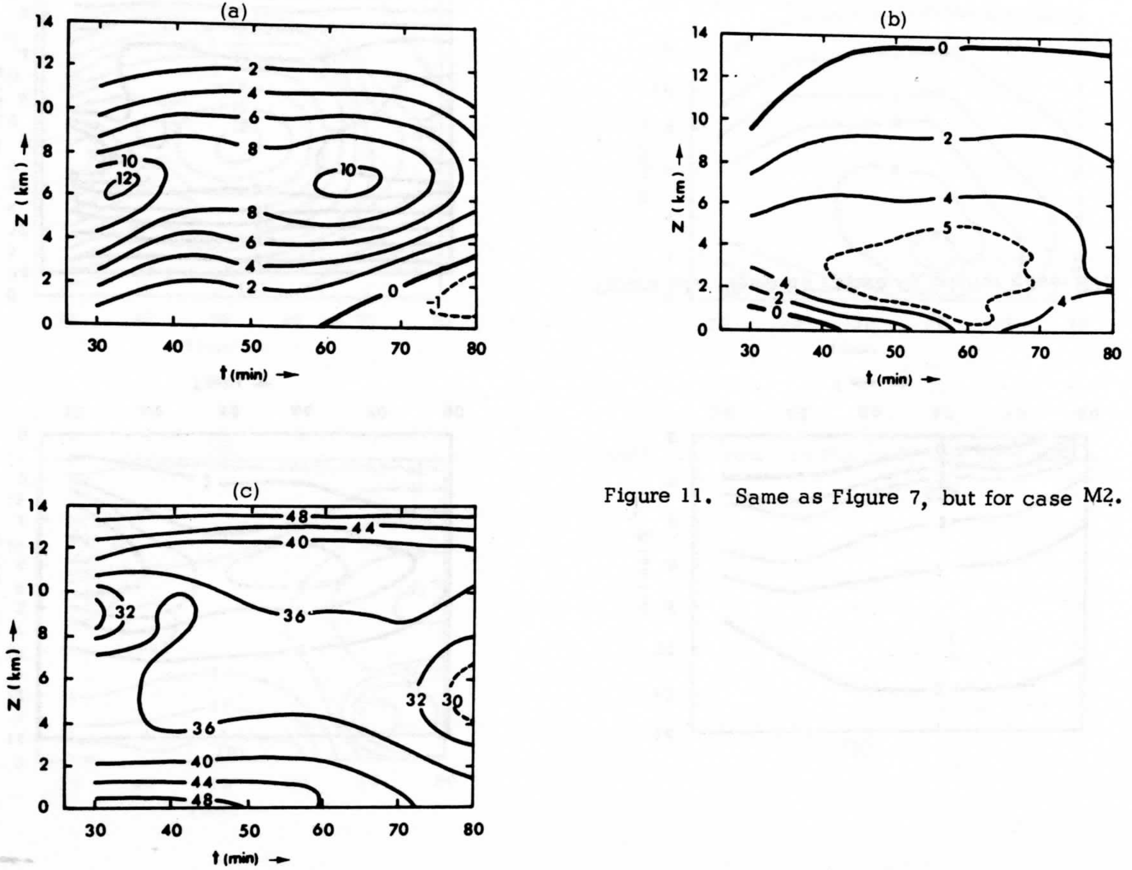

Figure 11. Same as Figure 7, but for case M2.

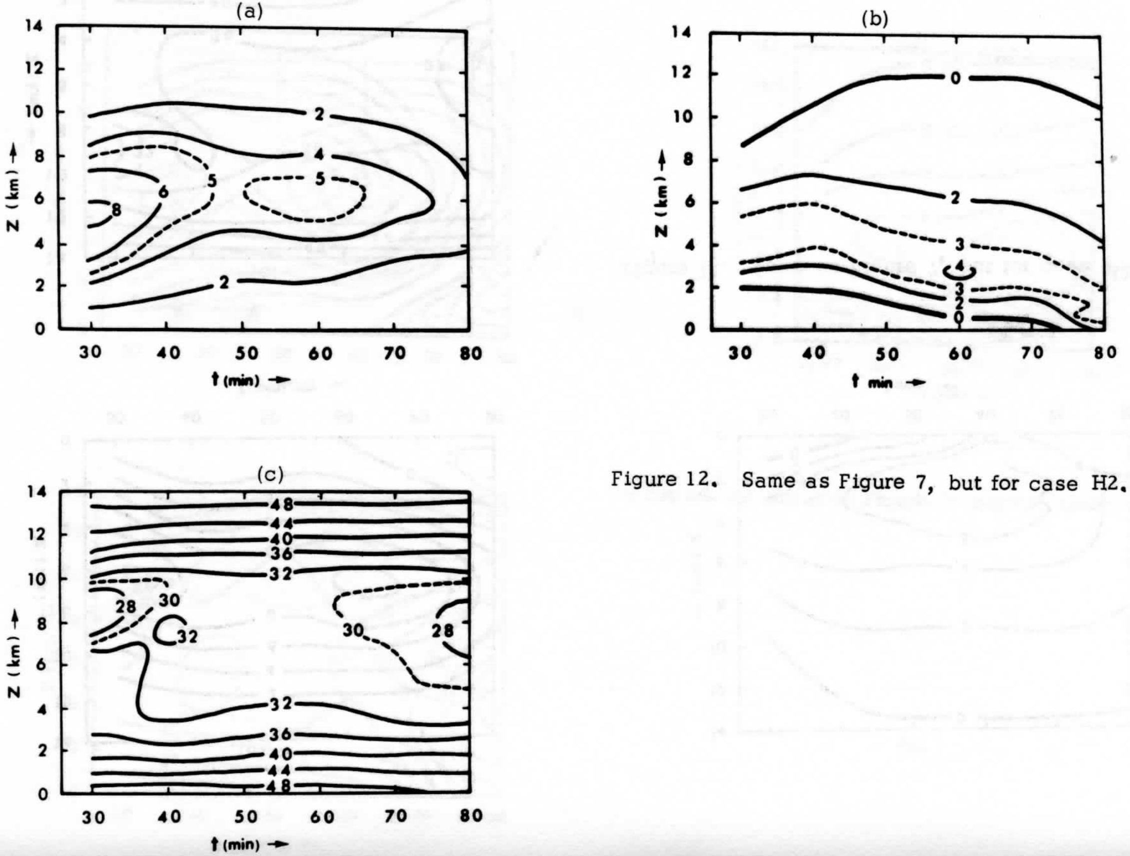

Figure 12. Same as Figure 7, but for case H2.

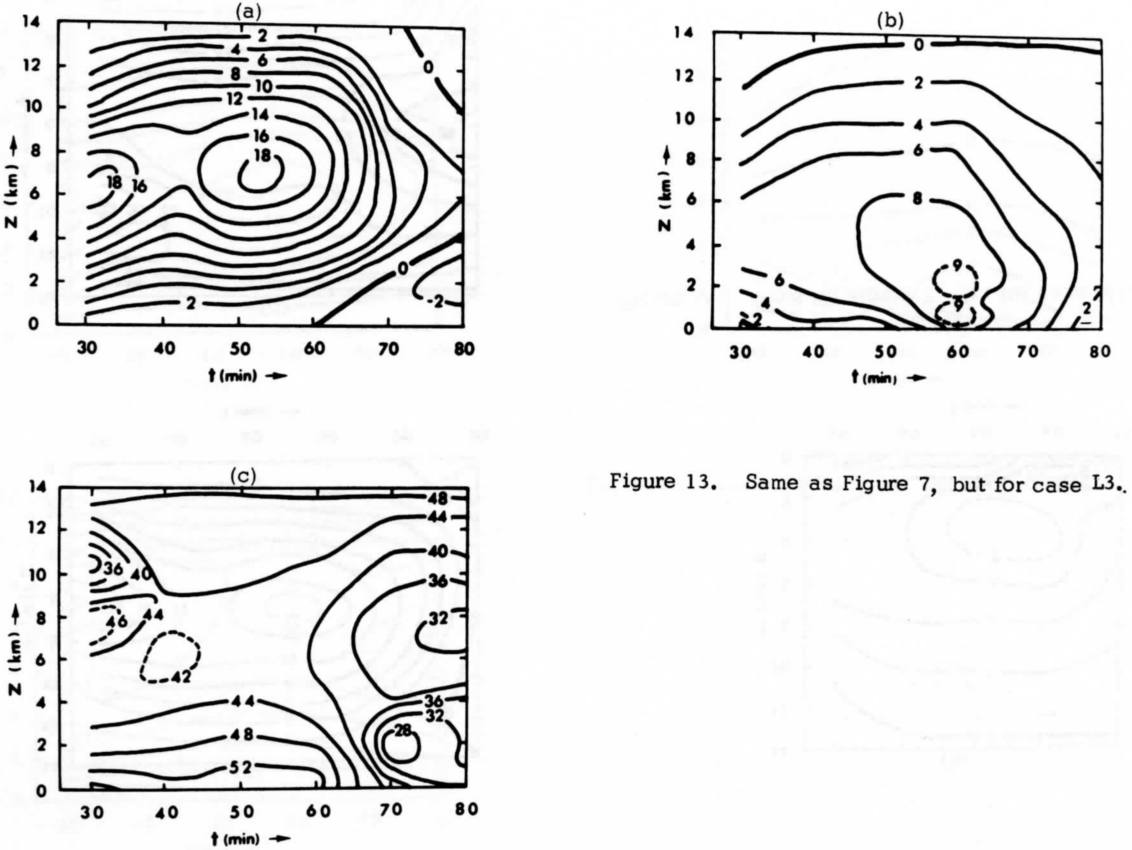

Figure 13. Same as Figure 7, but for case L3.

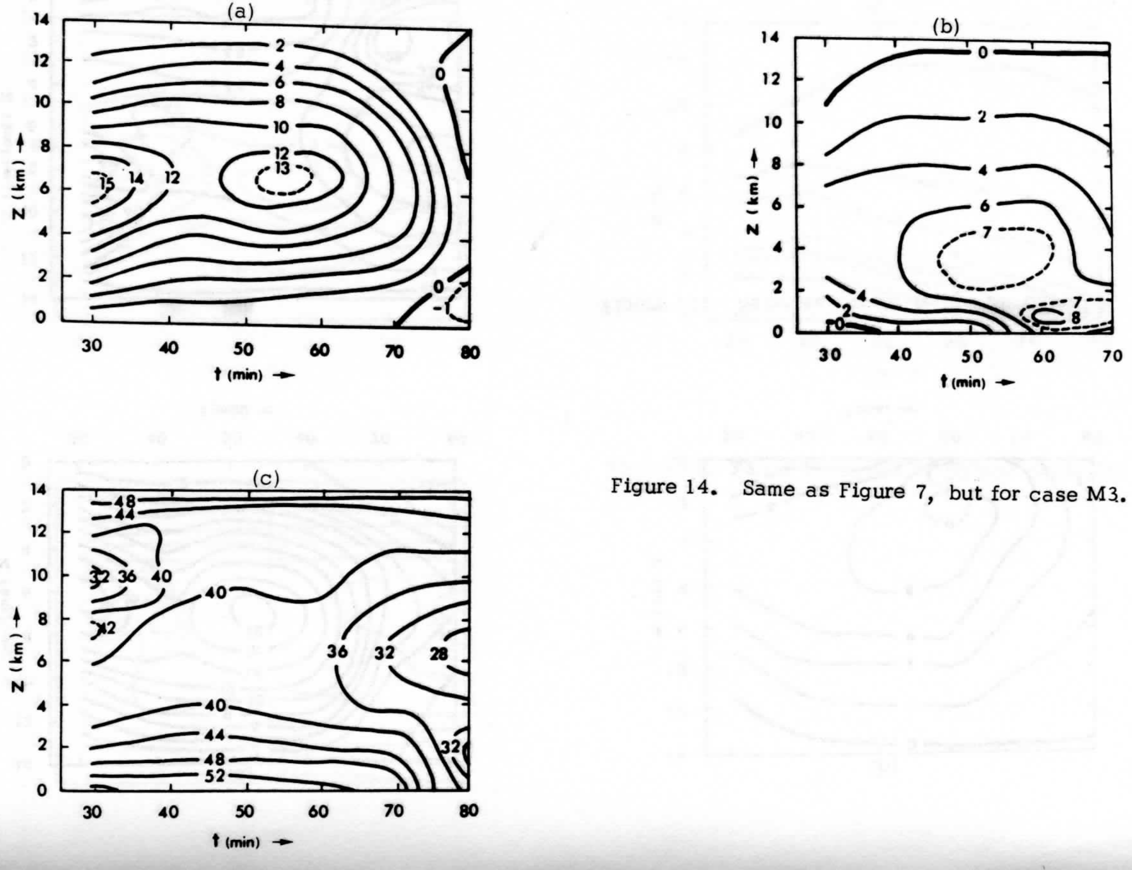

Figure 14. Same as Figure 7, but for case M3.

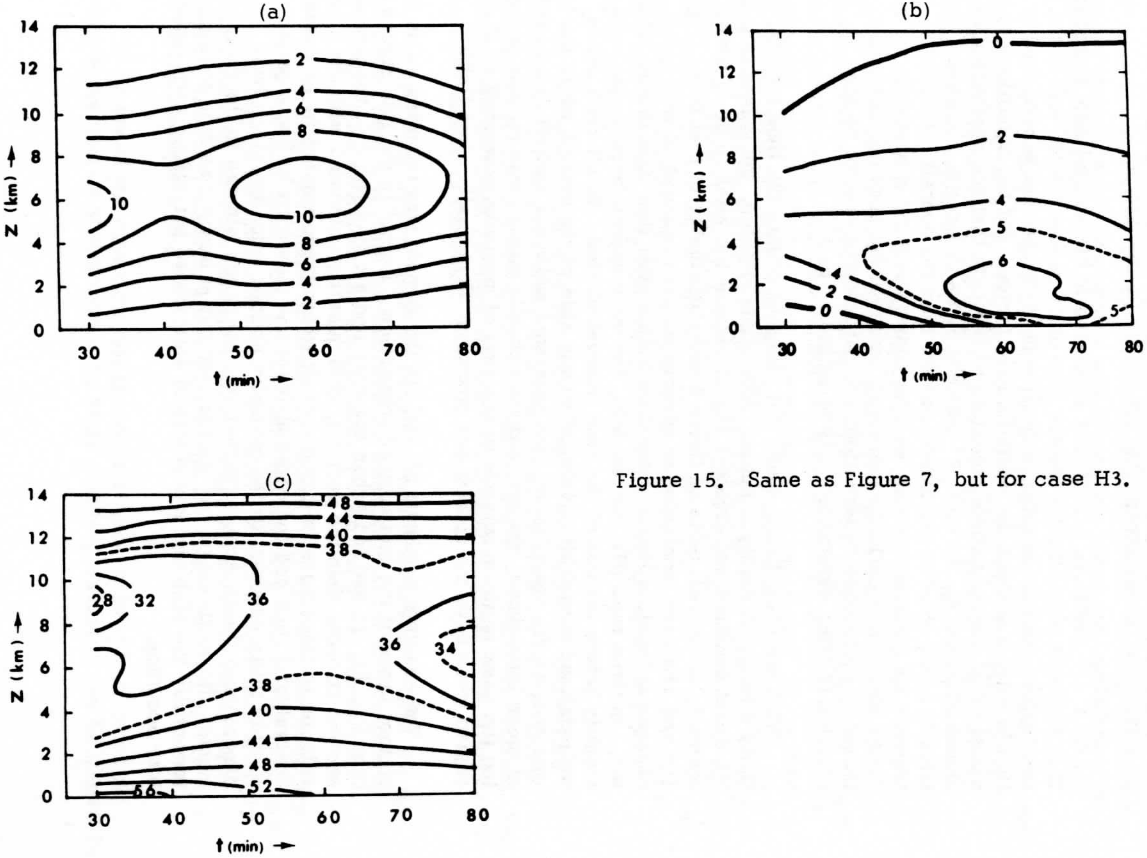

Figure 15. Same as Figure 7, but for case H3.

only. It is obtained by the approximate relation $\theta_e \doteq \theta + L_{vw}q_v/c_p$ where θ is computed from the usual definition in terms of T and p. Variations of p from the initial base state are neglected, but the resulting error in θ is about 1° at the worst. The approximate expression for θ_e is that given by Petterssen (1956) except that the multiplicative factor $(p_0/p)^{R_d/c_p}$ (with $p_0 = 1000$ mb) appearing in his second term is not included. This factor is only slightly greater than unity at low levels, and in the upper troposphere the mixing ratio is small enough so that the second term is negligible with or without the multiplicative factor. For the conditions in the model cloud cores, sample calculations indicate that the approximation underestimates θ_e by up to 3° between 800 and 400 mb. However, this error is a full order of magnitude smaller than the overall variation in θ_e between its surface maximum and the midtropospheric minimum in the base states for each numerical experiment, and relative humidity estimates obtained by radiosonde observations are sufficiently in error so that θ_e in practice is often determined only to within 1° to 3°.

With few exceptions, each z-t diagram covers the time interval from thirty minutes to eighty minutes. After sixty minutes, the convection in run H1 (least moisture and greatest shear) became too weak to be of further interest, so that all parts of figure 9 were terminated at that time. Figures 10b and 14b were terminated at seventy minutes because of very rapid changes in vertical liquid water distribution after that time in runs L2 and M3. In three runs (H1, L3 and M3), the main updraft became too weak to identify before the end of the time interval plotted. In all such cases, a well-defined downdraft developed to one side of the updraft while the latter was still easily identifiable, and persisted while the updraft dissipated; at these later times, the grid column actually plotted was the one occupying the same position relative to the axis of maximum downdraft as it occupied when both the updraft and downdraft were easily identifiable.

The absolute maximum of $|w|$ in the domain was regarded as an important index of the intensity of convection. Except in the late stages of runs H1, L2, L3 and M3 (when the main updraft dissipated or the downdraft became stronger than the updraft), this quantity coincided with the greatest velocity of the single in-cloud updraft which predominated in all cases. Several trial runs had indicated at least one pulsation having a period of roughly thirty minutes for the maximum updraft velocity; since two-dimensional fields were outputted only every ten minutes in the final experiments, the maximum of $|w|$ was printed out at every time step to resolve temporally the high and low points of anticipated pulsations with satisfactory accuracy.

Having covered these preliminary points, we will now enumerate some of the main characteristics of the convection revealed by the z-t diagrams.

1) Whether measured by the maximum value of w, the maximum value of L or the values of θ_e typical of the middle levels, the maximum intensity of the convection decreases with increasing shear and increases with increasing moisture.

2) In all cases, there is a maximum value of w between thirty minutes and thirty-five minutes. Except in Run H1 (figure 9a), this maximum is followed by a pulsation in the updraft strength with a second maximum from twenty to thirty-five minutes later.

3) The updrafts attaining the greatest severity do not necessarily show the greatest persistence. At least from forty-five minutes through seventy minutes, the convection in runs M1 (figure 8), M2 (figure 11) and H3 (figure 15) maintains what might be considered a quasi-steady state in the middle and upper levels. That is, the time variations of w, L and θ_e at these levels are slow and small; in particular, w remains within about ten percent of its average value at these levels during this time interval. In contrast, the greatest updraft speed (19.4 m $\sec^{-1}$) in run L3 (figure 13) is over half again as large as in runs M2 (12.1 m $\sec^{-1}$) and H3 (11.0 m $\sec^{-1}$) and over twice its value in run M1 (8.9 m $\sec^{-1}$), but rapid decay commences only slightly after sixty minutes in this very strong but relatively short-lived updraft.

4) If the wind shear is not very strong (L and M runs), increasing moisture supply is associated with decreasing persistency of the updraft despite its increasing strength. With strong shear (H runs), by contrast, the updraft becomes both stronger and more persistent (or dissipates later) as the moisture supply is increased.

5) With the largest moisture supply, shear prolongs the life of the updraft even though it does not increase its strength. At lower humidities, moderate shear lengthens the mature stage but strong shear shortens it.

6) Although the cloud top height is limited only by the upper boundary in six of the nine cases (L1, L2, L3, M2, M3 and H3), the updraft maximum ascends only to the middle levels. This altitude varies much less strongly among the runs than the maximum values of updraft speed or liquid water content, ranging only from about 5 km in the weakest case (H1) to 7 or 7.5 km in the stronger cases.

7) In six of the runs (low and moderate shear), a downdraft develops beneath the updraft at approximately sixty minutes, except in run L1 (figure 7a)

where the downdraft appears shortly after forty minutes. First appearing at the lowest levels, the downdraft generally intensifies and deepens thereafter. The z-t diagrams should not be used for determining the actual time of appearance of the cold low-level downdraft; no downdraft is evident throughout the time intervals covered in the strongly sheared cases, but in each of these runs a cold downdraft did develop in the low levels several kilometers to the left of the updraft, therefore in the wrong position to be detected in the diagrams.

8) When the updraft is most highly developed in any one run, θ_e is nearly constant with height over a layer several kilometers deep corresponding to the faster parts of the updraft. Except in case L1, θ_e also shows only slow changes with time while the updraft is at or near its peak intensity. In contrast, rapid decay of the updraft in the late stages of runs L2 (figure 10), L3 (figure 13) and M3 (figure 14) is accompanied by a decrease in θ_e of about 10° around 5 to 7 km, with even larger falls around 2 km in the cold downdraft. The close association between updraft dissipation and a pronounced drop in θ_e with time at middle levels suggests that potentially cool air drawn from outside the cloud into the previously well-protected updraft core is important to the dissipation process. Examination of the airflow relative to the moving cloud later in this section will indicate this to be the case.

9) Preliminary experiments indicated that prior to the onset of precipitation, the maximum liquid water content is located about two-thirds of the way from the cloud base to the cloud top. The main effect of the liquid water fallout is to shift the level of maximum liquid water content to the lower third of the cloud. Even in cases L3 and M3 with very strong updrafts which might be expected to keep much of the precipitation suspended at middle levels, the greatest liquid water content is found only about 4 km above the lower boundary.

10) Liquid water does not reach the ground until at least several minutes after the first peak of w, partly because precipitation is not assumed to occur in this model until the cloud top reaches the first level where the undisturbed temperature is -20°C or lower (7 km in all cases) and partly because the fully developed updraft between thirty and thirty-five minutes temporarily suspends much of the precipitation aloft. In case H1 (figure 9), no precipitation reaches the ground since what little precipitation is produced by the rather weak updraft is evaporated at the cloud base.

11) In all runs except for L1 (and H1, which shows only one maximum of w), there is no indication of a pulsation in L to parallel the pulsation of w with time.

12) The decrease of θ_e with height just beneath the stable layer in most runs before forty minutes is due to the ascent of saturated air into the potentially cool midtroposphere with forced lifting of still-unsaturated air located above the advancing cloud top. In view of the low saturation mixing ratio at and above the cloud top, destabilization is due more to the ascent of saturated air under very dry air than to evaporation at the cloud top. This temporary instability is soon eliminated as the upward penetration of cloudy air raises θ_e locally at 8 to 9 km.

7.2 Two-Dimensional Disturbance Fields

Despite their limitation to one space dimension (the vertical), the z-t diagrams just presented have revealed the influence of low-level moisture supply and middle-level wind shear upon the intensity and mode of the convection predicted by the two-dimensional model under consideration. Also, by indicating a close connection between rapid decay of the updraft (in some of the runs) and a large decrease of θ_e at a given level in the storm core, the z-t diagrams have already suggested indirectly that ingestion of potentially cool environmental air is important to the dissipation of the convection.

To make possible a fuller appreciation of the modification of both the storm and its surroundings by the convective flow, the full two-dimensional disturbed fields of ψ and T at fifty minutes and seventy minutes, along with the same type of field for p at fifty minutes, are shown for five of the nine runs in figures 17 through 41. The undisturbed parts of the initial fields at fifty minutes were constructed by the abbreviated technique described in appendix G.

The five runs are those with either moderate moisture (cases L2, M2 and H2) or moderate wind shear (M1, M2 and M3), overlapping with case M2. The most salient features will be enumerated for each field and time level in groups of five figures:

1) Streamlines at fifty minutes (figures 17 through 21)

2) Temperature at fifty minutes (figures 22 through 26)

3) Pressure at fifty minutes (figures 27 through 31)

4) Streamlines at seventy minutes (figures 32 through 36)

5) Temperature at seventy minutes (figures 37 through 41)

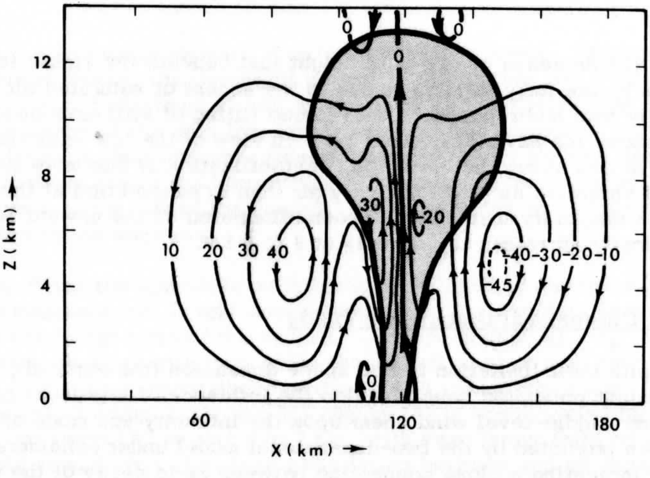

Figure 17. Streamlines of pure disturbance flow (deviation from the initial base state) for case L2 at 50 min. Contours are labeled in units of 10^6 gm m^{-1} sec^{-1} . The shaded region bounded by the heavy solid curve represents the cloud. In this and all subsequent figures in which the variable x appears, it denotes the distance to the right of the initial left boundary (km). (6 grid shifts)

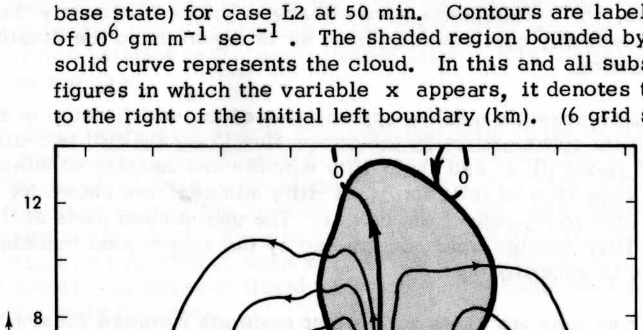

Figure 18. Same as figure 17, but for case M2. (10 grid shifts)

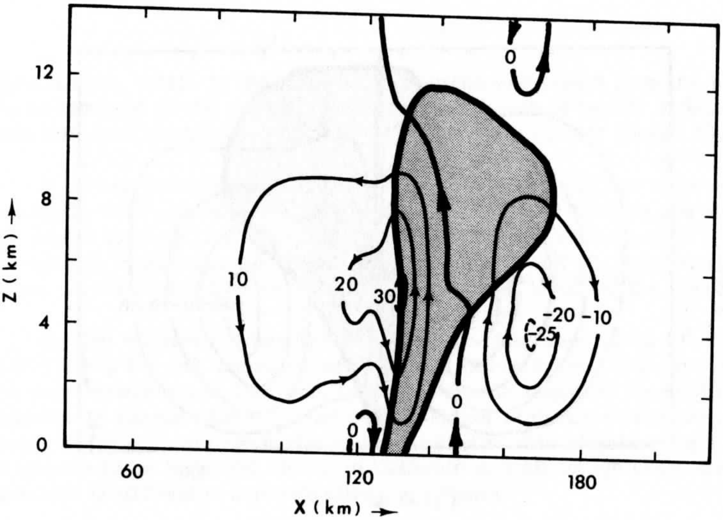

Figure 19. Same as figure 17, but for case H2. (13 grid shifts)

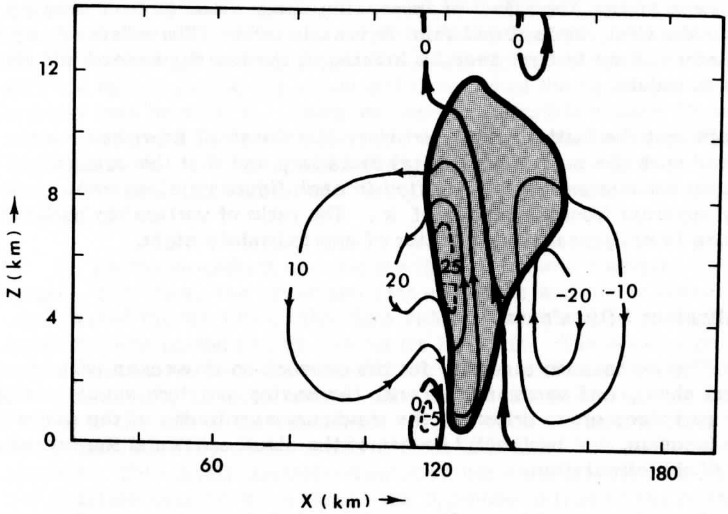

Figure 20. Same as figure 17, but for case M2. (7 grid shifts)

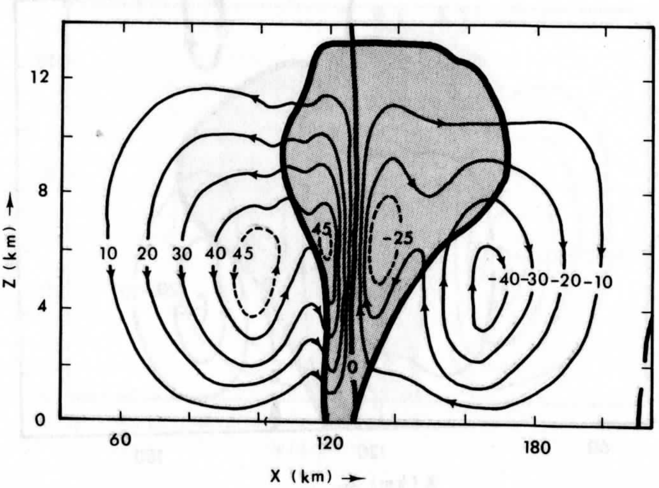

Figure 21. Same as figure 17, but for case M3. (13 grid shifts)

Within each group, the effect of increasing shear alone is best seen by studying the first, second and third figures in order. The effect of increasing moisture alone is best seen by looking at the fourth, second and fifth figures in order.

Note that the initial inflow boundary (for the total flow) has been identified with the zero of horizontal distance, and that the domain has been shifted by various amounts (specified in each figure caption) as is immediately apparent from the ranges of x . The ratio of vertical to horizontal distances is exaggerated by a factor of approximately eight.

Streamlines at fifty minutes

1) The systematic tendency for the convection to weaken with increasing wind shear, and to strengthen with increasing moisture supply, is apparent from three gross criteria: the maximum magnitudes of the disturbance stream function, the horizontal extent of the cloud anvil and the horizontal extent of the circulation.

2) Apart from notable smaller-scale perturbations to be pointed out below, the overall circulation at fifty minutes retains the two-roll configuration initially assumed, though its intensity and extent are all greatly increased. In the sheared cases, the left branch is more intense than the

right branch, while in the run which is unsheared (apart from the slight shear assumed in the moist layer), the circulation is nearly symmetrical with the right branch very slightly stronger than the left (figure 17).

3) Weak gravity waves 10 to 15 km long and up to 500 m in vertical amplitude with almost vertically oriented crests and troughs are evident in the stable layer (9.1 to 10.5 km) mostly within the cloud and to the left of the updraft in at least two cases (see figures 17 and 18, especially). These waves result from excitation of the stable layer by the convection.

4) The strongest downdraft is located at and near cloud edges, especially along the left boundary of the cloud below 6 km. This suggests that the main downdraft at this time is mainly due to negative thermal buoyancy induced by evaporation at cloud edges, rather than due to the drag of the liquid water. If drag were the dominant factor, one should expect the downdraft to be initiated closer to the main updraft axis, where the heaviest liquid water concentrations are found.

5) The downdraft just referred to is considerably weaker than the updraft in all cases shown. Its maximum velocities in figures 17 through 21 are about 2.5, 2.5, 2, 3 and 1.5 m sec^{-1}, respectively; the corresponding maximum updrafts are approximately 12, 9, 5, 6 and 12 m sec^{-1}. In view of the considerable convective instability of the lower layer even in the "driest" experiments, the rather small values of the downdraft velocities are due in part to the numerical damping of the upstream advection scheme (see section 3). However, another possible reason for the rather weak downdrafts is the omission of frozen precipitation, especially hail, from this model. If included, frozen precipitation would have further cooled the lower levels through partial melt, thereby imparting more negative buoyancy to the air.

6) As the downdraft approaches the rigid lower boundary, it must diverge. Therefore, the air at and just above the surface is horizontally accelerated ($du/dt > 0$) on the right side of the downdraft core, and horizontally decelerated ($du/dt < 0$) on its left side. The decelerated air, flowing leftward toward the fast-moving air on the underside of the left-hand convective roll, induces convergence which in turn causes weak upward motion to the left of the downdraft. Thus, each streamline field has a shallow clockwise eddy which constricts the left-hand convective roll from beneath. This small counter-circulation varies inversely in strength with the moisture supply, even though the opposite is true of the main circulation. This is not surprising, since the strength of the reverse eddy is roughly proportional to that of the downdraft; the lower the initial relative humidity outside the cloud, the more evaporation can occur subsequently.

7) In run L2 (figure 17), both convective rolls have two circulation centers rather than one. Correspondingly, especially on the left side, there is noticeable sinking near 4 km along the cloud edges, dividing the region of ascent into the strong in-cloud updraft and much weaker upcurrents outside of the cloud. It will soon be seen that this splitting is largely due to the horizontal temperature distribution around 4 km. Note that no secondary clouds have formed in the secondary upcurrents, which consist of air that has been dried as well as warmed adiabatically in previous descent further outside the cloud.

8) The anvil becomes increasingly asymmetric as wind shear is increased. However, the anvil in the more sheared cases develops mainly on the downshear side of the updraft, even though the upshear branch of the disturbed flow is more intense than the downshear branch.

Temperature at Fifty Minutes

1) The most conspicuous thermal feature is the warm core in the cloudy updraft, with temperatures up to 7°C above the initial undisturbed values in runs L2 (figure 22) and M3 (figure 26). This maximum excess is a good index of updraft intensity, being nearly proportional to its maximum velocity. Note that compensatory sinking of the cloud surroundings has warmed the middle levels outside the cloud by up to 2°C or more, making the warm updraft core appreciably less buoyant than would be indicated by the temperature excess plotted, namely that over the undisturbed initial value. The height of the updraft maximum in this model (only around 7 km in the stronger storms) is still well below what one would expect even after taking environmental changes into account, since the cloud core is still most buoyant in the middle levels. This indicates that liquid water drag, vertical decelerations due to pressure perturbations, and possibly computational diffusion may contribute to loss of net buoyancy in the updraft.

2) Between about 3 and 8 km, the regions of significant warming on either side of the cloud become narrower with increasing height. However, the effects of the stable layer (9.1 to 10.5 km) are evident both in a strong decrease of disturbed temperature with height (in the layer itself) and in a pronounced horizontal spreading of the outermost positive isolines immediately underneath it.

3) The regions of compensatory warming slope increasingly downshear as wind shear is increased. Also, the heating to the left of the cloud exceeds the heating to the right. However, the sharp temperature ridge in the updraft core is nearly vertical, suggesting that even with appreciable shear, the updraft may be nearly erect over a considerable part of its depth. This

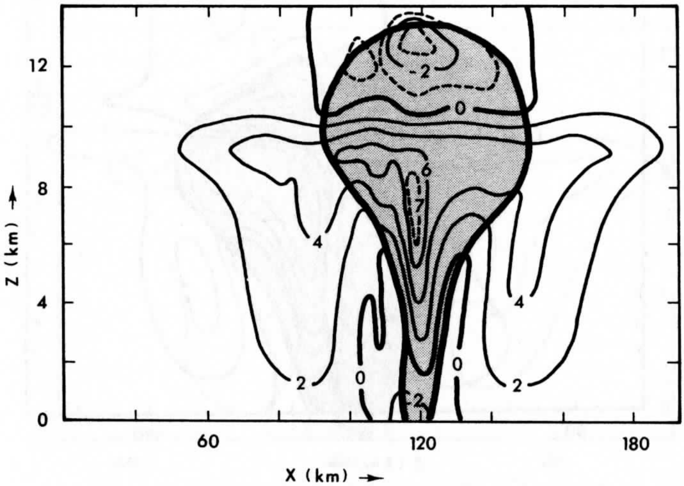

Figure 22. Deviation of air temperature from the initial base state (°C) for case L2 at fifty minutes. The shaded region bounded by the heavy solid curve represents the cloud.

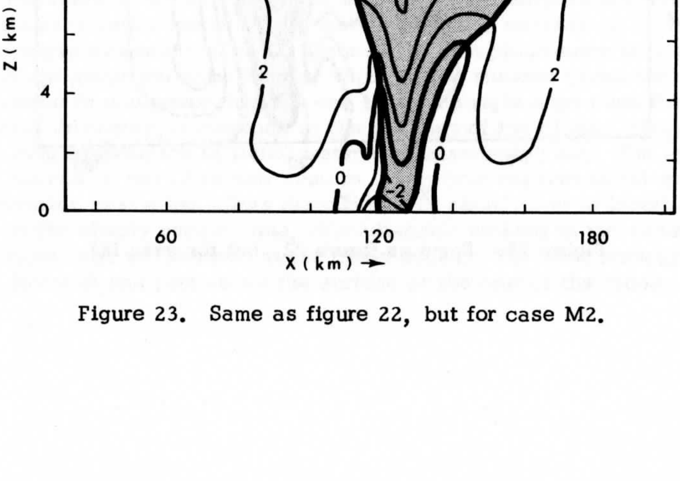

Figure 23. Same as figure 22, but for case M2.

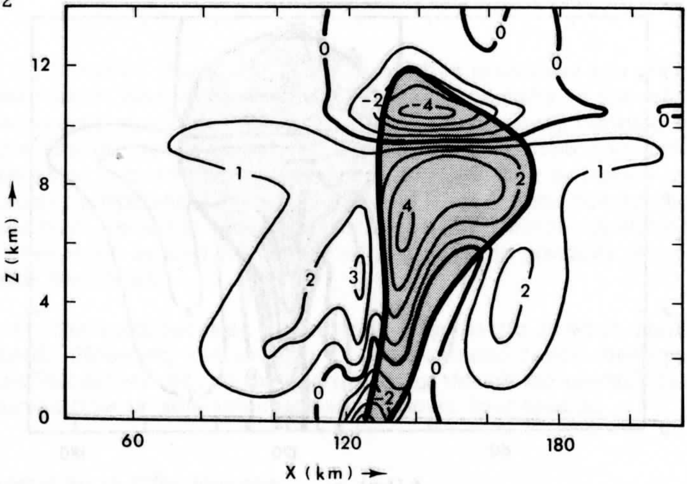

Figure 24. Same as figure 22, but for case H2.

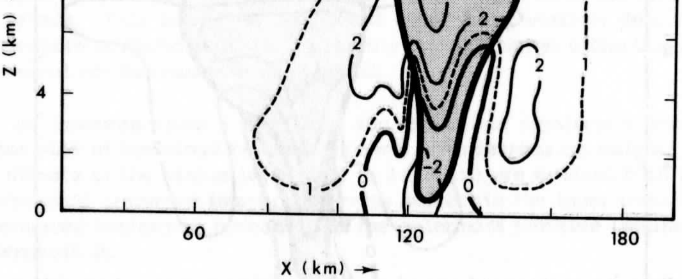

Figure 25. Same as figure 22, but for case M1.

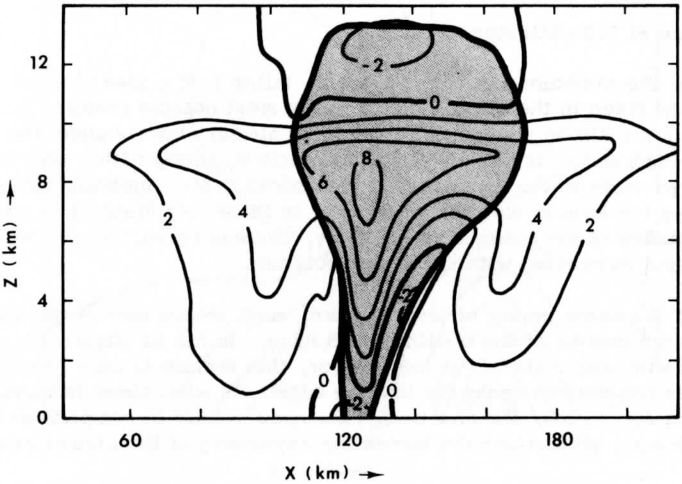

Figure 26. Same as figure 22, but for case M3.

will be seen to be true in some of the sheared cases when the flow relative to the cloud motion is examined.

4) The uppermost parts of the cloud are significantly cold, from 2 to 4°C colder than the undisturbed temperatures at these levels. This particular feature is more prominent in the weaker storms (figures 24 and 25) than in the others. The less developed the cloud, the less latent heat is released into air previously cooled by forced ascent through the stable layer.

5) Cooling has occurred in the lowest 2 km of the cloud interior and along the lower cloud edges, where sharp inverted temperature troughs are formed by the zero contour. The right-hand trough extends up to about 6 km; in the nearly symmetric case L2 (figure 22), both cloud-edge temperature troughs are about the same height, while in the sheared cases the left-hand cold tongue is shallower than the one along the right edge even though the low-level downdraft is confined to the left part of the cloud. The cold tongues result from evaporation of liquid water into unsaturated air. The splitting of the updraft in run L2 is now seen to result from the horizontal temperature configuration near 4 km. This distribution is clearly due to latent heat release in the cloudy middle zone, dry-adiabatic sinking in the unsaturated environment and evaporation at the cloud edges. The most pronounced cooling is found at and just above the surface at the rear of the cloud.

Pressure at Fifty Minutes

1) The pressure has, on the whole, fallen in the lower half of the domain and risen in the upper half. The two most notable features in all runs shown are a strong center of low pressure almost directly under the leading cloud edge and most pronounced at the surface, along with a core of elevated pressure in the upper part of the updraft. The algebraic difference between the largest pressure deviations in these two features is an additional index of the convective intensity, decreasing with increased wind shear and increasing with increased moisture.

2) A second center of low pressure, most pronounced at the surface, is located upwind of the trailing cloud edge. In run L2 (figure 27), with no initial wind shear above the moist layer, this feature is only slightly weaker than its counterpart under the leading edge. As wind shear is increased (figures 28 and 29), the rear trough becomes weaker in comparison to the front trough, paralleling the increasing asymmetry of the cloud anvil.

3) A very shallow dome of relatively high pressure (in comparison with its surroundings at similar levels) is found where the maximum cooling at

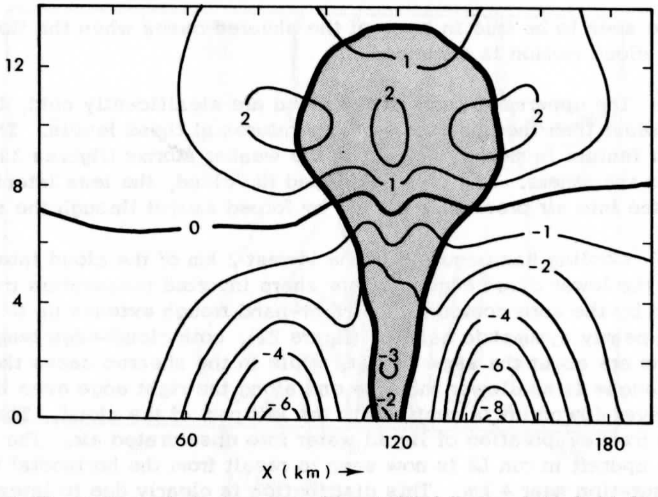

Figure 27. Deviation of air pressure from initial base state (mb) for case L2 at fifty minutes. The shaded region bounded by the heavy solid curve represents the cloud.

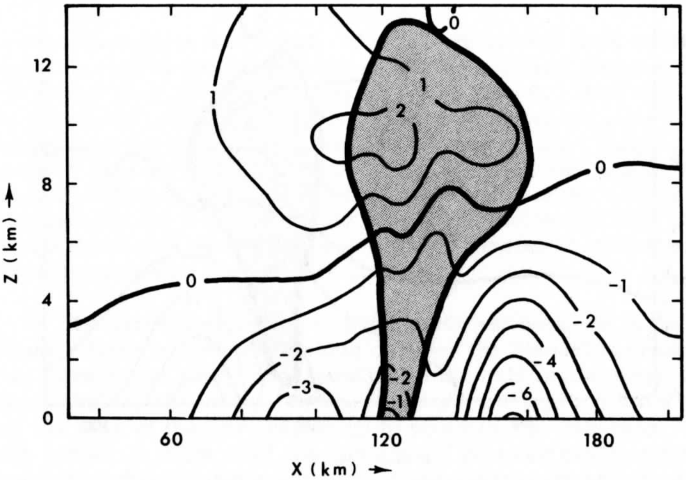

Figure 28. Same as figure 27, but for case M2.

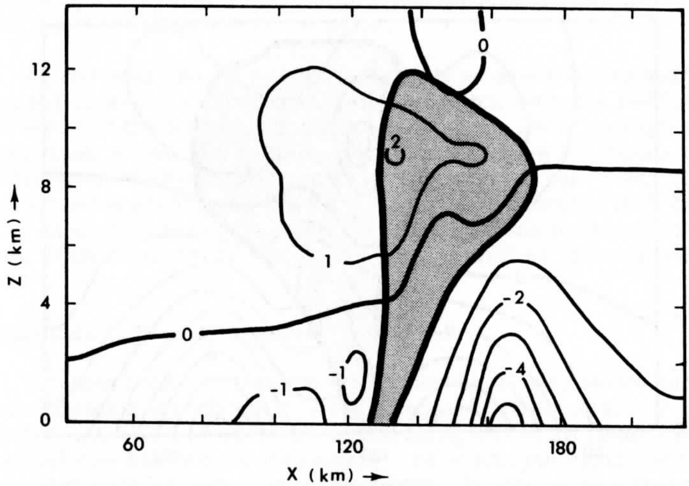

Figure 29. Same as figure 27, but for case H2.

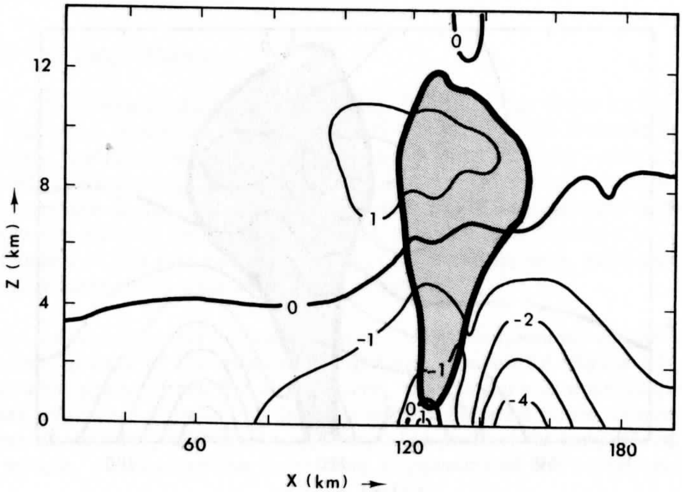

Figure 30. Same as figure 27, but for case M1.

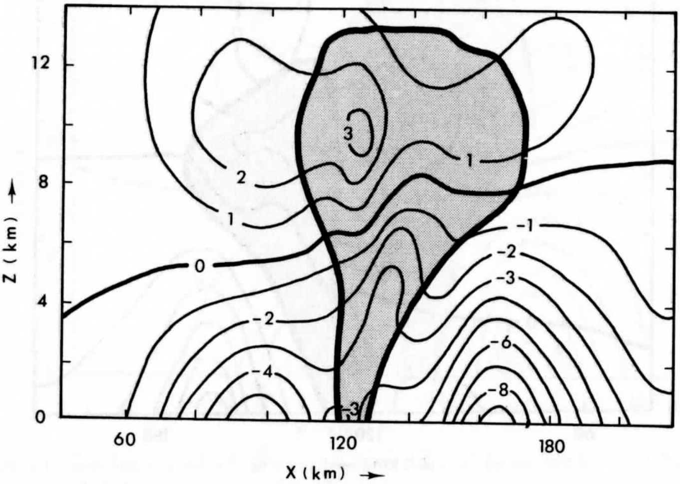

Figure 31. Same as figure 27, but for case M3.

and near the surface was noted. This feature is very weak in run H2 (figure 29), but in the other cases shown its maximum pressure is at least 2 mb greater than in the secondary trough to its left. Note that the pressure difference between this high and the primary trough varies much less strongly from run to run than does the updraft intensity, ranging from about 5.5 mb in case H2 to 7 mb in case M3. One factor which may (for the moderately sheared cases) reduce the dependence of the surface pressure variation upon the moisture supply is the fact that the surface cooling in the high decreases with increasing moisture, therefore reducing hydrostatic contributions toward high surface pressure.

4) The vertical distribution of the perturbed pressure in the cloud core induces a force which considerably opposes the thermal buoyancy force. In the lowest 2 to 3 km, corresponding to the cold region noted in the temperature fields, the vertical (disturbed) pressure gradient force is upward. From the base of the warm region up to about 10 km, this force is downward, while further up in the cold cap, an upward pressure gradient force opposes the negative thermal buoyancy. In the strongest parts of the updraft, in particular, the downward pressure gradient force is roughly half as great as the thermal buoyancy. This in itself indicates that the one-dimensional theories, by neglecting pressure differences between a cloud and its surroundings, considerably overestimate net vertical accelerations (and, in turn, vertical velocities) in the cloud.

5) The zero line for perturbed pressure is nearly horizontal in run L2 (figure 27), which exhibits a virtually symmetric pressure field in the upper two-thirds of the domain. In the other runs, the zero line slopes upward to the right, especially in the strongly sheared case H2 (figure 29). Since the pressure decreases from left to right across the zero contour, air is accelerated predominantly toward the right upon emerging from the updraft core, especially in run H2. This partially explains the increasing predominance of the anvil to the right of the main updraft as shear is increased.

Streamlines at Seventy Minutes

1) Since fifty minutes, the circulation in all runs shown has become more complex and horizontally more elongated. The overall circulation is still recognizable as consisting of two rolls, but in all cases the right-hand roll now has two closed centers, one within the cloud and the other in its surroundings under the leading edge. It will be seen that this splitting is largely due to the horizontal temperature distribution between 4 and 6 km.

2) In Run L2 (figure 32), whose circulation above the lowest few

kilometers was nearly symmetrical at fifty minutes, the left roll is now appreciably stronger than the right roll. The minor wind shear initially prescribed in the moist layer may therefore lead to appreciable asymmetry over a sufficiently long time interval. Also, purely numerical effects cannot be ruled out. Even if the ambient wind were completely constant, an initially symmetric perturbation would not be expected to remain perfectly symmetric; the ambient wind would make $|u|$ (and thereby the horizontal viscosity coefficient for the upstream differencing scheme, as discussed in section 3) asymmetric about the central axis of the perturbation.

3) In runs L2 (figure 32) and M2 (figure 33), weak gravity waves are still evident in the stable layer, especially to the left of the updraft core. In all runs, the very weak counterclockwise eddy between the anvil and the upper boundary suggests some limited gravity wave activity. At these altitudes, both moist- and dry-adiabatic motions are absolutely stable, so that some gravity wave formation might be expected.

4) In all cases, the anvil has spread considerably since fifty minutes. The more intense the foregoing convection, the longer the anvil, since the horizontal divergence which leads to anvil formation is roughly proportional to the updraft speed. The low-level stem containing the heaviest rainfall has also broadened since fifty minutes, especially in run M3 (figure 36), reflecting the continuing fall of condensation products from the wettest parts of the anvil.

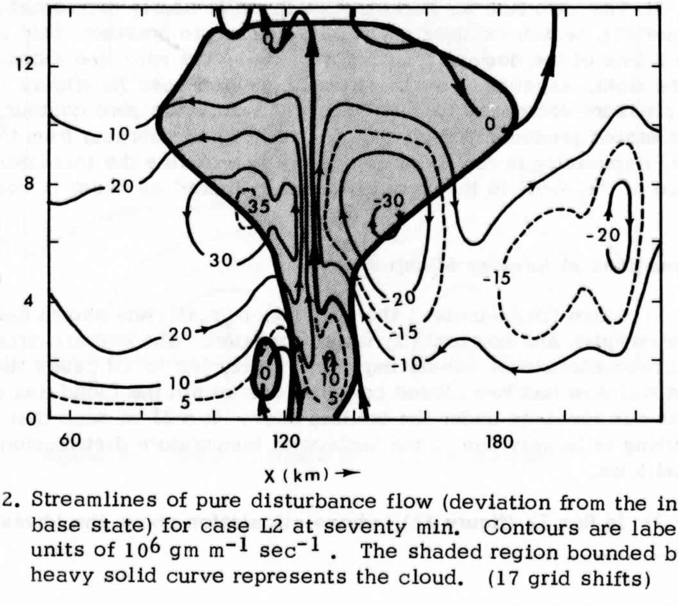

Figure 32. Streamlines of pure disturbance flow (deviation from the initial base state) for case L2 at seventy min. Contours are labeled in units of 10^6 gm m^{-1} sec^{-1}. The shaded region bounded by the heavy solid curve represents the cloud. (17 grid shifts)

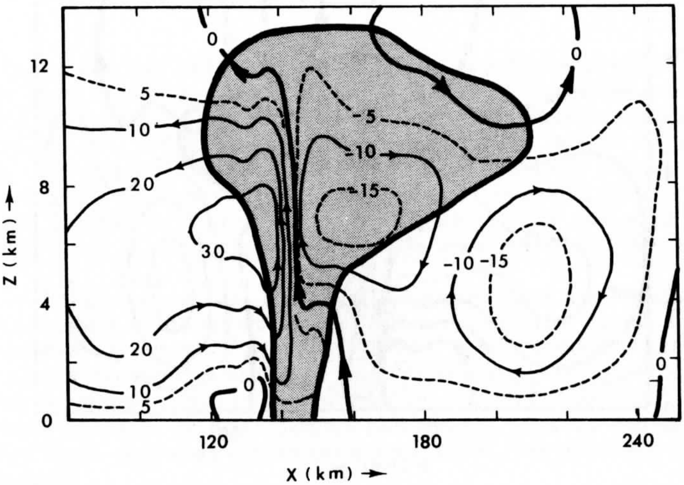

Figure 33. Same as figure 32, but for case M2. (25 grid shifts)

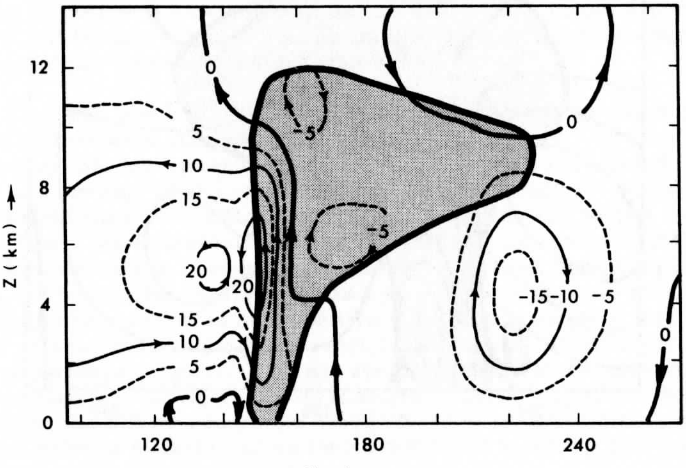

Figure 34. Same as figure 32, but for case H2. (30 grid shifts)

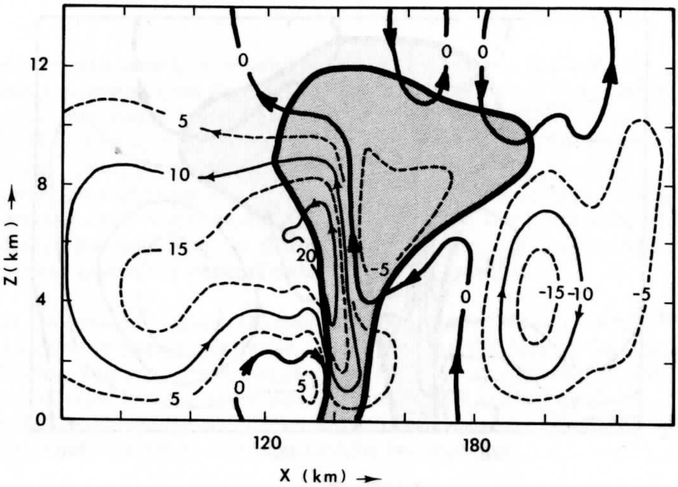

Figure 35. Same as figure 32, but for case M1. (20 grid shifts)

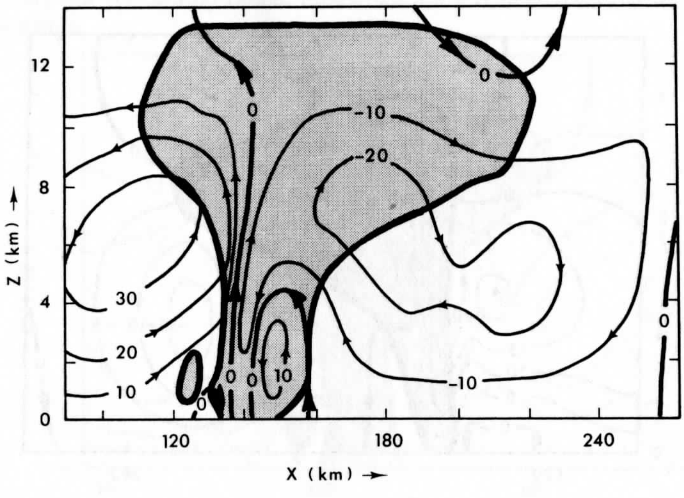

Figure 36. Same as figure 32, but for case M3. (28 grid shifts)

5) As was true at fifty minutes, the low-level reverse eddy at the rear of the storm is best developed in run M1 (figure 35) and least developed in run M3 (figure 36). Note that run M3 now shows a strong downdraft (about 5 m sec^{-1}) well within the cloud, beneath and to the right of the main updraft. The reasons for this shift in the primary downdraft site will become apparent when the flow relative to the storms is examined later in this section. In runs L2 (figure 32) and M2 (figure 33), the downdraft is also showing signs of spreading further into the lower interior of the cloud.

6) In runs L2 and M3, a shallow secondary cloud has formed in the weak upcurrent in the reverse eddy. Although the rising motion does not exceed about 1.5 m sec^{-1}, the considerable humidification of this region from earlier evaporation has made possible the secondary cloud formation. Unlike the primary cloud at the initial time, the secondary cloud is not thermally buoyant. At sixty minutes (not shown), runs M1 and M2 also showed small secondary clouds behind the storm, but they have since evaporated.

7) In all cases, the left-hand boundary flow at seventy minutes is significantly disturbed. Due to the horizontal stretching of the convective circulation and repeated shifting of the domain (by the method described in section 5), the inflow boundary has been transferred so as to lose a sizable portion of the left branch. Expressed as a percentage of the maximum at the center of counterclockwise flow, the greatest stream function perturbation at the left boundary ranges from about forty percent in run M1 (figure 35) to over eighty percent in run M3 (figure 36).

8) It can now be readily appreciated why attempts to maintain undisturbed inflow were doomed to disappointment. However, in all of figures 32 through 36, the streamlines extrapolate quite smoothly to the left boundary, with no sign of any physically unreasonable gradients or other numerical instabilities even after 28 grid shifts in run M3 and 30 grid shifts in run H2. (The total displacement of the grid domain amounts to slightly over half its total length in these two cases.) Also, even though the horizontal flow due to the disturbance alone is toward the left at upper levels, the absolute u-component is still positive at all left boundary points in each case shown. It is only fair to remark that in one of the other four comparative experiments, namely L3 (least shear and greatest moisture supply), the disturbance was so vigorous that absolute outflow of up to 9 m sec^{-1} occurred at the left boundary from about fifty-five minutes onward, but even in that extreme situation all variables continued to extrapolate smoothly to the boundary.

9) No gross computational errors are evident at the right boundary. In three cases (figures 33, 34 and 36) involving 25 or more grid shifts up to

seventy minutes, there is a very small region of slightly positive values for the perturbation stream function near and along the lower half of this boundary. Since the values throughout the right branch of the circulation were mainly negative at fifty minutes in all runs shown, this phenomenon was regarded as a computational error resulting from successive extrapolations of the stream function to a new boundary at every grid shift. Error due to grid shifts could, at least in theory, have been evaluated by repeating an experiment with unchanged grid resolution but adding enough grid points in the horizontal to keep the region of significant disturbance well removed from lateral boundaries without any shifts. Unfortunately, the required core storage for such a run would have exceeded that available in central memory. However, considering that no previous models have used a movable domain, the numerical uncertainties at the right-hand boundary did not cause severe difficulties. Also, as had been hoped, no absolute inflow developed at the right-hand boundary in any experiment.

Temperature at Seventy Minutes

1) Paralleling the horizontal expansion of the circulation, the temperature disturbance field has shown considerable broadening since fifty minutes.

2) In the stronger storms, the warm core of the updraft has ascended to just beneath the stable layer (figures 37, 38 and 41), although the level of maximum updraft velocity has shown little or no rise since fifty minutes. The warm core has spread horizontally, leaning noticeably downshear in all cases except for L2. This leaning is most pronounced in the strongly sheared case H2 (figure 39).

3) The initial stable layer has been considerably destabilized by the prolonged moist-adiabatic ascent in the cloud and by subsidence outside of it, as evidenced by the packing of perturbation isotherms from positive at the bottom of this layer to negative at its top.

4) In the surroundings of the most intense storms (figures 37 and 41), subsidence through the stable layer has produced restricted regions of warming greater than that due to condensation in the cloud. This greatly reduces the actual thermal buoyancy in the cloud core, even though the in-cloud temperatures throughout the middle levels are several degrees warmer than the undisturbed initial values. The rapid weakening of the updraft after seventy minutes in these two cases (refer back to figures 10a and 14a) is apparently due in part to this destruction of thermal buoyancy.

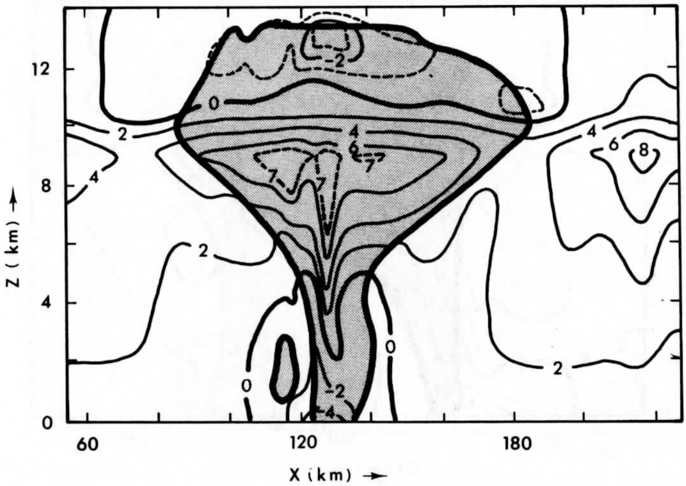

Figure 37. Deviation of air temperature from initial base state (°C) for case L2 at seventy minutes. The shaded region bounded by the heavy solid curve represents the cloud.

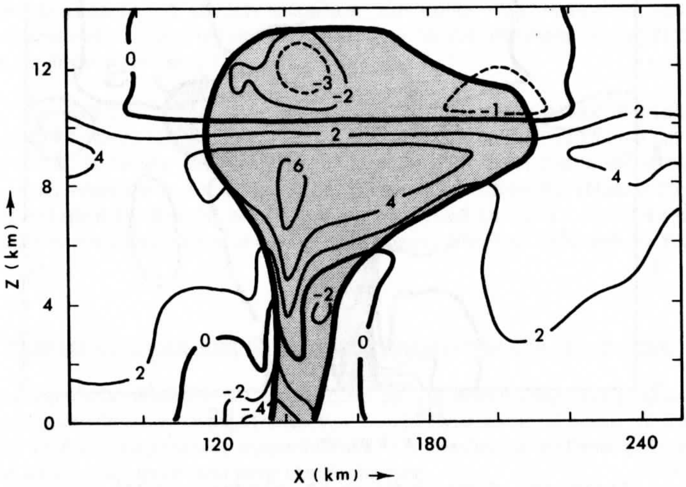

Figure 38. Same as figure 37, but for case M2.

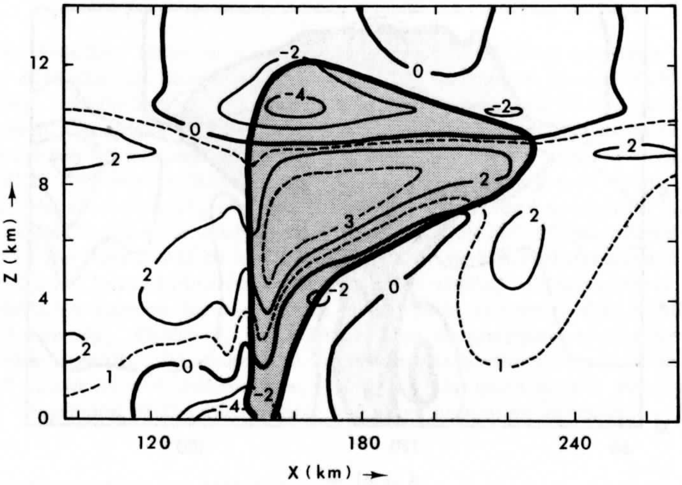

Figure 39. Same as figure 37, but for case H2.

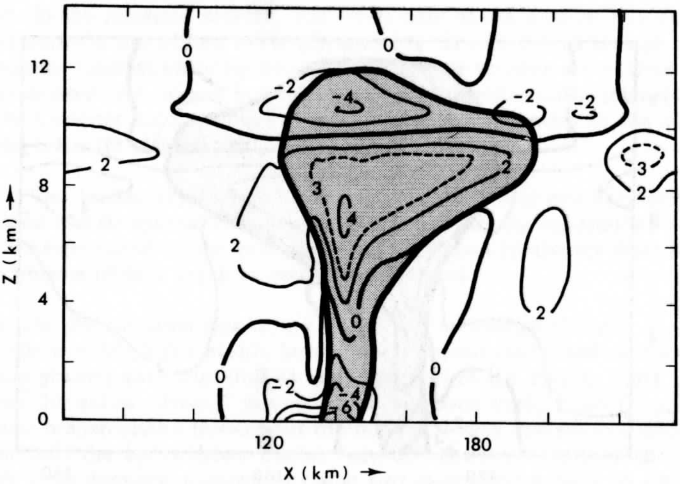

Figure 40. Same as figure 37, but for case M1.

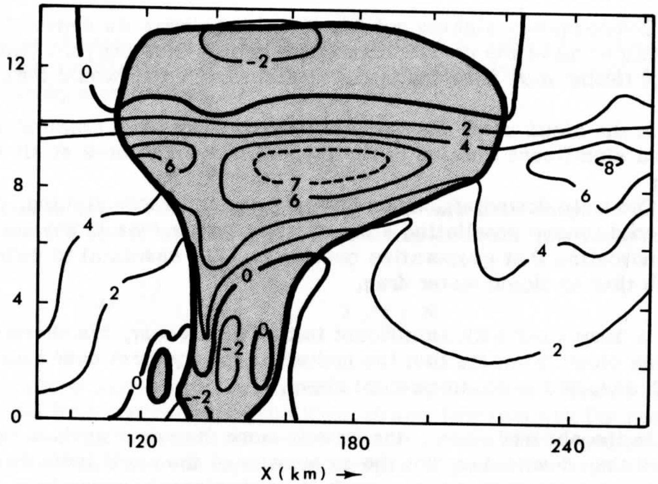

Figure 41. Same as figure 37, but for case M3.

5) Due to divergence, the region of cooling in and near the uppermost parts of the cloud has spread considerably in the horizontal. However, for the same reason noted at fifty minutes, the upper cold region is again better developed in the weaker storms than in the stronger ones, with little change in maximum intensity.

6) The region of cooling at lower and middle levels has stretched horizontally but otherwise retained the configuration it had at fifty minutes. The zero line extends noticeably outside the cloud; in the moderately sheared cases, and even more so in the strongly sheared case H2 (figure 39), the cooling extends further in back of the cloud than in front. This asymmetry results from predominantly rearward low-level outflow relative to the moving cloud core.

7.3 Dynamics of Cloud and Environment Relative to the Storm Core

The pure disturbance fields studied in the preceding paragraphs have provided considerable insight into the basic dynamics of some of the storms modeled in the comparative experiments. A number of salient points have thus far emerged, most notably the following:

1) Compensatory sinking outside the cloud warms its surroundings sufficiently to make the updraft core considerably less buoyant than the excess of temperature over the initial undisturbed value would indicate.

2) In the cloud core, the vertical perturbed pressure gradient force opposes a significant fraction of the thermal buoyancy force at all levels.

3) The main downdraft, apart from dry compensatory sinking, develops along a cold tongue paralleling a cloud edge, rather than in the core of the cloud, indicating that evaporative cooling is more essential to downdraft formation than is liquid water drag.

4) In some runs with significant initial wind shear, the thermal pattern in the cloud suggests that the updraft is nearly erect over much of its depth despite the environmental shear.

5) In the sheared cases, the flow is more disturbed upshear of the updraft core than downshear, yet the asymmetry of the anvil indicates that the divergent outflow from the updraft is predominantly downshear.

The first two points already indicate that pressure perturbations and environment modification, two factors altogether ignored by one-dimensional models, may in fact be vitally important to the updraft dynamics. The third statement attributes less importance to liquid water drag in downdraft formation than is indicated in the <u>Thunderstorm Project</u> report of Byers and Braham (1949) or in one-dimensional precipitating cumulus models such as those of Das (1964) and Srivastava (1967). These interesting results notwithstanding, little emphasis has thus far been directed in this paper toward investigating the last two points or toward explaining the tendency for wind shear to inhibit, rather than encourage, strong updraft development in this model.

When referring to erect or tilted updrafts, the earlier mentioned schematic modelers of severe thunderstorms had in mind not the flow relative to the ambient wind but the flow relative to the velocity of the storm core (usually identified by a radar echo). Therefore, in order to make possible truly meaningful comparisons between the numerical model and the schematic models, the airflow relative to the storm core was obtained as described in the next paragraph.

In all runs except H1, a representative storm core velocity, c, for the mature storms was obtained by calculating the total horizontal displacement from forty to seventy minutes of the vertical axis used for constructing the z-t diagrams, taking grid shifts into account. For case H1, the mean velocity was taken from thirty to sixty minutes in view of the early termination of the z-t diagrams. A fictitious stream function ψ_c corresponding to this velocity was defined by

$$\frac{\partial\psi_c}{\partial z} = \bar{\rho}c \tag{109}$$

At all points above the lower boundary, ψ_c was then obtained by setting $\psi_c = 0$ at the lower boundary and integrating equation (109) numerically:

$$(\psi_c)_j = \frac{c\Delta z}{2} \sum_{J=1}^{j-1} (\bar{\rho}_J + \bar{\rho}_{J+1}), \qquad 2 \leq j \leq N \tag{110}$$

Finally, along each row of grid points, the appropriate value of ψ_c was subtracted from the values of the total stream function and the resulting function was contoured at the same interval as was the pure disturbance stream function shown in figures 18 through 22 and 32 through 36.

Figures 42 through 49 show the relative flow over about two-thirds of the horizontal extent of the grid for each of the comparative runs at fifty minutes. In all cases except H1, the cloud contains an area of at least 20 km^2 in which the local rainfall rate R is 30 mm hr^{-1} (roughly 1.2 in hr^{-1}) or greater. In this model, R was first computed as a downward mass flux:

$$R = \begin{cases} L_p(V - w), & w < V \\ 0, & w \geq V \end{cases} \tag{111}$$

where the terminal fall velocit V for raindrops is obtained from equation (35) and the precipitation content L_p is calculated from (33). Regions where $R \geq 30$ mm hr^{-1} are indicated by light shading and regions where $R \geq 90$ mm hr^{-1} are shaded more heavily. For the purposes of this discussion, the lightly shaded areas can be regarded as containing "significant" rainfall and the darker areas as containing "heavy" rainfall. In view of the importance attached by Newton (1967) to updraft tilt for the perpetuation of severe storms in a sheared environment, it was deemed important to consider simultaneously the main rainfall regions and the updraft slope as predicted by the numerical model.

Before examining several interesting points which emerge from figures 42 through 50, it should be mentioned that the comparative experiments are run through in the same order as with the z-t diagrams. Figures 42 through 44, 45 through 47, and 48 through 50 cover the cases of least,

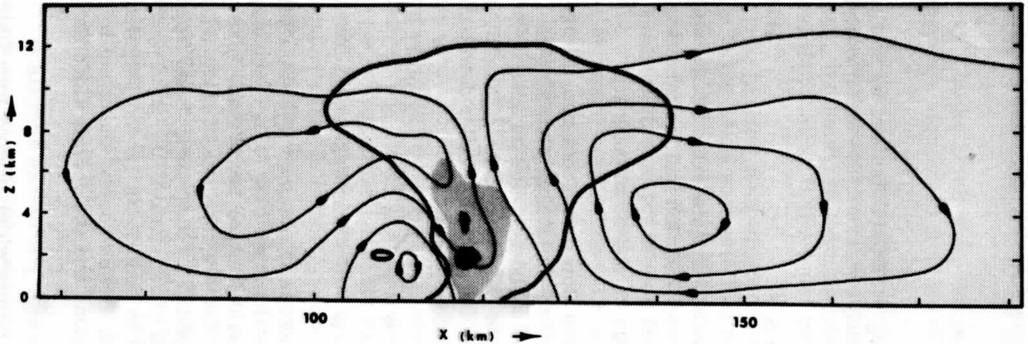

Figure 42. Airflow streamlines relative to the moving cloud core and rainfall pattern for case L1 at fifty minutes. The heavy solid curve represents the cloud boundary. Thinner solid curves with arrows are streamlines at intervals of 10^7 gm m^{-1} sec^{-1} . Dashed streamlines (if any) indicate half-intervals. Light shading (if any) represents rainfall with an intensity of at least 30 mm hr^{-1}; heavy shading (if any) represents rainfall with an intensity of at least 90 mm hr^{-1}.

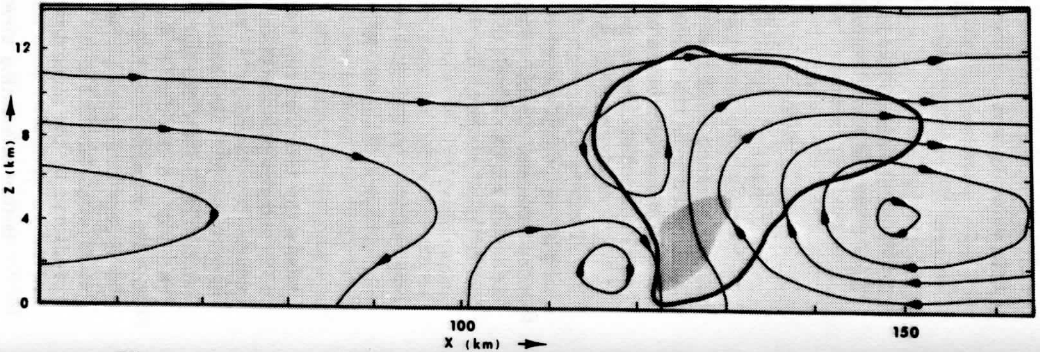

Figure 43. Same as figure 42, but for case M1 at fifty minutes.

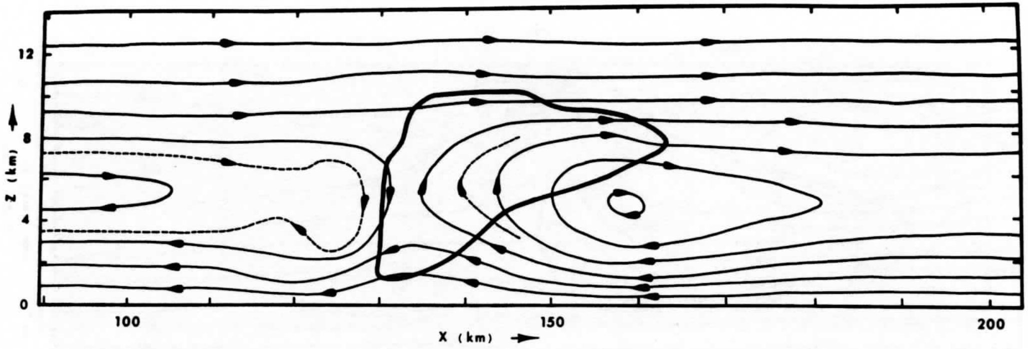

Figure 44. Same as figure 42, but for case H1 at fifty minutes.

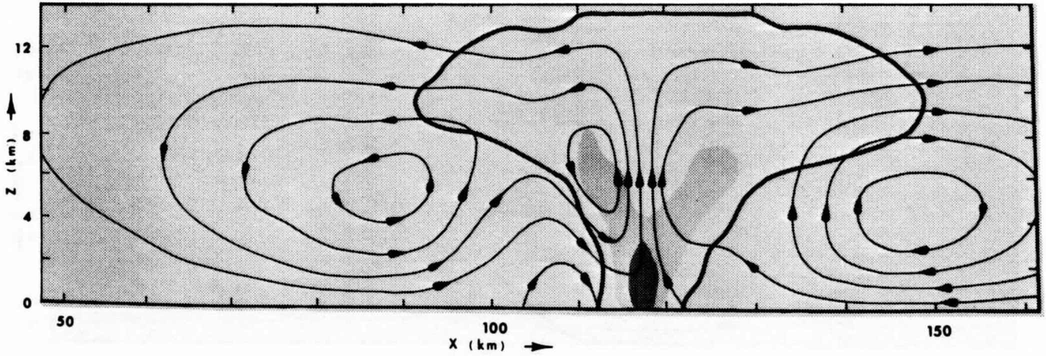

Figure 45. Same as figure 42, but for case L2 at fifty minutes.

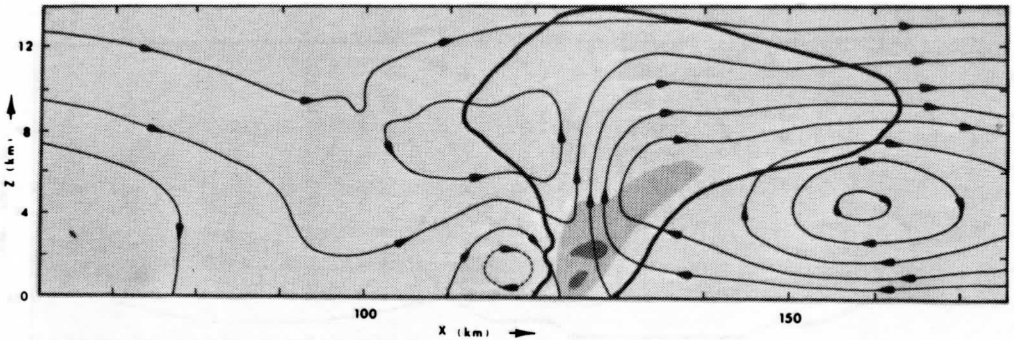

Figure 46. Same as figure 42, but for case M2 at fifty minutes.

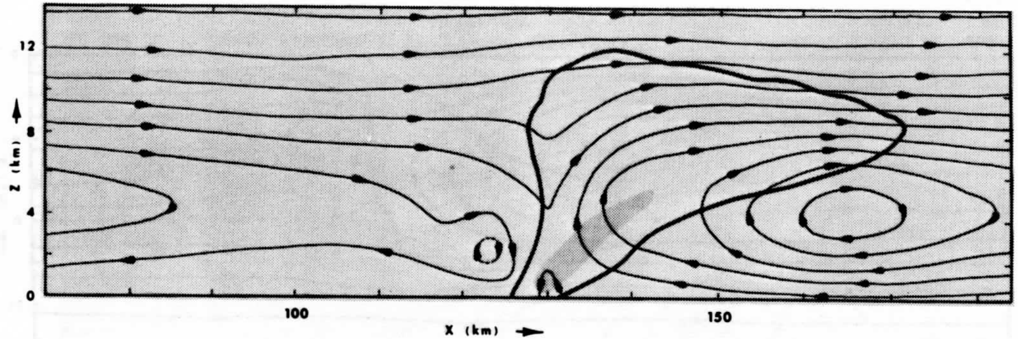

Figure 47. Same as figure 42, but for case H2 at fifty minutes.

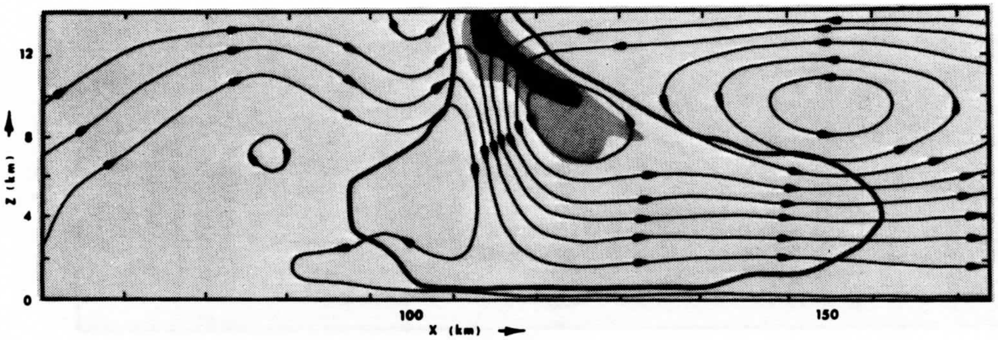

Figure 48. Same as figure 42, but for case L3 at fifty minutes.

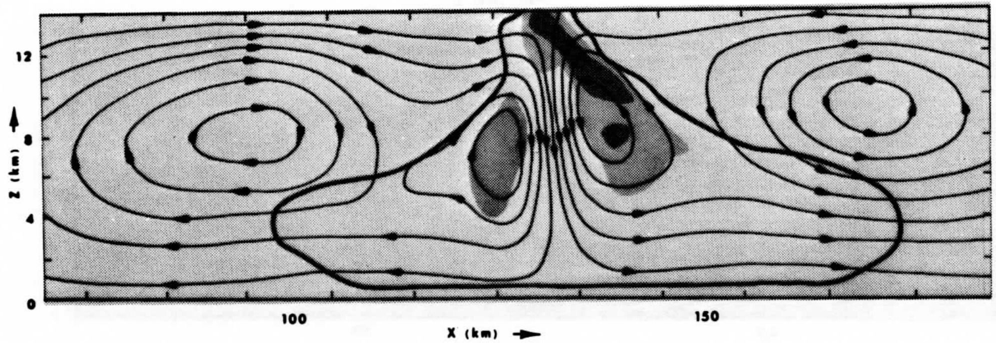

Figure 49. Same as figure 42, but for case M3 at fifty minutes.

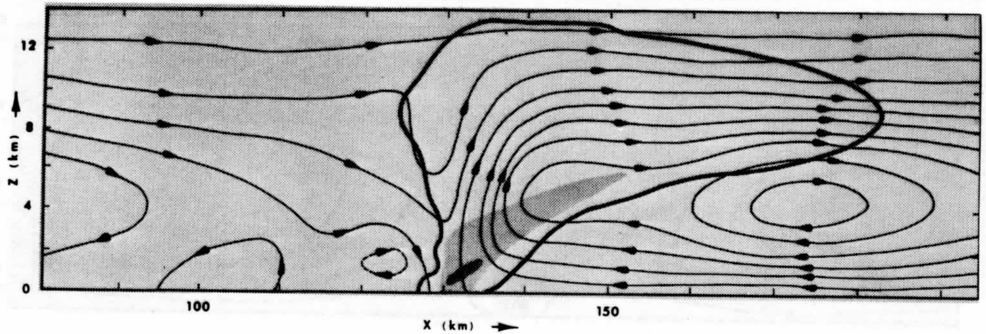

Figure 50. Same as figure 42, but for case H3 at fifty minutes.

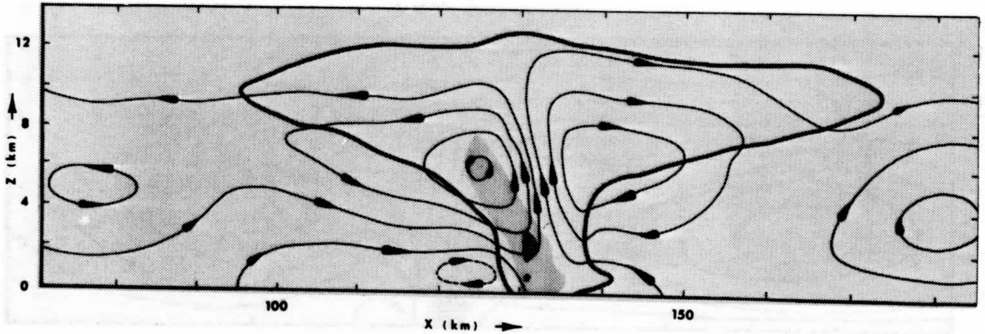

Figure 51. Same as figure 42, but for case L1 at seventy minutes instead of fifty minutes.

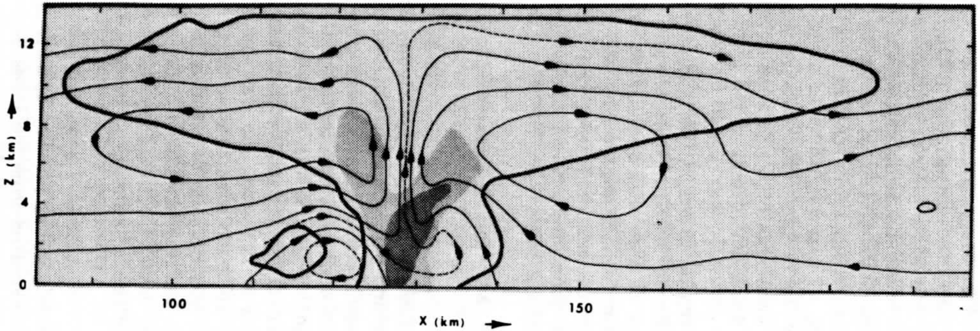

Figure 52. Same as figure 42, but for case L2 at seventy minutes.

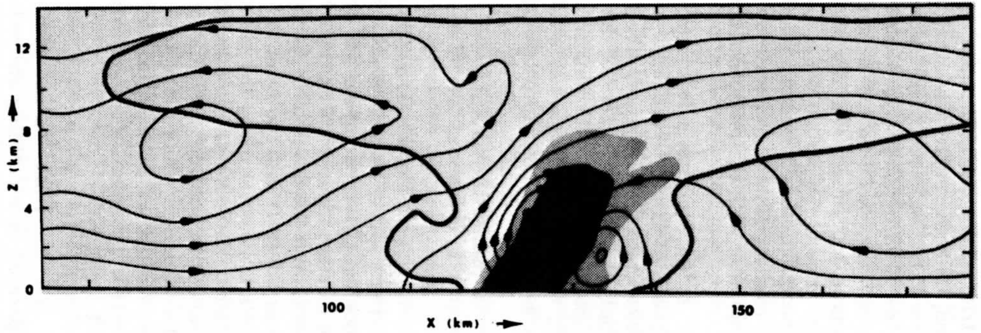

Figure 53. Same as figure 42, but for case L3 at seventy minutes.

intermediate and greatest moisture supply, respectively, with each three-figure group proceeding in order from least to greatest wind shear.

1) As wind shear is increased, the circulation becomes more asymmetric. Since the storm core velocity, rather than the undisturbed ambient wind, is being subtracted from the total flow, the asymmetry in the more sheared cases is radically different from that shown in the earlier diagrams. At low shear (figures 42, 45 and 48), two branches of comparable intensity are present, much as for the pure disturbance flow. But at moderate shear (figures 43, 46 and 49), the left branch is considerably weaker than the right branch. At strong shear (figures 44, 47 and 50), there is no longer a recognizable left branch. Note that unlike the pure disturbance flow, the relative flow at moderate and strong shear exhibits a type of asymmetry consistent with the predominance of the anvil downshear of the updraft core.

2) As wind shear is increased, the region in which the rainfall rate exceeds 30 mm hr^{-1} becomes smaller and more inclined downshear. Not unexpectedly, this region also diminishes in area with decreasing moisture supply. The areal extent of the significant rainfall region may be regarded as another measure of storm intensity. In the weakest case, run H1 (figure 44), no part of the cloud is shaded; some precipitation is produced, but the maximum rainfall rate is only about 27 mm hr^{-1}.

3) Six of the runs (L1, M1, L2, M2, M3, and H3) have the following features in common:

(a) The channels in between streamlines sharing in the cloudy updraft originate partly from in front of the storm and partly from in back of it. Since equal masses of air per unit time are flowing through each channel, the relative mass contributions of air from each side can be gauged by inspection of the diagrams. Except in case M1 (figure 43), there is a secondary updraft into the front flap of the anvil, with little vertical motion or slight descent along the cloud boundary in between. As was noted in regard to the pure disturbance flow, this splitting results from significant evaporative cooling along the right cloud boundary up to about 6 km. In all such cases, only those flow channels leading into the primary updraft are regarded as contributing to the storm, since the anvil is relatively inactive dynamically. If a closed streamline is present, it is regarded as half a channel.

(b) The front-fed and back-fed channels of the primary updraft are separated by a dividing streamline (DS) emanating from the lower boundary and ascending through the cloud core and into the anvil.

(c) A shallow reverse eddy is present just to the rear of the lower part of the storm. The eddy is separated from the flow at higher levels by an arched streamline which emanates from the lower boundary in back of the downdraft (except run H3, in which the separating streamline originates from higher levels), continues toward the storm and then sinks back to the lower boundary as part of the downdraft. The ascent on the left "leg" of the arched streamline (absent in run H3) is due to convergence between the outflow from the rear of the storm and the accelerated air flowing righward toward the storm from the more distant subsiding surroundings.

(d) Between the DS and the right "leg" of the arched streamline, the right-hand part of the downdraft outflow moves toward the right relative to the cloud. This region of accelerated horizontal flow perhaps corresponds in the model to the "squall gust" after which the squall line has been named. Compared to the undisturbed value of 6 m $\sec^{-1}$ for u at the surface, the maximum value of u relative to the earth in this region ranges from 13 m $\sec^{-1}$ in run L2 to 18 m $\sec^{-1}$ in run H3. Although these values appear quite moderate, it should be stressed that the model can only resolve sustained space-averaged winds, so that these values do not include considerably stronger winds which might result from subgrid-scale turbulence or small convective cells excluded by the two-dimensional assumption.

4) In the six runs featuring both a DS and a reverse eddy, the updraft channels to the right of the DS have a higher mean θ_e than those to its left. This is because the air entering the front of the storm includes air from the lowest (and potentially warmest) levels of the moist layer, whereas the air entering the rear of the storm arrives from above the separation streamline marking the top of the reverse circulation. It might therefore be expected that a predominance of mass flux from in front of the DS would be conducive to an updraft stronger or more persistent than if the mass flux were mainly from in back of the DS.

5) The location of the heaviest rainfall, and to a smaller extent that of the larger region of significant rainfall, is determined largely by the orientation of the DS. In run L1 (figure 42), in which the DS is tilted toward the left over nearly its entire depth, all significant rainfall occurs to the left of the DS. In runs M1 (figure 43) and M2 (figure 46), the DS as a whole is nearly erect, tilting toward the back of the storm up to the middle levels and then gradually sloping toward the anvil. Some of the significant rainfall in these cases overlaps the front channels of the updraft, but the heaviest precipitation is in back of the DS. The updraft in run M3 (figure 49) shows a slight downshear tilt on the whole, causing much of the significant rainfall (including heavy rain up to 140 mm hr^{-1}) to lie to the right of the DS.

6) Whether or not a DS or reverse eddy is present, the leftmost updraft streamline originating from in front of the cloud approaches its left edge more closely as shear is increased and the moisture supply kept the same. This may be at least partially explained as follows: as wind shear is increased, the velocity of the cloud core is also increased and the cloud is more likely to overtake the incoming low-level air before this air can ascend far into the cloud core. The closer the approach of the updraft to the left cloud edge, the more its buoyancy is likely to be reduced due to mixing with the evaporatively cooled air along and near the edge.

Since the effective horizontal eddy viscosity coefficient of the advective differencing scheme used in the model is an order of magnitude greater than appears reasonable for deep moist convection, the model is felt to overestimate the effects of mixing despite the omission of any explicit heat diffusion term. In view of this, the loss of updraft buoyancy due to mixing with evaporatively cooled air is probably greater than in actual storms.

7) Especially outside the stronger storms, the inflow toward the cloud at low and middle levels is considerably stronger than one would estimate by comparing the cloud core velocity to the undisturbed ambient wind alone. The two-roll circulation superimposed on the undisturbed flow increases u to the left of the cloud and decreases u to the right, apart from the additional perturbation due to outflow from the cold downdraft. In each run, the greatest perturbations of u at low levels are comparable in magnitude to the maximum updraft speed. Most noticeably, run L3 (figure 48) shows maximum inflow of about 18 m sec^{-1} at the surface; relative to the earth, u reaches 25 m sec^{-1} at the surface under the trailing edge of the anvil. In run M2, a more moderate case, the surface maximum of u upwind of the storm (nearly 18 m sec^{-1}) is over 2 m sec^{-1} larger than its local maximum under the cloud core. It is suspected that the rectangular geometry of the model has caused compensating motions to be exaggerated, since the flow outside actual convective storms (even the individual storms making up a squall line) is three-dimensional and therefore spread over a larger area (relative to that of the storm core) than the geometry of the model allows.

8) The strongest storm among the nine cases, namely L3, shows a DS but has not yet developed enough of a low-level downdraft for an appreciable reverse eddy to form. Therefore, the lowest-lying (and potentially warmest) air feeds the main updraft from both sides. The resulting exceptionally high θ_e in the storm core (see figure 13c) is probably responsible for the very large second maximum of w (19.4 m sec^{-1}) about three minutes after the time shown. Its comparatively short life appears mainly due to the accumulation of the very heavy rainfall (up to 180 mm hr^{-1}) in the lower part of the updraft.

9) The two weakest storms, cases H1 (figure 44) and H2 (figure 47), fail to exhibit a DS in the sense explained under point (3). This indicates that the potentially warmest strata of the moist air are not entering the updraft. This anomalous situation helps to explain the weak intensity of these storms, especially in run H1. In this case, neither of the two lowest-lying inflow channels ascends into the cloud core. As a result, θ_e in the cloud core is considerably lower than in the other runs (see figure 9c), and the cloud begins dissipating after a single vertical velocity peak of only 5.8 m $\sec^{-1}$ is reached. The cloud velocity at fifty minutes (19 m $\sec^{-1}$) is about twenty percent greater than for either of the two other strongly sheared cases, H2 and H3; evidently the lowest-level air flowing toward the cloud cannot increase its horizontal momentum fast enough to remain in the rapidly translating cloud.

In this and the next few paragraphs, we now synthesize the points described above. Among them, (3) through (6) relate most directly to the intensity and persistence of the main updraft among the comparative experiments. For a given moisture supply, the intensity of the updraft depends largely upon its degree of protection from the outside air, as explained under point (6). The strengthening with increasing moisture, for a given initial shear, is due (as one would expect) to the increase of convective instability with relative humidity since the vertical temperature profile is the same in all cases. For the six cases exhibiting a dividing streamline and a reverse eddy at fifty minutes, the persistence of the updraft appears determined mainly by the location of the heaviest rainfall relative to the dividing streamline (which in turn is influenced largely by the updraft orientation) and by the relative mass fluxes of air into the front and back of the updraft.

The reverse eddy, especially when it is well developed (as in cases L1, M1 and M2), cuts off the potentially warmest air from the back of the storm, so that an updraft fed predominantly from the front should persist longer than one fed predominantly from the back. Also, the further rearward the heaviest precipitation is located, the longer the updraft is likely to persist. The liquid water concentration in the region of heaviest rainfall provides two possible sources of vertical deceleration: downward drag due to its weight, and negative thermal buoyancy due to the maintenance of a large liquid water supply for evaporative cooling at the nearer cloud edge. If the heaviest rain falls into the front of the cloud, the low-level air ascending into the updraft will be decelerated, whereas a concentration of rainfall toward the back of the cloud tends to perpetuate the downdraft at the rear with relatively little adverse effect on the updraft.

The persistence of the two storms whose updrafts are most nearly quasi-steady after about forty minutes, namely M1 (moderate shear and least moisture) and H3 (strong shear and greatest moisture), is favored both by the location of the DS and by the rainfall distribution. In run M1, there are 4.5 front channels and 1.5 back channels in the updraft at fifty minutes; the corresponding numbers of channels in run M3 at fifty minutes
The heaviest rainfall is largely bypassed by the front channels. Case M2 (moderate shear and intermediate moisture), which also exhibits a quasi-steady updraft but not quite as persistently as the preceding two cases, is less favorable in terms of channel distributions (2 in front, 2.5 in back) but about as favorable as run H3 regarding precipitation distribution. The long life of the strongly pulsating updraft in run L1 (low shear and least moisture) may be anticipated mainly from the confinement of significant rainfall to the rear of the dividing streamline. Since the reverse eddy is weak in runs L2 (low shear and intermediate moisture) and M3 (moderate shear and greatest moisture), the channel distributions are less significant than in the other cases, but note that the rainfall distribution is less favorable in run L2 than in run L1 and quite unfavorable in case M3 which shows some of the heaviest rain far in front of the dividing streamline. These two runs, especially M3, show faster and earlier decay of the main updraft than do the other strong cases. As noted in point (9), the weak development in the remaining two strongly sheared cases (H1 and H2) is mainly due to the separation of the potentially warmest air from the updraft, and the very strong but relatively short-lived updraft of run L3 (low shear and greatest moisture) was explained under point (8).

We have already noted the most salient changes between fifty and seventy minutes for five of the runs by examining the perturbation streamlines and isotherms. It was therefore considered unnecessary to compare relative flow patterns at fifty and seventy minutes for most cases. Apart from the considerable horizontal stretching of the cloud anvil and the overall circulation, four of the more sheared runs (M1, M2, H2 and H3) otherwise showed no large changes between fifty and seventy minutes. The weak cloud of case H1 continued to dissipate. Run M3 did exhibit a dramatic change in configuration, but this change was similar to that which occurred in run L3. The most striking changes occurred in the low-shear runs, even though the cases involving moderate or strong shear have been of chief interest in this work. The changes in the L runs between fifty and seventy minutes may be seen from a comparison of figure 51 with 42, 52 with 43, and 53 with 44, and will be briefly pointed out next.

Although the downdraft at the left cloud edge in run L1 (figure 51) has weakened somewhat (from nearly 4 to 2.5 m sec^{-1}), the in-cloud updraft has strengthened from 6 to 14 m sec^{-1} near the 7 km level and has become narrower (due to the splitting effect mentioned earlier). This remarkable strengthening, more pronounced than in any other comparative runs, may occur partly because the part of the updraft to the right of the DS completely bypasses the region of significant precipitation (30 mm hr^{-1} or more). If the undisturbed wind is completely free of shear, the updraft should be erect; evidently, the slight shear in the moist layer along with a tendency for slow-moving air drawn into the front of the updraft to conserve its low horizontal momentum combine to produce the updraft tilt.

In run L2, the region of heavy rainfall has expanded considerably between fifty and seventy minutes (figure 52), spreading into one of the updraft channels ahead of the DS. The downdraft has widened and is now developing in the right-hand part of the heaviest precipitation, as emphasized by the dashed partial streamline. In a region humidified by earlier evaporation, the weak ascent upwind of the downdraft has formed a secondary cloud about 2 km deep. This cloud formation is forced, i. e., not due directly to thermal buoyancy, as is evident from the disturbance temperature field in figure 39. At eighty minutes (not shown), however, the secondary cloud has become about 4 km deep and up to 2°C warmer, merging with the main cloud; the downdraft strengthens to over 6 m sec^{-1} in the cloud core while the original updraft above it decays rapidly (from 12 m sec^{-1} at 70 minutes to 3 m sec^{-1} at eighty minutes).

The flow in run L3 has changed dramatically since fifty minutes in and near the cloud (figure 53). There is considerably more asymmetry, as reflected in the rightward leaning of the significant rainfall region with height. The lower region of cloud and precipitation is very broad (about 35 km) with extremely heavy rainfall up to 300 mm hr^{-1} in its core. What was previously the DS now ascends rearward to only 4 km and returns to the ground in the strong downdraft (8. 8 m sec^{-1}) where the heaviest rain is located. The relative outflow on either side of the vigorous downdraft results in a maximum surface wind of 20 m sec^{-1} in advance of the heavy rain. The preponderance of heavy precipitation in the lower right portion of the cloud at fifty minutes has provided a larger supply of liquid water for evaporative cooling at the right edge than at the left edge. As the low-level saturated region widens, negative thermal buoyancy near the right edge leads to a downdraft which later becomes saturated-adiabatic with increasing protection of the cold air from the unsaturated surroundings. The main updraft has weakened considerably since fifty minutes, and slopes to the right with height, having taken on some of the high horizontal momentum of the air ascending into the storm from the back. The lowering of the maximum updraft altitude from about 7 to 4 km, together with its still considerable strength (9. 4 m sec^{-1}), indicate that the strong surface convergence between the downdraft outflow and the air entering the storm from the rear is inducing new upward motion in the same location as the decaying main updraft, effectively slowing its dissipation.

7.4 Moisture-Shear Diagrams

In view of the complexity of the results thus far presented, it is now fitting to summarize in highly condensed form the most salient points. To this purpose, various parameters have been contoured in figures 54a through 55e (see the figure captions for explanations of these parameters). Here each comparative run is represented as a point in the "moisture-shear" plane diagrammed in figure 4. Recall that moisture increases to the right and shear increases upward in this space.

It is immediately evident that five of the plotted parameters follow basically similar patterns. These are the first and last absolute maxima of w, the average maximum rainfall rate from forty to seventy minutes, and the areas in which either liquid water content or rainfall rate exceeds fixed values indicated in the appropriate captions. These five parameters all increase with decreasing shear and increasing moisture, and both factors are of comparable importance since the isolines of each parameter are greatly inclined to both abscissa and ordinate. If any of these five variables is taken as a criterion of convective development, it is apparent that shear suppresses storm development and moisture aids it.

Note that figure 55b shows essentially the area of the RHI (range-height indicator) radar echo corresponding to the two-dimensional model storm. Since Takeda's parametrization (see section 2) has been used for handling precipitation, the area enclosed by the 1 gm m^{-3} contour of L coincides with the region containing precipitation particles regardless of whether they are falling toward the ground. The parameter plotted in figure 55c is simply the area of the shaded region of actual rainfall in each of figures 42 through 50.

The downdraft velocity plotted in figure 54e depends mainly upon the moisture, although some dependence upon shear is also evident. The downdraft velocities shown in this diagram have been evaluated at fifty minutes rather than at a later time in order to provide a meaningful comparison among all nine experiments. (Recall that in runs L2, L3 and M3, the downdraft at and near the left cloud edge weakened between sixty and eighty minutes while a much stronger downdraft developed in the right center region of the cloud.) At all values of wind shear, especially at low shear, the downdraft intensity decreases with increasing moisture, indicating the importance of evaporative cooling to downdraft formation.

The parameter plotted in figure 54c is the elapsed time from the initial instant until the maximum updraft velocity has decreased by twenty percent from its last peak before dissipation. This is its second maximum in all runs except for H1, which shows only one peak. Although the choice of

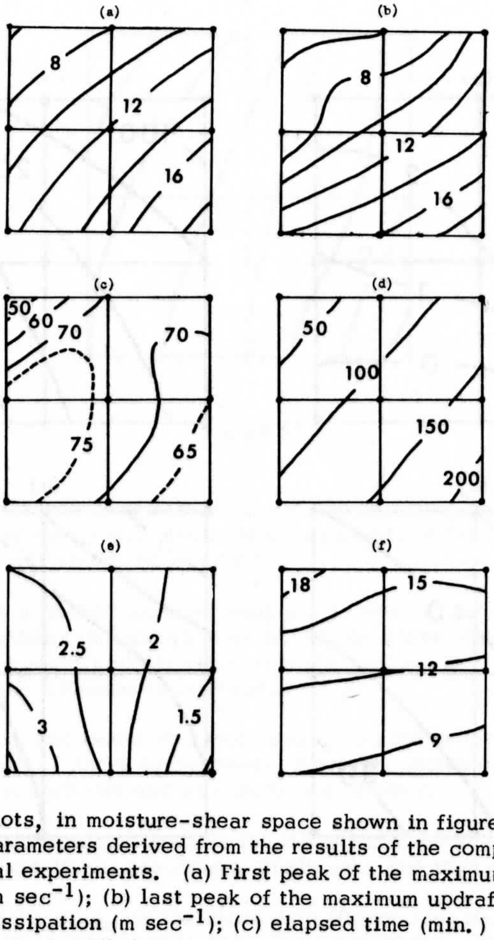

Figure 54. Plots, in moisture-shear space shown in figure 5, of selected parameters derived from the results of the comparative numerical experiments. (a) First peak of the maximum updraft velocity (m sec^{-1}); (b) last peak of the maximum updraft velocity before dissipation (m sec^{-1}); (c) elapsed time (min.) from the initial instant until the maximum updraft velocity decreases to 80% of its last peak before dissipation; (d) average value of the maximum rainfall rate at any point (mm hr^{-1}) from forty through seventy minutes; (e) Maximum downdraft velocity (m sec^{-1}) at fifty minutes at the 2.1 km level to the left of the updraft; (f) average propagation velocity (m sec^{-1}) of the storm core from forty through seventy minutes.

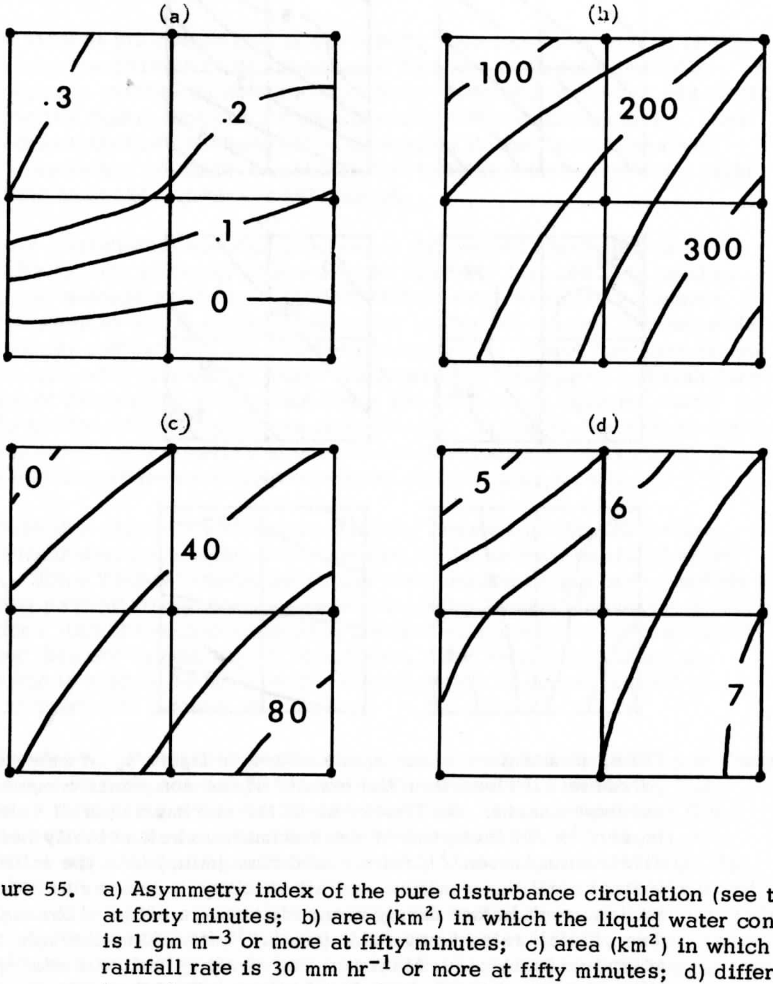

Figure 55. a) Asymmetry index of the pure disturbance circulation (see text) at forty minutes; b) area (km^2) in which the liquid water content is 1 gm m^{-3} or more at fifty minutes; c) area (km^2) in which the rainfall rate is 30 mm hr^{-1} or more at fifty minutes; d) difference in surface pressure (mb) between the thunderstorm "high" and the downstream "low" at fifty minutes; e) excess of equivalent potential temperature above initial base value (°K) at 4.2 km level in the updraft core at fifty minutes.

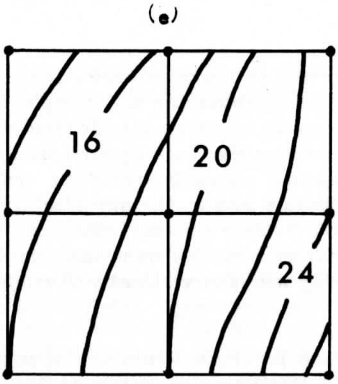

Figure 55e.

twenty percent was somewhat arbitrary, the resulting parameter was felt to provide a reasonably good index of the longevity of the main updraft. The following points should be stressed:

1) With a limited moisture supply ("1" and "2" runs), moderate shear slightly lengthens the updraft life, but strong shear leads to earlier dissipation. With a sufficiently large moisture supply ("3" runs), the updraft persists longer as shear is increased.

2) At low and moderate shear, increasing the moisture supply shortens the updraft life. Under strong shear, however, increased moisture does not shorten the updraft life and may prolong it slightly.

3) If the moisture supply is too limited and the shear too strong, the updraft is short-lived, reaching a single peak and then dissipating.

The excess of θ_e in the cloud core (figure 55e) increases more strongly with increasing moisture than with increasing shear. This is not surprising; the height-averaged value of θ_e in the undisturbed moist layer (which, through its convective instability, provides the key latent energy source) depends only on the moisture supply in these experiments, since the vertical temperature profiles are assumed identical in all cases. The weak but definite decrease of excess θ_e with increasing shear partially parallels the decrease of updraft velocity, since the updraft becomes less far removed from unsaturated air to the rear of the cloud as shear is increased, and should therefore be more susceptible to reduction of buoyancy.

The cloud velocity (figure 54f) increases with the vertically averaged wind velocity and corresponds approximately to the initial ambient wind at

4 to 5 km in the moderately and strongly sheared cases. For those runs with moderate or no initial shear above the moist layer, the slight decrease of storm velocity with increasing moisture supply reflects a tendency for the model storms to slow down as the main updraft dissipates; weakening of the updraft, and the attendant cloud deceleration, occur earlier as moisture is increased at low and moderate shear, thereby slightly lowering the average displacement rate during forty to seventy minutes. The anomalously high cloud velocity in run H1 reflects its weak development which may cause it to travel more nearly with the vertically averaged ambient wind than in any other case.

In figure 55d, the surface pressure difference at fifty minutes between the "thunderstorm high" and the low-pressure center in front of it is plotted. Note that while the updraft maxima in figure 54a vary by a factor of 3 from the weakest to the strongest storm, the pressure difference varies by a factor of only about 1.5, and that at low and moderate shear the increase of this difference with increasing moisture is especially weak. This reflects two opposing tendencies: the strengthening of the overall circulation with increasing moisture, and the tendency for the high-pressure region under the storm core to become more developed as moisture is decreased. As mentioned earlier, it is suspected that this tendency is due to increased evaporation which in turn enhances cold air production and the hydrostatic contribution toward high surface pressure.

The asymmetry index plotted in figure 55a was the quantity $\ln|\psi'_{max}/\psi'_{min}|$, where ψ'_{max} and ψ'_{min} are the positive and negative extremes of the disturbance stream function at forty minutes. The relatively early time was chosen since after about fifty minutes at least one run showed a double positive center or a double negative center. The logarithm was used so that the asymmetry index would change sign but not magnitude if applied to the mirror image of a disturbance. The main result shown by figure 55a is that as shear is increased, the disturbance circulation becomes more asymmetric.

7.5 Comparative Experiments versus Observations

We now point out some similarities and dissimilarities between the model storms and actual storms as indicated either by observations or by schematic models whose motivation is at least partly observational. Four main aspects will be considered in the discussion: airflow patterns, temperature, pressure and precipitation. Most comparisons will involve severe thunderstorms which were not necessarily members of squall lines, but which still produced similar surface weather. As each aspect is considered, it will also be instructure to compare the results with those of the

Thunderstorm Project described by Byers and Braham (1949), although the project was concerned mainly with isolated air-mass thunderstorms.

Airflow Patterns

As mentioned earlier, one of the limitations upon the ability of the numerical model to produce a completely realistic convective circulation is its two-dimensional rectangular geometry. Although a squall line as a whole is mainly two-dimensional, mesoscale analyses such as those of Fujita (1955) have indicated that the surface outflow in squall line thunderstorms spreads out in all directions, as was also the case for individual thunderstorm cells observed in the Thunderstorm Project. The degree of disturbance in the surface wind outside of the model storms was considerably greater than is usually observed. In particular, the maximum departure of the surface wind from its undisturbed value was comparable to the maximum updraft velocity. The comparison presented by Newton (1950) between in-cloud shear and environmental shear does not apply closely in the numerical model, since Newton compared the in-cloud winds with the undisturbed environmental winds and treated the cloud as essentially rectangular over its depth. Such an argument would hold if the outside air was virtually undisturbed except in the most immediate vicinity of the cloud core, but not if the horizontal wind component well outside the cloud becomes significantly disturbed as in the numerical model.

Browning and Ludlam (1962) proposed a schematic three-dimensional model based on observations of the Wokingham hailstorm referred to in the Introduction. The main feature is a shallow layer of moist inflow into the front of the storm which becomes an updraft tilted toward the back of the storm (upshear) unit it curves sharply into the front of the storm as part of the anvil. Much drier midtropospheric air was visualized to enter the back of the storm, descending under and parallel to the tilted updraft and then flowing rearward out of the storm at low levels. Two of the moderately sheared cases, M1 (figure 43) and M2 (figure 46), exhibit these characteristics although to a smaller extent: the updraft in both cases tilts toward the rear of the cloud up to middle levels, and the downdraft originates at the rear of the cloud in potentially cool air, but at a somewhat lower level than indicated in the Browning-Ludlam model.

Recently, Fankhauser (1971) described midtropospheric chaff trajectories near the core of an individual severe thunderstorm which traveled through parts of Texas and Oklahoma. These trajectories indicated that the storm core diverted air around it much like a cylindrical obstacle in a wind tunnel. This lent support to the earlier mentioned hypothesis of Newton and Newton (1959). In the two-dimensional numerical model, by contrast, air which moves horizontally or nearly so must travel through the cloud unless its horizontal velocity is the same as that of the storm. Fankhauser's model showed that there is not only barrier flow about the storm core but also an updraft which rotates cyclonically by about 270° from where it enters the right flank of the storm (looking in the direction of its movement) to where it exits into the anvil, in contrast to the plane updraft of the numerical model.

For the right-moving severe storm emphasized by Browning (1964), the storm's movement to the right of the midtropospheric ambient wind enables dry air from middle altitudes to enter the right rear quadrant of the storm (again looking in the direction of its movement). After descending into the cloud as evaporating precipitation makes it negatively buoyant, this air exits in a direction opposite to that of the storm's motion. These three-dimensional features, of course, cannot all be directly represented in the two-dimensional model; while the high-altitude outflow from the updraft and the low-level outflow from the downdraft would indeed be along the direction of movement of the storm, the low-level inflow would be into the plane of the paper from the right (looking down at any one of the preceding diagrams showing two-dimensional features) while the middle-level inflow would be into the same plane from the left.

Goldman (1968) incorporated the features of both the Browning model and the cylindrical-obstacle representation. Using complex potentials for translation plus a source or sink, or for flow about a cylindrical obstacle, Goldman represented each of five main layers approximating the surroundings of a storm having a single large erect updraft. These five layers, from bottom to top, were designated "cold air outflow," "warm air inflow," "dry air inflow," "barrier flow," and "warm air outflow." In the layers of inflow or outflow, the translational part of the potential flow was oriented as in Browning's model, while the barrier flow (in a layer where the updraft was assumed to have a constant velocity equal to its maximum) bypassed the storm core just as in Newton's model, with the translational component in the direction of the storm's travel.

Despite the three-dimensionality of Goldman's model, some of the comparative runs did exhibit to some extent each of the layers designated by Goldman except for the barrier flow layer. The similarity is most noticeable in the two moderately sheared cases M1 and M2 and in the strongly sheared case H3. The warm air inflow and warm air outflow, into the lower front part of the cloud and into the right flap of the anvil, respectively, are especially strong, reinforced by the convective circulation. Similarly, the dry air inflow above the reverse eddy behind the storm is reinforced by the increased horizontal momentum throughout the lower left part of the overall circulation. The cold air outflow along the bottom of the reverse eddy is relatively weak because it originally developed as a small perturbation upon this high-momentum flow. Some air still enters the updraft from the rear even after the development of the downdraft and its attendant reverse eddy. In this connection, note that the relative inflow and outflow patterns in all of the schematic storm models described above were formulated in terms of the undisturbed ambient wind, not taking into account possible reinforcing or canceling effects due to perturbations in the surroundings of the storm. Most notably, each of the models portrayed the updraft as being fed exclusively from in front of the storm, and the low-level outflow as descending and then continuing indefinitely rearward with no suggestion of secondary convergence to the rear of the storm. The airflow configuration in actual severe thunderstorms and their vicinity probably lies between the extremes shown in the idealized schematic models and in the numerical model.

Except in the late stages of cases L3 (figure 53) and M3, in which strong convergence near a severe downdraft caused a rather shallow secondary updraft to form during the dissipation of the original updraft, the comparative runs exhibit a single main updraft and downdraft as in the schematic models. Possible variations in physical properties along the squall line being simulated have been averaged out, including cells larger than turbulent eddies but smaller than an individual cumulonimbus . For instance, some severe thunderstorms appear to be actively maintained by cumulus clouds first forming in back of them, then approaching and building, finally merging with the storm as new cloud turrets. These so-called "feeder clouds" have been described by Musil (1970) and Dennis et al. (1970). Some storms observed during the Thunderstorm Project exhibited several updrafts and downdrafts, and new cloud turrets appeared at intervals of eighteen to thirty minutes. Recall that all comparative runs except H1 show a pulsation of twenty to thirty-five minutes in the maximum updraft velocity; however, dissipation either is or appears to be taking place after one pulsation, and in some cases the first updraft peak may represent an overshoot arising from the initial conditions.

It is interesting that while the storms in runs M1, M2 and H3 each resemble Goldman's or Ludlam's prototype of a severe thunderstorm, the updraft velocities resemble those in the relatively moderate thunderstorms observed during the Thunderstorm Project, i. e., on the order of 10 m $\sec^{-1}$. The strong computational diffusion undoubtedly caused vertical velocities in the numerical model to be somewhat underestimated, but one or more of the following physical forces are also operating in addition to just the thermal buoyancy: the perturbed vertical pressure gradient force, liquid water drag and pressure buoyancy. It will be seen later that these additional forces greatly reduce the net vertical acceleration.

The schematic storm models assumed the storm to be steady state; we have noted observational evidence that severe thunderstorms in a sheared environment may maintain an approximately steady state for thirty minutes or considerably longer, and that among the comparative runs, three cases (M1, M2 and H3) show an updraft core whose intensity during the mature stage varies only slightly for about thirty minutes. (The overall circulation outside of the updraft cannot be considered quasi-steady since it elongates horizontally with time.) A three-dimensional numerical model with its presumably weaker compensatory motions might produce a longer quasi-steady phase than a two-dimensional model is able to, since the smaller degree of environmental warming would tend to keep the updraft more buoyant in the three-dimensional model.

Temperature

Among the five comparative experiments whose disturbed temperature fields were examined, the following main features have been noted earlier in this section:

1) a region of temperature excess within the cloud, extending from about 2 km to the base of the thin moderately stable layer, with the greatest excess near and slightly above the site of greatest upward motion;

2) a region of temperature deficiency in and near the cloud above the stable layer;

3) cooling along the cloud edges up to the middle levels, and in the lowest 2 km of the cloud core, mainly at the surface underneath or somewhat in back of the rear edge of the cloud; and

4) warming on either side of the cloud, most noticeable under the leading edge and somewhat behind the trailing edge (of the anvil).

The physical significance of these features, which are also present to varying degrees in the other four runs, has already been discussed. While there is little direct observational basis for comparing the second and fourth features in the model with reality, the remaining two features can be compared with actual data, as will be done in the next paragraphs.

In the balloon observation described by Barnes (1970), the updraft near 500 mb was 10°C warmer than at the same location an hour before the updraft passed through. In the three most vigorous model storms (L2, L3 and M3), the maximum temperature excess over the undisturbed initial value is about 10°C in cases L2 and M3 and up to 13°C in case L3. These large values occur at thirty minutes, when the first updraft peak occurs, and at levels near 6 km or not far from 500 mb; the peak updraft velocity is somewhat smaller than, but still comparable to, the 23 m $\sec^{-1}$ value in the Oklahoma storm. Also, the lapse rates between about 3 and 8 km in the cores of the model storms are close to moist-adiabatic. In light of the balloon data, the large temperature excesses in the strongest model updrafts appear to be realistic. The balloon apparently deviated out of the updraft near the 6.6-km level, so that there was no way of knowing whether the superadiabatic lapse rates of up to 14°C km^{-1} between the updraft cores and the cloud tops in the model reasonably approximate reality. In their numerical cumulus model, Murray and Anderson (1965) also noted a shallow superadiabatic layer between the warm cloud core and the relatively cold cloud top, and speculated that the commonly observed knobbed appearance of the tops of growing cumulus clouds might reflect the presence of such static instability.

Until about the time of the first updraft peak, each of the model storms is in a "cumulus stage" as described by Byers and Braham (1949) in connection with the Thunderstorm Project. That is, no rain has reached the ground and no significant cloudy downdraft has yet developed (although the dry compensating descent outside of each cloud is considerably stronger before forty minutes than at later times). In the comparative runs, the temperature around 6 km within the updraft at thirty minutes ranges from about 3° to 12° higher than the horizontal mean outside the cloud. Most of these excesses are considerably greater than those found at a similar level (20, 000 feet) in ten updrafts during the Thunderstorm Project, with four of the updrafts being probed in the "cumulus stage" and six of them early in the "mature stage" (when both updrafts and downdrafts were present within a thunderstorm cloud). The observed excesses averaged slightly over 2° and in no case exceeded 4°. Whereas the thunderstorms studied in the Thunderstorm Project were typically a few kilometers in diameter during the cumulus stage, the model clouds are 15 to 20 km wide by thirty minutes.

In all comparative runs except H1 (least moisture supply and greatest shear), some precipitation reaches the surface, and the lower boundary conditions described in section 5 simulate the arrival and subsequent spreading of cold air there. Although the surface cooling spreads both in front of and in back of the precipitation zone, it extends further behind than in front of this zone in the sheared cases. Maximum surface cooling in the model ranges from about 3 to 8°C, therefore taking on reasonable values. As may be seen from the diagrams showing the two-dimensional temperature disturbances, the location of greatest surface cooling is at or immediately behind the back edge of the precipitation region at both fifty and seventy minutes.

Thunderstorm Project observations indicated that the cold outflow extended considerably further in front of than in back of a storm cell. The location of greatest surface cooling was under the core of the cell during the early mature stage, but was later located behind the cell and relatively stationary in position despite the predominant spreading of cooled air ahead of the main disturbance. At least in the sheared cases, the cooled air extends mainly behind a model storm partly because the downdraft outflow is predominantly rearward (relative to the storm) and partly because the downdraft itself is at and near the back edge. The forward displacement of the site of maximum surface cooling in the model is due to the nature of the lower boundary conditions. The earth's surface is not treated as a source of water vapor even though the advection of unsaturated air to a lower grid point where precipitation is just ending creates temporary evaporative cooling. The local persistence of a surface temperature minimum as long as an hour after cessation of precipitation was observed during the Thunderstorm Project, and was attributed to evaporation of residual ground moisture into air passing over the surface, rather than to evaporation of still falling precipitation into unsaturated air arriving at the rear edge of the shower.

Pressure

The tendency in this model for the disturbed part of the pressure to change from negative to positive with increasing height in the updraft has been noted earlier. In the earlier mentioned thunderstorm cited by Barnes (1970), a rather similar height variation of the disturbed pressure was noted. Near the updraft base, the pressure was about 1 mb lower than that at the same level about 30 km upwind of the storm, but the algebraic difference between the pressure in the updraft and at the upwind location became more positive with altitude, so that near 500 mb the pressure in the updraft was at least 3 mb greater than in the surroundings. The pressure excess in the model occurs mainly at a somewhat greater altitude than in this actual case, but the height variation of the perturbation pressure is still of similar magnitude.

The fifty-minute pressure disturbance fields shown in figures 28 through 32 all show a shallow region within and near the cloud trunk where the pressure is higher than on either side. During the growing stages of the storm, or about the first thirty minutes, this relatively high pressure is not present and the greatest deficit is located at the surface and just downwind of the cloud core. At these times there is a pressure deficit throughout the lower 4 to 6 km of the domain and an excess at higher levels. A similar basic distribution of disturbed pressure was found in the shallow cumulus model developed by Arnason et al. (1968). Since the grid domain in the cumulus model was only 3 km high and 3 km across, and the experiment was run out to only eight minutes, the pressure perturbations were far smaller than in the deep convection model. Pressure perturbations are as large as several millibars by thirty minutes in the deep convection model, but two orders of magnitude smaller in the experiment of Arnason et al. Also, the domain in their model represented half of a slab-symmetric box, and the greatest pressure excess and deficit were both located along the axis of symmetry.

The surface pressures in the model's "thunderstorm highs" (except for figure 31) are lower than the initial values because these features are developing in what was earlier a general region of pressure falls, and are not sufficiently developed as of fifty minutes to reverse the sign of the net pressure change. Surface pressure falls as large as those in run M2 (about 7 mb) and M3 (about 9 mb) are not commonly observed; factors contributing to the very low pressures will be brought up in the next paragraph. However, such large changes in pressure are not unheard of in situations involving thunderstorms (not including the much larger pressure falls which may occur in tornados). As noted by Brunk (1949), local pressure falls as large as 15 mb were observed in Illinois in connection with a thunderstorm-producing disturbance in April 1944. Still, the pressure falls occurring at low levels in the model are several times greater than the values of about 1 mb reported in the Thunderstorm Project. The surface pressure variations in the model are two to three times greater than the observed "pressure jump" which Tepper (1950) discussed in connection with observations for an actual squall line over Ohio.

The low-level pressure falls outside the model storms are large mainly because the warming of the surroundings, and therefore the hydrostatic contribution toward low surface pressure, are overestimated. Also, the low-level winds are speeded up too much on the left of the cloud, and slowed down too much on the right, so that the respective negative and positive horizontal accelerations undergone by parcels ascending toward the updraft core are exaggerated. Provided that friction outside the cloud can be neglected (as has been done in the model), this in turn implies that low-level horizontal pressure gradients are too strongly positive on the left of the cloud and too strongly negative on the right. Thus, both thermal and dynamic effects account for the strength of the low-pressure regions outside the cloud.

Precipitation

Since the representation of precipitation in this model was considerably simplified, certain aspects of the precipitation process are not realistic; in particular, after the static phase adjustment has been applied wherever necessary (see appendix B), the air is saturated wherever precipitation is present, thus precluding the incorporation of the humidity dip observed in some cases by the Thunderstorm Project.

Also, the omission of the freezing process has prevented the inclusion of hail, which is commonly present in squall line thunderstorms. Some aspects of the precipitation in the model are in reasonable agreement with observations. Thunderstorm Project observations indicated that at least during the early mature stage of a thunderstorm cell, the greatest surface rainfall rate and the greatest surface wind (in the direction of the storm's motion) were usually near the center of the cell. From the streamline and rainfall patterns shown in figures 42 through 50, this may be seen to hold at fifty minutes in six of the comparative runs (L1, L2, L3, M2, H2 and H3). In the other cases, precipitation has not reached the surface (M1 and H1) or the heaviest surface rain is ahead of the strongest surface wind (M3). The average of the maximum rainfall rate from forty through seventy minutes anywhere in the cloud ranges from about 70 mm hr^{-1} in cases M1 and H2 to 220 mm hr^{-1} in case L3 (disregarding run H1 in which no precipitation reaches the ground at any time). The greatest surface rainfall in the model is usually half to three-fourths of the maximum anywhere in the cloud. For twenty-seven squall lines observed over the Ohio surface network during the Thunderstorm Project, the station reporting the heaviest total rainfall had a mean rainfall rate (over the duration of the rain) between 30 and 90 mm hr^{-1} in 17 of the 27 cases. These are comparable to the mean surface rainfall rates during the model showers.

Certain features of the precipitation patterns for some actual thunderstorms are absent in the numerical model. As already noted, no humidity dip can occur in this model. Also, the vault referred to in the Introduction is not evident. The updraft velocities near the front edges of the model clouds are insufficient to suspend a significant part of the precipitation, and the rather coarse grid cannot accurately resolve features as small as the vault. Accumulation zones, or localized regions of especially large precipitation content, are not present at high altitudes in the model, although they do occur in the lower halves of the model clouds. Dennis et al. (1970) have described vertical radar reflectivity profiles indicating accumulation zones as high as 10 km within Great Plains hailstorms.

7.6 The Applicability of a Recent Hypothesis of Takeda to the Results of the Model

In a recent two-dimensional model of deep convection with precipitation, Takeda (1971) performed four experiments in which the initial ambient wind shear changed from negative to positive with increasing height. From one experiment to another, the initial perturbation (a shallow buoyant cloud with no momentum perturbation) and the initial base state were not changed except for the height of the negative jet (which ranged from 1.5 to 5.5 km in a domain 10 km deep). Running each experiment out to sixty minutes of simulated time, Takeda found that the updraft maximum in each case reached a peak between about twenty-five and thirty-five minutes and that this peak varied rather little among the four cases (from about 6.5 to 8.2 m sec^{-1}). At later times, however, the updraft decayed monotonically in the extreme cases but became nearly steady-state after about ten minutes of decay in the two intermediate cases. The remainder of this discussion will be concerned with a hypothesis put forth by Takeda in order to explain these results, including some modifications which appear needed regarding this theory to account for the results of the present model.

Takeda considered two critical heights for the negative jet. A jet below the first critical height F should lead to a downdraft to the right of the updraft, whereas if the jet is below F the downdraft should form to its left.* A jet below the second critical height S should favor a new updraft to the right of the downdraft, while a jet above S should favor its development to the left of the downdraft. The expected relative locations of the primary updraft and downdraft were based on the implied assumptions that the tilt of the primary updraft should be in the direction of the ambient wind relative to the cloud, and that the downdraft should form where most of the precipitation falls out of the updraft. The expected relative locations of the downdraft and the new updraft were based on the assumption that the downdraft on approaching the surface should have horizontal momentum equal to the average for the undisturbed ambient wind over the depth of the downdraft; the new updraft should occur where there is convergence between the downdraft and the mean ambient wind. From these assumptions, it is readily deduced that if the jet is either above or below both critical levels (regardless of whether S is above or below F), the downdraft should be between the updrafts. If the jet is between the two critical levels and $F < S$, the downdraft should occur to the left of the primary updraft and the new updraft should be to the right of the downdraft; if $F > S$, a similar situation should hold with right and left interchanged. In particular, the new updraft might reinforce the primary one, in effect postponing its dissipation. If the jet is too high or too low, the location of the updrafts on opposite sides of the downdraft indicates that neither updraft can reinforce the other. Takeda's results therefore gave his hypothesis some support, especially since the relative locations of the downdraft and primary updraft in each experiment were consistent with what the assumptions imply. Also, the tilt of the primary updraft in Takeda's experiments did tend to reflect the direction of the initial ambient wind relative to the cloud.

In the present numerical model, the updraft tilt is not dependent solely on the vertical wind profile. Among the M runs (moderate shear), the updraft

---

*In this context, left and right refer to directions of negative and positive wind shear respectively, looking toward the plane of the model clouds.

at fifty minutes tilts upshear up to about 6 km in cases M1 (figure 43) and M2 (figure 46) but only up to about 3 km in case M3 (figure 49). Even in the L runs (low shear), with the initial ambient wind shear confined to the moist layer, the overall updraft tilt is not the same in all three cases; the updraft is inclined leftward throughout its depth in run L1 (figure 42), is practically erect to run L2 (figure 45) and shows a very slight overall lean toward the right in run L3 (figure 48). This variation of updraft tilt is reflected in the different locations of significant rainfall within the cloud. In the low-shear runs, this dependence of updraft orientation upon moisture supply is associated with a decrease of the rightward storm core velocity from 9 m sec^{-1} in Case L1 to 7 m sec^{-1} in case L3. However, the reason for this decrease is unclear, and the difference in updraft tilt between cases L1 and L3 is greater than would be expected simply by comparing the undisturbed ambient wind to the storm core velocity. In the experiments involving strong shear, the updraft tilt changes sharply from upshear to downshear near 6 km in the two weak cases H1 (figure 44) and H2 (figure 47), while in the strong case H3 (figure 50) the updraft shows much less curvature, with a tilt similar to the updraft in case M3. (The core velocities in cases H2 and H3 are not significantly different.) In summary, the updraft orientation and curvature depend not only upon the ambient wind profile but also on the updraft intensity and the movement of the cloud core.

It was pointed out earlier that for the cases exhibiting a dividing streamline within the main updraft (all runs except for H1 and H2), the location of the heaviest rainfall is determined mainly by the updraft tilt. Interestingly, no accumulation of heavy rain (at least 90 mm hr^{-1}) occurs far to the right of the dividing streamline in case H3, unlike in case M3, even though the updraft as a whole is similarly inclined in both cases (despite the stronger shear in case M3). This difference is apparently due to the somewhat weaker intensity of the updraft in case H3. Liquid water is not carried as high as in case M3 before falling toward the ground, so that less of the precipitation begins its descent at high altitudes where the horizontal velocity of the updraft (and therefore of the raindrops, whose horizontal velocity is assumed equal to that of the air) is much greater toward the right than the displacement rate of the storm core. In the two weakest cases, H1 and H2, the updraft is too slow to carry much of the precipitation above the level where the tilt changes so that most of the rainfall (not shown in figure 44 because the maximum rainfall rate in case H1 is less than 30 mm hr^{-1}) is located under the vertex of the sharply curved updraft. In short, the location of significant rainfall is determined both by the shape of the updraft and by its strength, which partly determines the height at which most of the precipitation is stored.

In the present model, the separate locations of the primary updraft and the new updraft in most runs do not favor early decay of the primary updraft, even though Takeda's hypothesis suggested that the primary updraft could not persist for a long time if separated from a new updraft. At fifty minutes, five of the runs (L1, L2, M1, M2 and H3) show a downdraft to the left of the updraft, and a weak secondary updraft outside the main cloud and to the left of the downdraft. In Takeda's experiments with a negative jet in the ambient wind, this situation corresponded to a jet above both critical levels; the primary updraft in this case decayed without taking on a quasi-steady state. In contrast, the primary updraft in the present model is actually longer-lasting in the five cases just referred to than in the other cases. (In runs H1 and H2, the relative draft locations are similar to those in these five cases, but the primary updraft is not long-lived for reasons already covered, notably the failure of the potentially warmest air to feed the updraft at fifty minutes.) This difference is felt to result largely because some simplifications inherent in Takeda's hypothesis do not appear valid in the present model. Indeed, the ambient wind profile in each of the nine comparative runs corresponds to the limiting case of a negative jet at the ground, with positive wind shear in the moist layer and either zero or positive wind shear above, and if Takeda's hypothesis were truly valid there would be in all cases a downdraft to the right of the primary updraft and a secondary updraft to the right of the downdraft. The opposite situation has been seen to hold in seven of the cases, at least at fifty minutes.

In considering where a new updraft should form, Takeda based the location of the corresponding covergence region solely upon differences between the horizontal momentum of the downdraft (assumed to equal the average momentum of the undisturbed ambient wind over the depth of the downdraft) and that of the undisturbed wind at the surface. In the present model, the horizontal wind in the surroundings of the cloud becomes significantly disturbed as the overall convective circulation broadens horizontally. The divergence in the downdraft creates outflow in one or both directions relative to the traveling storm. Also, low-level winds well outside of the cloud are accelerated toward its core on both sides. Convergence has been seen to result between the leftward downdraft outflow (relative to the storm) and the positively accelerated air approaching the storm from further to the left, producing a weak but definite updraft to the left of the storm. At the same time, the right branch of the downdraft outflow reinforces the convergence between surface air underneath the storm core and negatively accelerated air rushing leftward toward the front of the updraft. This effect, as well as the sidestepping of most of the heaviest precipitation by air feeding the primary updraft, tends to maintain the updraft.

We have seen that in the low-shear and moderate-shear cases with the greatest moisture supply (L3 and M3), in which most of the heavy rainfall occurs to the right of the updraft core, the dominant downdraft is to the right of the updraft core, the dominant downdraft is to the right of the primary updraft while new updrafts develop on either side of the downdraft. Although the downdrafts are stronger in these two cases than in any of the others (up to about 9 m sec^{-1} in run L3 and nearly 10 m sec^{-1} at the end of run M3), they strengthen at the expense of the primary updraft, which has become cut off from the most unstable air and is also weakened by ingestion of potentially cool outside air. In each case, the strong outflow from the downdraft converges with air approaching the storm from either side, causing the new updrafts to form. The left-hand secondary updraft in case L3 temporarily slows the otherwise rapid dissipation of the primary updraft because it forms underneath the core of the decaying updraft. However, the new updrafts form in air having considerably less convective instability than the air feeding the primary updraft at earlier times, due to cooling of the low-level air in and close to the cloud. Therefore, the new updrafts are shallower and less intense than the primary one, and cannot counteract its dissipation sufficiently to effect a quasi-steady state.

From the last two paragraphs, it appears that while Takeda's hypothesis did provide a plausible explanation for the results of his experiments, it nevertheless did not take into account three factors which were considered important in explaining the results for the present model. These factors, present at low levels, are the divergent outflow from the downdraft, modification of the environmental wind by the overall convective circulation, and reduction of convective instability in and near the cloud through cooling due to cloud-edge evaporation or moist-adiabatic downdrafts. The first two of these factors can produce new updrafts in locations not predicted by Takeda's hypothesis, while the third can counteract the prolonging effect of an otherwise favorably located new updraft upon the primary updraft.

8. THE PROTOTYPE STORM AND SOME VARIATIONS

The "prototype" storm referred to in the Introduction is case M2 (intermediate moisture and moderate shear). This case was chosen largely because its configuration, more than in the other cases, resembled in some ways the observationally motivated schematic models cited earlier.

Several features of the prototype not covered in depth thus far will be studied:

1) trajectories of selected air parcels, and precipitation streamlines relative to the moving cloud;

2) equivalent potential temperature fields;

3) fields of individual force components, both horizontal and vertical;

4) horizontal divergence; and

5) pointwise vertical transports of heat, water vapor and horizontal momentum.

The seven variations on the prototype as presented in the Introduction are listed below in the same order as the seven questions which they were intended to investigate:

M2-A: Liquid water drag suppressed

M2-B: Precipitation suppressed

M2-C: Pressure perturbations suppressed in the buoyancy

M2-D: Upper jet maximum in wind profile

M2-E: Deeper transition layer

M2-F: Shallow and more unstable moist layer

M2-G: Initial perturbation altered

8.1 The Prototype Storm

In order to study the trajectories of selected air parcels and streamlines of precipitation particles over a significant portion of the prototype storm's life, and some of the differences between the quasi-steady and dissipating stages, diagrams will be presented showing these features at ten-minute intervals from forty through eighty minutes, inclusive. The equivalent potential temperature field at sixty and eighty minutes will also be examined in order to further reveal the contrast between the quasi-steady and dissipating stages. The remaining features to be considered, namely the force fields, horizontal divergence and vertical transports, will be examined at sixty minutes.

Air Parcel Trajectories, Precipitation Streamlines and Equivalent Potential Temperature Fields

The positions of twelve selected air parcels, together with the cloud and perturbation streamlines, are shown at the initial time in figure 56. Forward trajectories for each of parcels No. 1-12 were computed by a straightforward method presented in appendix F. Figures 57 through 61 show each parcel, together with a few relative precipitation streamlines represented by dotted curves, at successive ten-minute intervals from forty through eighty minutes. Also shown in these figures are the streamlines of airflow relative to the moving cloud core and the region of significant rainfall, plotted as in section 7. Although the rightward displacement rate of the storm appeared to be slowing somewhat between seventy and eighty minutes, the average velocity between forty and seventy minutes (about 12 m $\sec^{-1}$) was taken to approximate the displacement rate at each time shown. The equivalent potential temperature fields at sixty and eighty minutes are plotted in figures 62 and 63, respectively.

The broadening with time of the disturbance outside the updraft core is quite apparent from a study of the relative flow in figures 57 through 60. Although the maximum updraft velocities are quite similar from one time to another from forty through seventy minutes, the cloud anvil lengthens by a factor of about three during this period. Correspondingly, the arched streamline enclosing the shallow reverse circulation at the rear of the storm broadens greatly even though its height changes little from fifty to seventy minutes. Also, the region of significant rainfall is less nearly steady in character than the updraft strength. The maximum rainfall rate, somewhat less than 90 mm hr^{-1} at forty minutes, is slightly over 120 mm hr^{-1} at sixty and seventy minutes.

Despite the above qualifications, however, the closeness of the updraft to a steady state is strikingly evident from the paths of parcels No. 11 and 12. Initially in the moist lower layer to the right of the cloud, these slow-moving parcels are overtaken by the faster-moving storm. They rise through the right-hand channels of the concentrated updraft within about twenty minutes and then are carried rapidly toward the right in the anvil. Note that parcel No. 11 remains in the first channel to the right of the dividing streamline (DS) from forty through seventy minutes, while parcel No. 12 remains in the second channel to the right of the DS. This shows how closely streamlines and trajectories correspond to each other in the updraft core, further justifying the use of the term "quasi-steady state" for describing the mode of the storm; in true steady-state flow, streamlines and trajectories would coincide. Although the closed counterclockwise circulation in the upper rear part of the updraft widens with time, parcel No. 7 remains within this feature through seventy minutes. Similarly, even though the arched stream-

Figure 56. Case M2 at the initial time, showing the initial airflow disturbance and positions of air parcels numbered 1 through 12 which are tracked at subsequent times (see text). The parcels are identified by numbered circles. The dashed lines represent boundaries of the perturbed region. The thin solid contours with arrows represent streamlines of pure disturbance flow (deviation from the initial base state); the contour interval is 2×10^6 gm m^{-1} sec^{-1}. The heavy curve represents the cloud boundary.

Figure 57. Streamlines for airflow and precipitation (both relative to the moving cloud core), rainfall patterns and tracked air parcels for case M2 at forty minutes. The cloud boundary, airflow streamlines and significant rainfall regions are indicated in the same way as in figures 42 through 53. Dotted curves represent precipitation streamlines. Numbered circles identify the tracked air parcels shown in their initial locations in figure 56.

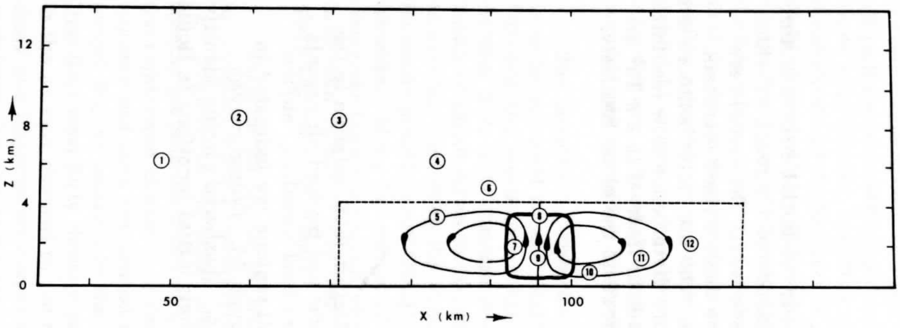

Figure 56

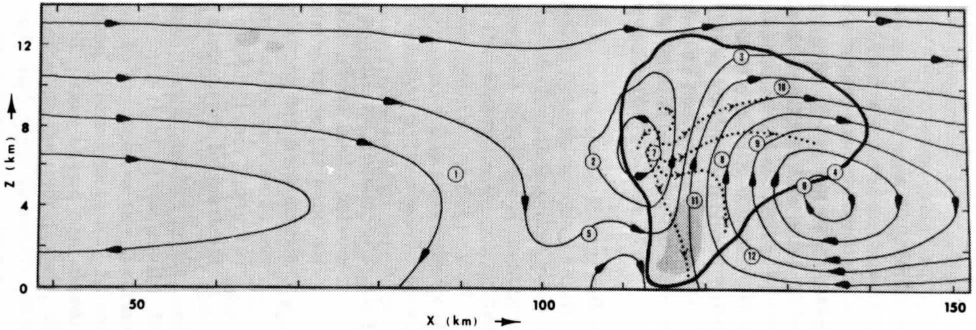

Figure 57

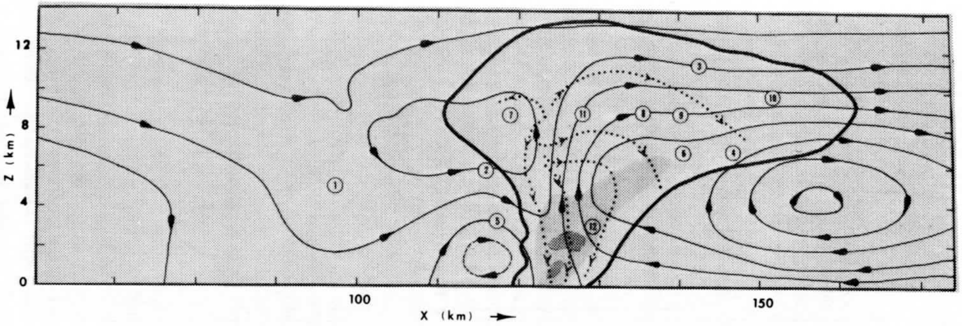

Figure 58. Same as figure 57, but at fifty minutes.

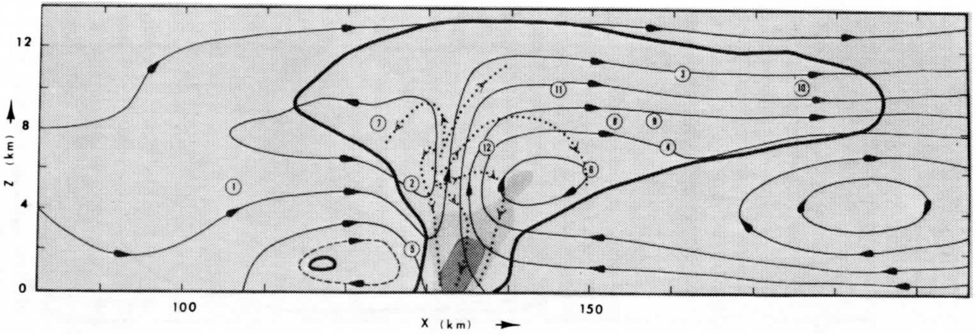

Figure 59. Same as figure 57, but at sixty minutes.

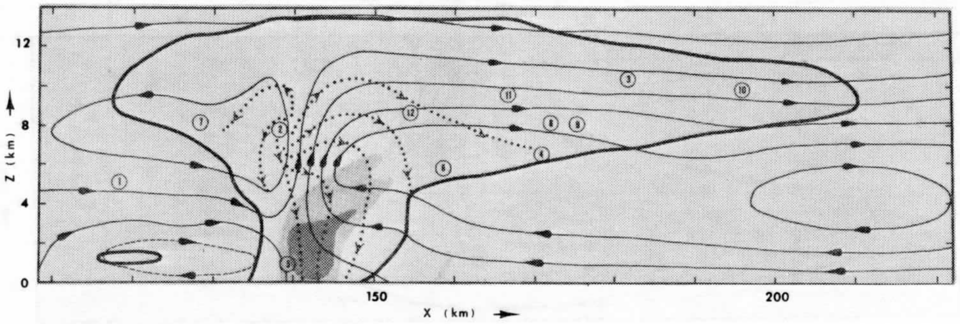

Figure 60. Same as figure 57, but at seventy minutes.

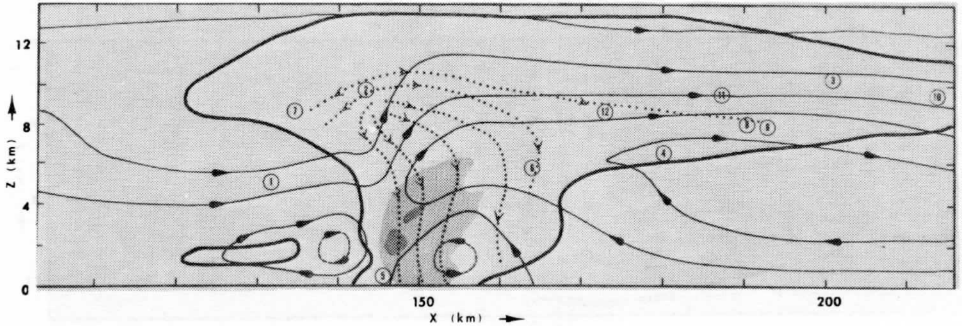

Figure 61. Same as figure 57, but at eighty minutes.

line behind the storm also widens with time, parcel No. 5 can be seen to remain on its right leg from fifty through seventy minutes as it descends into the cloud. Since parcel No. 5 is initially in the transition zone between the moist and dry layers, and since much of the descending air at the left edge of the cloud is above parcel No. 5 at sixty and seventy minutes, this indicates that inflow of potentially cool air is important to downdraft formation.

Much like No. 11 and 12, parcel No. 10 is drawn into the updraft from ahead of the cloud and is diverged at upper levels into the anvil. Having been swept into the updraft earlier than either No. 11 or 12, parcel No. 10 is closer to the edge of the anvil and thereby further removed from the quasi-steady updraft; note that between fifty and seventy minutes, its trajectory shifts from one streamline to a neighboring streamline. Parcels No. 8 and 9, initially in the core of the cloudy updraft, remain well within the main updraft at later times until they are diverged into the anvil, and apparently do not leave the cloud throughout the run.

The trajectory of parcel No. 2 indicates that some of the air from far above and upwind of the shallow initial cloud is drawn into the left-hand branch of the developing convective circulation, just skirting the upper limits of the downdraft as the cloud is first entered but then rising into the rear of the updraft. Although parcel No. 1, initially even further upwind and also well up in the middle levels, has not yet entered the cloud at eighty minutes, it appears destined to overtake the cloud and also become part of the back of the updraft. Parcel No. 3, which is initially also above and upwind of the cloud but further to the right than either No. 1 or 2, is drawn into the top of the deepening updraft some time before forty minutes and subsequently becomes part of the anvil. Some of the air initially above and to the left of the cloud drifts nearly horizontally without really becoming part of the updraft; as exemplified by parcels No. 4 and 6, this air becomes caught within the relatively inactive region of horizontally elongating circulation along the underside of the anvil, and just skirts the cloud edge.

The precipitation streamlines, calculated from the relative wind field and the assumed terminal velocities, show a quasi-steady configuration as long as the updraft is also quasi-steady, and therefore approximate trajectories of precipitation particles. Near the 8-km level, at the rear edge of the updraft, precipitation is diverged and spun into surrounding parts of the cloud. Suspended light precipitation ascends by as much as 2 to 3 km, and a minor part of the precipitation falls into the interior of the anvil to the right of the updraft. The bulk of the precipitation falls into the comparatively narrow cloud trunk extending up to approximately 4 km, with rain first reaching the ground shortly after forty minutes. The considerable broadening of the trunk after sixty minutes is evidently due to the fall of some precipitation into the anvil. Note that no precipitation streamlines extend outside of the cloud, in fact terminating slightly short of the cloud edges (unless they reach the ground). This is due to the way in which precipitation has been handled in this model, as explained in section 2. The outermost parts of the cloud contain no precipitation since the liquid water content decreases outward from the interior.

We next emphasize the contrasts between the quasi-steady and dissipating stages of the prototype storm. From forty through seventy minutes, the updraft is nearly erect, marked by a dividing streamline which ascends from the surface to between 10 and 11 km before continuing nearly horizontally into the anvil. The rapid weakening of the updraft between seventy and eighty minutes (from 9.3 to 4.9 m $\sec^{-1}$) is attended by a radical change in the streamline pattern. At eighty minutes, the updraft appears cut off from the low-level moist air to the right of the storm. The downshear leaning of the updraft indicates partly that w has decreased and partly that the horizontal momentum of the air comprising it has increased, apparently because it is now being infiltrated by fast-moving air entering the back of the cloud near 6 km. The dividing streamline has collapsed, having evolved into an arched separating streamline about 4 km high; this indicates a widening of the downdraft into the cloud interior. The reverse eddy at the rear of the cloud is still present, and the secondary cloud within it has stretched horizontally, but the old separating streamline has disappeared. The region of heavy rainfall (90 mm hr^{-1} or more) has shrunk somewhat since seventy minutes, but the decrease in rainfall intensity is much less striking than the decrease in updraft intensity. This is largely because precipitation formerly suspended aloft is now approaching the ground, even though the decaying updraft is producing much less new liquid water to add to the existing accumulation. Also, the maximum surface wind under the cloud trunk has not yet decreased, as yet maintaining a value of 15 to 16 m $\sec^{-1}$ although the location of this apparent squall gust has shifted from the zone of heaviest surface rain to the much lighter precipitation nearer the right edge of the cloud.

The sharp contrast between the quasi-steady and dissipating stages of the prototype storm is further brought out by the change in the equivalent potential temperature distribution between sixty minutes (figure 62) and eighty minutes (figure 63). At sixty minutes, the contrast between the equivalent potential temperature distributions within and away from the storm is immediately apparent. Away from the cloud, the isolines of θ_e are nearly horizontal even though the flow pattern is appreciably disturbed; this reflects the unsteady character of the widening overall circulation. The foregoing subsidence of the more distant surroundings during the preceding time is evident up to at least 8 km in the lowering of the isolines from their initial

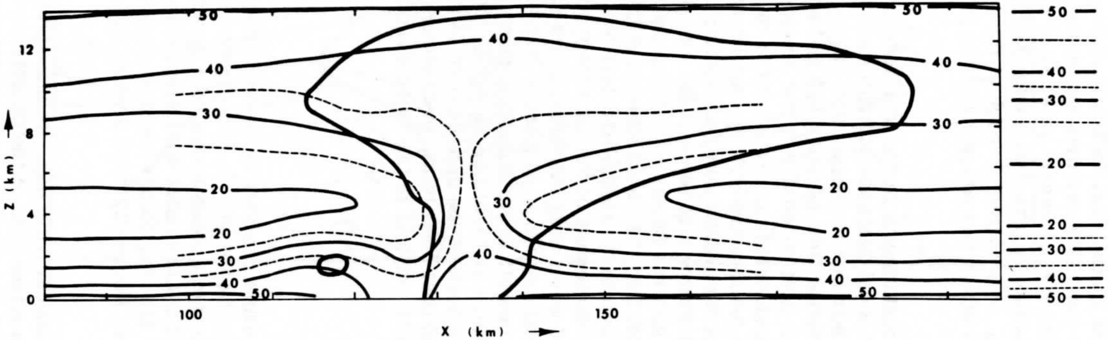

Figure 62. Equivalent potential temperature field for case M2 at sixty minutes. The heavy solid curve represents the cloud boundary. Thinner solid curves denote equivalent potential temperature (excess in °K above 300°K), with half-intervals indicated by dashed curves. At the extreme right of the diagram, initial base values of the equivalent potential temperature are indicated by horizontal line segments, with numerals and dashed segments having the same meanings as in the remainder of the diagram.

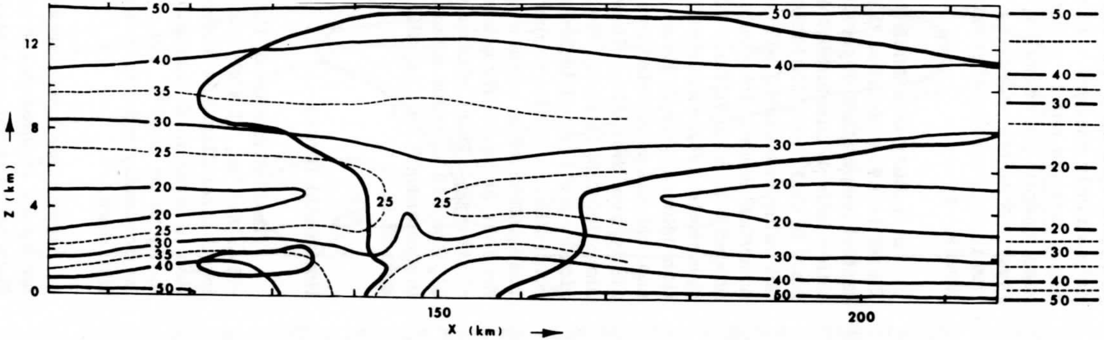

Figure 63. Same as figure 62, but at eighty minutes.

positions (shown at the extreme right of the figure), but their orientation is only slightly changed. In sharp contrast, the 335°K isolines within the cloud core are nearly vertical between 4 and 8 km, closely paralleling the erect updraft and revealing its saturated-adiabatic structure throughout that layer. Note the relatively low surface θ_e immediately in back of the storm, due to evaporation of precipitation into air which has descended from higher levels.

In a study of a small synoptic-scale disturbance in the Line Islands, Zipser (1969) concluded that a pronounced local decrease of equivalent potential temperature observed near 900 mb was due to evaporation of precipitation into an unsaturated downdraft originating from between 400 and 600 mb. In that case, the downdraft was much more extensive in the horizontal, not being associated with an individual cumulonimbus. Returning to the numerical model, the equivalent potential temperature at the cloud edges around 4 to 6 km is fully 10° lower than in the updraft core, indicating systematic large-scale entrainment by the inflow just beneath the circulation centers seen in figure 59. At eighty minutes (figure 63), the potentially cool air has penetrated considerably further into the cloud interior, especially from the right. Since the precipitation in the right-hand part of the cloud interior is light, the loss of upward momentum of the air entering the cloud cannot be attributed mainly to liquid water drag but rather to its low equivalent potential temperature which facilitates loss of thermal buoyancy. The unsteadiness of the rapidly decaying updraft is graphically indicated by the loss of similarity between the streamlines and isolines of θ_e in the cloud core. Most noticeably, both in and outside the updraft seen in figure 61, the 330° isoline around 7 to 8 km is almost horizontal, even though the instantaneous flow is still much more nearly vertical in the cloud than outside of it.

Horizontal Forces

The distribution of the horizontal pressure gradient force per unit mass, $-(1/\bar{\rho})\partial p'/\partial x$, at sixty minutes is shown in figure 64. In this diagram and in all other diagrams showing individual or net accelerations, the acceleration is given in thousandths of gravity. This is almost equivalent numerically to cm sec^{-2}. For convenience and brevity, forces per unit mass will be frequently referred to as "forces" as has frequently been done in the literature.

It is clear from figure 64 that the strongest horizontal pressure gradient forces are located in the cloud interior on either side of the updraft core. Here air is being accelerated into the anvil in an asymmetric manner paralleling the preferred development of the anvil to the right of the updraft. The

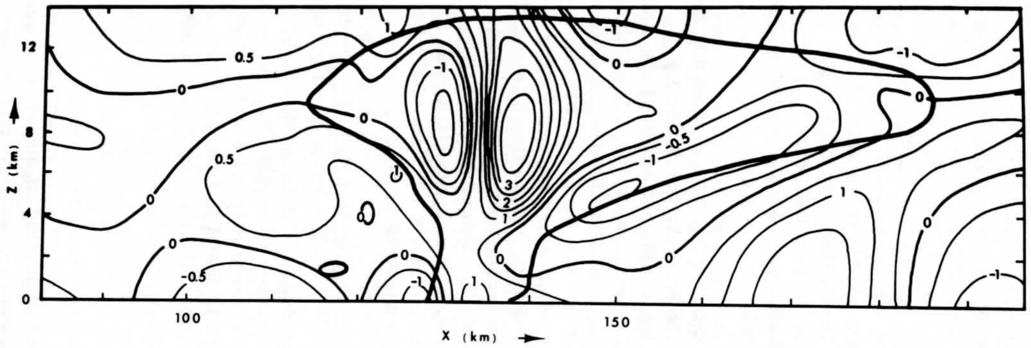

Figure 64. Horizontal component of the pressure gradient force per unit mass for case M2 at sixty minutes. The isolines are labeled relative to gravity, which is arbitrarily taken to be 10^3 units. The heavy solid curve represents the cloud boundary.

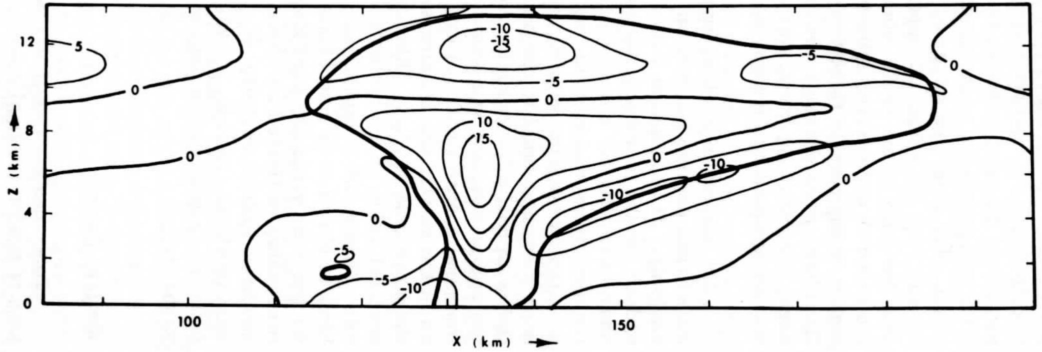

Figure 65. Thermal buoyancy force per unit mass for case M2 at 60 minutes. Otherwise the same as figure 64.

maximum rightward force, nearly 4 cm sec^{-2}, is slightly more than twice the maximum leftward force. Large-scale entrainment near the 6 km level has already been inferred from the equivalent potential temperature distribution in figure 62, and its presence is verified by the distribution of the horizontal pressure gradient force. On each side of the cloud, from about 2 km to near the tip of the anvil, outside air is being accelerated into the cloud, with maximum forces of slightly over 1 cm sec^{-2} on the left and 1.5 cm sec^{-2} on the right. At upper levels, there is very weak detrainment near the ends of the anvil; more significantly, air at the lower rear edge of the cloud is accelerated leftward at up to 1 cm sec^{-2} with a very shallow region of comparable rightward acceleration in the region of heavy rain. Therefore, once the high-pressure dome at the back of the storm has developed, the resulting horizontal pressure gradient forces tend to maintain the outflow induced by divergence in the downdraft.

The horizontal friction force F_x in the cloud core, as calculated in the model (see section 6), may be seen to be quite small by the following analysis. It is apparent from figure 59 that the height and width of the main updraft for the prototype storm at sixty minutes are comparable. Neglecting compressibility for simplicity in estimating F_x, let the disturbance flow in the updraft be approximated by a stream function $\Psi = \Psi_0 \sin mx \sin mz$ over a suitably restricted region; here m is the vertical wave number for the updraft (assumed equal to the horizontal wave number), whose depth is identified with half of a vertical wavelength. If the parameters α and L have the values assumed in section 6, with m and Ψ_0 chosen so as to give the same updraft depth (14 km) and maximum updraft velocity (10 m sec^{-1}) as in the model, one obtains an upper limit of about 5×10^{-2} cm sec^{-2} for the magnitude of F_x. This is two orders of magnitude smaller than the greatest value of the horizontal pressure gradient force per unit mass (figure 64). This value is comparable to the maximum magnitude which F_x would have in the case of pure Fickian diffusion $\nu \nabla^2 \bar{u}$ with a value of $10^3 m^2 sec^{-1}$ for the eddy viscosity coefficient ν (a value which was suggested to be reasonably motivated by observations, as indicated in section 3). For a maximum updraft velocity $\bar{w}_{max}$, the maximum magnitude of Fickian diffusion would be $2m^2 \nu \bar{w}_{max}$ which in this case is about 0.1 cm sec^{-2} or twice the maximum obtained from the Lettau formulation in the form adopted to the model.

Vertical Forces

To estimate three of the individual forces appearing in the vertical equation of motion (thermal buoyancy, pressure buoyancy and the vertical perturbation pressure gradient force) at sixty minutes, the disturbed virtual temperature T_v' and pressure p' had to be estimated in a way which takes into account the modification of the cloud environment since the initial time. In particular, since warming of 2°C or more had occurred throughout the middle levels of the grid domain, it was clear that the thermal buoyancy would be systematically overestimated by taking T_v' to be simply the departure of T_v from the undisturbed initial value. In their model of a shallow precipitating cumulus, Arnason et al. (1968) computed vertical forces in terms of departures from the initial base state, but their model was not run out long enough for the surroundings of the cloud to become significantly modified.

As emphasized in section 2, p' and T_v' are not independent of each other since p' is determined from an elliptic partial differential equation once T_v' is known. However, this was not done in view of limitations on computing time. The pressure perturbations computed by the short method described in appendix G were used to estimate p' by subtracting out the average pressure change at each level as of sixty minutes, and T_v' was identified similarly with the departure of T_v from its horizontal average at that time. In the denominators of $gT_v'/\bar{T}_v$ and $-gp'/\bar{p}$, initial horizontal averages could still be used without serious error since the percentage changes in the averages were quite small.

The thermal buoyancy, $gT_v'/\bar{T}_v$, is shown in figure 65. As would be expected from the thermal patterns described in section 7, the greatest upward buoyancy (about 18 cm sec^{-2}) is located in the fastest part of the updraft. There are three significant regions of negative thermal buoyancy, each showing maximum magnitudes of at least 10 cm sec^{-2}:

1) at and near the rear of the cloud trunk, especially below 1.5 km;

2) along the base of the anvil from 3 to 8 km; and

3) throughout the left half of the cloud above the thin stable layer (9.1 to 10.5 km).

The first two of these negatively buoyant regions have formed as a result of evaporative cooling; in the first instance, heavy precipitation which has just fallen at the lowest levels is evaporating as the storm recedes toward the right, and in the second case cloud droplets have been evaporating along the underside of the anvil. The third, and most strongly developed, region of negative buoyancy has resulted from the moist-adiabatic rise of air parcels through the stable layer; since the moist-adiabatic lapse rate is nearly as steep as the dry-adiabatic at these high altitudes, parcels which enter the stable layer warmer than their surroundings emerge from this layer colder that their surroundings.

The term $-gp'/\bar{p}$, the contribution of pressure perturbations to the buoyancy $-g\rho'/\bar{\rho}$, is plotted in figure 66. It is considerably smaller in magnitude than the thermal buoyancy. In the cloud core, this force is at most only about one-fourth of the greatest thermal buoyancy. For convenience, we refer to this quantity as the "pressure buoyancy" or "pressure buoyancy force."

The most conspicuous regions of upward pressure buoyancy are the following:

1) at low levels directly underneath the leading edge of the anvil;

2) at middle levels, most noticeably just to the right of the main updraft but also projecting into the accelerating part of the updraft itself; and

3) at the cloud top.

The first of these regions, the primary site of pressure falls in front of the storm, thus contributes to the ascent of the low-level inflow once it has passed under the leading edge. The upward pressure buoyancy in the second region strengthens the updraft, being positive together with the thermal buoyancy. The rather strong upward pressure buoyancy at the cloud top suggests that without the inhibiting upper boundary, which crudely simulates the effect of the tropopause, the cloud top might perhaps reach a greater height than would be predicted by the parcel theory (which neglects pressure perturbations entirely). Significant downward pressure buoyancy is found throughout the upper part of the main updraft and in a very shallow area within and in back of the cloud trunk. The first of these regions, associated with the pressure excess in the upper half of the cloud core, may partly explain the relatively low altitude of the updraft maximum since the updraft core passes through this region not far above that altitude. Within the shallow layer of relatively high pressure at and near the back edge of the storm, the resulting negative pressure buoyancy acts together with the negative thermal buoyancy to perpetuate the downdraft. The lack of vertical development of the secondary cloud is due in part to its negative thermal buoyancy (figure 65), but negative pressure buoyancy also suppresses its growth.

As has been inferred from the distribution of pressure changes from the initial time to fifty minutes (figure 29), a substantial part of the thermal buoyancy force is canceled by the vertical pressure gradient force $-(1/\bar{\rho})\partial p'/\partial z$. A comparison of figure 67 with 65 shows that these two forces tend to oppose one another throughout the part of the domain shown. Within the cloud, this cancellation is virtually complete in the upper and lower

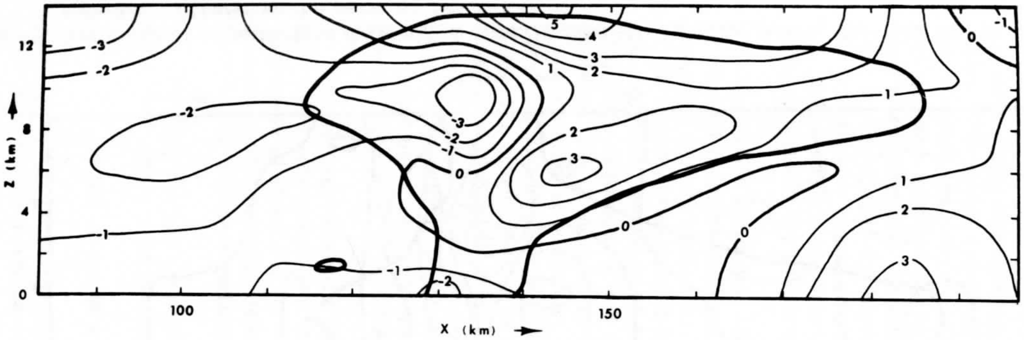

Figure 66. Pressure buoyancy force per unit mass (contribution to the gravitational buoyancy due to pressure perturbations rather than temperature perturbations) for case M2 at sixty minutes. Otherwise the same as figure 64.

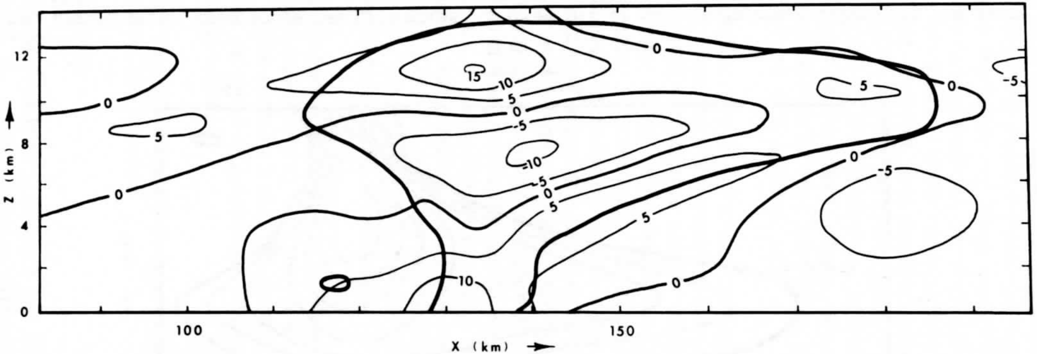

Figure 67. Vertical component of the perturbation pressure gradient force per unit mass for case M2 at sixty minutes. Otherwise the same as figure 64.

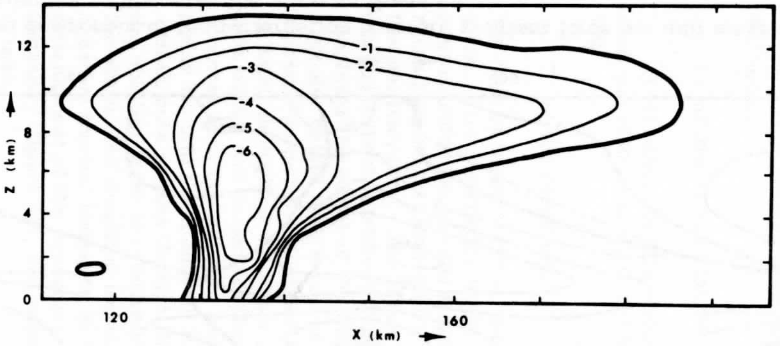

Figure 68. Liquid water drag force per unit mass for case M2 at sixty minutes. Otherwise the same as figure 64.

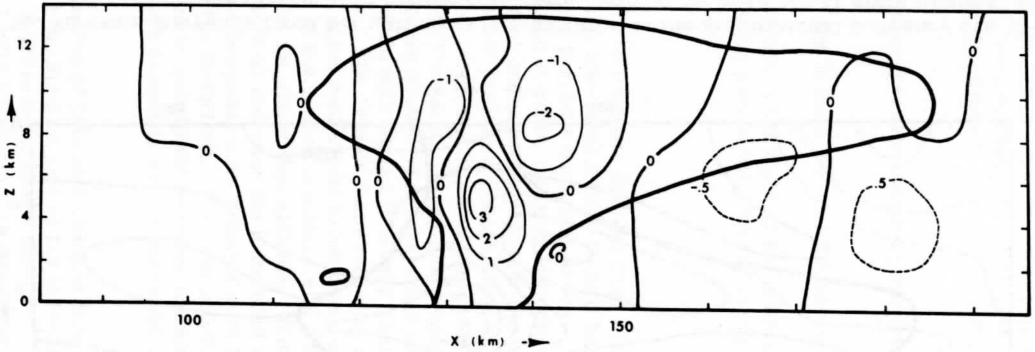

Figure 69. Net vertical acceleration determined directly from the velocity fields, for case M2 at sixty minutes. Otherwise the same as figure 64.

levels, while about half of the thermal buoyancy is canceled where it is most positive. Since the evaluation of p' is only approximate, as explained earlier, the vertical derivative of p' is still less exact. Nevertheless, we can infer rough cancellation, especially in the upper and lower parts of the cloud. The strong opposing tendency does have a definite physical significance which suggests that the errors are not major. If the thermal buoyancy and pressure gradient forces were equal and opposite, and the buoyancy were purely thermal, the pressure perturbations would be hydrostatic. We have just seen that the buoyancy in the model is mainly thermal, although the contribution due to pressure perturbations is important. Thus, despite the crucial importance of net vertical accelerations to the convection, significant parts of the pressure perturbations are still hydrostatic.

The liquid water drag (figure 68) is weaker than the thermal buoyancy or vertical pressure gradient force, but stronger than the pressure buoyancy. Since the drag is given by $-gL/\bar{\rho}$, its spatial variation is similar to that of the liquid water content but decreases more slowly with height due to the monotonic decrease of density with height. Accordingly, the strongest drag force is located 1 to 2 km above the point of maximum liquid water content. The greatest drag occurs near and just below the location of maximum thermal buoyancy, canceling out about forty percent of the thermal buoyancy and is located partly above the significant rainfall region shown in figure 59, since the drag is proportional to the weight of the liquid water regardless of whether precipitation particles are actually approaching the ground. Also, the region of greatest drag is not coincident with the site of the cold downdraft, which was found at and near the left edge of the cloud. It is once again apparent that at least in this model, the liquid water drag serves much more to curb the updraft than to initiate the downdraft.

By the same analysis used earlier to estimate F_x, it may be shown that F_z in the cloud core is of comparable magnitude to F_x with a maximum value of about 5×10^{-2} cm sec^{-2}. This indicates that the vertical friction is of minor importance, being over an order of magnitude smaller than any of the other vertical forces per unit mass.

Finally, the net vertical acceleration dw/dt is shown in figure 69. Note that dw/dt was computed directly from the identity

$$dw/dt = \partial w/\partial t + u\partial w/\partial x + w\partial w/\partial z$$

calculating the local time derivative over the last time increment and the advective terms from current values of u and w, using upstream differencing for calculating the space derivatives. This was done to avoid gross errors which might result from directly adding the individual forces. Since the individual vertical forces (apart from friction, which is quite small) show

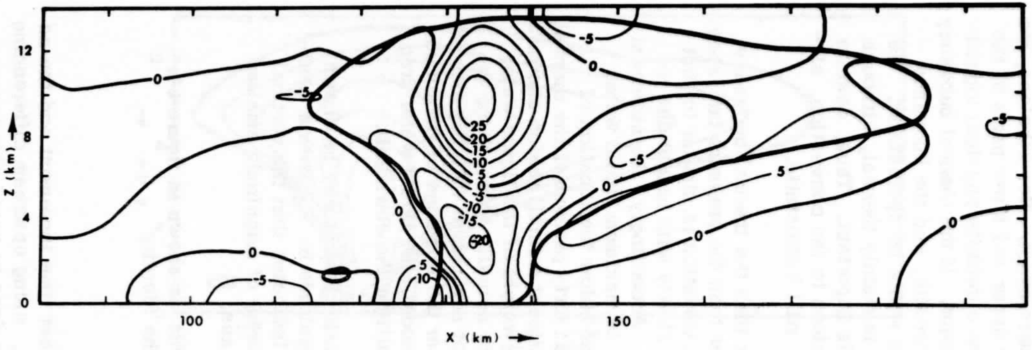

Figure 70. Horizontal divergence for case M2 at sixty minutes. The isolines are labeled in unts of 10^{-4} $\sec^{-1}$. The heavy solid curve represents the cloud boundary.

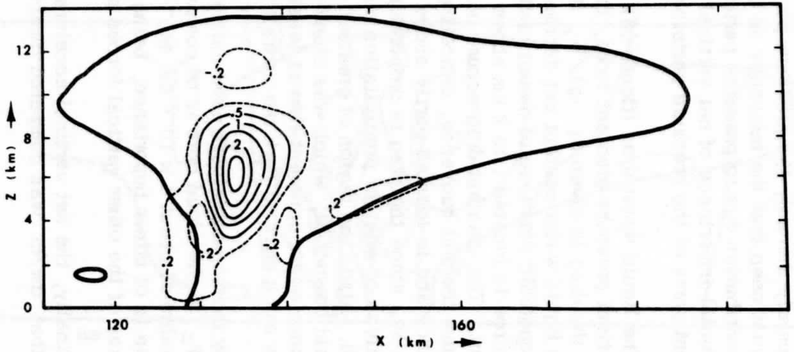

Figure 71. Pointwise vertical heat transport (in units of 10^7 ergs cm^{-2} $\sec^{-1}$) for case M2 at sixty minutes. The heavy solid curve represents the cloud boundary.

strong partial cancellation, and the forces involving p' have not been estimated by a strictly correct procedure, errors which may be quite tolerable for the larger individual forces might partly obscure the pattern of the considerably weaker resultant force field. A glance at figure 69 shows that the maximum net acceleration is only about one-fifth as great as the maximum thermal buoyancy and is only comparable to the greatest pressure buoyancy. Not surprisingly, parcels are accelerated upward most strongly somewhat beneath the site of fastest upward motion, then declerated into the anvil top on both sides of the updraft core. Parcels are decelerated into the right flap of the anvil about twice as strongly as into the left flap, also paralleling the asymmetry of the horizontal pressure gradient force in figure 64. The cold downdraft is situated in a zone of net deceleration extending over the depth of the domain, even though its initiation site has been found to be mainly at 4 to 6 km.

Horizontal Divergence

It is apparent from figure 70 that the most pronounced convergence and divergence occur in the updraft core and within the downdraft at the left edge of the cloud. Note that the convergence in the far interior of the cloud extends to only about 6 km, with divergence overlying it at all higher altitudes. In the anvil, convergence extends considerably higher.

It is interesting to compare the vertical divergence profile in the cloud core with the findings of Byers and Braham (1949) for five Ohio thunderstorms, all in the precipitating stage. By releasing balloons into the thunderstorms and their nearby surroundings, they obtained estimates of convergence and divergence up to about 10 km. The results indicated divergence up to between 1 and 1.5 km, convergence up to about 6 km and then divergence above that level, with maximum magnitudes of approximately 3×10^{-4} $\sec^{-1}$. Since these figures represent values averaged over the thunderstorms and their near surroundings, it is not surprising that they are smaller than the values predicted by the numerical model along the main updraft axis. Due to the predominance of the downdraft near the left edge rather than the interior of the model cloud, the lowest levels of the cloud trunk show predominant convergence rather than divergence, so that the mean divergence found by Byers and Braham in the lowest levels is not evident from a horizontal averaging between, say, $x = 125$ and 145 km in figure 70. Otherwise, however, such an averaging would evidently produce a vertical profile similar to that found in the Thunderstorm Project, although with two to three times the amplitude.

The divergence beneath the downdraft is similar in magnitude to that observed in the Thunderstorm Project, although Byers and Braham pointed

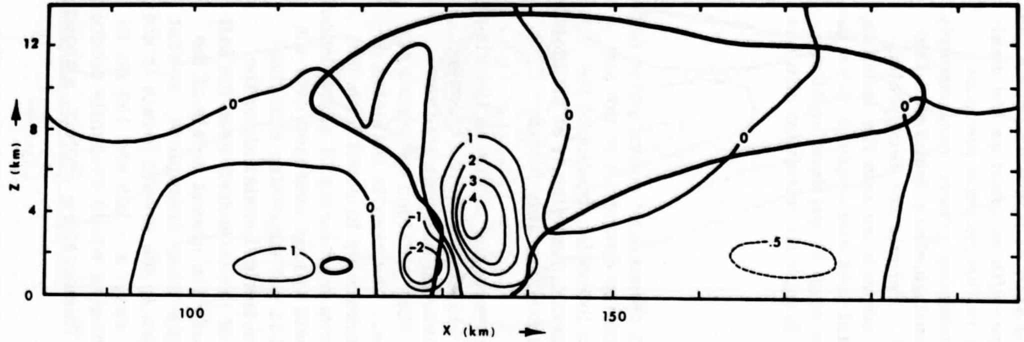

Figure 72. Pointwise vertical water vapor transport (in units of 10 gm m^{-2} sec^{-1}) for case M2 at sixty minutes. The heavy solid curve represents the cloud boundary.

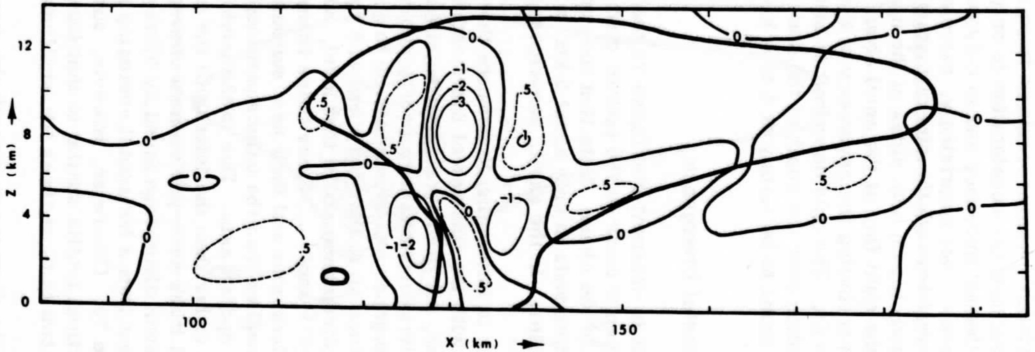

Figure 73. Pointwise vertical transport of horizontal momentum (in units of 10^{-2} gm m^{-1} sec^{-2}) for case M2 at sixty minutes. The heavy solid curve represents the cloud boundary.

out that extreme values of surface divergence were as high as about 8×10^{-3} sec^{-1}, roughly five times the value in the prototype storm. Recall that the maximum downdraft velocities in the prototype storm are only about 2.5 m sec^{-1}, partly due to numerical damping. The low-level convergence of up to 6.5×10^{-4} sec^{-1} which induces the formation of the small secondary cloud results from the outflow of downdraft air toward the faster-moving air which flows rightward toward the cloud as part of the compensatory current. The extensive region of divergence along the lower edge of the anvil indicates the main zone of transition from the low-momentum air entering the front of the updraft to the high-momentum air of the jet created by the outflow near the leading edge of the anvil.

Vertical Transports

Figures 71 through 73 show the two-dimensional distributions for the vertical transports of heat, water vapor and horizontal momentum, respectively, in and near the prototype storm at sixty minutes. Note that these are scalar fields, rather than vector fields, since only the vertical components of the transports were considered to be of interest. Also, one usually considers the horizontal averages of transports rather than the pointwise values plotted in these diagrams. We are considering pointwise values in order to see where the cloud and its near surroundings the main contributions toward the horizontal average are located.

The vertical transport of heat by the disturbance is given by $c_p \bar{\rho} T'w'$, and the vertical transport of horizontal momentum by $\bar{\rho}u'w'$, where the primed quantities in this context indicate departures from the horizontal average across the grid domain at sixty minutes. Unlike the horizontal average of T, the horizontal averages of the wind components show sufficiently small changes so that u' and w' can be calculated reasonably by subtracting out the initial horizontal averages of u and w. In particular, w' is simply the vertical velocity itself. The vertical transport of water vapor is simply $\bar{\rho}\, q_v w$, expressed in terms of the total mixing ratio, so that the quantity is the actual amount of water vapor being transferred upward per unit area per unit time. The other two vertical transports are best regarded as fluxes due to the macroscale eddies, i.e., the disturbance flow explicitly resolvable by the model, subtracting out the base state.

Although the pointwise vertical heat transport (figure 71) shows numerous sign changes, only those regions where its magnitude exceeds a certain amount (2×10^6 ergs cm^{-2} sec^{-1}) are considered significant; lines of zero transport are omitted to avoid complication or confusion. As might be expected, the greatest upward heat transport by far occurs in the updraft core near and just under the level of greatest updraft velocity. The small region of weak positive transport along the anvil base near $x = 150$ km results from the descent of evaporatively cooled air, although less marked than the main downdraft below and to the left of the updraft. Only two small regions of downward heat transport are to be noted. One of them, at the upper right corner of the cloud trunk, reflects the entrance of the updraft through the evaporatively cooled cloud boundary. The other, directly above the main core of upward transport, results from the ascent of the main updraft through the stable layer. It is clear from figure 71 that the horizontally averaged vertical heat transport would have a vertical profile similar in shape to that of the pointwise transport along the main updraft axis—positive throughout the lower two-thirds of the atmosphere, especially between 4 and 8 km, and slightly negative at higher levels.

The two most significant regions of vertical water vapor transport (figure 72), not surprisingly, are in the lower 8 km of the main updraft and throughout the downdraft. The greatest pointwise upward transport, about 45 gm m^{-2} sec^{-1} , is found about 3 km below the level of maximum upward velocity because the saturation mixing ratio decreases rapidly with height. Note that the leftward tilt of the foot of the updraft is reflected in the slant of the maximum transport axis below 4 km. Although the maximum velocity of the downdraft is only about a fourth that of the updraft, the much lower altitude of the downdraft places it in air of considerably higher density and mixing ratio than the fastest parts of the updraft. This enables the downdraft to transport downward a more significant amount of water vapor (up to about 25 gm m^{-2} sec^{-1}) than its velocity alone would suggest. The small region of upward transport exceeding 10 gm m^{-2} sec^{-1} just to the left of the secondary cloud results from the earlier noted convergence behind the storm. One can see from figure 72 that the horizontally averaged vertical transport of water vapor is generally positive up through 6 km with a maximum near 4 km; at low levels, the downward transport by the downdraft is more than compensated for by the upward transport by the main and secondary updrafts.

The complexity of the convective circulation is once again evident from the pattern for vertical transport of horizontal momentum (figure 73). Three significant regions of negative transport greater than 10^{-2} gm m^{-1} sec^{-2} are evident, two in the main updraft and one in the downdraft, and seven regions of positive transport in excess of 5×10^{-3} gm m^{-1} sec^{-2} . The presence and location of the negative regions supports the argument of Newton (1950) that the in-cloud drafts transfer low momentum upward and high momentum downward, with negative transport in either case. Since air enters the downdraft mainly at levels where the undisturbed horizontal wind velocity is algebraically equal to or somewhat less than the displacement rate of the cloud core, the large downward transport of horizontal momentum at these levels is due to the horizontal acceleration previously undergone by this air while further behind the cloud. The regions of significant positive transport reflect processes such as the following:

1) positively accelerated low-level air well behind the cloud core converges with outflow from the downdraft and is therefore forced upward;

2) some of the ascending air in the cloud trunk has been horizontally accelerated to a velocity greater than that of the undisturbed low-level wind although smaller than that of the storm core; and

3) partly due to evaporative cooling, relatively low-momentum air along the anvil base near 6 km is descending.

Interestingly, despite the presence of regions having marked negative and positive vertical transport of horizontal momentum, it is apparent from figure 73 that the horizontally averaged transport is small. This reflects the lack of a definite tilt to the disturbed part of the flow pattern as such.

8.2 Variations Upon the Prototype

We now present some of the main results of the seven variations on run M2, treating each experiment separately in the order listed in the Introduction. Variation G was run out to 140 minutes after the initial time because of the delaying effects of the different initial perturbation. The other variations (A through F) were run out to eighty minutes, with z-t diagrams (figures 74, 75, 76, 78, 80, 83 and 84) constructed much as for the comparative experiments. Each z-t diagram should be compared to the corresponding part of figure 13. For each variation except M2-E (which exhibited a configuration similar enough to case M2 so that a chart was unnecessary), diagrams like those in section 7(c) have been included (figures 85 through 90) to show the significant rainfall zones and the airflow relative to the moving storm core at one particular time. In variations A, B, C and F, this time is sixty minutes, while it was seventy minutes in variation D and 130 minutes in variation G for reasons to be given later. In all cases, the storm core velocity was represented by the thirty-minute average of the horizontal displacement rate beginning twenty minutes before the time shown. Each such diagram should be compared to figure 59, which shows the prototype storm at sixty minutes. Those diagrams not yet mentioned show the differences in initial base state between the prototype run and each of variations D, E and F .

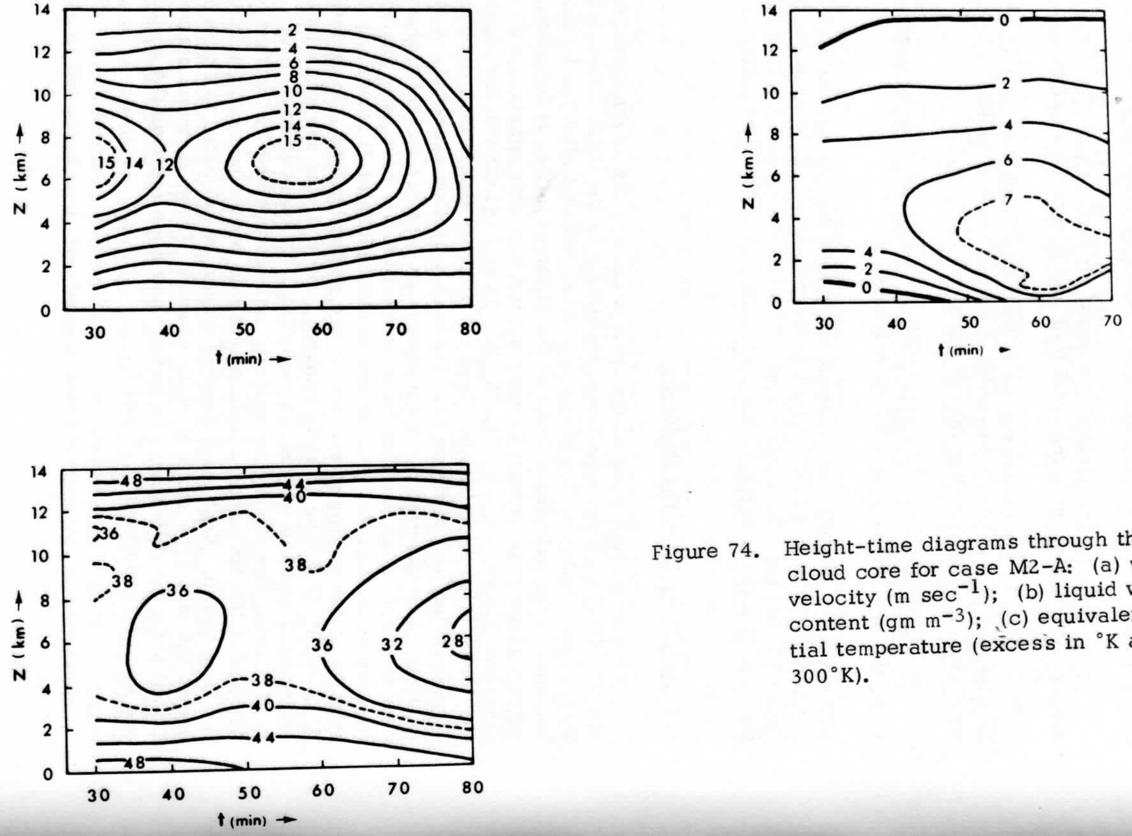

Figure 74. Height-time diagrams through the cloud core for case M2-A: (a) vertical velocity (m sec^{-1}); (b) liquid water content (gm m^{-3}); (c) equivalent potential temperature (excess in °K above 300°K).

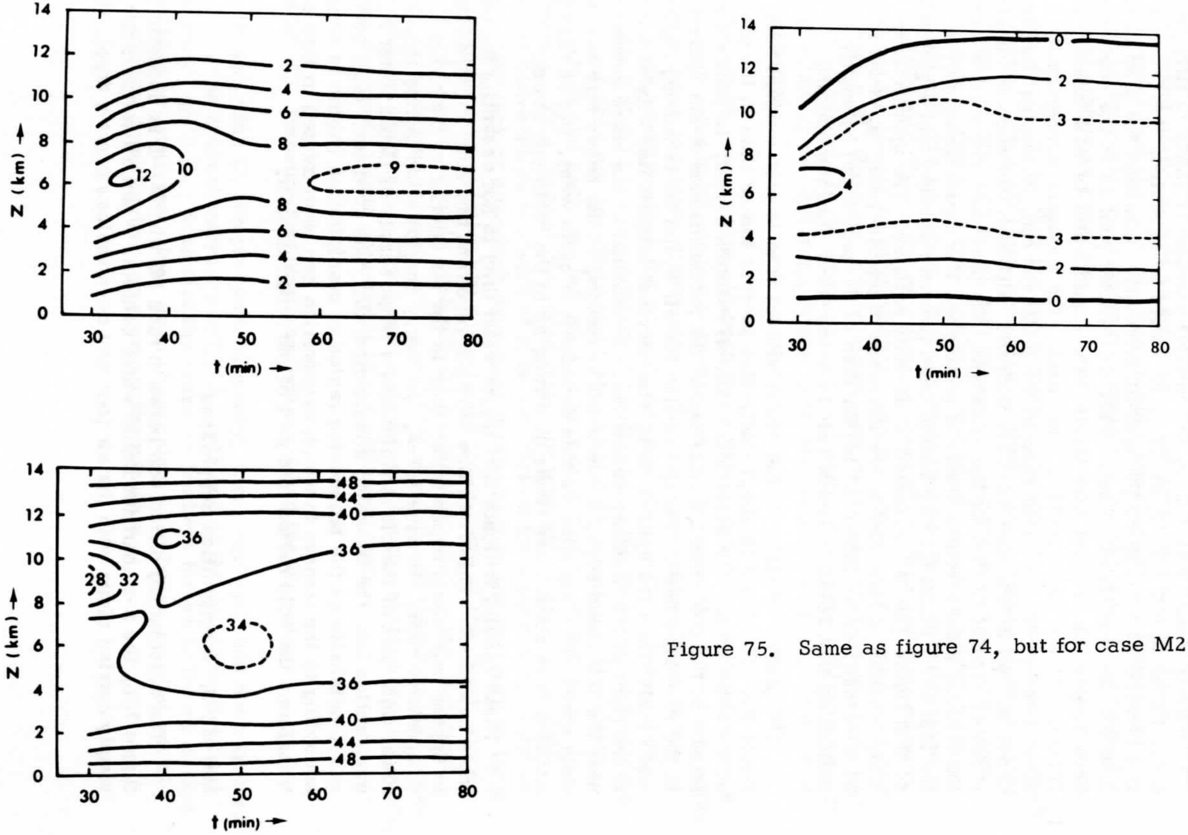

Figure 75. Same as figure 74, but for case M2-B.

Run M2-A: Liquid Water Drag Suppressed

Without liquid water drag, the updraft velocity is thirty to fifty percent greater than in run M2 (figure 74a). As would be expected, then, the drag is essential as a brake on the updraft intensity. Although the drag is being ignored, the precipitation mechanism is retained just as in the comparative experiments; as is clear from figure 74b, liquid water is most heavily concentrated in the lower parts of the cloud. The maximum concentration is about twenty percent larger than in the prototype run, reflecting the greater condensation in the more vigorous updraft. Although the mode of convection is rather similar to that for the prototype, the drag-free storm goes through the various stages sooner than the prototype. The liquid water profile changes too fast to be satisfactorily interpolated between seventy and eighty minutes, so that figure 74b is terminated at seventy minutes. The updraft decay after sixty minutes is reflected in the decrease of middle-level θ_e from its quasi-steady value (about 2° higher than in the prototype) by eighty minutes, indicating that potentially cool air is being drawn into the updraft.

The greater severity of the storm without drag is also evident from figure 85. The anvil is about thirty-five percent longer than in the prototype at the same time. The significant rainfall extends higher, so that a greater portion of the precipitation falls out of the jet downshear of the updraft than in the prototype case. Partly because the air in the jet is moving rightward much faster than the updraft core, the heaviest rainfall lies almost entirely to the right of the dividing streamline. In addition to the weak downdraft near the left cloud edge, a downdraft is forming in the heavy rain near the right edge. At sixty minutes this downdraft is quite weak, but at eighty minutes it is about three times as strong as in the prototype storm.

These results indicate that liquid water drag is not essential for initiating a downdraft. This is in line with the recurrent tendency for downdrafts to appear near cloud edges rather than in the far interior of the cloud in the comparative runs. In case M2-A, the heavy precipitation falling through the lower right part of the cloud maintains a large supply of liquid water for evaporation into the incoming unsaturated air. The downdraft later becomes moist-adiabatic as the broadening region of precipitation (which is saturated according to the manner in which evaporation has been treated in this model) transforms the cold region into part of the cloud interior.

Run M2-B: Precipitation Suppressed

The outstanding difference between runs M2 and M2-B is apparent in figure 75b, the z-t chart for liquid water content. When all water drops are simply carried along with the air (but may nevertheless exert a drag), the largest value of L is located around 8 km, much higher than in any of the comparative experiments (all of which allow precipitation). This maximum is only about sixty percent as great as in the prototype storm, indicating in retrospect that the precipitation process not only greatly lowers the altitude of heaviest liquid water concentration but also leads to accumulations not otherwise possible.

Figure 75 shows that the precipitation mechanism is important to updraft dissipation, since all three variables plotted reach a steady state at about fifty-five minutes with no sign of decay as of eighty minutes. Until about fifty minutes, there is little difference in updraft intensity between the prototype and this variation. It is apparent that the temporary decrease in the updraft velocity for the prototype between thirty-four and fifty minutes is not mainly caused by precipitation, since a comparable decrease occurs in variation B. However, the reinforcement of the updraft between fifty and sixty-five minutes in the prototype may be partly due to the redistribution of liquid water by precipitation, since much less regeneration occurs without precipitation.

Figure 86 reveals that although the overall circulation at sixty minutes is in some ways quite similar to that of the prototype at the same time, there are also some important differences. The stub-like protuberance in the cloud base never reaches the ground, since precipitation is suppressed. This cloud stub is the counterpart of the precipitating trunk in the prototype storm, but does not broaden appreciably after forty minutes. The slight downdraft at and under its left edge is less than half as strong as in the prototype. This minimal downdraft does not intensify significantly later, and the convergence rearward of it is insufficient for a secondary cloud to form. The lack of downdraft development results from the inability of large liquid water accumulations to occur in the lower parts of the cloud; since much less liquid water is available for evaporation than in the prototype, there is much less cooling (only about 1°C at most) and therefore less negative thermal buoyancy. The temperature never changes at the lower boundary, since the static phase adjustment is not activated there.

Run M2-C: Pressure Perturbations Suppressed in the Buoyancy

In variation C, the pressure buoyancy, i.e., $-gp'/\bar{p}$, has been ignored and only the thermal buoyancy $gT_v'/\bar{T}_v$ retained in the total gravitational buoyancy $-g\rho'/\bar{\rho}$. Note that the pressure gradient forces in the equations of motion are still operating, even though they have been canceled out of the vorticity equation through cross-differentiation.

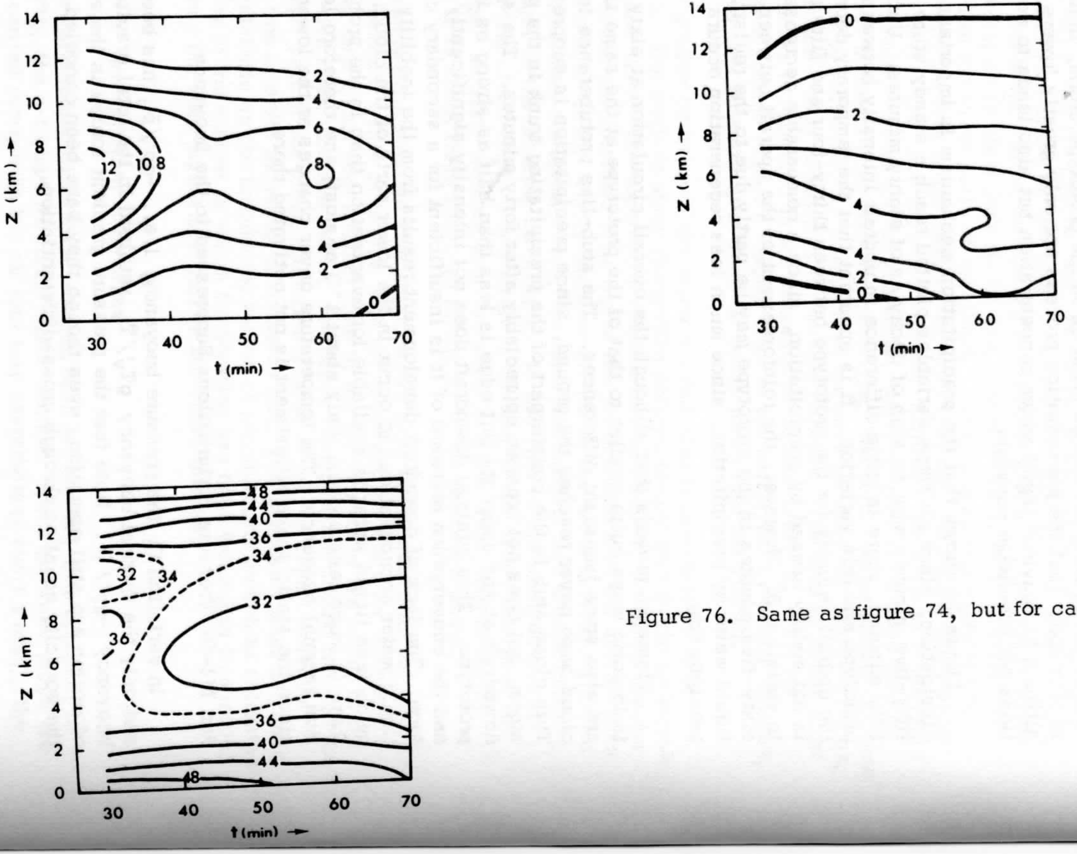

Figure 76. Same as figure 74, but for case M2-C.

Comparing figure 76 with figure 13, note that at thirty minutes the altitudes of both the cloud top and of the maximum updraft are appreciably greater in case M2-C. As implied by this difference, the updraft throughout the first thirty minutes is somewhat stronger in variation C than in the prototype case, although the initial momentum perturbations are identical. Recall from figure 66 that the prototype storm showed positive pressure buoyancy in the lower front part of the updraft, and pronounced negative pressure buoyancy in the upper part of the updraft. Also, preliminary runs showed that before thirty minutes the prototype storm exhibited low pressure below the updraft core and high pressure above it. Thus, in variation C, without the downward acceleration provided by the upper level pressure excess, air parcels in the developing updraft acquire extra vertical momentum not because they are accelerated more at low levels but because they are decelerated less in the upper half of the cloud.

After thirty-five minutes, the convection in run M2-C becomes appreciably weaker than in the prototype run, apparently because the low pressure in front of and within the lower part of the updraft dominates the dynamics more than the pressure excess at higher levels. In case M2-C, the absence of the extra upward push provided by the resulting positive pressure buoyancy eventually overrides the invigorating effect described in the preceding paragraph. Correspondingly, the maximum liquid water content after forty minutes is about twenty-five percent smaller than in the prototype storm, due to slower condensation. The equivalent potential temperature in the moist-adiabatic region after forty minutes is some 4° lower than in the prototype storm, paralleling the weaker intensity of the updraft. All parts of figure 76 were terminated at seventy minutes, because the updraft collapsed rapidly between seventy and eighty minutes while a downdraft rapidly developed in the lower levels of the cloud.

The updraft orientation and the location of significant rainfall at sixty minutes (figure 87) are much as in the prototype storm, but the dividing streamline of the updraft approaches the left cloud edge more closely than in case M2; the increased vulnerability of the updraft to mixing with evaporatively cooled air may contribute to its weaker intensity. The region of significant rainfall in case M2-C is smaller than in case M2 although the location within the cloud is similar. The importance of the low pressure ahead of the storm is seen indirectly in the smaller mass flux of air toward the storm (there is only one uninterrupted channel, rather than two, to the right of the cloud). One other noteworthy difference between runs M2 and M2-C is revealed by the streamline oscillation above 8 km inside and downwind of the anvil. This oscillation, apparently a gravity wave, with crests near $x = 140$ and 190 km, is quite weak in case M2, but about three times stronger in case M2-C. In appendix A, the moisture-free counterparts of the governing equations (1)-(4) are linearized about a base

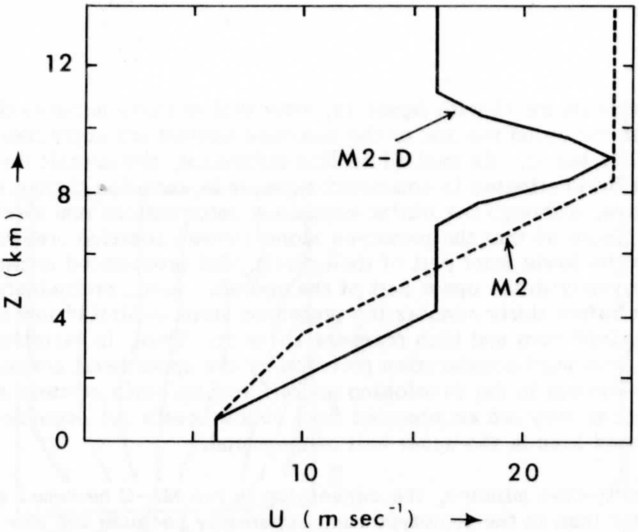

Figure 77. Comparison of wind profiles for initial base states in cases M2 (dashed curve) and M2-D (solid curve).

state of rest with a constant stable lapse rate*; it is shown that stable gravity waves should in fact intensity more strongly with height if p' is neglected in the buoyancy than if it is retained.

Run M2-D: Upper Jet Maximum in Wind Profile

In variation D, the range of u for the undisturbed initial wind was the same, from 6 m sec^{-1} at the surface to 24 m sec^{-1} at upper levels, but the shape of the vertical wind profile was altered as shown in figure 77, with a jet nose between 7 and 11.2 km. The 24 m sec^{-1} maximum wind is at 9.1 km. The profile shape is based on the projection of the environmental winds along the direction of movement of the Geary, Oklahoma thunderstorm mentioned in the Introduction.

The z-t charts in figure 78 show that neither the mode nor the intensity of the convection is greatly changed by replacing the initial wind profile

---

*Although it does not apply in the moist convection model, this very simple base state is chosen for mathematical tractability in the linearized analysis without moisture. Although moisture is crucial to the numerical model, the gravity wave above 8 km occurs in a region of absolute stability and very small moisture content.

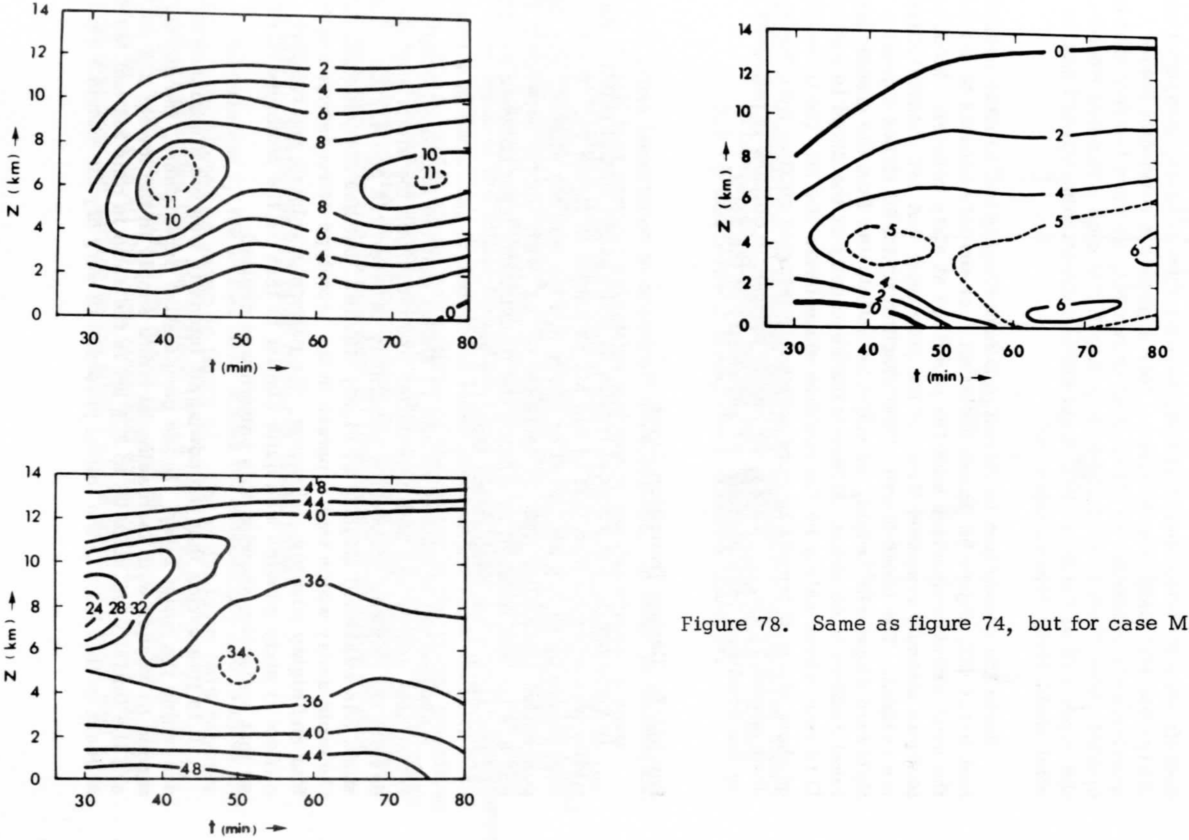

Figure 78. Same as figure 74, but for case M2-D.

of run M2 with that of variation D. However, the corresponding stages are delayed to a slowly increasing extent with time. The two peaks in updraft velocity occur near forty and seventy-five minutes, compared with thirty-four and sixty-four minutes. This suggests a somewhat longer quasi-steady phase in run M2-D than in run M2, as does the fact that the updraft above 7 km is still increasing slightly at eighty minutes whereas the upper half of the prototype cloud showed diminishing upward motion after about sixty-five minutes.

Since the convection in variation D lags roughly ten minutes behind that in run M2, figure 88 shows variation D at seventy minutes to provide the most direct comparison with the prototype at sixty minutes. Most key features strongly resemble those of the prototype, but two dissimilarities are evident. The lower fourth of the cloud in figure 88 shows a greater rightward slope with height, as might be anticipated from the greater low-level ambient wind shear. Although the asymmetry of the cloud in variation D is determined mainly by the positive shear below the jet, the reversal of shear above it results in more noticeable leftward outflow from the updraft around 11 km. This more nearly symmetric outflow is reflected by the somewhat less pronounced asymmetry of the anvil.

Run M2-E: Deeper Transition Layer

In variation E, the vertical profile of undisturbed initial relative humidity was changed from that of run M2 as shown in figure 79. The initial atmosphere up to 2.8 km and at or above 8.4 km was not altered, but the convective instability (rate of decrease of θ_e with height) between 2.8 and 8.4 km was reduced by making the transitional layer between the moist and dry air 4.9 km deep rather than 1.4 km.

A comparison of figures 80 and 13 shows that the increased supply of latent heat energy has both intensified and prolonged the storm slightly, despite the reduced convective instability between 2.8 and 4.2 km. The storm has weakened slightly by eighty minutes, but has not yet exhibited the rapid decay which was apparent in the prototype storm between seventy-four and eighty minutes. However, the pattern of rainfall and relative airflow at sixty minutes was quite similar to that for the prototype case, so that a diagram showing this pattern was omitted.

It is interesting that the downdraft intensity was not diminished by deepening the moist layer. In the comparative experiments, the downdraft tended to weaken with increasing moisture supply in the lowest 2.8 km, and the initial base state up to 2.8 km is the same in runs M2 and M2-E. At least in this model, the initial presence of very dry air around 4 km is

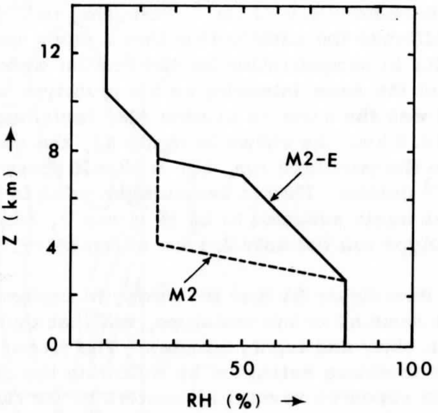

Figure 79. Comparison of relative humidity profiles for initial base states in cases M2 (dashed curve) and M2-E (solid curve). Above 7.7 km and below 2.8 km, the two cases coincide.

not of prime importance to downdraft development. In order to understand this, recall that vertical velocities and hence the departures of other physical variables from their initial base values are overestimated in the two-dimensional model. Where the sinking parcels to the left of the cloud reach their lowest altitudes, the relative humidity by forty minutes has decreased almost as greatly in variation E as in the prototype. The much greater depth of the initial transition layer in variation E loses its importance because of the strong drying which takes place in the layer initially occupied only by moist air (to say nothing of the drying in the initial transition layer). While this model indicates that a very sharp initial stratification of dry air over moist is not conducive to either a more intense or longer lasting storm, this conclusion must be interpreted with ample caution.

Run M2-F: Shallower and More Unstable Moist Layer

In variation F, the initial base states for temperature and relative humidity were altered as shown in figure 81. The moist layer (80% relative humidity) extended from the surface to 1.4 km instead of 2.8 km, again with a 1.4 km transition layer above it. The surface temperature was again 28 °C, as in all the other numerical experiments, but the constant lapse rate from the surface to the middle of the transition layer was 6 °C

$(700\ \mathrm{m})^{-1}$, or approximately 8.6°C km^{-1}, compared to 7°C km^{-1} in the prototype. This reflected the anticipation that a storm would require greater low-level instability in compensation for the smaller water vapor supply in order to attain about the same intensity as the prototype storm. In the dry air, the lapse rate was the same as in case M2, including in the stable layer from 9.1 to 10.5 km. As shown in figure 82, the shear above 3.5 km was the same as in the prototype run, but u itself above this level was uniformly 4 m sec^{-1} greater. This is because the wind in the middle of the transition layer was again assumed to be 10 m sec^{-1}, while this level was 3.5 km in the prototype run but only 2.1 km in run M2-F.

It is apparent from figure 83 that the strength attained by the updraft is indeed much the same as in the prototype, but that the updraft dissipates completely between sixty and eighty minutes. The former updraft axis at eighty minutes was therefore estimated by following the displacement of the downdraft which appeared several kilometers to the right of the updraft while the latter was still well marked.

As shown by figure 89, the most important difference between cases M2 and M2-F at sixty minutes involves the updraft tilt. Although the maximum intensities attained by the storms are nearly the same, the downshear leaning of the updraft in variation F results in a concentration of heavy rainfall downshear of the updraft core, isolating it from its low-level source and hastening its dissipation. At eighty minutes, the downdraft is about three times as strong as in the prototype case, while the maximum surface cooling (9.3°C) is about half again as great as in the prototype, and is greater than in any of the other experiments. Since the region of cloud and precipitation is spreading downshear more rapidly than the location of greatest evaporative cooling, which in this case is downshear of the updraft, the main downdraft becomes protected from the unsaturated surroundings and subsequently develops moist-adiabatically.

Run M2-G: Initial Perturbation Altered

In run M2-G, the final variation on the prototype, the initial base state was the same but the initial perturbation was changed in order to gauge the sensitivity of the convection, in terms of the mature or final state and the evolution toward that state, to the initial perturbation. Rather than a shallow cloud with a weak convective circulation already superimposed on the basic flow, a thermally buoyant impulse with higher relative humidity than the surroundings but without any liquid water or momentum perturbation was assumed. Its dimensions were the same as those of the initial updraft in the prototype run. The positive perturbations of temperature and moisture were greatest at the center and decreased outward. The maximum temperature

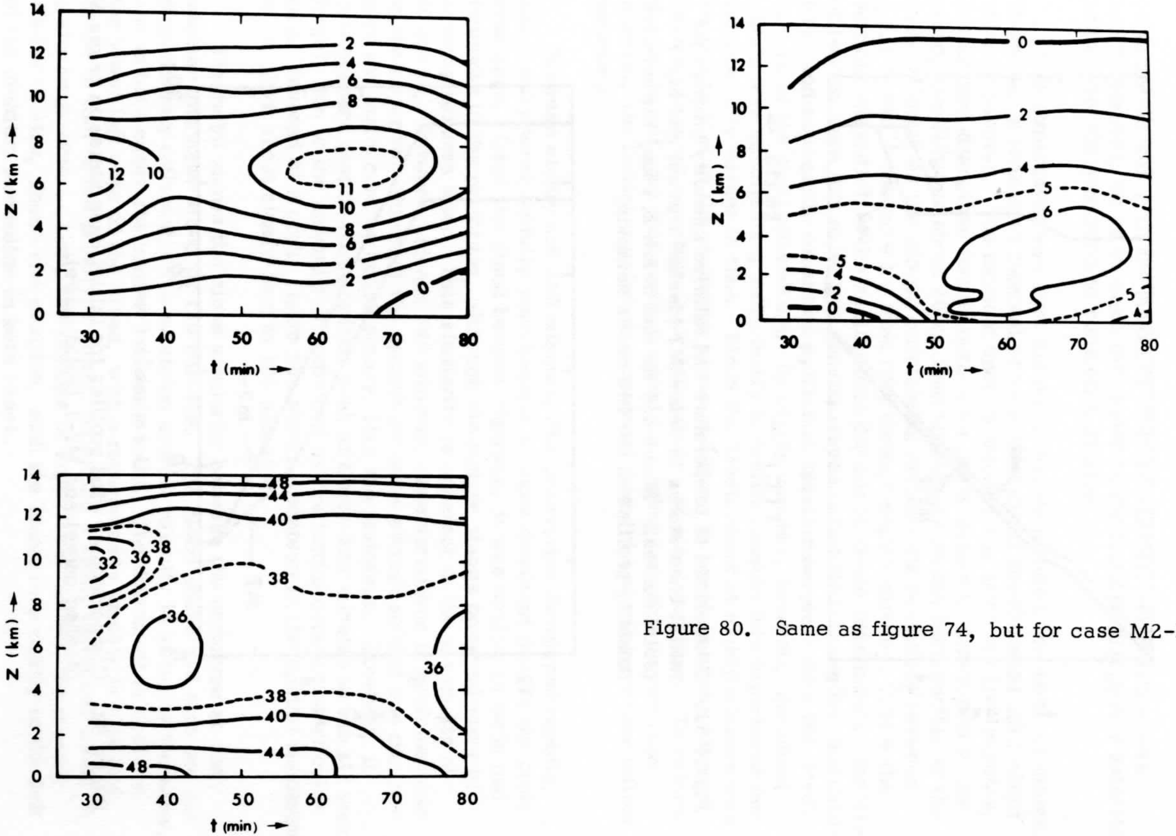

Figure 80. Same as figure 74, but for case M2-E.

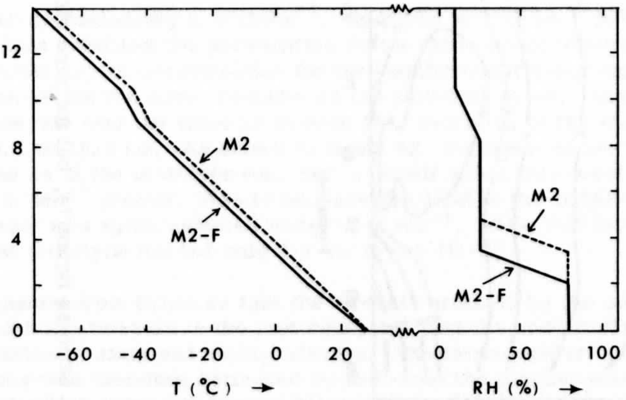

Figure 81. Comparison of temperature and relative humidity profiles for initial base states in cases M2 (dashed curves) and M2-F (solid curves). Above 4.9 km and below 2.1 km, the relative humidity profiles in the two cases coincide.

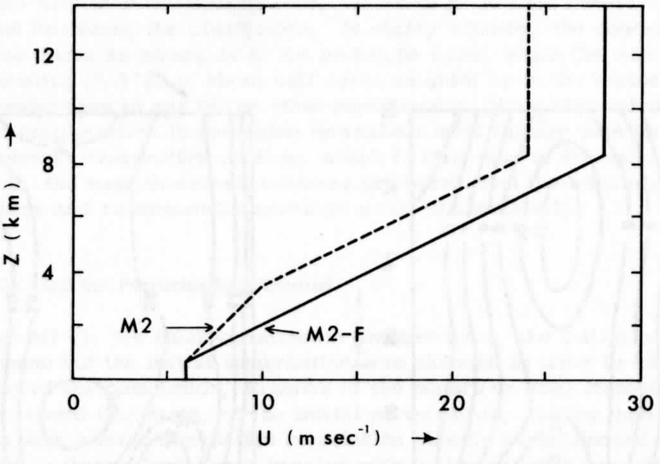

Figure 82. Comparison of wind profiles for initial base states in cases M2 (dashed curve) and M2-F (solid curve).

perturbation was 1°C; the maximum relative humidity perturbation was twenty percent, so as to make the center of the impulse just barely saturated and enable condensation to commence at once.

This experiment was first run out to eighty minutes, as were all others. There was a prolonged interval of very slow cloud development until about seventy minutes. The nascent updraft reached 1 m sec^{-1} by five minutes, but did not strengthen further until after thirty minutes. Downwind of the cloud, oscillations about 20 km long propagated nearly horizontally at the same velocity as the cloud, maintaining vertical air velocities between $\pm$ 3.5 m sec^{-1} around 9 km from fifty through eighty minutes. Since the vertical velocities in the oscillations did not increase indefinitely, the oscillations were felt to be true gravity waves rather than numerical instabilities, and apparently consumed sufficient kinetic energy to slow the development of the main convection. By eighty minutes, however, the cloud growth was accelerating sufficiently to justify running this experiment out considerably further in time. Since its development at eighty minutes was similar to that of the prototype cloud at fifteen to twenty minutes, it was decided to rerun variation G for 140 minutes of simulated time. To reduce the number of grid shifts which would be needed over this longer time interval, the initial impulse was centered $5\Delta x$ (16 km) closer to the inflow boundary.

Between eighty and 100 minutes, the convection developed rapidly, and gravity wave activity soon became no more dominant than in the prototype case. Once the cloud became vigorous, it was similar in mode and intensity to the prototype, although the mature stages occurred sixty to seventy minutes later. This similarity is apparent in the z-t charts of figure 84. Between 115 and 140 minutes, time variations in each variable in the upper two-thirds of the updraft are slow enough so that one can regard the storm core as quasi-steady, like the prototype. However, it now appears that the first updraft peak at thirty-four minutes in run M2 was largely due to the upward push provided by the initial convective circulation. Instead of a peak, figure 84a shows a plateau in the spatial maximum of w from about ninety-four to 108 minutes.

Figure 90 shows the close similarity between the prototype at sixty minutes and case M2-G at 130 minutes. The cloud shape and size are not significantly different. The maximum updraft velocity is virtually the same, and in both cases the updraft is nearly erect. The downdraft is again at the lower left edge of the cloud, with a reverse eddy similar in size and shape to that of the prototype storm, including a small secondary cloud in a similar position. Also, the regions of significant rainfall are closely similar in size, shape and position, with the heavy rain mostly to the left of the dividing streamline in both cases.

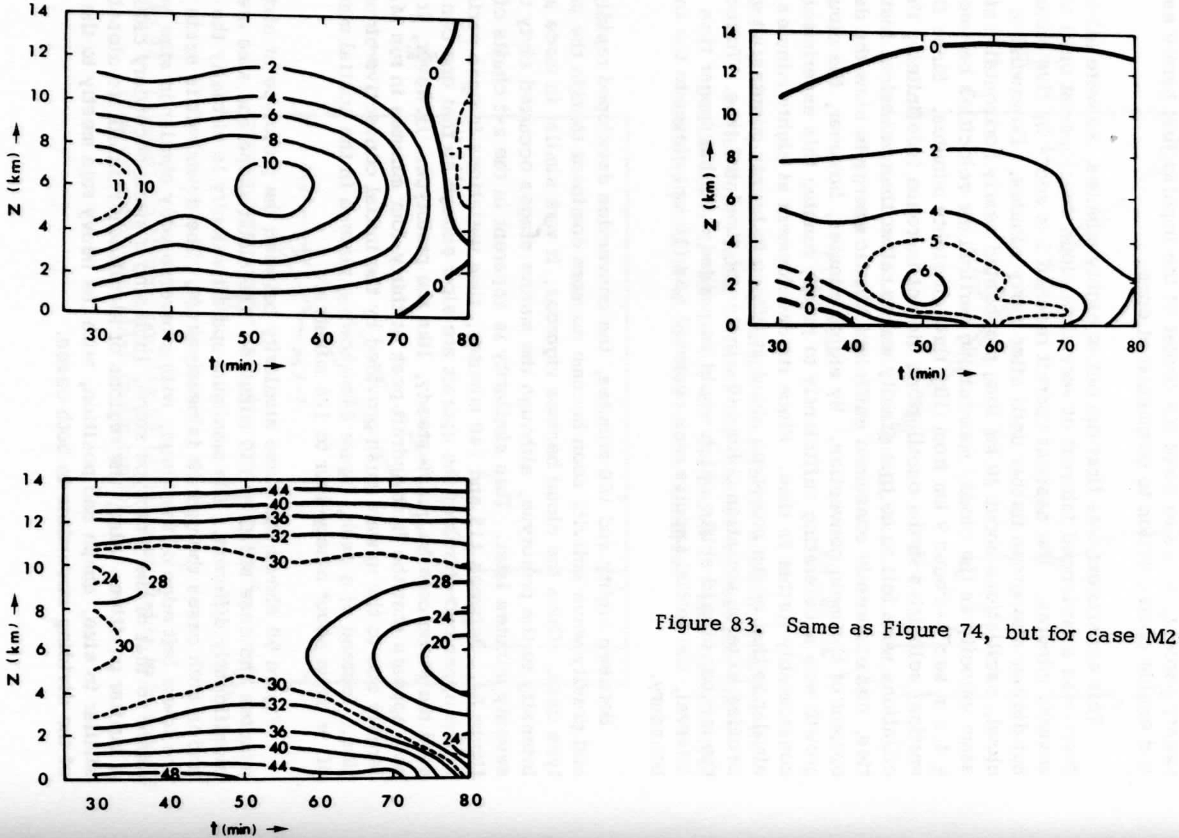

Figure 83. Same as Figure 74, but for case M2-F.

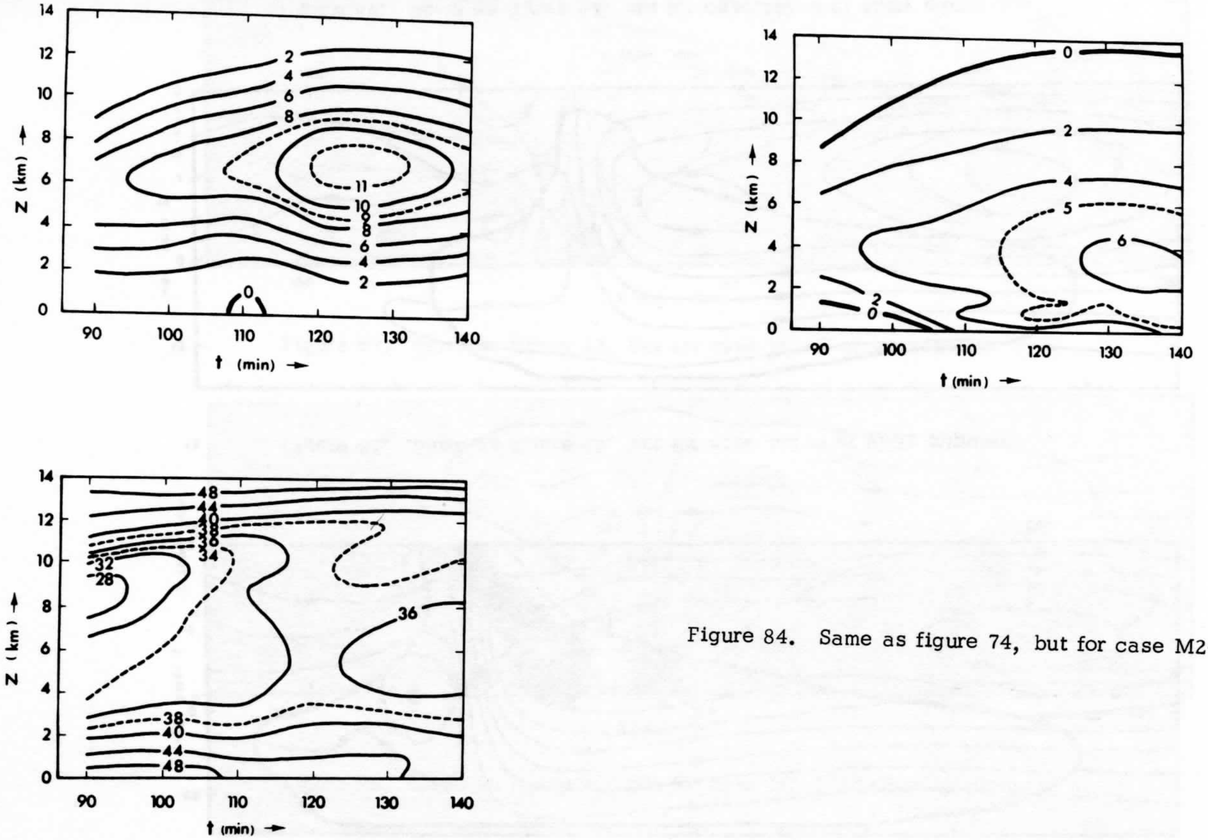

Figure 84. Same as figure 74, but for case M2-G.

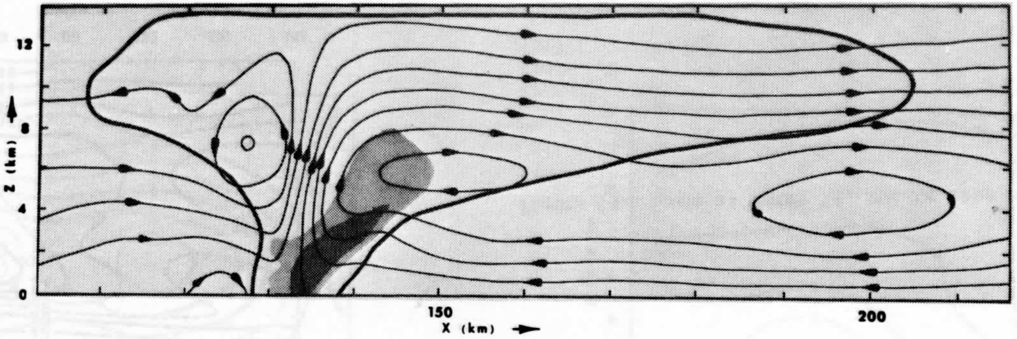

Figure 85. Same as figure 43, but for case M2-A at sixty minutes.

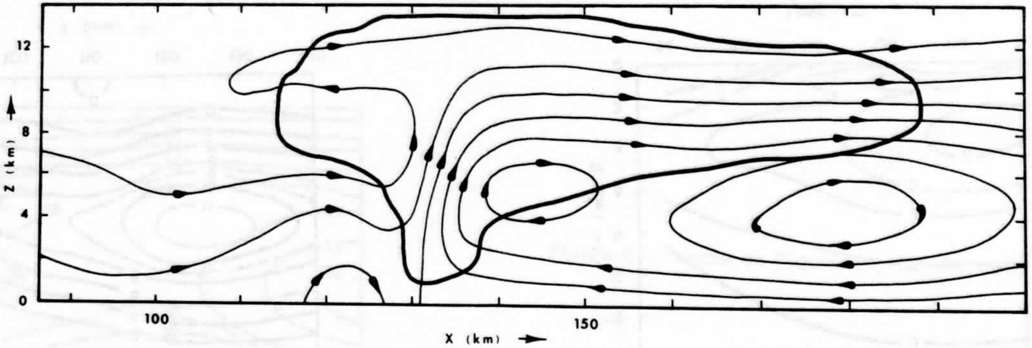

Figure 86. Same as figure 43, but for case M2-B at sixty minutes.

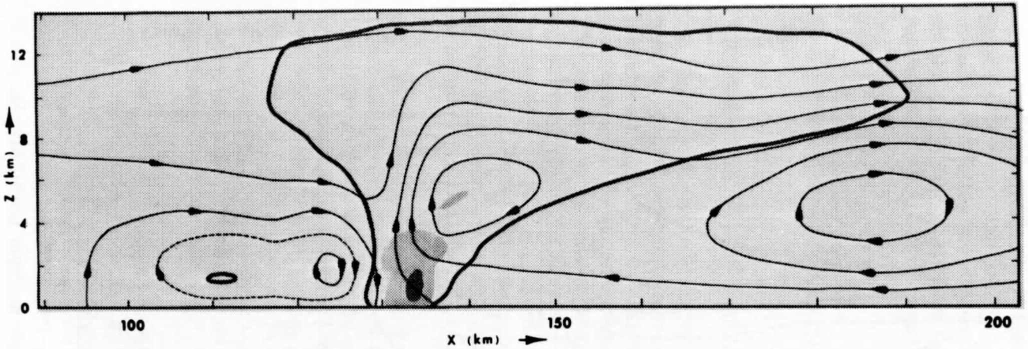

Figure 87. Same as figure 43, but for case M2-C at sixty minutes.

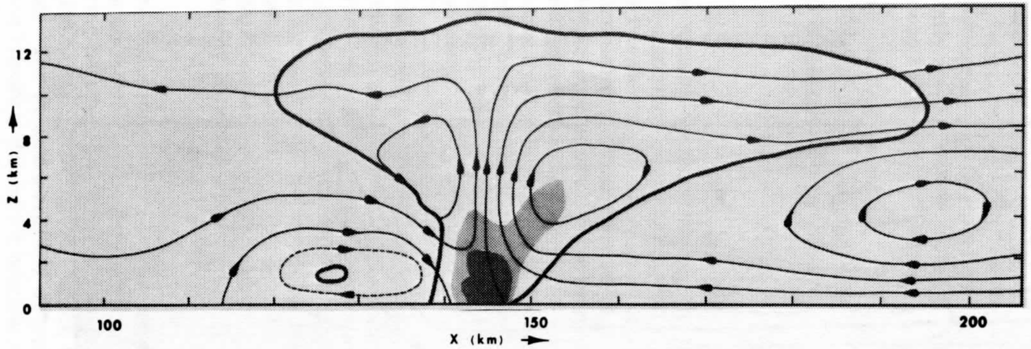

Figure 88. Same as figure 43, but for case M2-D at seventy minutes.

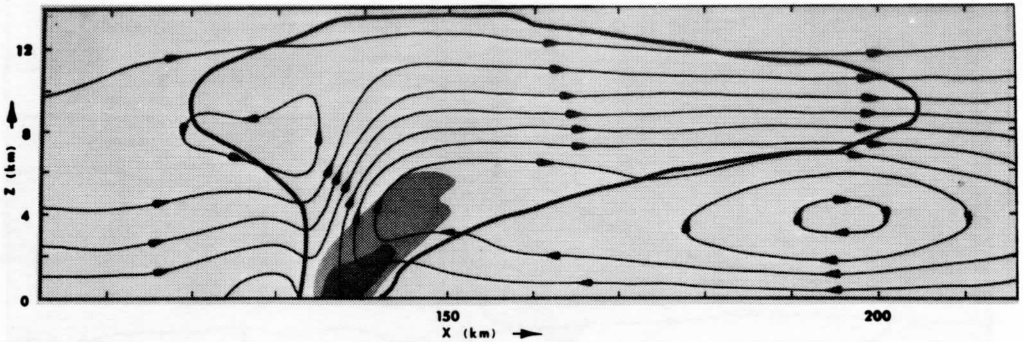

Figure 89. Same as figure 43, but for case M2-F at sixty minutes.

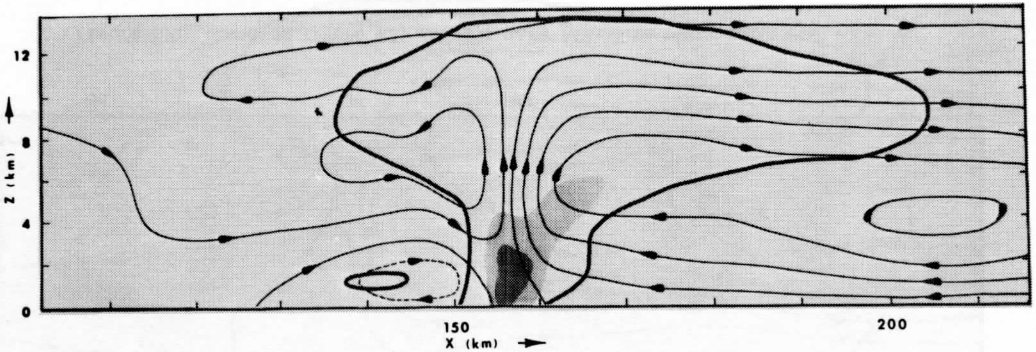

Figure 90. Same as figure 43, but for case M2-G at 130 minutes.

In comparing cases M2 and M2-G, the main point is that at least for weak buoyant initial perturbations of particular dimensions, the evolution toward the final or quasi-steady state may be strongly influenced by the nature of the impulse but that the size, strength and configuration of the mature circulation are determined almost entirely by the initial environment. It appears that there is essentially a unique quasi-steady state, rather than two or more, and in this sense is physically stable.

9. SUMMARY AND CONCLUDING REMARKS

9.1 Summary of Main Conclusions

The results of the comparative experiments have indicated that the intensity of convection (maximum updraft velocity, maximum rainfall rate or the size of the precipitation region) increases with increasing low-level moisture supply and decreases with increasing midtropospheric wind shear. The strengthening with increasing moisture supply would be expected from the corresponding increase of low-level convective instability (since the temperature profile has been assumed identical in all the comparative experiments). With increasing wind shear, the main updraft is shifted closer to the left boundary of the cloud,* becoming less buoyant due to the effects of evaporative cooling at the cloud boundary.

As the wind shear is increased, the cloud anvil develops more predominantly on the downshear side. This asymmetry is closely related to the airflow relative to the moving storm core. At low shear, the relative airflow is nearly symmetric, while at moderate shear the right branch of the convective circulation is considerably stronger than the left-hand branch and at strong shear the left branch nearly disappears. Despite the pronounced asymmetry of the cloud outline at moderate and especially at strong shear, the updraft core shows considerably less shear than the initial surroundings and may be nearly erect.

Except in one case (least moisture and strong shear), the storms in the comparative runs show two peaks of updraft velocity twenty to thirty-five minutes apart. The first peak, occurring between thirty and thirty-five minutes, may be an overshoot due to the initial perturbation, which already includes a weak convective circulation. The second peak may be partly a result of reinforced surface convergence between downdraft outflow and the

---

*In regard to the two-dimensional model, left and right are defined in the plane of the model and are toward the inflow and outflow boundaries, respectively.

air approaching the cloud from further to the right. Although the dominant downdraft develops to the right of the updraft in two cases (low and moderate shear with greatest moisture), a downdraft first appears along the left edge of the cloud after the first peak, and its diverging outflow increases the wind under the cloud core, thus enhancing the convergence between the air under the core and in front of the updraft.

The persistence of a storm does not necessarily increase with its maximum intensity. Although intense storms are favored by weak shear and a large moisture supply, long-lived storms are favored by moderate shear or even (for a very moist lower atmosphere) by strong shear. The most important points concerning the moderately and strongly sheared cases are the following:

1) While the precise orientation of the updraft depends on the relative mass fluxes of low-momentum air and high-momentum air feeding it from the right and left, respectively, the streamlines of the updraft in each case tilt toward the left through the lower atmosphere and toward the right above the middle levels. In other words, the air in the lower levels of the updraft is moving toward the back of the traveling storm, while air in the upper levels of the updraft is moving toward the front of the storm.

2) The storm core is traveling at a velocity intermediate between that of the undisturbed low-level ambient wind and the higher velocity of the undisturbed upper-level ambient wind. The convective circulation superimposed on the basic flow enhances both the moist low-level inflow from the right (relative to the moving storm core) and the dry middle-level inflow from the left.

3) Since precipitation particles have the same horizontal velocity component as the air (by assumption) but fall relative to the air, the curvature of the updraft implies that precipitation stored at or below its middle levels falls to the left of the updraft core, whereas precipitation stored at high altitudes in the updraft falls to the right of the updraft core. In the first case, the left edge of the cloud is nearer to the low-level accumulation of liquid water than is the right edge. This favors evaporative cooling and downdraft formation at the left edge. In the second case, the opposite is true.

4) Since the downdraft must diverge upon approaching the rigid lower boundary, the surface flow near the downdraft converges with the surrounding flow, thereby producing upward motion on either side of it. If the new upward motion is produced near the foot of the pre-existing primary updraft, this may help to maintain the primary updraft provided the air in the region is sufficiently unstable and free from excessive drag due to heavy precipitation.

The points just noted provide some explanation of why a very severe updraft may be shorter-lived than a moderately strong one, as indicated by the numerical results. In the long-lived storms, the updraft is well developed but not sufficiently strong to suspend a large portion of the precipitation in its upper levels. As a result, most of the rainfall occurs to the left of the updraft core. The downdraft and the strongest low-level cooling occur at the left edge of the cloud; the surface convergence between its outflow and the surrounding flow toward the storm causes upward motion in back of the cloud and also in the same region as the pre-existing updraft. Since the air feeding the original updraft bypasses the heaviest precipitation and the main region of low-level cooling, its ascent into the cloud is not greatly hindered by liquid water drag or stabilization, and the updraft is able to persist relatively long. On the other hand, a very intense updraft may store much of the precipitation in its upper levels, causing some of the heaviest rain to fall to the right of the updraft core. The downdraft is initiated near the right edge of the cloud, isolating the updraft from the supply of potentially warm air further to the right. The downdraft becomes moist-adiabatic and quite strong as the region of rain reaching the ground broadens and protects the downdraft from the unsaturated surroundings. Strong convergence between the diverging downdraft outflow and the surrounding flow induces upward motion near the right cloud edge (after the downdraft becomes moist-adiabatic) and near the base of the primary updraft. The upward motion induced by the convergence slows but does not fully counteract the decay of the primary updraft.

In the weakest storm among the comparative runs (strong shear with least moisture), the relative positions of the primary updraft, downdraft and secondary updraft are similar to those in the long-lived storms. However, the lowest-lying (and potentially warmest) air does not ascend into the updraft core, but flows under and past the cloud. The air which does ascend into the updraft core has a relatively low equivalent potential temperature and does not acquire sufficient thermal buoyancy to maintain the updraft for a long interval of time.

The fact that downdrafts in this model first appear at and near cloud edges, rather than in the far interiors of clouds, indicates that liquid water drag is an important brake on the maximum strength attained by the updraft but is not essential to the initiation of a downdraft. The negative thermal buoyancy produced by evaporation near cloud edges (where liquid water drag is small) is sufficient to initiate a downdraft which may even become vigorous. In view of the model results, the contentions of Byers and Braham (1949), Das (1964) and Srivastava (1967) that liquid water drag is important to downdraft formation are open to question. However, as the next paragraph will emphasize, precipitation does appear essential to the formation of a significant downdraft even though the drag does not.

The precipitation process, i.e., the relative fall of liquid water relative to the air, causes liquid water to accumulate in the lower part of the cloud. If all the liquid water were cloud droplets, with zero fallspeed relative to the air, the greatest liquid water content would be in the middle and upper parts of the cloud. Precipitation also leads to greater concentrations of liquid water than would otherwise be possible. The accumulation in the lower levels of the cloud provides a larger supply for evaporative cooling than in the absence of precipitation, and the more efficient cooling leads in turn to a considerably stronger downdraft. The precipitation process also appears essential to the dissipation of the updraft, which evolves to a steady state in the absence of precipitation but eventually decays rapidly in its presence. The low-level cooling due to precipitation ultimately cuts off the updraft from the potentially warmest air, its main source of buoyancy.

One-dimensional cloud models, e.g., those of Squires and Turner (1962), Das (1964), Srivastava (1967) and Weinstein (1970), have been highly instructive and have provided surprisingly good agreement with observations, but the inability of such models to incorporate pressure perturbations appears to be a serious weakness. In the present model, the vertical perturbed pressure gradient force cancels a large fraction of the thermal buoyancy in the most buoyant parts of the updraft. This indicates that despite the importance of net vertical accelerations to the convection, significant parts of the pressure perturbations are hydrostatic. In addition, while considerably smaller than the vertical pressure gradient force, the pressure contribution to buoyancy effects has two main results: under the leading edge of the cloud and in the lower part of the main updraft, positive buoyancy (due to relatively low pressure) maintains the updraft and enhances the mass flux of low-level air into the updraft, while negative buoyancy (due to relatively high pressure) in the upper levels of the updraft significantly decelerates the updraft at lower altitudes than would be predicted by the parcel theory or other theories which neglect pressure perturbations. In the building stage of a storm, the second of these effects overrides the first, making the updraft slightly less intense and shallower than would otherwise be the case. In the mature stage, however, the first of these two effects predominates. As a result, the pressure buoyancy helps to keep the mature updraft significantly stronger than if the buoyancy were purely thermal. Also, as may be predicted from linearized theory for dry convection, the pressure buoyancy limits considerably the development of gravity waves which might propagate in the absolutely stable upper levels.

In light of the conclusion that sizable portions of the pressure perturbations are hydrostatic, the most prominent features of the pressure disturbance field can be largely explained by examining the disturbed temperature field. Before precipitation reaches the ground, there is a pressure deficit in the lower half of the cloud and an excess in its upper half, with the greatest excess just under the cloud top and the greatest deficit at the surface; the pressure near the upper boundary is almost undisturbed. There is warming in the cloud core with cooling due to forced ascent of air at and above the cloud top. After precipitation has reached the ground, the pressure rises in a shallow layer in and near the rainfall region, while regions of relatively low pressure are located in the lower and middle levels under the leading cloud edge and somewhat behind the trailing edge. With wind shear, the downshear trough is stronger than the upshear trough, this asymmetry becoming more pronounced as wind shear is increased. The pressure rise under the storm appears to result largely from low-level cooling brought about by evaporation of precipitation or moist-adiabatic descent, as suggested by Fujita (1959). The main factors contributing to the troughs are the diverging of warm air from the updraft into the anvil and the dry-adiabatic warming of the storm's surroundings. Also, the upshear trough is weaker than the downshear trough, and is behind rather than under the trailing edge mainly because the low-level cooling extends further upshear than downshear of the storm core, while the opposite is true of the warming in the anvil. The large values of the pressure falls ahead of the model storms appear to be due to the model's geometry, which results in exaggerated compensation outside the storm, with overestimation of dry-adiabatic warming and horizontal accelerations.

The increasing asymmetry of the cloud anvil with increasing wind shear is paralleled by an increasing symmetry of the horizontal pressure gradient force in the diverging upper parts of the updraft. As shear is increased, the gradient between the excess pressure core and its surroundings is concentrated more predominantly to the right of the core (downshear of it). Accordingly, the anvil develops more toward the right than toward the left. The horizontal pressure gradient force is also important to both the dissipation of the updraft and the maintenance of the downdraft. Potentially cool middle-level air is accelerated horizontally into the cloud from both sides, ultimately reducing the buoyancy of the updraft. The downdraft outflow, initiated by continuity requirements as the downdraft decelerates vertically toward the ground, is then dynamically sustained by the pressure gradient force which causes air in the "thunderstorm high" to accelerate outward.

In this model, a sharp upper-level jet does not result in a more intense storm than a broad wind maximum throughout the upper levels, although the growth stage and possibly the mature stage are prolonged. However, this conclusion should be regarded cautiously since the severity of actual thunderstorms may be increased through synoptic-scale destabilizing mechanisms not incorporated into the model. In particular, large-scale mass convergence has not been included in the horizontally homogeneous base state initially assumed.

An initial moisture stratification featuring a sharp decrease of relative humidity with height is not conducive to either a more severe or a longer-lasting storm than a stratification featuring a gradual transition from moist to dry air, assuming the moist layers to have equal depths and humidity profiles. Indeed, the storm in the former case is slightly weaker and shorter-lived than in the latter case. The smaller total supply of latent heat energy apparently more than counteracts the greater convective instability just above the moist layer. Subsequent middle-level drying due to compensatory sinking is a more important determinant of the amount of cloud-edge evaporation in this model than the initial relative humidity at middle levels. Thus, the initially important contrast between the profiles loses much of its importance even before the convection is fully mature. The geometry of the model appears largely responsible for this result; since the compensating motions in the unsaturated surroundings are exaggerated, the same is true of the drying with time in the moist layer and in the transition layer above it.

If the initial moist layer is made shallower but sufficiently more unstable thermally for the storm to attain about the same maximum intensity as under the original initial conditions, the smaller supply of potentially warm air results in a shorter-lived storm. Another reason for the shorter life in this model is the unfavorable tilt of the updraft which is inclined so that the heaviest rain and the main downdraft are located in front of the updraft core, isolating it from the main supply of warm moist air.

A comparison of the prototype case with the others indicates that the intensity and persistence of the convection depends strongly upon the initial environmental base state, as might be expected. Also, for the same base state, the convection may take much longer to evolve to a mature state from a buoyant cloudless perturbation without appreciable vertical motion than from a shallow cloudy region in a weak updraft having similar horizontal and vertical dimensions to those of the cloudless perturbation. However, the flow configurations and intensities of the mature convection are very similar in both cases. It thus appears that at least for weak buoyant initial perturbations of given dimensions, the subsequent evolution to maturity depends strongly on the properties of the particular impulse but that the mature stage itself is determined almost completely by the initial environmental base state and is nearly independent of the disturbance.

9.2 Potential Applications and Future Improvements

Some of the potential applications of the two-dimensional numerical convection model covered in this paper have already become apparent. Perhaps the most obvious use is to provide insight into the basic dynamics of cumulonimbus convection, without the considerable risks entailed in a detailed program of aircraft observations. More importantly, the ability to vary one parameter in a given set enables one to isolate by controlled experiment the specific role of that parameter in a way not possible in the real atmosphere. In this research, the consequences of varying the low-level moisture or the midtropospheric wind shear have thus been isolated. A related application of the model is also apparent from some of the variations performed upon the prototype. Although liquid water drag, precipitation and the buoyancy due to pressure perturbations cannot be eliminated in the real atmosphere, the corresponding terms can be eliminated from the governing equations one at a time in separate numerical experiments, thus helping make possible indirectly but systematically an understanding of the cumulative effects each process has upon the convection.

Although the observations cited in this work have concerned middle-latitude storms almost exclusively, the model could equally well be applied to tropical convection since the Coriolis parameter (and hence any restriction on latitude) is being ignored; convective cloud ensembles such as the spiral bands of hurricanes might be of interest. In the Introduction, we noted the conclusion of Riehl and Malkus (1958) that deep moist convective elements in the equatorial trough zone are of dominant importance to the general circulation. Also, such well-known meteorological projects as the Line Island Experiments, Project Storm Fury and the planned GARP program are directly concerned with an improved understanding of tropical convection. In particular, one paramount problem is to understand where and to what extent cumulonimbus convection will develop for given synoptic-scale distributions of relative humidity and wind shear.

Despite limitation to two dimensions, an oversimplified treatment of precipitation and definite limitations on the accuracy of the numerical scheme, the results of the model show some basic similarities to actual thunderstorms, e.g., overall cloud shape, surface rainfall intensity or a shallow cold high-pressure dome under the storm core. However, the present model should be improved in one or more areas where obvious imperfections are currently present.

In order to apply the model as realistically as possible to a more complete understanding of severe local storms, it should be made three-dimensional. The veering of wind with height has been a crucially important factor in nearly all of the schematic storm models referred to in this paper. In such an environment, actual thunderstorms exhibit asymmetries normal to as well as along their directions of movement. Their updrafts may not only tilt but also turn with height. While some air moves through an actual storm, part of the ambient air may flow around its core as if it were a cylindrical obstacle. We have seen that a few of the conclusions obtained from the present model are open to some question because its geometry has caused environmental changes to be overestimated. At present, however, the extension of this model to three dimensions must be regarded as a long-term possibility rather than an immediate refinement. There would be a need for far more computing time and storage due to the much larger number of grid points required to retain acceptable spatial resolution. The balance of the needed information would have to be stored peripherally, e.g., on disks or drums, since its sheer magnitude would far exceed that which can be stored in central memory.

The advective finite-difference scheme should be improved. We have seen that the upstream differencing scheme contains a purely numerical pseudo-diffusion with an effective viscosity coefficient proportional to the fluid velocity and the distance between grid points. The pseudo-diffusion in the present model is much larger than what one would expect for actual turbulent diffusion in thunderstorms. Since the model in its present state does simulate with considerable realism some of the main features observed in actual storms, this handicap has not been nearly as detrimental as might be expected purely from the magnitude of the computational diffusion. On the other hand, a potential application of the model not as yet mentioned is the calculation of budgets for physical properties such as water vapor and various types of energy at different stages in a storm's lifetime. Since the pseudo-diffusion of the present differencing scheme would introduce spurious losses of such properties, it is important to reduce if not eliminate this effect. Furthermore, it appears inadvisable to attempt explicit inclusion of turbulent mixing for heat and water vapor until the computational diffusion is reduced. This can be done by adopting a more accurate scheme, but this will require great care since we have seen that some of the more accurate schemes can produce purely numerical oscillations that offset considerably the advantage of reduced pseudo-diffusion.

The movable grid used in the final experiments has not caused any severe difficulties throughout the running times of each experiment. However, revisions appear in order if the model is to be used for simulating thunderstorms over time intervals considerably longer than the eighty minutes simulated in the comparative experiments. The grid is being translated at essentially the same rate as the leading cloud edge (in an average sense, since the translation is done in instantaneous finite steps), which moves much more rapidly toward the right than the trailing cloud edge. If carried out sufficiently long, the present scheme would cause the trailing cloud edge and eventually the storm core to be lost through the left boundary. An alternative approach might be to use a stationary grid domain with variable horizontal resolution, having the finest resolution in the middle parts of the grid and much coarser resolution nearer the lateral boundaries. Without greatly increasing the number of points in the horizontal, such a method could considerably increase the horizontal extent of the domain. For instance, rows consisting of 50 grid boxes 3 km wide flanked on each side by 10 boxes 10 km wide would give a domain 350 km long, fully twice as long as the present domain but with only about one-third more points per row. By placing the initial perturbation within the region of finer resolution, one might hope that variables near the inflow boundary can remain nearly undisturbed so that inflow can be specified as undisturbed for all time with reasonable success.

Since the research has focused on the dynamics rather than microphysics of cloud droplets and precipitation, the treatment of precipitation has been grossly simplified. The model cloud base reaches the ground whenever precipitation does, whereas real thunderstorm clouds retain a well-defined base beneath which precipitation falls into unsaturated air without completely saturating it. In the static phase adjustment, no distinction has been made between evaporation of cloud droplets and evaporation of precipitation. Therefore, the two types of evaporation should be modeled separately and precipitation should be allowed to fall through unsaturated air. In order to model more realistically the production and growth of raindrops, terms representing autoconversion (the production of precipitation by coalescence of cloud droplets) and accretion (the growth of preexisting precipitation particles by coalescence with cloud droplets or other precipitation particles) are needed. To this purpose, parametrizations such as have been used by Kessler (1969) or Takeda (1971) should be incorporated. Since all cumulonimbus clouds contain ice crystals and many such clouds produce hail, frozen precipitation should be included. This would clearly make an already complex model considerably more intricate, since several additional processes such as the growth of hailstones or their partial melt would have to be at least parametrized. However, the inclusion of the ice phase appears necessary if the model is to be applied as a diagnostic or predictive tool in hail suppression projects.

Finally, in view of the central importance of pressure perturbations to storm dynamics, the pressure perturbations should be computed by relaxing the elliptic equation given in section 2 rather than estimated by the short method presented in appendix G. As pointed out earlier, this may significantly increase the required computing time, and there is an undetermined integration constant because boundary conditions on pressure involve its normal derivatives rather than the pressure itself. Perhaps this difficulty could be at least partly sidestepped by formulating boundary conditions in two steps at each time level: while inverting the equation, use the boundary values of p' itself from the preceding time step, and then revise the boundary values by applying the conditions on the normal derivatives after the current interior values have been found to within the accuracy desired. However, further experimentation will be required in order to decide the suitability of this possible approach.

APPENDIX A:

Linearized Analysis of Stable Gravity Waves in a Dry Atmosphere

Consider gravity wave motions in a dry inviscid atmosphere whose base state is at most a function of z, hydrostatically balanced with no wind and a constant stable lapse rate. Let the basic variables u, w, p, ρ and T be decomposed into mean (barred) and perturbation (primed) components:

$$\begin{aligned} u &= \bar{u} + u' \\ w &= \bar{w} + w' \\ p &= \bar{p} + p' \\ T &= \bar{T} + T' \\ \rho &= \bar{\rho} + \rho' \end{aligned} \tag{112}$$

so that

$$\bar{u} = \bar{w} = 0 \tag{113}$$

$$\partial\bar{p}/\partial z = -g\bar{\rho} \tag{114}$$

$$\partial\bar{T}/\partial z = -\gamma \tag{115}$$

where γ is constant and smaller than the dry-adiabatic lapse rate γ_d.

In terms of u, w, T and p, the basic equations are

$$\frac{\partial u}{\partial t} = -u\frac{\partial u}{\partial x} - w\frac{\partial u}{\partial z} - \frac{1}{\bar{\rho}}\frac{\partial p'}{\partial x} \tag{116}$$

$$\frac{\partial w}{\partial t} = -u\frac{\partial w}{\partial x} - w\frac{\partial w}{\partial z} - \frac{1}{\bar{\rho}}\frac{\partial p'}{\partial z} + g\left(\frac{T'}{\bar{T}} - \frac{p'}{\bar{p}}\right) \tag{117}$$

$$\frac{\partial T}{\partial t} = -u\frac{\partial T}{\partial x} - w\left(\frac{\partial T}{\partial z} + \gamma_d\right) + \frac{1}{c_p\bar{\rho}}\left(\frac{\partial p'}{\partial t} + u\frac{\partial p'}{\partial x} + w\frac{\partial p'}{\partial z}\right) \tag{118}$$

$$\frac{\partial(\bar{\rho}u)}{\partial x} + \frac{\partial(\bar{\rho}w)}{\partial z} = 0 \; . \tag{119}$$

Note that ρ' has been eliminated by writing the buoyancy term in (117) in terms of T' and p', and by neglecting local density variations in (119) as has been done in the moist convection model. We now linearize (116)–(119)

by substituting from (112), expanding the resulting terms and assuming that perturbations about the base state are small enough so that all products involving perturbations and/or their derivatives can be neglected. Noting that (116)—(119) are satisfied by the base state (with $T' = 0$ and $p' = 0$ in particular) and that (119) is already linear, we obtain the following equations with the aid of (113) and (115):

$$\frac{\partial u'}{\partial t} = -\frac{1}{\bar{\rho}}\frac{\partial p'}{\partial x} \tag{120}$$

$$\frac{\partial w'}{\partial t} = -\frac{1}{\bar{\rho}}\frac{\partial p'}{\partial z} + g\left(\frac{T'}{\bar{T}} - \frac{p'}{\bar{p}}\right) \tag{121}$$

$$\frac{\partial T'}{\partial t} = -Sw + \frac{1}{c_p\bar{\rho}}\frac{\partial p'}{\partial t} \tag{122}$$

$$\frac{\partial(\bar{\rho}u')}{\partial x} + \frac{\partial(\bar{\rho}w')}{\partial z} = 0 \tag{123}$$

where $S = \gamma_d - \gamma$.

To investigate the effects of including the perturbation pressure p' in the buoyancy term of (121) or in the thermodynamic equation (122), we rewrite these two equations as

$$\frac{\partial w'}{\partial t} = -\frac{1}{\bar{\rho}}\frac{\partial p'}{\partial z} + g\left(\frac{T'}{\bar{T}} - \lambda\frac{p'}{\bar{p}}\right) \tag{124}$$

$$\frac{\partial T'}{\partial t} = -Sw' + \frac{\mu}{c_p\bar{\rho}}\frac{\partial p'}{\partial t} \tag{125}$$

where λ and μ, equal to 1 and 0, respectively, in the moist convection model, have been introduced as tagging parameters. There are four possible cases of interest involving these parameters:

Case 1. $\mu = 0$, $\lambda = 0$ (Neglect p' both in buoyancy and thermodynamics)

Case 2. $\mu = 0$, $\lambda = 1$ (Neglect p' in thermodynamics only)

Case 3. $\mu = 1$, $\lambda = 0$ (Neglect p' in buoyancy only)

Case 4. $\mu = 1$, $\lambda = 1$ (Include p' both in buoyancy and thermodyamics)

Note that case 2 corresponds most closely to the approximations adopted in the moist model.

Equations (120), (123), (124) and (125) are next transformed into a set of linear algebraic equations with constant or nearly constant coefficients in order to obtain a frequency relation for wave motions. Over the depth of the troposphere, the coefficients involving $1/\bar{\rho}$ and $1/\bar{p}$ in the original equations vary too strongly with height to be considered even approximately constant. However, if transformed perturbations u*, w*, p* and T* are defined by

$$\begin{pmatrix} u' \\ w' \\ p' \\ T' \end{pmatrix} = \begin{pmatrix} \bar{\rho}^{\,-1/2} u^* \\ \bar{\rho}^{\,-1/2} w^* \\ \bar{\rho}^{\,1/2} p^* \\ \bar{\rho}^{\,-1/2} T^* \end{pmatrix} \tag{126}$$

and (126) is substituted into these equations, the resulting system

$$\frac{\partial u^*}{\partial t} = \frac{\partial p^*}{\partial x} = 0 \tag{127}$$

$$\frac{\partial w^*}{\partial t} + \frac{\partial p^*}{\partial z} + \frac{(2\lambda-1)g}{2R_d\bar{T}} p^* - \frac{g}{\bar{T}} T^* = 0 \tag{128}$$

$$\frac{\partial T^*}{\partial t} + Sw^* - \frac{\mu}{c_p} \frac{\partial p^*}{\partial t} = 0 \tag{129}$$

$$\frac{\partial u^*}{\partial x} + \frac{\partial w^*}{\partial z} - \frac{g}{2R_d\bar{T}} w^* = 0 \tag{130}$$

has coefficients which are either constant or proportional to $1/\bar{T}$, which varies by only about thirty percent over the depth of the troposphere and can therefore be treated as constant without serious error. The usual analysis is for the isothermal case. In the present context, S is constant (and positive) and generally different in magnitude from what it would be in an isothermal atmosphere. To transform (127)–(130) into a set of linear algebraic equations, we assume wave solutions given by

$$\begin{pmatrix} u^* \\ w^* \\ p^* \\ T^* \end{pmatrix} = \begin{pmatrix} \hat{u} \\ \hat{w} \\ \hat{p} \\ \hat{T} \end{pmatrix} e^{i(kx + mz - \omega t)} \tag{131}$$

where $\hat{u}$, $\hat{w}$, $\hat{p}$ and $\hat{T}$ are complex constants; k is assumed real, as is ω since only oscillations which do not amplify with time would be expected to occur in a stable atmosphere. Strictly speaking, only the real part of the right-hand side of (131) is of interest since the primed variables (and hence the starred variables) must be real, but we are only considering a single wave component in complex Fourier form and a real solution to (127)–(130) can always be found by adding the wave component to its complex conjugate.

Using (131), equations (127)–(130) are transformed into the matrix equation

$$\underset{\sim}{M}\,\underset{\sim}{X} = \underset{\sim}{0} \tag{132}$$

where

$$\underset{\sim}{M} = \begin{pmatrix} -i\omega & 0 & ik & 0 \\ 0 & -i\omega & im + \frac{(2\lambda - 1)g}{2R_d\bar{T}} & -\frac{g}{\bar{T}} \\ ik & im - \frac{g}{2R_d\bar{T}} & 0 & 0 \\ 0 & S & \frac{\mu}{c_p}\, i\omega & -i\omega \end{pmatrix} \tag{133}$$

$$\underset{\sim}{X} = \begin{pmatrix} \hat{u} \\ \hat{w} \\ \hat{p} \\ \hat{T} \end{pmatrix} \qquad\qquad 0 = \begin{pmatrix} 0 \\ 0 \\ 0 \\ 0 \end{pmatrix}$$

For nontrivial solutions to exist, the determinant of M must vanish. By some straightforward but tedious algebra, this condition yields the frequency relation

$$\omega^2 = \frac{gk^2 \frac{S}{\bar{T}}}{m^2 + k^2 + \frac{im(1-\lambda)}{H} + \frac{2\lambda - 1}{4H^2} - \frac{\mu R_d}{2c_p H^2} + \frac{i\mu R_d m}{c_p H}} \tag{134}$$

where

$$H = \frac{R_d \bar{T}}{g} \, . \tag{135}$$

The relation between the temperature $\bar{T}$ and the adiabatic speed of sound c_s

$$c_s^2 = \frac{c_p}{c_v} R_d \bar{T} = \frac{c_p}{c_v} gH \tag{136}$$

is also handy. Since only real values of k and ω are of interest, ω^2 must be nonnegative and m must be chosen so that the denominator in (134) is real. This may be done by allowing m to be complex

$$m = m_R + im_I \tag{137}$$

with m_I such that the imaginary part of the denominator vanishes. It is readily found that

$$m_I = \frac{\lambda - \mu \frac{R_d}{c_p} - 1}{2H} \, . \tag{138}$$

Substitution of (135)–(138) into the frequency relation then yields

$$\omega^2 = \frac{gk^2 \frac{S}{\bar{T}}}{m_R^2 + k^2 + \left(\frac{c_p}{c_v}\right)^2 \frac{g^2}{4c_s^4} \left(\mu \frac{R_d}{c_p} - \lambda\right)^2} \, . \tag{139}$$

Since k is real and $S > 0$, ω^2 is clearly nonnegative. Hence ω is real.

Logarithmically differentiating the definition for θ with respect to z, applying the resulting relationship to the base state and then eliminating $\bar{p}$ by the equation of state and the hydrostatic equation, one obtains

$$\frac{gS}{\bar{T}} = \omega_B^2 \equiv \frac{g}{\bar{\theta}} \frac{\partial \bar{\theta}}{\partial z} \tag{140}$$

where ω_B is the well-known Brunt-Vaisala frequency, the upper limiting frequency for gravity waves. Therefore (139) may be rewritten as follows:

$$\omega^2 = \frac{\omega_B^2 k^2}{m_R^2 + k^2 + \left(\frac{c_p}{c_v}\right)^2 \frac{g^2}{4c_s^4} \left(\mu \frac{R_d}{c_p} - \lambda\right)^2} \; . \tag{141}$$

Taking $c_p/c_v = 7/5$, the frequency relations for each of the four cases follow from (141) by substituting appropriate values of λ and μ. Likewise, taking $R_d/c_p = 2/7$, substitution of (137) and (138) into (131) and use of (126) with the approximate proportionality

$$\bar{\rho} \propto e^{-z/H} \tag{142}$$

yields the height dependencies of $|u'|$, $|w'|$, $|T'|$ and $|p'|$ shown for table 2.

For any values of m_R and k, a comparison of cases 2 and 4 in table 2 shows that neglecting p' in the thermodynamics causes the frequency to be underestimated. However, this error is quite small for gravity waves such as were encountered in the numerical model. Vertical wavelengths in the model are at most twice the depth of the domain, or 28 km, placing a lower limit of 2.2×10^{-4} m^{-2} on m_R. The vertically averaged temperature in the model is close to 260°K. If this value is assumed for $\bar{T}$, and m_R is set equal to the lower limit just mentioned, one finds that even in the worst possible case $(k = 0)$ the difference between ω in cases 2 and 4 is only about two percent.

It is evident from table 2 that the amplitudes of u', w' and T' increase with height in every case. The amplitude of p' decreases with height in cases 2 and 4, is independent of height in case 1 and increases slightly with height in case 3. These differences are significant over a region with a depth of 14 km, which is almost twice the scale height H corresponding to $\bar{T} = 260$°K. Over this depth, the factor by which the amplitude varies from bottom to top is about 100 percent too large if p' is neglected both in the buoyancy and in the thermodynamics, and nearly 200 percent too large if p' is neglected in the buoyancy alone. This factor is about twenty-five percent too small if p' is neglected in the thermodynamics but retained in the buoyancy. It is thus apparent that neglecting pressure perturbations in the thermodynamics alone involves considerably less error than neglecting them in the buoyancy term.

Table 2

Principal Results of Linear Analysis for Stable Gravity Waves without Moisture

Case	Frequency Equation	Height Variation of Amplitude u', w', T'	Height Variation of Amplitude p'
1 ($\mu = 0,\ \lambda = 0$)	$\omega^2 = \dfrac{\omega_B^2 k^2}{m_R^2 + k^2}$	$e^{\frac{z}{H}}$	1
2 ($\mu = 0,\ \lambda = 1$)	$\omega^2 = \dfrac{\omega_B^2 k^2}{m_R^2 + k^2 + .49 g^2/c_s^4}$	$e^{\frac{1}{2}\frac{z}{H}}$	$e^{-\frac{1}{2}\frac{z}{H}}$
3 ($\mu = 1,\ \lambda = 0$)	$\omega^2 = \dfrac{\omega_B^2 k^2}{m_R^2 + k^2 + .04 g^2/c_s^4}$	$e^{\frac{8}{7}\frac{z}{H}}$	$e^{\frac{1}{7}\frac{z}{H}}$
4 ($\mu = 1,\ \lambda = 1$)	$\omega^2 = \dfrac{\omega_B^2 k^2}{m_R^2 + k^2 + .25 g^2/c_s^4}$	$e^{\frac{9}{14}\frac{z}{H}}$	$e^{-\frac{5}{14}\frac{z}{H}}$

Since energetics was outside of the scope of the research, a consideration of the energy integral which may be obtained from the system (127)–(130) under appropriate boundary conditions is not included here. However, it should be briefly noted that much of the motivation for describing the system (and the corresponding system in the moist convection model) as "anelastic" has been motivated by such a study. Ogura and Charney (1962) used this term to describe an analogous system of linearized equations (using θ instead of T), since neglecting $\partial\rho/\partial t$ in the continuity equation was found to remove an elastic energy term from the energy integral. In each of cases 1 through 4, the same may be found to hold for (127)–(130); this might be anticipated from the fact that the frequency relation (141) yields no acoustic waves.

APPENDIX B:

The Static Phase Adjustment

In this appendix, we present the mathematical details of the static phase adjustment described in section 2. Let us denote with the subscript P the provisional values of T, q_v and L obtained from the governing equations or boundary conditions, and let the final values of these variables after the static phase adjustment be denoted with the subscript F. Throughout this appendix, the subscripts i and j will be omitted since the adjustment involves only one grid point at a time.

The static phase adjustment, assumed instantaneous and isobaric, is used under either of two conditions: (a) $q_{vP} < q_{vs}(T_P, \bar{p})$ and $L_P > 0$, i. e., when liquid water is present in unsaturated air, and (b) $q_{vP} > q_{vs}(T_p, \bar{p})$, i. e., when supersaturation occurs. In case (a), the provisional and final temperatures and mixing ratios are related by

$$c_p(T_P - T_F) = L_{vw}[q_v\ (T_F, \bar{p}) - q_{vp}] \tag{143}$$

while in case (b),

$$c_p(T_F - T_P) = L_{vw}[q_{vp} - q_{vs}(T_F, \bar{p})] \tag{144}$$

where

$$T_e = T_P + \frac{L_{vw}}{c_p}[q_{vp} - q_{vs}(T_P, \bar{p})] \ .^{*} \tag{145}$$

Physically, (143) and (144) state that the sensible heat gained (or lost) by the air must balance the latent heat released (or absorbed) through condensation (or evaporation). T_e is the temperature which would result if all of the excess water vapor over saturation were condensed. Actually, as (144) indicates, T_F is lower than T_e ; as condensation takes place and T increases, the saturation mixing ratio also increases, so that exact saturation is reached before all the original excess water vapor can condense. Since local variations of p and ρ are not important to these calculations, $\bar{p}$ and $\bar{\rho}$ have been used in their place.

In case (a), there may be enough liquid water to saturate the air by its evaporation, cooling the air to the wet-bulb temperature T_w which is computed by an iterative technique to be described later in this appendix. Mathematically, if $L_P > \bar{\rho}[q_{vs}(T_w, \bar{p}) - q_{vP}]$ then

---

[*] This temperature would result if all of the excess water vapor over saturation in case (b) were condensed.

$$\begin{aligned} T_F &= T_w, \quad q_{v_F} = q_{vs}(T_w, \bar{p}), \\ L_F &= L_P - \bar{\rho}[q_{v_F} - q_{v_P}] \;. \end{aligned} \tag{146}$$

Alternatively, all the liquid water may be consumed before saturation can be reached. If $L_P < \bar{\rho}[q_{vs}(T_w, \bar{p}) - q_{v_P}]$, then

$$\begin{aligned} T_F &= T_P - \frac{L_{vw}}{c_p \bar{\rho}} L_P \, , \quad q_{v_F} = q_{v_P} + \frac{L_P}{\bar{\rho}} \, , \\ L_F &= 0 \; . \end{aligned} \tag{147}$$

In case (a), let T_d denote the dew point prior to the adjustment and defined by

$$e_s(T_d) = e_s(T_P) \frac{q_{v_P}}{q_{v_s}(T_P, \bar{p})} \; . \tag{148}$$

At any temperature T, the saturation vapor pressure $e_s(T)$ is taken over liquid water since the ice phase is not explicitly included in the model, and is computed from the Clausius-Clapeyron equation

$$\frac{de_s}{dT} = \frac{L_{vw}}{R_v} \frac{e_s}{T^2} \tag{149}$$

as given by Haltiner and Martin (1957) and neglecting any variation of the latent heat of vaporization L_{vw}. Then (149) is readily integrated, yielding

$$e_s(T) = e_0 \exp\left[\frac{L_{vw}}{R_v}\left(\frac{1}{T_0} - \frac{1}{T}\right)\right] \tag{150}$$

where $T_0 = 0°C\ (273°K)$ and $e_0 = e_s(T_0) = 6.1078$ mb. From (148) and (150), T_d is given explicitly by

$$T_d = T_0 \left\{ 1 - \frac{R_v T_0}{L_{vw}} \ln \frac{[q_{v_P} / q_{vs}(T_P, \bar{p})] e_s(T_P)}{e_0} \right\} \; . \tag{151}$$

The crucial facts to note are that

$$T_d < T_w < T_P \tag{152}$$

and that the quantity

$$c_p(T_P-T) - L_{vw}[q_{vs}(T,\bar{p}) - q_{v_P}]$$

decreases monotonically as T increases from T_d to T_P. This assures the convergence of the following method which successively approximates T_W by repeated bisection of the interval $[T_d, T_P]$. Letting T_m and q_{v_m} denote the m^th^ guesses for T and q_v,

$$T_1 = (T_P + T_d)/2, \quad q_{v_1} = q_{v_s}(T_1, \bar{p}),$$

$$T_m = \begin{cases} T_{m-1} + (T_P-T_d)/2^m & \text{if } c_p(T_P-T_{m-1}) > L_{vw}(q_{v_{m-1}} - q_{v_P}) \\ T_{m-1} - (T_P-T_d)/2^m & \text{if } c_p(T_P-T_{m-1}) < L_{vw}(q_{v_{m-1}} - q_{v_P}) \end{cases} \quad (153)$$

where

$$q_{v_{m-1}} = q_{v_s}(T_{m-1}, \bar{p}) \cdot \quad (154)$$

Note that $|T_m - T_{m-1}| = |T_{m-1} - T_{m-2}|/2$, so that the method must converge since the difference between T_m and T_F cannot exceed $(T_P-T_d)/2^m$ which approaches zero as m increases.

In case (b), the key facts are that

$$T_P < T_F < T_e \quad (155)$$

and that the quantity

$$c_p(T-T_P) - L_{vw}[q_{v_P} - q_{v_s}(T,\bar{p})]$$

increases monotonically as T increase from T_P to T_e. Much as in case (a), T_F is successively approximated by repeated bisection of the interval $[T_P, T_e]$ and must converge. Letting T_m and q_{v_m} have the same meaning as in case (a),

$$T_1 = (T_e + T_P)/2, \qquad q_{v_1} = q_{vs}(T_1, \bar{p}),$$

$$T_m = \left[\begin{array}{ll} T_{m-1} - (T_e - T_P)/2^m & \text{if } c_p(T_{m-1} - T_P) > L_{vw}(q_{v_P} - q_{v_{m-1}}) \\ T_{m-1} + (T_e - T_P)/2^m & \text{if } c_p(T_{m-1} - T_P) < L_{vw}(q_{v_P} - q_{v_{m-1}}) \end{array}\right. \tag{156}$$

where $q_{v_{m-1}}$ is defined as in equation (154).

In the computer program, the iterations have been terminated as soon as $(T_P - T_d)/2^m$ or $(T_e - T_P)/2^m$ becomes smaller than 5×10^{-3} °C, since it was felt that temperature errors of this magnitude would be insignificant. Even if $(T_P - T_d)$ or $(T_e - T_P)$ is as large as 2°C, which is unlikely, only nine iterations should be necessary. A significant degree of adjustment should be needed only at points on or near the cloud edge, comprising only a small fraction of the grid points.

APPENDIX C:

Computation of Pressure and Density for Initial Base State

The pressure and density for the initial base state are computed by numerical integration from the bottom to the top of the grid, taking the initial temperatures $\bar{T}_j$ $(1 \leq j \leq N)$ as known and prescribing the surface pressure $\bar{p}_1$. Each interval between successive grid levels is treated as though the corresponding layer had a constant virtual temperature equal to the arithmetic mean of the values at the ends of the interval. For reasons which will become apparent shortly, the pressure and virtual temperature at all levels above the surface are computed in two steps—first to obtain preliminary values and second to obtain improved estimates.

At a given temperature T and pressure p, the saturation vapor pressure $e_s(T)$ and the saturation mixing ratio $q_{vs}(T, p)$ are calculated as follows:

$$e_s(T) = e_0 \exp\left[\frac{L_{vw}}{R_v}\left(\frac{1}{T_0} - \frac{1}{T}\right)\right] \tag{157}$$

$$q_{vs}(T, p) = \frac{R_d}{R_v} \frac{e_s(T)}{p - e_s(T)} \tag{158}$$

taking $e_s(T)$ over liquid water regardless of T and neglecting any variation of the heat of vaporization L_{vw}. This is consistent with the omission of the ice phase from the model; Hess (1959) has pointed out that the variation of L_{vw} is less than 0.1 percent per °C temperature change, implying that its variation even over a 100°C range is somewhat smaller in magnitude than the omitted latent heat of fusion. In the following treatment overbars over quantities refer to the initial base state; in particular, $\bar{h}_j$ denotes the initial base value of the relative humidity at the j<u>th</u> level $(1 \leq j \leq N)$ expressed as a number between 0 and 1 and assumed known.

With the surface pressure $\bar{p}_1$ prescribed and assumed equal to 1000 mb, the surface virtual temperature $(\bar{T}_v)_1$ is given by

$$(\bar{T}_v)_1 = \bar{T}_1[1 + (\frac{R_v}{R_d} - 1)\bar{h}_1 q_{vs}(\bar{T}_1, \bar{p}_1)] \; . \tag{159}$$

For all higher levels $(2 \leq j \leq N)$, preliminary values p_j^* and $(T_v^*)_j$ for the pressure and virtual temperature are computed. We have

$$p_j^* = \bar{p}_{j-1} \exp(\sigma_j^*) \tag{160}$$

where

$$\sigma_j^* = -2g\Delta z \{R_d[(\bar{T}_v)_{j-1} + \bar{T}_j]\}^{-1} \; . \tag{161}$$

Next,

$$(T_v^*)_j = \bar{T}_j[1 + (\frac{R_v}{R_d} - 1)\bar{h}_j q_{vs}(\bar{T}_j, p_j^*)] \; . \tag{162}$$

In equation (161), note that $\bar{T}_j$ appears rather than $(\bar{T}_v)_j$. This is because $(\bar{T}_v)_j$ cannot be computed unless $q_{vs}(\bar{T}_j, \bar{p}_j)$, and by necessity $\bar{p}_j$ itself, is known. But to know $\bar{p}_j$ once $\bar{p}_{j-1}$ is known, one must know both $(\bar{T}_v)_{j-1}$ and $(\bar{T}_v)_j$. That is, the relationship between $(\bar{T}_v)_j$ and $\bar{p}_j$ is implicit. Accordingly, an improved approximation p_j^{**} for $\bar{p}_j$ is obtained by using $(\bar{T}_v)_{j-1}$ with $(T_v^*)_j$ rather than with $\bar{T}_j$:

$$p_j^{**} = \bar{p}_{j-1} \exp(\sigma_j^{**}) \tag{163}$$

where

$$\sigma_j^{**} = -2g\Delta z\,\{R_d[(\bar{T}_v)_{j-1} + (T_v^{*})_j]\}^{-1} \;. \tag{164}$$

Equations (160)–(164) are used for each value of j from 2 through N in increasing order. Then $\bar{p}_j$ is identified with the second approximation p_j^{**}; unlike the first approximation p_j^{*}, which can take into account only the moisture at the lower endpoint of the $(j-1)$st interval, the second approximation takes into account the moisture at both endpoints. In (162), the error incurred by using $q_{vs}(\bar{T}_j, p_j^{*})$ rather than $q_{vs}(\bar{T}_j, \bar{p}_j)$ is very small since, as is apparent from comparing equations (161) and (163), the quantities σ_j^{*} and σ_j^{**} used for calculating p_j^{*} and p_j^{**} are nearly equal in magnitude. Finally, for $1 \le j \le N$, $(\bar{T}_v)_j$ is identified with the close approximation $(T_v^{**})_j$ given by

$$(T_v^{**})_j = \bar{T}_j[1 + (\frac{R_v}{R_d} - 1)\bar{h}_j\, q_{vs}(\bar{T}_j, p_j^{**})] \tag{165}$$

and, using the equation of state for moist air,

$$\bar{\rho}_j = \bar{p}_j[R_d(\bar{T}_v)_j]^{-1} \;. \tag{166}$$

APPENDIX D:

Liebmann Relaxation

At each time level $m \geq 1$, prior to any grid shift, the elliptic equation $\nabla^2\psi = \hat{\eta}$ is solved numerically by a slightly more general version of the Liebmann relaxation method described by Thompson (1961), who assumed time-independent boundary conditions and equal grid separations Δx and Δz in his treatment.

Let $(\psi_p)^m_{i,j}$ denote the approximation to ψ at the mth time step after p iterations of the Liebmann relaxation process. At all interior points, the initial guess for ψ at the $(n+1)$st time step $(n \geq 0)$ is the final value at the nth time step:

$$(\psi_0)^{n+1}_{i,j} = \psi^n_{i,j}\,, \quad 2 \le i \le M-1, \quad 2 \le j \le N-1 \;. \tag{167}$$

At the boundaries, values of $(\psi_p)^{n+1}$ are not iterated during the relaxation process, but are set equal to the undisturbed values of ψ on the horizontal boundaries and equal to the values of ψ at the preceding time step on the vertical boundaries:

$$
\begin{aligned}
(\psi_p)^{n+1}_{1,j} &= \psi^{n}_{1,j}\ , \quad (\psi_p)^{n+1}_{M,j} = \psi^{n}_{M,j}\ , \quad 2 \le j \le N-1 \\
(\psi_p)^{n+1}_{i,1} &= \bar{\psi}_1\ , \quad (\psi_p)^{n+1}_{i,N} = \bar{\psi}_N\ , \qquad 1 \le i \le M \ .
\end{aligned}
\tag{168}
$$

The (p+1)st iterate $(\psi_{p+1})^{n+1}_{i,j}$ at an interior point is calculated from the pth iterate by the formula

$$(\psi_{p+1})^{n+1}_{i,j} = (\psi_p)^{n+1}_{i,j} + \alpha S (R_p)^{n+1}_{i,j} \tag{169}$$

where α is the optimum overrelaxation coefficient referred to by Thompson and is given by

$$\alpha = \frac{2}{1 + \sin(\cos^{-1} \frac{1}{2} Q)} \tag{170}$$

where

$$Q = \cos\left(\frac{\pi}{N+1}\right) + \cos\left(\frac{\pi}{M+1}\right) \tag{171}$$

For generally unequal Δx and Δz,

$$S = \frac{1}{2} \frac{(\Delta x)^2 (\Delta z)^2}{(\Delta x)^2 + (\Delta z)^2} \tag{172}$$

The residual $(R_p)^{n+1}_{i,j}$ is given by

$$(R_p)^{n+1}_{i,j} = (\nabla^2_c \psi_p)^{n+1}_{i,j} - \eta^{n+1}_{i,j} \tag{173}$$

where

$$(\nabla^2_c \psi_p)^{n+1}_{i,j} = \left(\frac{\delta^2_c \psi_p}{\delta x^2}\right)^{n+1}_{i,j} + \left(\frac{\delta^2_c \psi_p}{\delta z^2}\right)^{n+1}_{i,j} \tag{174}$$

while the quantities $\left(\frac{\delta_c^{\,2}\psi_p}{\delta x^2}\right)^{n+1}_{i,j}$ and $\left(\frac{\delta_c^{\,2}\psi_p}{\delta z^2}\right)^{n+1}_{i,j}$ are finite-difference approximations to $\frac{\partial^2\psi}{\partial x^2}$ and $\frac{\partial^2\psi}{\partial z^2}$ defined separately for $j = 2$ and for $3 \leq j \leq N-1$. This distinction is made for reasons to be indicated following the mathematical formulas for these approximations.

<u>For $j = 2$ only:</u>

$$\left[\begin{aligned} &\left(\frac{\delta_c^{\,2}\psi_p}{\delta x^2}\right)^{n+1}_{2,2} = \left[(\psi_p)^{n+1}_{3,2} + (\psi_p)^{n+1}_{1,2} - 2(\psi_p)^{n+1}_{2,2}\right] \Big/ (\Delta x)^2 \,, \\ &\left(\frac{\delta_c^{\,2}\psi_p}{\delta x^2}\right)^{n+1}_{i,2} = \left[(\psi_p)^{n+1}_{i+1,2} + (\psi_{p+1})^{n+1}_{i-1,2} - 2(\psi_p)^{n+1}_{i,2}\right] \Big/ (\Delta x)^2, \quad 3 \leq i \leq M-1 \end{aligned}\right. \tag{175}$$

$$\left(\frac{\delta_c^{\,2}\psi_p}{\delta z^2}\right)^{n+1}_{i,2} = \left[(\psi_p)^{n+1}_{i,3} + (\psi_p)^{n+1}_{i,1} - 2(\psi_p)^{n+1}_{i,2}\right] \Big/ (\Delta z)^2, \qquad 2 \leq i \leq M-1 \tag{176}$$

<u>For $3 \leq j \leq N-1$:</u>

$$\left[\begin{aligned} &\left(\frac{\delta_c^{\,2}\psi_p}{\delta x^2}\right)^{n+1}_{2,j} = \left[(\psi_p)^{n+1}_{3,j} + (\psi_p)^{n+1}_{1,j} - 2(\psi_p)^{n+1}_{2,j}\right] \Big/ (\Delta x)^2, \\ &\left(\frac{\delta_c^{\,2}\psi_p}{\delta x^2}\right)^{n+1}_{i,j} = \left[(\psi_p)^{n+1}_{2,j+1} + (\psi_{p+1})^{n+1}_{2,j-1} - 2(\psi_p)^{n+1}_{2,j}\right] \Big/ (\Delta x)^2, \quad 3 \leq i \leq M-1 \end{aligned}\right. \tag{177}$$

$$\left(\frac{\delta_c^{\,2}\psi_p}{\delta z^2}\right)^{n+1}_{i,j} = \left[(\psi_p)^{n+1}_{i,j+1} + (\psi_{p+1})^{n+1}_{i,j-1} - 2(\psi_p)^{n+1}_{i,j}\right] \Big/ (\Delta x)^2, \tag{178}$$

$$2 \leq i \leq M-1 \,.$$

Note that most values of $\left(\frac{\delta_c^2 \psi_p}{\delta x^2}\right)_{i,j}^{n+1}$ and $\left(\frac{\delta_c^2 \psi_p}{\delta z^2}\right)_{i,j}^{n+1}$ expressed in terms of both ψ_p and ψ_{p+1} in asymmetric form. This is because the interior of the grid is swept through from left to right (increasing i) in successive rows (constant j) from immediately above the lower boundary to immediately above the lower boundary to immediately below the upper boundary, with only one value of ψ being stored at each grid point throughout an iteration. This is the so-called Liebmann process.

The relaxation process is terminated after the smallest number P of cycles such that

$$\max_{\substack{2 \leq i \leq M-1 \\ 2 \leq j \leq N-1}} \left| (R_P)_{i,j}^{n+1} \right| < \epsilon \tag{179}$$

where ϵ is a suitably small tolerance. In the model, $\epsilon = 10^{-2}$ gm m^{-3} sec^{-1} has been chosen. No noticeable irregularities have developed in the final ψ-field at any time step when ϵ has been assigned this value, which is 0.1–0.3 percent of the typical magnitudes of $\hat{\eta}$ encountered in the model. At each time step, about thirty iterations have been sufficient to satisfy the convergence requirement (179) with $\epsilon = 10^{-2}$ gm m^{-3} sec^{-1}. The computer time required for relaxation on the final 55-by-21 grid has been roughly 1.5 sec per time step on the Univac 1108 computer and 0.8–1.0 sec per time step on the CDC 6600 computer, involving roughly one-third the total computing time in any one run. The right-hand boundary conditions on ψ described in section 5 are not applied until after the relaxation has been completed, since ψ at the outflow boundary would not be expected to change enough between two consecutive time steps to warrant revising the outflow values of ψ with each iteration of the process.

APPENDIX E:

Equations for Initial Perturbations

In this appendix we present the mathematical equations for the initial stream function ψ, temperature T, relative humidity h and liquid water content L within the rectangular perturbed region described in section 4 and shown in figure 6. In the 55-by-21 computational grid domain, the perturbed region along with its boundaries includes all grid points (x_i, z_j) such that $23 \leq i \leq 39$ and $1 \leq j \leq 7$. In connection with the equations to be listed, we define the following symbols, indicating particular values in the model wherever appropriate:

x_c = x-coordinate of the center of the perturbed region (with the origin at the lower left corner of the domain), 96 km

R_1 = half-width of the updraft, 6.4 km

R_2 = half-width of the perturbed region, 25.6 km

H = vertical extent of the perturbed region, 4.2 km

h = relative humidity

Q'_{max} = maximum perturbation in the variable Q throughout a region

$\bar{Q}$ = undisturbed values for the variable Q

In the model, we have $\psi'_{max} = 6 \times 10^6$ gm m^{-1} sec^{-1}, $T'_{max} = 1°C$, $h'_{max} = .03$ (expressed as a pure number rather than a percentage) and $L'_{max} = 1$ gm m^{-3}. Note that $\bar{L} = 0$ since no cloud or precipitation is included in the base state, and that the maximum relative humidity perturbation referred to above applies to the subsiding part of the perturbed region since the air is assumed saturated ($h = 1$) where air is initially ascending. The undisturbed profiles of horizontal wind, temperature and relative humidity are plotted in section 4, and the base state for the stream function is obtained from that for the horizontal wind by numerical integration as explained in section 7.

The equations are the following:

$$\psi = \bar{\psi} - 2R_1\psi'_{max}F(x - x_c, R_2, R_1) \sin\frac{\pi z}{H} \qquad (180)$$

$$T = \bar{T} = R_1^2 T'_{max} |G(x - x_c, R_2, R_1)| \sin\frac{\pi z}{H}$$

$$\text{for } 0 \leq z \leq H, \quad |x - x_c| \leq R_2 \qquad (181)$$

$$h = \begin{cases} 1 \quad \text{for } 0 < z < H, \; |x - x_c| < R_1 \\ \bar{h} + 8R_1^2 h'_{max} \; G(x - x_c, R_2, R_1) \sin \frac{\pi z}{H} \\ \qquad \text{for } 0 < z < H, \; R_1 < |x - x_c| < R_2 \end{cases} \tag{182}$$

$$L = \begin{cases} L'_{max} \cos \pi \frac{x-x_c}{2R_1} \sin \frac{\pi z}{H} \quad \text{for } 0 < z < H, \; |x - x_c| < R_1 \\ 0 \quad \text{for } 0 < z < H, \; R_1 < |x - x_c| < R_2 \, , \end{cases} \tag{183}$$

where the functions F and G are given for arbitrary arguments A, B and C by

$$F(A, B, C) = A(A^2 + C^2)^{-1} \cos \frac{\pi A}{B} \tag{184}$$

$$G(A, B, C) = (C^2 - A^2)(C^2 + A^2)^{-2} \cos \frac{\pi A}{B} \, . \tag{185}$$

Note that the factor $(C^2 - A^2)(C^2 + A^2)^{-2}$ in (185) is the partial derivative with respect to A of the factor $A(A^2 + C^2)^{-1}$ in (184). The functions F and G have been thus related in order to make the initial in-cloud temperature deviations at each level roughly proportional to the upward velocity. In (180)–(182), the common "modulating factor" $\cos \pi(x - x_c)/R_2$, which vanishes at the lateral boundaries of the perturbed region, is present in order to confine the initial disturbance horizontally and thereby have all horizontal gradients well removed from the lateral boundaries of the full domain. In equation (181), the absolute value sign is used since both the ascent in the cloud and the descent in its surroundings should warm the air.

Note that no initial pressure perturbation is prescribed. This is not wholly consistent, since by the diagnostic elliptic equation (19) the presence of liquid water or a disturbance in the wind and temperature field implies a disturbance in the pressure. Therefore, pressure cannot be specified independently of the other variables. However, due to limitations on computing time, this equation was not solved. Pressure perturbations at later times were estimated by calculating the horizontal pressure gradient from equation (20) and then integrating numerically by a method explained in appendix G. In this way, the contribution of pressure deviations to the buoyancy is neglected in the vorticity equation during the first time step only, and is taken into account at all later times. The horizontal and vertical pressure gradient forces, although cross-differentiated out of the vorticity equation, operate implicitly at all times.

APPENDIX F:

Air Trajectory Calculations

The air parcel trajectories discussed for the prototype experiment were obtained by forward integration in time, estimating velocity components by double linear interpolation within appropriate grid boxes, as described below.

Let X' and Z' denote the coordinates of a given parcel at the end of the nth time increment, with the origin taken at the lower left corner of the grid (i = j = 1). It is assumed that any needed shift of the grid has been performed. The lower left corner of the grid box containing the parcel has indices i' and j', where

$$i' = 1 + [X'/\Delta x]$$

$$j' = 1 + [Z'/\Delta z] \tag{186}$$

and [Q] denotes the greatest integer not exceeding (but possibly equal to) an arbitrary quantity Q. The parcel velocity components U' and W' at the nth time level are estimated by the following double linear interpolation formula using the corner points $(x_{i'}, z_{j'})$, $(x_{i'+1}, z_{j'})$, $(x_{i'}, z_{j'+1})$ and $(x_{i'+1}, z_{j'+1})$ of the grid box:

$$U' = a_1' + a_2'(X'-x_{i'}) + a_3'(Z'-z_{j'}) + a_4'(X'-x_{i'})(Z'-z_{j'}) \tag{187}$$

$$W' = b_1' + b_2'(X'-x_{i'}) + b_3'(Z'-z_{j'}) + b_4'(X'-x_{i'})(Z'-z_{j}) \tag{188}$$

where

$$a_1' = u^n_{i',j'} \tag{189a}$$

$$a_2' = (u^n_{i'+1,j'} - u^n_{i',j'})/\Delta x \tag{189b}$$

$$a_3' = (u^n_{i',j'+1} - u^n_{i',j'})/\Delta z \tag{189c}$$

$$a_4' = (u^n_{i'+1,j'+1} - u^n_{i'+1,j'} - u^n_{i',j'+1} + u^n_{i',j'})/(\Delta x \Delta z) \tag{189d}$$

and the coefficients b_1' through b_4' are defined analogously with u replaced by w.

Preliminary estimates of the parcel coordinates at the (n+1)st time level are then given by

$$X'' = X' + U'\Delta_{n+1}t \tag{190a}$$

$$Z'' = Z' + W'\Delta_{n+1}t \tag{190b}$$

where $\Delta_{n+1}t$ is the time increment between the nth and the (n+1)st time levels. If any of the four conditions $X'' < 0$, $X'' > (M-1)\Delta x$, $Z'' < 0$ or $Z'' > (N-1)\Delta z$ hold, then the parcel has been carried outside the grid domain and is no longer tracked. Otherwise, the preliminary location of the parcel at the (n+1)st time level is now in the grid box whose lower left-hand corner has indices i'' and j'' given by

$$i'' = 1 + [X''/\Delta x] \tag{191a}$$

$$j'' = 1 + [Z''/\Delta z] \quad . \tag{191b}$$

Parcel velocity components U'' and W'' at the (n+1)st time level are estimated by the same double interpolation scheme used for obtaining U' and W'.

Finally, a revised estimate (X''', Z''') of the parcel location at the (n+1)st time level is made by using the average velocity components during the (n+1)st time increment instead of the velocity components at the nth time level. Mathematically,

$$X''' = X' + (U' + U'')(\Delta_{n+1}t)/2 \tag{192a}$$

$$Z''' = Z' + (W' + W'')(\Delta_{n+1}t)/2 \quad . \tag{192b}$$

If the grid is shifted at the (n+1)st time level, then X''' is decreased by Δx while Z''' is unchanged. If the parcel is removed from the grid as a result of the shift (in case X''' as calculated from equation (192a) is less than Δx), tracking is then discontinued. Otherwise, X''' and Z''' play the same role as did X' and Z' at the end of the nth time increment, and the parcel is then followed through the (n+2)nd time increment.

APPENDIX G:

Estimation of Perturbation Pressure

As explained in section 2, the use of a vorticity equation made it possible to incorporate the effects of pressure perturbations upon the gravitational buoyancy without needing to know p' itself, but only $\partial p'/\partial x$. This is fortunate, since the proper determination of p' requires the inversion of the elliptic equation (19), a process that would have required considerable additional computing time. However, it was desired to reconstruct at least approximately the disturbance pressure field by some explicit (and therefore much shorter) method for two main reasons: to determine to what extent the model reproduced such frequently observed pressure disturbances as the thunderstorm high, and to obtain some insight into the possible importance of vertical gradients of disturbed pressure to the dynamics of the convection.

Note that for any one value of z and any two values x_1 and x_2 of x,

$$p'(x_2, z) = p'(x_1, z) + \int_{(x_1, z)}^{(x_2, z)} \frac{\partial p'}{\partial x}(x, z)dx \ . \tag{193}$$

In finite-difference form, for $2 \leq i \leq M$ and $2 \leq j \leq N-1$, identifying (x_1, z) with a left-hand (inflow) boundary point

$$p'^{\,n}_{i,j} = p'^{\,n}_{1,j} + \sum_{I=1}^{i-1} \left[\left(\frac{\delta p'}{\delta x}\right)^n_{I,j} + \left(\frac{\delta p'}{\delta x}\right)^n_{I+1,j}\right]\frac{\Delta x}{2} \tag{194}$$

where $\delta p'/\delta x$ denotes a suitable finite-difference expression for $\partial p'/\partial x$ at the indicated location and time. Initially $(n = 0)$, p' was assumed equal to zero everywhere; this assumption was justified in section 3. In this appendix, p' is identified with the departures of p from the initial undisturbed values. This should be contrasted with the meaning of p' in the vertical equation of motion (2), in which it denotes departures of p from horizontal averages at the time of evaluation.

For $n \geq 1$, $(\delta p'/\delta x)^n_{i,j}$ was computed by equation (70), provided $2 \leq i \leq M-1$. If $p'_{1,j}$, $(\delta p'/\delta x)^n_{1,j}$ and $(\delta p'/\delta x)^n_{M,j}$ are somehow given, the last equation can then be applied to calculate p' explicitly everywhere except at the lower and upper boundaries ($j = 1$ and $j = N$). The treatment of p' along these boundaries will be indicated briefly following the description of the lateral boundary conditions.

It must be emphasized that lateral boundary conditions on p' and $\partial p'/\partial x$ were not deemed as critical as those on the other variables. Values of p' thereby estimated by equation (194) were used strictly for diagnostic purposes and were not used in integrating the governing equations themselves. (In particular, terms involving p' in the thermodynamic equation were neglected as explained in section 2.) Nevertheless, since p' across a grid row is found by integration starting at the left boundary, any error in $p'^{n}_{1,j}$ is transmitted simultaneously across the entire row. This is in strong contrast to possible errors arising from boundary conditions on the other variables; even when unreasonably large horizontal gradients developed near the inflow boundary in the disappointing trial run with all inflow variables kept undisturbed, all fields more than a few grid points in from the inflow boundary were not seriously affected.

The treatment of p' and $\partial p'/\partial x$ at inflow points was the same as for the other variables at these points (see section 5); in particular, $p'^{n}_{1,j}$ and $(\delta p'/\delta x)^{n}_{1,j}$ were maintained at zero prior to the first translation of the domain. At outflow points, it was assumed that $(\delta p'/\delta x)^{n}_{M,j} = (\delta p'/\delta x)^{n}_{M-1,j}$. Note that values were not assigned to $p'_{M,j}$ which was instead calculated from equation (194) with $i = M$.

Values of p' were extrapolated to the upper and lower boundaries by straightforward finite-difference analogues of the equation

$$\frac{\partial p'}{\partial z} = \bar{\rho} G \tag{195}$$

where

$$G = g\left(\frac{T'_v}{\bar{T}_v} - \frac{p'}{\bar{p}} - \frac{L}{\bar{\rho}}\right) + F_z \,. \tag{196}$$

Equation (195) is merely the vertical equation of motion with $w = 0$ (which also implies $\partial w/\partial x = 0$ since the boundaries are flat). In finite-difference form,

$$p'^{n}_{i,1} = p'^{n}_{i,2} - \bar{\rho}_2 G^{n}_{i,2} \tag{197}$$

$$p'_{i,N} = p'^{n}_{i,N-1} - \bar{\rho}_{N-1} G^{n}_{i,N-1} \,. \tag{198}$$

This technique gave smooth extrapolations of p' in all cases, even though T'_v and p' as they appear in equation (196) should really denote departures from current horizontal averages of T_V and p since (195) and (196) are derived from the vertical equation of motion.

Values of p' obtained by this method were produced only as long as no value at the left boundary exceeded 0.5 mb in magnitude. This was seven to ten percent as large as the horizontal variation in p' at low levels (where horizontal variations in p' were largest). This restriction was made because in some trial runs using the 55-by-21 grid, p' became as much as 10 mb too high near the surface and 5 mb too low around 10 km. Since the horizontal gradients of p' computed from equation (70) remained reasonable even then, these large errors were entirely due to unrealistic values of p' which developed at the left boundary.

In all comparative runs, the inflow values of $|p'|$ remained smaller than 0.5 mb for at least the first fifty minutes simulated. Therefore, despite its gross inaccuracies at later times, the short method described in this appendix was sufficiently successful to yield reasonable patterns of p' through the early mature stages of the model storms.

ACKNOWLEDGMENTS

I am indebted to Professor John A. Young for his valuable and constructive guidance during the writing of this paper and during the development of the numerical model described therein. Special thanks are also extended to Professors David D. Houghton, Heinz H. Lettau and Frank S. Sechrist.

The numerical computations were performed on the CDC 6600 at the National Center for Atmospheric Research (NCAR) and on the Univac 1108 at the University of Wisconsin Computing Center (UWCC). I would like to thank Daniel Anderson at NCAR, and Peter Guetter at UWCC, for their aid in programming.

The research was supported by NOAA Grant E-230-68-G, with partial funding by NSF Grant GA 30676.

REFERENCES

Ackerman, B., 1967: "The Nature of the Meteorological Fluctuations in Clouds," J. Appl. Met., 6, 61-71.

Arnason, G., R. S. Greenfield and E. A. Newburg, 1968: "A Numerical Experiment in Dry and Moist Convection Including the Rain Stage," J. Atmos. Sci., 25, 404-415.

Asai, T., 1964: "Cumulus Convection in the Atmosphere with Vertical Wind Shear," J. Met. Soc. Japan, 42, 245-259.

Barnes, S. L., 1970: "Some Aspects of a Severe Right-Moving Thunderstorm Deduced from Mesonetwork Rawinsonde Observations," J. Atmos. Sci., 27, 634-648.

Beebe, R. G., and F. C. Bates, 1955: "A Mechanism for Assisting in the Release of Convective Instability," Monthly Wea. Review, 83, 1-10.

Bjerknes, J., 1938: "Saturated-Adiabatic Descent of Air through Dry-Adiabatically Descending Environment," Quart. J. Roy. Met. Soc., 64, 47-69.

Browning, K. A., 1964: "Airflow and Precipitation Trajectories within Severe Local Storms which Travel to the Right of the Winds," J. Atmos. Sci., 21, 634-639.

__________, and R. J. Donaldson, 1963: "Airflow and Structure of a Tornadic Storm," J. Atmos. Sci., 20, 533-545.

__________, and F. H. Ludlam, 1962: "Airflow in Convective Storms," Quart. J. Roy. Met. Soc., 88, 117-135.

Brunk, I. W., 1949: "The Pressure Pulsation of 11 April 1944," J. Met., 6, 181-187.

Byers, H. R., and L. T. Battan, 1949: "Some Effects of Vertical Wind Shear on Thunderstorm Structure," Bull. Am. Met. Soc., 30, 168-175.

__________, and R. R. Braham, Jr., 1949: The Thunderstorm, U. S. Govern-Printing Office, Washington, D. C.

Crowley, W. P., 1968: "Numerical Advection Experiments," Monthly Wea. Review, 96, 1-11.

Das, P., 1964: "Role of Condensed Water in the Life Cycle of a Convective Cloud," J. Atmos. Sci., 21, 404-418.

Dennis, A. S., C. A. Schock and A. Koscielski, 1970: "Characteristics of Hailstorms of Western South Dakota," J. Appl. Met., 9, 127-135.

Fankhauser, J. C., 1971: "Thunderstorm-Environment Interactions Determined from Aircraft and Radar Observations," Monthly Wea. Review, 99, 171-192.

Fawbush, E. J., and R. C. Miller, 1953: "A Method for Forecasting Hailstone Size at the Earth's Surface," Bull. Am. Met. Soc., 34, 235-244.

Fujita, T., 1955: "Results of Detailed Synoptic Studies of Squall Lines," Tellus, 7, 405-436.

___________, 1949: "Precipitation and Cold Air Production in Mesoscale Thunderstorm Systems," J. Met., 16, 454-466.

Goldman, J. L., 1968: "The High Speed Updraft—The Key to the Severe Thunderstorm," J. Atmos. Sci., 25, 222-248.

Haltiner, G. J., and F. L. Martin, 1957: Dynamical and Physical Meteorology, McGraw-Hill Book Co., New York.

Hess, S. L., 1959: Introduction to Theoretical Meteorology, Holt, Rinehart, and Winston, New York.

Hirt, C. W., 1968: "Heuristic Stability Theory for Finite-Difference Equations," J. Comp. Phys., 2, 339-355.

Hitschfeld, W., 1960: "The Motion and Erosion of Convective Storms in Severe Vertical Wind Shear," J. Met., 17, 270-282.

Houghton, H. G., and H. E. Cramer, 1951: "A Theory of Entrainment in Convective Currents," J. Met., 8, 95-102.

Huschke, R. E., ed., 1959: Glossary of Meteorology, American Meteorological Society, Boston, Mass.

Johnson, D. R., and F. S. Sechrist, 1970: "Dynamic Destabilization and Squall Line Formation" (unpublished manuscript).

Kessler, E., 1969: "On the Distribution and Continuity of Water Substance in Atmospheric Circulations," Met. Monographs 10, No. 32.

Lettau, H. H., 1967: "New Hypothesis for the Relationship between Eddy and Mean States," Phys. Fluids Supplement, S79-S83.

Lilly, D. K., 1962: "On the Numerical Simulation of Buoyant Convection," Tellus, 14, 148-172.

List, R., and E. P. Lozowski, 1970: "Pressure Perturbations and Buoyancy in Convective Clouds," J. Atmos. Sci., 27, 168-170.

Liu, J. Y., and H. D. Orville, 1968: "Numerical Modeling of Precipitation Effects on a Cumulus Cloud," Report 68-9, Institute of Atmospheric Sciences, South Dakota School of Mines and Technology, Rapid City, S. D.

Ludlam, F. H., 1963: "Severe Local Storms—A Review," Met. Monographs, 5, No. 27, 1-30.

Malkus, J. S., and G. Witt, 1959: "The Evolution of a Convective Element: A Numerical Calculation," The Atmosphere and the Sea in Motion (Rossby Memorial Volume), Rockefeller Institute Press, New York.

Marshall, J. S., and W. M. Palmer, 1948: "The Distribution of Raindrops with Size," J. Met., 5, 165-166.

Miller, R. C., 1959: "Tornado-Producing Synoptic Patterns," Bull. Am. Met. Soc., 40, 465-472.

Molenkamp, C. R., 1968: "Accuracy of Finite-Difference Methods Applied to the Advection Equation," J. Appl. Met., 7, 160-167.

Murray, F. W., 1970: "Numerical Models of a Tropical Cumulus Cloud with Bilateral and Axial Symmetry," Monthly Wea. Review, 98, 14-28.

__________, and C. E. Anderson, 1965: "Numerical Simulation of Cumulus Towers," Douglas Report SM-49230, Douglas Missiles and Space Systems Division, Santa Monica, Cal.

Musil, D. J., 1970: "Computer Modeling of Hailstone Growth in Feeder Clouds," J. Atmos. Sci., 27, 474-482.

Newton, C. W., 1950: "Structure and Mechanism of the Prefrontal Squall Line," J. Met., 7, 210-222.

__________, and H. R. Newton, 1959: "Dynamical Interactions between Large Convective Clouds and Environment with Vertical Shear," J. Met., 16, 483-496.

__________, 1967: "Severe Convective Storms," Adv. in Geophys., 12, 257-308.

Nitta, T., 1962: "The Outflow Boundary Condition in Numerical Time Integration of Advective Equations," J. Met. Soc. Japan, 40, 13-24.

Ogura, Y., 1962: "Convection of Isolated Masses of a Buoyant Fluid: A Numerical Calculation," J. Atmos. Sci., 19, 492-502.

__________, 1963: "The Evolution of a Moist Convective Element in a Shallow, Conditionally Unstable Atmosphere: A Numerical Calculation," J. Atmos. Sci., 20, 407-424.

__________, and J. G. Charney, 1962: "A Numerical Model of Thermal Convection in the Atmosphere," International Symposium on Numerical Weather Prediction, Proc. Tokyo, Japan, Nov. 1960, 431-451.

__________, and N. A. Phillips, 1962: "Scale Analysis of Deep and Shallow Convection in the Atmosphere," J. Atmos. Sci., 19, 173-179.

Orville, H. D., 1964: "On Mountain Upslope Winds," J. Atmos. Sci., 21, 622-633.

__________, 1968: "Ambient Wind Effects on the Initiation and Development of Cumulus Clouds over Mountains," J. Atmos. Sci., 25, 385-403.

__________, and L. J. Sloan, 1970: "A Numerical Simulation of the Life History of a Rainstorm," J. Atmos. Sci., 27, 1148-1159.

Petterssen, S., 1956: "Weather Analysis and Forecasting," 2nd ed., Vol. II: Weather and Weather Systems, McGraw-Hill Book Co., New York.

Prandtl, L., 1925: "Bericht über Untersuchungen zur ausgebildeten Turbulenz," Zeitschr. angew. Math. Mech., 5, 136-139.

Rhyne, R. H., and R. Steiner, 1964: "Power Spectral Measurement of Atmospheric Turbulence in Severe Storms and Cumulus Clouds," NASA TN D-2469, National Aeronautics and Space Administration, Washington, D. C.

Riehl, H., 1954: Tropical Meteorology, McGraw-Hill Book Co., New York.

_______, and J. S. Malkus, 1958: "On the Heat Balance of the Equatorial Trough," Geophysica, 6, 503-537.

Roache, P. J., and T. J. Mueller, 1968: "Numerical Solutions of Compressible and Incompressible Laminar Separated Flows," Paper No. 68-741, AIAA.

Sasaki, Y., 1959: "A Numerical Experiment of Squall-Line Formation," J. Met., 16, 347-353.

Scorer, R. S., and F. H. Ludlam, 1953: "Bubble Theory of Penetrative Convection," Quart. J. Roy. Met. Soc., 79, 94-103.

Squires, P., and J. S. Turner, 1962: "An Entraining Jet Model for Cumulonimbus Updraughts," Tellus, 14, 422-434.

Srivastava, R. C., 1967: "A Study of the Effects of Precipitation on Cumulus Dynamics," J. Atmos. Sci., 24, 36-45.

Stommel, H., 1947: "Entrainment of Air into a Cumulus Cloud," J. Met., 4, 91-94.

Takeda, T., 1965: "The Downdraft in Convective Shower-Cloud Under the Vertical Wind Shear and its Significance for the Maintenance of Convective System," J. Met. Soc. Japan, 43, 302-309.

_______, 1966a: "The Downdraft in the Convective Cloud and Raindrops: A Numerical Computation," J. Met. Soc. Japan, 44, 1-11.

_______, 1966b: "Effects of the Prevailing Wind with Vertical Shear on the Convective Cloud Accompanied with Heavy Rainfall," J. Met. Soc. Japan, 44, 129-143.

_______, 1971: "Numerical Simulation of a Precipitating Convective Cloud: The Formation of a 'Long-Lasting' Cloud," J. Atmos. Sci., 28, 350-376.

Tepper, M., 1950: "A Proposed Mechanism of Squall Lines: The Pressure Jump Line," J. Met., 7, 21-29.

Thompson, P. D., 1961: Numerical Weather Analysis and Prediction, Macmillan Publishing Co., New York.

Warner, J., 1970: "The Microstructure of Cumulus Cloud. Part III: The Nature of the Updraft," J. Atmos. Sci., 27, 682-688.

Weinstein, A. I., 1970: "A Numerical Model of Cumulus Dynamics and Microphysics," J. Atmos. Sci., 27, 246-255.

Zipser, E. J., 1969: "The Role of Organized Unsaturated Convective Downdrafts in the Structure and Rapid Decay of an Equatorial Disturbance," J. Appl. Met., 8, 799-814.